Black Hole Binary Formation and Mergers in Supermassive Black Hole Discs

Connar Rowan

St. Edmund Hall

University of Oxford

A thesis submitted for the degree of

Doctor of Philosophy

Trinity 2024

The lesson of the Impressionists is that it is better to be a big fish in a little pond than a little fish in a big pond.

– David and Goliath; Malcolm Gladwell

Abstract

Following the first gravitational wave (GW) detection in 2015, there have now been 90+ detections of merging black holes (BHs). In this thesis, BHs embedded in the gas discs of supermassive BHs within active galactic nuclei (AGN) are studied as a potential astrophysical source of these detections. In this channel, isolated BHs embed themselves in the AGN disc, encounter another in the disc, become bound via a complex interaction with the gas during the encounter, before gradually merging via gas driven inspiral. The binary formation and merger mechanism is modelled using both high resolution hydrodynamics and Monte-Carlo simulations.

Here, hydrodynamical simulations are performed of BH-BH interactions in AGN discs, showing that the energy of such encounters can be efficiently dissipated by the surrounding gas through a combination of accretion and gravitational drag, leaving behind a bound binary BH system (BBH). Binary capture of prograde and retrograde binaries can be successful in a range of AGN disc densities including cases well below that of theoretically predicted disc density. The majority of these captured binaries are then subsequently hardened by the surrounding gas. The eccentricity evolution depends strongly on the orbital rotation, where prograde binaries are governed by gravitational torques form their circumbinary mini-disc, with eccentricities being damped, while for retrograde binaries the eccentricities are excited to $\gtrsim 0.9$ by accretion torques. In certain cases, retrograde binaries can undergo a close periapsis passage which results in rapid merger via gravitational waves after only a few thousand binary orbits. Thus, the merger timescale can be far shorter than the AGN disc lifetime. These simulations support an efficient AGN disc merger pathway for BHs.

Exploring specifically the binary formation process using a large number of simulations over a range of impact parameters allowed further aspects of the mechanism to be quantified. A single range of impact parameters, typically of width $\sim 0.8 - 1.6$ binary Hill radii (depending on the AGN disk density) reliably leads to binary formation. The periapsis of the first encounter is the primary variable that determines the outcome of the initial scattering. The energy dissipated follows a power-law $\Delta E \propto r^{-0.42\pm0.16}$ with the periapsis, where deeper encounters dissipate more energy. An analytic criterion for predicting the outcome of an encounter is constructed that utilises only the pre-encounter energy and impact parameter to

determine the outcome of an encounter, with a reliability rate of >90%. As the criterion is based directly on the simulations, it provides a reliable and physically motivated criterion for predicting binary scattering outcomes which can be used in population studies of BH binaries and mergers around AGN.

Using a simplified Monte Carlo approach, a population of BHs and their interactions in AGN are simulated using the aforementioned capture criterion showing the AGN channel can be a non-negligible contributor to the observed BH merger rate. The model suggests the merging mass distribution is flatter than the observed distribution, where the anticipated rate relative to the observed rate for low mass BBHs ($<20M_{\odot}$) is $1\% - 33\%$ and $15\% - 100\%$ at the high mass end ($>50M_{\odot}$). Due to the complexity of the AGN channel, several simplifying assumptions are made throughout this thesis. Further more detailed work is needed to assess the sensitivity of these observational predictions to these assumptions.

In summary, the AGN channel remains an important mechanism for BH mergers, in particular for high mass BHs, with much work still to be done to further constrain its observational features.

Statement of Originality

I hereby declare that no part of this thesis has been accepted, or is currently being submitted, for any degree or diploma or certificate or any other qualification at the University of Oxford or elsewhere. Except where otherwise stated, the work in this thesis is entirely my own, and has been carried out under the supervision of Professor Bence Kocsis.

Chapter 4 was published in The Monthly Notices of the Royal Astronomical Society: Rowan, C., Boekholt, T., Kocsis, B., & Haiman, Z., **'Black Hole Binary Formation in AGN Discs: From Isolation to Merger'**, 2023, MNRAS, 524, 2770.

Chapter 5 was published in The Monthly Notices of the Royal Astronomical Society: Rowan, C., Whitehead, H., Boekholt, T., Kocsis, B. & Haiman, Z., **'Black hole binaries in AGN accretion discs - II. Gas effects on black hole satellite scatterings'**, 2024, MNRAS, 527, 10448.

Chapter 6 will be published in The Monthly Notices of the Royal Astronomical Society: Rowan, C., Whitehead, H. & Kocsis, B., **'Black Hole Merger Rates in AGN: Contribution from Gas-Assisted Binaries'**, est 2024.

This work was produced as part of the GALNUC group[1] and supported by the following sponsors: Science and Technology Facilities Council Grant Number ST/W000903/1, the European Research Council (ERC) under the European Union's Horizon 2020 research and innovation program under grant agreement No 638435 (GalNUC) attributed to Prof. Bence Kocsis, NASA ATP grant 80NSSC22K0822 attributed to Prof. Zoltan Haiman. The simulations of Chapter 5 utilised the Cambridge Service for Data Driven Discovery (CSD3), part of which is operated by the University of Cambridge Research Computing on behalf of the STFC DiRAC HPC Facility (www.dirac.ac.uk). The DiRAC component of CSD3 was funded by BEIS capital funding via STFC capital grants ST/P002307/1 and ST/R002452/1 and STFC operations grant ST/R00689X/1. DiRAC is part of the National e-Infrastructure.

[1] http://galnuc.elte.hu/

Acknowledgements

Personal

Above all, I would like to thank my supervisor, Bence Kocsis, for his encouragement, guidance, time, patience and the occasional beer. I could not have asked for a better mentor to help kickstart my academic career and it has been a privilege to be your student over the last four years. I thank my collaborators Tjarda Boekholt, Henry Whitehead and Zoltan Haiman for their input, discussions and the joy of working alongside. I also thank Robbie Ewart, Georgia Acton and Hanxi Wang of office 50.09 for their tremendous company and banter within the department.

I thank my friends Shannon Harris, David Hallengren[2] and Eleanor Braithwaite for being great friends and their support. Beth Mabbutt, Joe Morse, Jennifer Barton and Tatiana Eleanora receive my thanks for my venture into amateur theatre over the course of my PhD and their friendship. A special thank you goes to Charlotte Street for her love, support, wit and listening to my scientific rambles. My appreciation goes to my Suzuki SV650 for the two-wheeled rides to/from Oxford and rides alongside Kyle Jackson, providing zen during stressful times. Additional shout outs go to creme eggs, Hidetaka Miyazaki and Dr. Pepper. Finally, I would like to give my thanks and love to my parents Nicola and Craig for their relentless encouragement and belief in me. Thank you all!

[2]David Hallengren receives an additional thank you for the proof reading of this thesis.

Contents

List of Figures

Glossary

c	speed of light
G	gravitational constant
c_s	sound speed
Σ	surface density
ρ	density (three-dimensional)
T	Temperature
H	accretion disc scale height
M	mass
M_d	AGN disc mass
$\mathrm{M}_\odot$	solar mass
$M_\bullet$	SMBH supermassive black hole mass
$\dot{M}$	mass accretion rate
m_p	SPH particle mass
μ	reduced mass of two-body system
L_edd	Eddington Luminosity
r_H	Hill radius
r_acc	accretion radius
r_soft	softening radius
r_ap	apoapsis
r_per	periapsis
r_gw	gravitational wave radius
r_s	Schwarzschild radius of black hole
$r_\mathrm{min,i}$	orbital closest approach number i
R	two-dimensional radius (i.e cylindrical radius)
R_in	radius of inner edge of AGN disc

$\mathrm{R_{out}}$	radius of outer edge of AGN disc
R_{mid}	radial midpoint of AGN disc
i_{in}	inclination of inner binary orbit
i_{out}	inclination of outer binary orbit
e	eccentricity (scalar) of an orbit
α	disc viscosity
α_{SS}	Shakura-Sunyaev disc viscosity
l_{e}	Eddington ratio
ϵ	radiative efficiency
$\hat{\kappa}$	opacity relative to electron scattering opacity
E	energy
E_{bin}	binar two-body energy
q	binary mass ratio
t	time
$\varepsilon_{\mathrm{acc}}$	binary energy dissipation rate due to accretion
$\varepsilon_{\mathrm{grav}}$	binary energy dissipation rate due to gravitational interaction with gas
$\varepsilon_{\mathrm{SMBH}}$	binary energy dissipation rate due to gravitational interaction with SMBH
Δx	change in some quantity x
$\langle x \rangle$	quantity x averaged over a specified parameter
χ_{eff}	effective spin parameter of a binary
$\boldsymbol{r}$	position
$\boldsymbol{v}$	velocity
$\boldsymbol{a}$	acceleration
$\boldsymbol{L}$	angular momentum
$\boldsymbol{\tau}_{\mathrm{acc}}$	torque on binary due to accretion
$\boldsymbol{\tau}_{\mathrm{grav}}$	torque on binary due to gravitational interaction with gas
$\boldsymbol{\tau}_{\mathrm{SMBH}}$	torque on binary due to gravitational interaction with SMBH
$\boldsymbol{e}$	eccentricity (vector)

List of Abbreviations

1D, 2D, 3D . . One- or two- or three-dimensional, referring in this thesis to spatial dimensions in an image.

SPH . . . . . smooth particle hydrodynamics

GW . . . . . gravitational wave

BH . . . . . black hole

BBH . . . . . binary black hole

IMBH . . . . . intermediate mass black hole

SMBH . . . . . supermassive black hole

AGN . . . . . active galactic nuclei

CSMD . . . . . circum-single mini disc, here referring to the gas disc around a singular BH

CBMD . . . . circum-binary mini disc, here referring to the gas disc around two BHs in a binary system

ISCO . . . . . innermost stable circular orbit of two massive objects under general relativity

LS . . . . . left sided (encounter)

RS . . . . . right sided (encounter)

TA . . . . . turnaround (encounter)

ZAMS . . . . . Zero Age Main Sequence

IMF . . . . . initial mass function

BIMF . . . . . black hole initial mass function

SgrA* . . . . . Sagittarius A*

P^n**N** . . . . . Post Newtonian correction to order n from zeroth order post Newtonian expansion of binary motion.

1

Introduction

The observation of the inspiral and merger of black holes (BHs), predicted by Albert Einstein's theory of general relativity (Einstein, 1918), represents a paradigm-shifting discovery in astrophysics. Over the last decade, advanced observational techniques using laser interferometry from observatories such as LIGO, VIRGO and KAGRA have successfully detected and characterised gravitational waves emanating from these mergers. These detections have not only further confirmed the existence of BHs but have provided the opportunity to explore the cosmos through the ripples in spacetime itself. This work embarks on a multifaceted journey, embracing the challenge of deciphering BH mergers at the crossroads of theoretical astrophysics, gravitational wave astronomy, and numerical simulations. The ultimate aim is to unravel the mechanisms of these events and their profound consequences for our understanding of the newly discovered gravitational wave signals. This involves exploring the dynamics of binary black hole (BBH) systems, the intricacies of their inspiral and merger, as well as how frequently we should expect this to happen for a given set of initial conditions.

A BH is a massive object first predicted mathematically by Karl Schwarzschild in 1916 (Schwarzschild, 1916, 1999). One is formed when some mass of matter at some given point in space can no longer support itself from its own self-gravitational collapse through electron degeneracy (Chandrasekhar, 1931) or even

neutron degeneracy pressure (Oppenheimer & Volkoff, 1939). As there is insufficient stopping force, this results in the mass collapsing to a singular point of infinite density or a 'singularity'. Such conditions are only met in sufficiently dense and massive objects such as the cores of giant stars. Upon their formation, BHs can gain mass if material flows within their *event horizon*, the maximum distance from the BH where the escape velocity still exceeds the speed of light. Additionally, BHs can grow in size by merging with other BHs and compact objects like neutron stars. Indeed, it is thought that the supermassive black holes (SMBHs) expected to be at the centre of every large galaxy formed early on in the universe through repeated consumption of stars and compact objects (Portegies Zwart & McMillan, 2002; Kormendy & Ho, 2013; Haiman, 2013; Askar et al., 2021)

In keeping with their name, BHs and even SMBHs do not emit detectable radiation themselves. However, their immense gravity allows for their indirect detection through several means, including: gravitational lensing (Walsh et al., 1979), mapping local star kinematics (Trippe et al., 2008; Ghez et al., 2008; Gillessen et al., 2009; Gültekin et al., 2009) and now recently gravitational wave events Abbott et al. (2016). Though, in the presence of dense gas, BHs can accrete gas highly efficiently.

If the gas is rotating sufficiently, BHs may form their own accretion disc of gas that orbits around them. The viscous heating from the inner portions of these discs close to the BHs excites the gas to such extreme temperatures that they become highly luminous. In the case of about $\sim 5\%$ of low redshift galaxies (Chung et al., 2014), their SMBHs have a particularly massive accretion disc at their centre, whose luminosities exceed the combined brightness of their stars and the energy accreted by the SMBH can exceed the binding energy of its host galaxy (Fabian, 2012). Such systems are known as Active Galactic Nuclei (AGN) and are among the brightest single objects in the Universe. Aside from their raw luminosity, AGN can be identified by specific electromagnetic (EM) features. These include: iron X-ray line emission (Reynolds et al., 1999), broad and narrow UV/optical emission line features (Boroson & Green, 1992; Bentz et al., 2013), large extended radio lobes (Fanaroff & Riley, 1974; Croton et al., 2006), relativistic jets (Doeleman et al., 2012) and high emission variability (Shappee et al., 2014).

For sufficiently nearby or bright sources, SMBHs in galaxies that are not host to AGN can also be observed through radio-synchrotron emission and resolved down

to very small scales using the event horizon telescope (Event Horizon Telescope Collaboration et al., 2019, 2022). The caveat of all EM observations is that they rely on the source being sufficiently bright against any background environment. Stellar mass BHs ($\sim 5 - 100 M_\odot$), which are vastly more common and far less massive than their SMBH ($> 10^6 M_\odot$) counterparts, have mostly been identified through GWs. EM evidence for stellar mass BHs include: X-ray binary systems (e.g. Remillard & McClintock, 2006) and systems with observable radial Doppler shifting (e.g. Thompson et al., 2019; Jayasinghe et al., 2021), discussed in detail in sec 2.5.6.

In order for a pair of $10 M_\odot$ BHs to merge within a Hubble time, their orbital separation must be extremely small, $\lesssim 0.1$au. Only then can gravitational waves (the emitted power of which scales with the orbital separation to the inverse fourth power) efficiently radiate enough of their remaining orbital energy and allow them to merge within this time constraint. Although we have now observed many gravitational wave events, which can only have come from compact object mergers, how they are evidently reaching small enough separations remains a mystery. At present, GW detections have only been made for BHs of stellar mass. There are several proposed mechanisms for binary mergers in this mass range, such as:

1. BH interactions in star clusters, where binaries may dynamically form through multibody interactions or stellar binary evolution and become increasingly hardened towards merger through subsequent encounters with stellar mass objects (i.e. stars or other BHs).

2. Isolated stellar binary evolution, where two high mass stars evolve together, forming BHs that then merge through interaction with the remaining gas.

3. BH-BH dynamical encounters within the massive accretion discs of AGN, where the high gas density is thought to assist their formation and reduce their separation through complex gravitational interplay between itself and the BHs.

The reported rates and properties (i.e. spins, masses and mass ratios) of BH mergers from each channel are still heavily debated, thus there is currently little consensus on which merger channel is producing the majority of events observed from GW observatories. Often, when predicted rates are combined, they overproduce

observed merger rates (for a review, see Mandel & Farmer, 2022). Predicting merger rates often requires performing population synthesis or semi-analytic studies which are dependent on making simplifications for physics on small spatial and time scales (e.g. Antonini & Rasio, 2016; Tagawa et al., 2020a; Mapelli, 2020; Ford & McKernan, 2022). Therefore, providing accurate prescriptions for small scale physics is essential for producing accurate rate estimates. This work aims to contribute significantly to our understanding of the AGN channel. This is primarily achieved through performing many high resolution hydrodynamical simulations of interacting BHs embedded in AGN discs. From these, the complex interaction between the gas and the binary BHs during the binary formation and evolution phase is examined. Where possible, elements of simulations are transposed into analytic form to provide physically informed prescriptions that may be used by the community to further the constrain BH merger rates and parameter distributions of the merging binaries from AGN.

This thesis is based on two publications, Rowan et al. (2023) and Rowan et al. (2024) as well as work from another paper in preparation. The structure of the thesis is as follows: An overview of each relevant component of the AGN system from the disc to the BH physics is given in Chapter 2. The code PHANTOM used to perform the hydrodynamics and the complexities of numerically simulating such a system are described in Chapter 3. Chapter 4 discusses the first 'proof of concept' simulations of BBH formation and evolution in AGN discs. The capture process itself is more rigorously analysed in Chapter 5. Finally, rates incorporating what was learnt from the previous two chapters are calculated in Chapter 6. The summary and conclusion of the thesis is given in Chapter 7.

2

Background

Contents

2.1 Overview of Gravitational Waves

2.1.1 Observing stellar mass BH mergers

In classical physics, GWs are a result of gravitational field changes being transmitted at the speed of light c and not instantaneously. A change in a gravitational field is only observed after the light travel time from the source to the observer. For the circular orbit of two BHs, an observer would experience field strength variations with a frequency of twice the binary period as the objects approach and recede from the observer (Peters & Mathews, 1963; Peters, 1964). These variations can be observed through measuring the contraction and stretching of space induced by the periodic ripples in space-time. Current GW observatories measure these warps using laser interferometry, where a carefully calibrated laser beam is split at 90° and directed down two long beam arms (4km for LIGO) before being reflected back to the point of origin by mirrors. An incident GW causes the length of one arm to increase while the other decreases, which is measured using the phase change between the split beams, since the photon flight time along each beam arm differs according to the change in beam length. The phase change is determined from the interference pattern produced when the two beams are recombined. From the phase difference, one can calculate the GW strain h, defined as the fractional change ΔL in length of each arm of the interferometer L_1 and L_2, where L is the unperturbed detector arm length.

$$h(t) = \frac{|L_1(t) - L_2(t)|}{L} = \frac{\Delta L(t)}{L}\,. \tag{2.1}$$

This strain is very small, with LIGO being able to detect length changes down to a minimum[1] of $\sim 10^{-21}$ (see Buikema et al., 2020).

[1]Making LIGO technically the worlds most accurate ruler!

Other GW sources

This thesis focuses solely on improving our understanding of GW signals from merging BBH systems. Other GW sources not discussed in this work include: BBH mergers in isolated triples and quadruples (Antonini et al., 2014; Meiron et al., 2017; Safarzadeh et al., 2020; D'Orazio & Loeb, 2020), primordial BH mergers (Sasaki et al., 2016; Kavanagh et al., 2018), BH dark matter (Clesse & García-Bellido, 2017; Bertone et al., 2020), mergers/deformations of neutron stars (Bildsten, 1998; Ushomirsky et al., 2000; Abbott et al., 2017a,b,c, 2019a; Burns, 2020), tight pulsar binaries (Demorest et al., 2010; Antoniadis et al., 2013), ambient stochastic GW background (Sesana et al., 2008; Fryer et al., 2012; Caprini & Figueroa, 2018; Ginat et al., 2024), supernovae (Dimmelmeier et al., 2008; Ott, 2009) and cosmic strings (Hindmarsh & Kibble, 1995; Chang & Cui, 2022).

2.1.2 Gravitational inspiral of two BHs

The Newtonian approximation

In a more mathematical context, GWs are generated by variations in the mass multipole moments of the system. Consider the mass moments of an isolated binary system. The monopole moment is the total mass of the system, which is non-oscillating. The dipole moment (centre of mass) is also non-oscillating as there are no negative masses. The quadrupole moment however, can oscillate in time, leading to the radiation of the binary orbital energy (and mass) in the form of GWs.

Consider a BBH on a circular orbit with orbital energy $E = -GM\mu/(2r)$ and frequency $\Omega = G^{1/2}M^{1/2}r^{-3/2}$, where $M = M_1 + M_2$ is the total binary mass, $\mu = M_1M_2/M$ is its reduced mass, r is the orbital separation and G is the gravitational constant. The inspiral rate is given by the loss of energy per time t, calculated from the Newtonian quadrupole formula (Einstein, 1918; Misner et al., 2018)

$$\frac{\mathrm{d}r}{\mathrm{d}t} = -\frac{r}{E}\frac{\mathrm{d}E}{\mathrm{d}t} = -\frac{64}{5}\frac{G}{c^5}\frac{\mu M^2}{r^3}\,. \tag{2.2}$$

Integrating Eq. (2.2) above gives the inspiral timescale from some initial separation r_i. For a sufficiently circular orbit, the inspiral timescale is given by (Peters, 1964)

$$t_\mathrm{inspiral} = \frac{5}{256}\frac{c^5}{G^3}\frac{r_\mathrm{i}^4}{M_1M_2(M_1+M_2)}\,. \tag{2.3}$$

For highly eccentric binaries, which are prevalent in the AGN channel as we will see in Chapter 4, the orbital energy dissipation via GWs is dominated by emission during periapsis. In this regime, the dissipation can be calculated explicitly per periapsis passage from the minimum separation $r_{\rm per}$ as (e.g. Turner, 1977; Samsing et al., 2018):

$$\frac{\Delta E_{\rm GW}}{P} \approx \frac{85\pi}{12\sqrt{2}} \frac{G^{7/2}}{c^5} \frac{M_1^2 M_2^2 \sqrt{M_1 + M_2}}{r_{\rm per}^{7/2}}. \tag{2.4}$$

From the r_i^4 scaling of Eq. (2.3) and $r_{\rm per}^{7/2}$ scaling of Eq. (2.4), the inspiral rate is highly nonlinear with separation. As the binary orbit shrinks, its orbital period also decreases rapidly. This leads to a sharply increasing frequency in the emitted GWs and the strain $h(t)$, producing the aptly named 'chirp' waveform associated with the observed GW signal during their inspiral.

To illustrate just how close BHs must reach to efficiently merge, consider two $10{\rm M}_\odot$ BHs at a distance of 0.1au. The merger timescale is $t_{\rm inspiral} \approx 1.1 H_t$, where H_t is a Hubble time. For a merger to occur in the span of a human lifetime, the relative separation of the same two BHs is on the order of just a few tenths of a solar radius. Given binary stars of sufficient mass to form BHs do not typically form at such small separations (e.g. Duquennoy & Mayor, 1991; Bate et al., 2002; Connelley et al., 2008), an additional mechanism of reducing the separation of a BH binary is required depending on their origin, which will be discussed in section 2.6.

Post-Newtonian expansion

The Newtonian approximation only applies when the ratio of the binary mass to its separation is sufficiently small, where $GM/(c^2 r) \ll 1$, so one can assume a nearly flat space with low velocities v such that $v/c \ll 1$. This assumption breaks down closer to merger. As a midway step between the Newtonian approximation and full numerical relativity, a post-Newtonian expansion of the energy dissipation in terms of increasing orders of $(M/r)^n$ can be made (e.g. Wagoner & Will, 1976; Blanchet, 2014). The expansion involves increasing orders of (v/c), where $GM/(c^2 r) \sim v^2/c^2$ for approximately circular orbits by Kepler's law. The nth PN term is labelled according to the expansion of order $(v/c)^{2n}$, i.e., $\mathcal{O}(v/c)^2 \sim 1$PN, $\mathcal{O}(v/c)^4 \sim 2$PN.

Elements of the expressions with odd n in the expansion $(1/c)^n$ are labelled 1.5PN, 2.5PN etc. The post-Newtonian acceleration of the BHs up to 2.5PN order is

$$\boldsymbol{a} = \underbrace{\boldsymbol{a}_0}_{\text{Newtonian}} + \underbrace{\overbrace{\boldsymbol{a}_2 c^{-2}}^{\text{1PN}} + \overbrace{\boldsymbol{a}_3 c^{-3}}^{\text{1.5PN}} + \overbrace{\boldsymbol{a}_4 c^{-4}}^{\text{2PN}}}_{\text{conservative terms}} + \underbrace{\overbrace{\boldsymbol{a}_4 c^{-5}}^{\text{2.5PN}}}_{GW rad.} + \mathcal{O}(v/c)^{-(6+)}\,, \tag{2.5}$$

$$\tag{2.6}$$

where the first term $\boldsymbol{a}_0$ is the Newtonian acceleration and the second and third terms ($\boldsymbol{a}_2$ and $\boldsymbol{a}_4$) are the conservative terms that induce a phase shift in the orbital periapsis (i.e. orbital precession). The last is the leading order non-conservative acceleration due to GW emission backreaction. A reliable Post-Newtonian expansion for highly eccentric binaries has not yet been provided in the literature due to the introduction of greater statistical errors compared to circular waveforms when fitting to observed signals (e.g. Loutrel & Yunes, 2017; Hinderer & Babak, 2017; Huerta et al., 2018; Tanay et al., 2019; Ramos-Buades et al., 2022).

2.2 GW signal properties

When detecting a GW, there are two polarisations in its waveform. The detected signal is then by construction a linear combination of the two polarisations, weighted by factors such as the relative orientation of the interferometer arms and the binary orbital inclination. As a binary enters the final moments of its inspiral and becomes detectable, its amplitude and frequency increase rapidly as its semi-major axis a rapidly shrinks, with the time averaged shrinkage given by Peters (1964):

$$\left\langle \frac{da}{dt} \right\rangle = -\frac{64}{5} \frac{G^2 M_1 M_2 (M_1 + M_2)}{c^5 a^3 (1-e^2)^{7/2}} \left(1 + \frac{73}{24} e^2 + \frac{37}{96} e^4\right). \tag{2.7}$$

Following the merger, a final GW signal is emitted due to oscillations of the merged remnant BH, known as the *ringdown* period (e.g. Ma et al., 2022), visible as an exponentially decaying amplitude at constant frequency[2]. Figure 2.1 shows the first GW detection from 2015 (Abbott et al., 2016). Several physical properties of the binary are discernible from the signal. The frequency drift during the inspiral

[2]One can compare inspiral to the final moments of a spinning coin when it loses most of its angular momentum and is nearly co-planar with a table, where the sound rapidly increases in frequency while its vertical amplitude decreases.

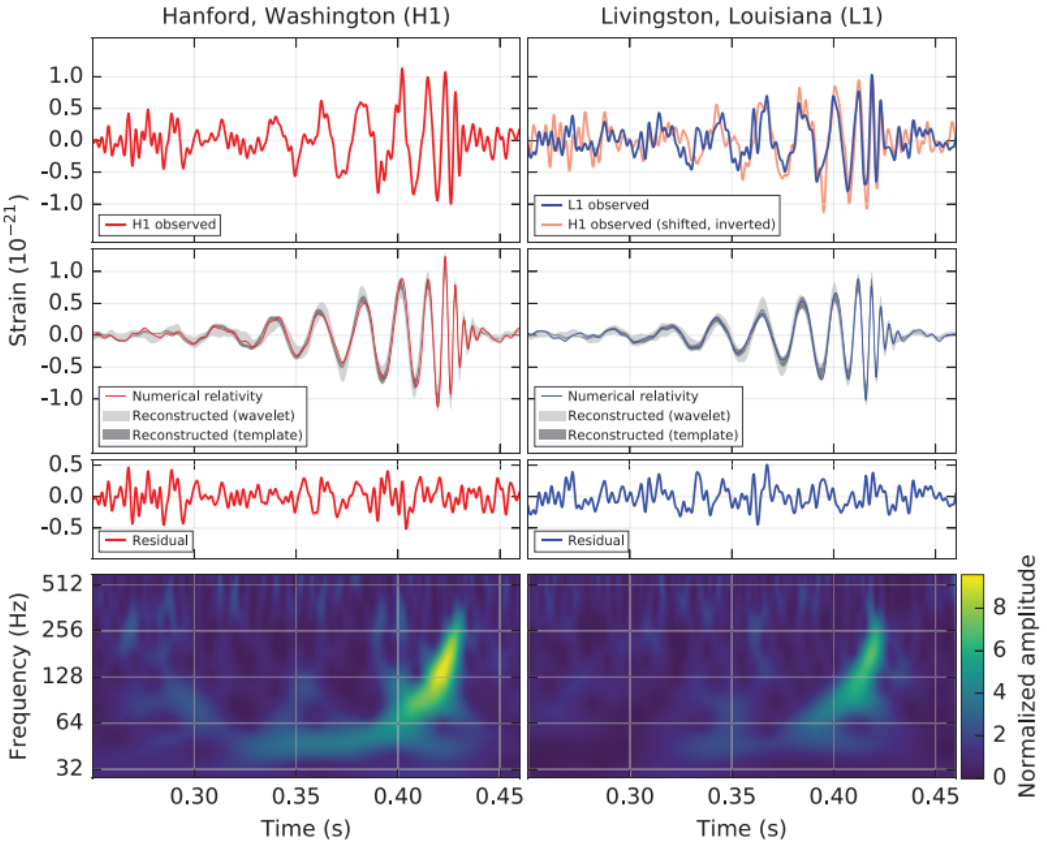

Figure 2.1: The first detection of a BH merger, made by LIGO in 2015 (taken from Abbott et al., 2016). *Top row:* the raw strain measured from LIGO. *Middle row:* the expected result from the best fit waveform constructed from numerical relativity. *Bottom row:* frequency and amplitude of the strain oscillations. The left and right columns represent the data from the Hanford and Livingston detectors respectively.

allows us to deduce the *chirp* mass, $\mathcal{M}$. Calculating its value requires determining both the GW frequency f and its derivative $\dot{f}$ as the binary coalesces (i.e. bottom panel in Figure 2.1), in addition to the redshift z (distance) to the source that can be calculated from the signal amplitude (e.g Cutler & Flanagan, 1994):

$$\mathcal{M}(1+z) = \frac{c^3}{G}\left(\frac{5}{96}\pi^{-8/3} f^{-11/3}\frac{\mathrm{d}f}{\mathrm{d}t}\right)^{3/5} . \tag{2.8}$$

The chirp mass is related to the actual total binary mass M and reduced mass μ via

$$\mathcal{M} \equiv \frac{(M_1 M_2)^{3/5}}{(M_1+M_2)^{1/5}} = \mu^{3/5} M^{2/5} = \left[\frac{q}{(1+q)^2}\right]^{3/5} M\,, \tag{2.9}$$

where $q = M_2/M_1$ is the mass ratio with $M_2 \leq M_1$. Closer to merger, expansion to 1.5PN order corrections beyond the leading order term in the BBH evolution

allows μ to be disentangled (from 1PN) and the presence of possible BH spins identified (from 1.5PN). The 1PN and 1.5PN (spin) correction to $\dot{f}$ in Eq. (2.8), assuming spinning BHs, is

$$\frac{\mathrm{d}f}{\mathrm{d}t} = \overbrace{\frac{96}{5}\pi^{8/3}\mathcal{M}^{5/3}f^{11/3}}^{\text{Newtonian}}\Bigg[1-\overbrace{\underbrace{\left(\frac{743}{336}+\frac{11\mu}{4M}\right)(\pi Mf)^{2/3}}_{\text{1PN}}+\underbrace{(4\pi-\beta)(\pi Mf)}_{\text{1.5PN Spin modification}}+\underbrace{\mathcal{O}(\pi Mf)^{4/3}}_{\text{2PN}}}^{\text{Post Newtonian}}\Bigg], \tag{2.10}$$

with β as the spin-induced modification to $\dot{f}$ (Cutler & Flanagan, 1994; Poisson & Will, 1995)

$$\beta \equiv \frac{\hat{\boldsymbol{L}}}{M^2}\cdot\left[\left(\frac{113}{12}+\frac{25M_2}{4M_1}\boldsymbol{S}_1\right)+\left(\frac{113}{12}+\frac{25M_1}{4M_2}\boldsymbol{S}_2\right)\right]. \tag{2.11}$$

Here, $\hat{\boldsymbol{L}} = \boldsymbol{L}/\|\boldsymbol{L}\|$ is the unit Newtonian angular momentum vector of the binary. Since the spins only affect the waveform's phase via particular combinations of their components, it is difficult to constrain them individually as we can only disentangle them by observing their precession (Vitale et al., 2014; Pürrer et al., 2016; Vitale & Evans, 2017). What can be measured (to leading order) is known as the *effective* spin parameter χ_{eff}, inferred from Eq. (2.11) as

$$\chi_{\text{eff}} \equiv \left(\frac{M_1\boldsymbol{\chi}_1+M_2\boldsymbol{\chi}_2}{M}\right)\cdot\hat{\boldsymbol{L}}\,, \tag{2.12}$$

where $\boldsymbol{\chi_i} = \boldsymbol{S}_i c/(Gm_i^2)$ are the dimensionless spin parameters of the binary BHs. It represents the mass-weighted combined spin of the BHs projected along the angular momentum vector of the binary. The BH spins produce a phase modulation in the GW signal, shown to leading order in Eq. (2.10), that can in principle be measured provided the GW signal remains in the detectable frequency/amplitude regime for enough periods and a sufficiently large signal-to-noise ratio (SNR). Additionally, if the spins of the BHs are not aligned with $\hat{\boldsymbol{L}}$ ($\chi_{\text{eff}} \neq 1$), then the orbital plane of the binary precesses about the total momentum vector of the binary, $\boldsymbol{L}+\boldsymbol{S_1}+\boldsymbol{S_2}$, inducing a modulation in the observed polarisation of the GW signal (see Apostolatos et al., 1994; Vecchio, 2004).

2.3 Measuring properties from GWs

To determine each of the binary parameters, wave templates are generated for combinations of each independent parameter ($\mathcal{M}$, μ, β etc.) and then compared to the detected GW waveform. This is computationally expensive: each parameter must be sampled with a high density and the parameter space for the analysis is typically over 15 parameters. The templates used by LIGO/VIRGO are 'hybrid' waveforms where the initial lead up to merger is analytically determined but as the post Newtonian assumption breaks down near merger (Tagoshi & Sasaki, 1994), the late stages of the waveform are generated from numerical relativity, adding to the expense. In numerical relativity, Einstein's equations are solved through numerical integration, for example using adaptive-mesh-refinement (Schnetter et al., 2004; Pretorius, 2005), spectral methods (Canuto et al., 2006; Pürrer, 2014; Khan et al., 2016) and excision methods (Anninos et al., 1995; Alcubierre & Brügmann, 2001; Baker et al., 2006). For a more detailed discussion of GW signals, see Cutler & Flanagan (1994); Poisson & Will (1995); Lehner (2001); Campanelli et al. (2006); Blanchet (2014); Khan et al. (2016).

2.4 Selection effects

Analogous to traditional astronomy, there is a selection bias towards detecting more massive/luminous systems. The amplitude of a GW signal and hence its maximal observable distance scales as $\mathcal{M}^{5/6}$ (O'Shaughnessy et al., 2010; Dominik et al., 2015; Yang et al., 2020). Therefore, the bias in the frequency of detections scales with the volume, i.e. $\mathcal{M}^{5/2}$. By the same logic, we can more easily observe mergers in our local cosmological vicinity; redshifts of current detections lie in the range of $0.05 < z < 0.9$ (Fishbach et al., 2021).

Eccentric mergers have additional harmonics in their GW signal, complicating the wave-form fitting procedure. Achieving a large SNR for eccentric binaries is easier (see O'Leary et al., 2009), however the waveform fitting requires significantly more templates, leading to greater uncertainties in the fit parameters (Romero-Shaw et al., 2019, 2023). In fact, early analysis of GW detections assumed circular or near circular waveforms as in Peters (1964), though later re-evaluation supports these early detections having near circular features with maximal eccentricities of

< 0.05 (Romero-Shaw et al., 2019). As the phase modulation of the GW signal from eccentricity and BH spin occurs on timescales larger than the binary orbital period, many periods (to measure e) and a few spin precession orbits (to measure spin) must occur within the timeframe the SNR is large enough. Further complicating eccentricity measurements is its degeneracy with spin effects (e.g. Romero-Shaw et al., 2023), since spin and eccentricity induce phase and amplitude modulations in the GW signal. Though the phase modification from each is different, the short time domain of the detections above significant SNR heavily restricts our ability to disentangle the two effects, leading to the degeneracy (Lower et al., 2018). There are also correlated uncertainties when fitting additional parameters, i.e. the binary orbital inclination, sky position and the distance to the source (Chassande-Mottin et al., 2019).

The task of fitting waveforms (Sec. 2.2 & 2.3) makes discerning physical parameters of the binaries a difficult endeavour. To comment on the astrophysical source of these mergers, we also need great enough statistics to begin to compare observed distribution of merging parameters with the anticipated distributions of each merger mechanism. As will be explained later, these are primarily the masses, spin and eccentricity distributions. Only in the last few years have we transitioned to this statistical era of GW detections and naturally there is a race in the community to explain what is driving the observed distributions.

2.5 Observations thus far

To date, there have been 90 announced GW events (e.g. Abbott et al., 2016, 2019b; Venumadhav et al., 2020; Abbott et al., 2020a,d,e, 2023b), with 105 more preliminary announcements from the LIGO public alerts list [3]. Created by the LIGO Scientific Collaboration, Figure 2.2 shows the masses of all observed compact objects from varying methods of detection. Since LIGO's first detection in 2015, GW mergers now make up a significant portion of compact object identifications.

[3] see https://gracedb.ligo.org/superevents/public/O4/ for the current number of alerts.

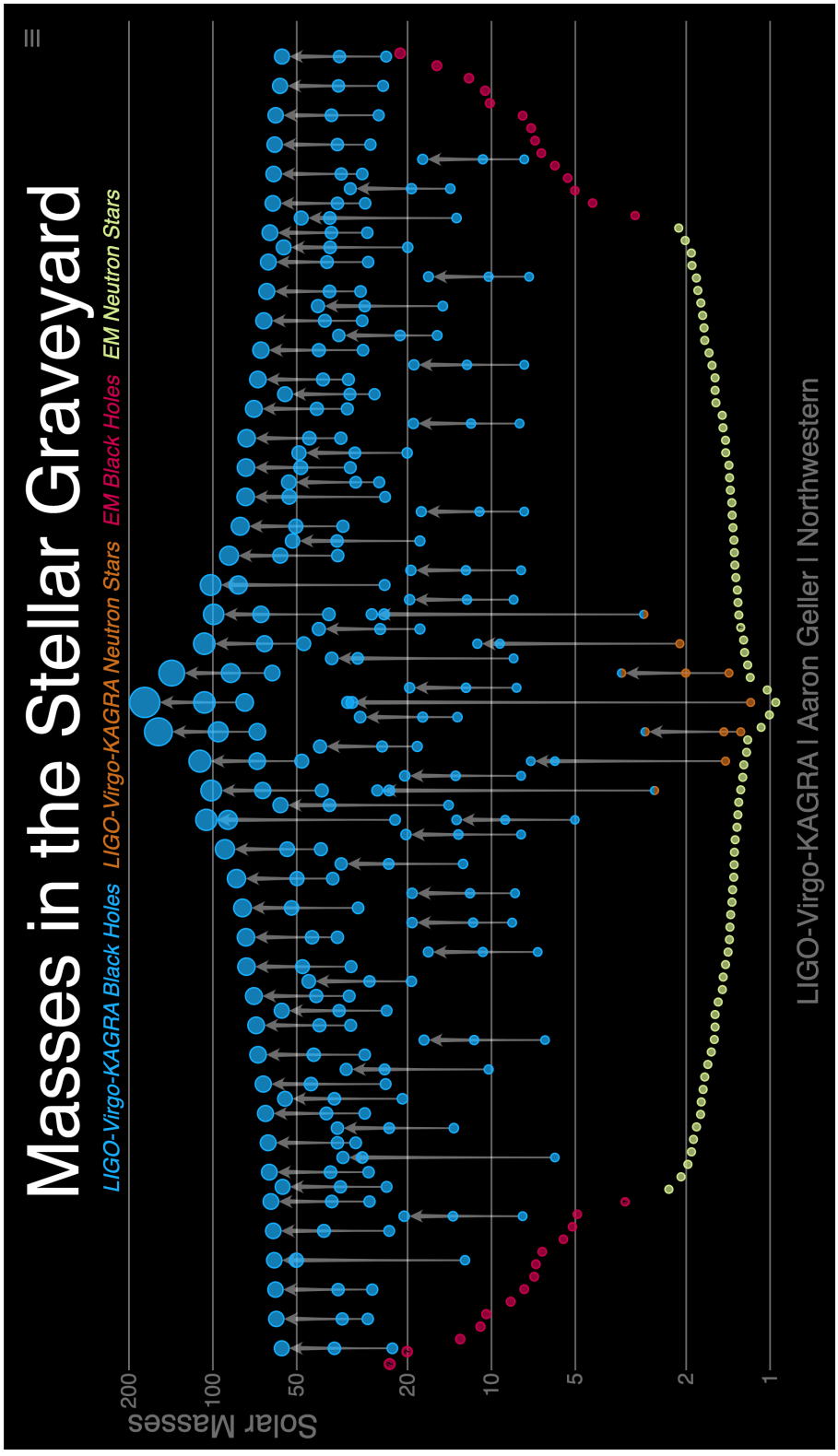

Figure 2.2: Masses of observed stellar mass compact objects to date. *Blue:* initial and resulting mass of objects from BH mergers. *Orange:* initial and resulting mass of objects from neutron star mergers. *Red:* BHs detected from EM observations. *Yellow:* neutron stars detected from EM observations. Image credited to: LIGO-Virgo Collaboration / Aaron Geller / Northwestern University.

2.5.1 BHs in the mass gap

Of particular interest to the astrophysics community is the detection of BH mergers where one or more of the original BHs have masses in the pair-instability mass gap. The first such detection, GW190521, had parent BHs with both masses ($66M_\odot$ and $85M_\odot$) in and above the mass gap of $\sim 45 - 120M_\odot$.

The gap arises from the final evolution of massive stars with zero age main sequence (ZAMS) masses between $\sim 130 - 250M_\odot$. Upon the collapse of their core, gamma rays have sufficient energy to become annihilated in the coloumb field of other charged particles to produce an electron and positron 'pair' (Fryer et al., 2001). The reduction in the photon density then reduces the radiation pressure, allowing the core to rapidly compress until the over-pressure induces runaway fusion and sudden neutrino production via reverse beta decay, producing on the order of $\sim 10^{46}$J of energy. The energy produced exceeds the binding energy of the star and it is entirely disrupted before any core remnant can be formed (Rakavy & Shaviv, 1967; Belczynski et al., 2016). Since BHs in this mass range cannot originate as stellar remnants, this implies the objects merging in these cases must themselves have been the result of prior mergers (O'Leary et al., 2016; Gerosa & Berti, 2019; Gerosa & Fishbach, 2021; Tagawa et al., 2021d) or accreted additional mass (Safarzadeh et al., 2020). That is to say, isolated stellar binary evolution likely cannot explain all the masses of the BHs observed from our GW detectors. The observed range of M_1 BH masses stretches from $\simeq 2.6M_\odot$ (GW190814, see Abbott et al. 2020e) to $\simeq 85M_\odot$ (GW190521, see Abbott et al. 2020b). Despite the observational mass bias in the likelihood of detections, the majority of merging BHs have both BH masses less than $\sim 45M_\odot$.

2.5.2 Spin and mass distribution

Following the first (-O1) and second (-O2) observing run by LIGO and VIRGO, which identified three and eight merger candidates respectively (Abbott et al., 2019b), the 80+ detections from the third (-O3) run have allowed us to begin to parameterise the distribution of the mergers. This has lead to the identification of substructure in the merger rate over the mass distribution (see Figure 2.3), after the selection effects described in Sec. 2.4 are accounted for. From Figure 2.3, the mass

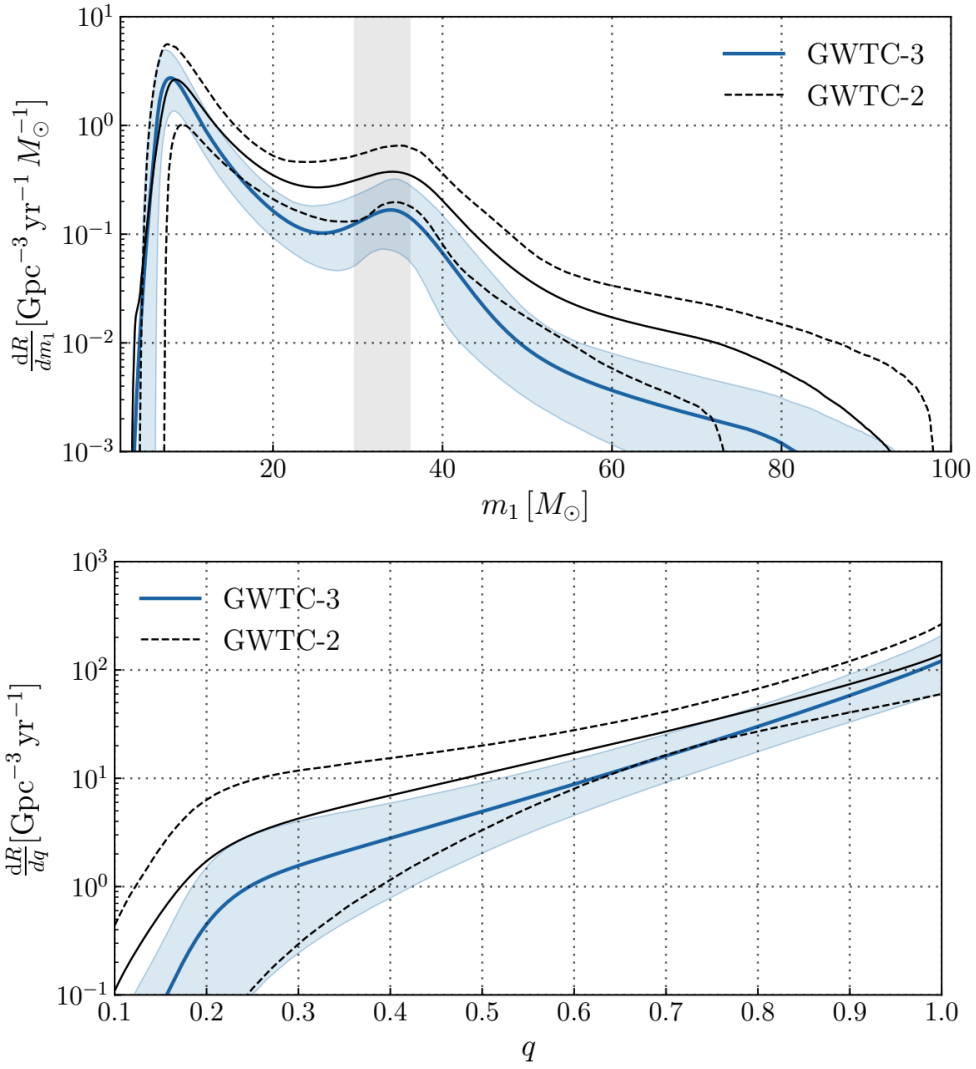

Figure 2.3: *Top*: Merger rate per primary mass m_1 of GW detections from the third and earlier LIGO-VIRGO-KAGRA observing runs as a function of m_1. *Bottom:* Merger rate distribution over mass ratio $q = m_2/m_1$. Adapted from Abbott et al. (2023a).

distribution for the more massive BH in the merger follows an approximate power law with a secondary peak at $\sim 35M_\odot$. The twin peak structure and high mass mergers like GW190521 point towards repeated mergers, where lower mass BHs merge to form higher mass BHs that then go on to merge again with another BH (Gerosa & Fishbach, 2021). The distribution of the binary mass ratio is strongly in favour of equal ($q = 1$) masses (Figure 2.3) with a power law slope above $q > 0.2$ of $f(q) \propto q^a$, $a = 1.1^{+1.7}_{-1.3}$. Observations of unequal mass mergers have been made,

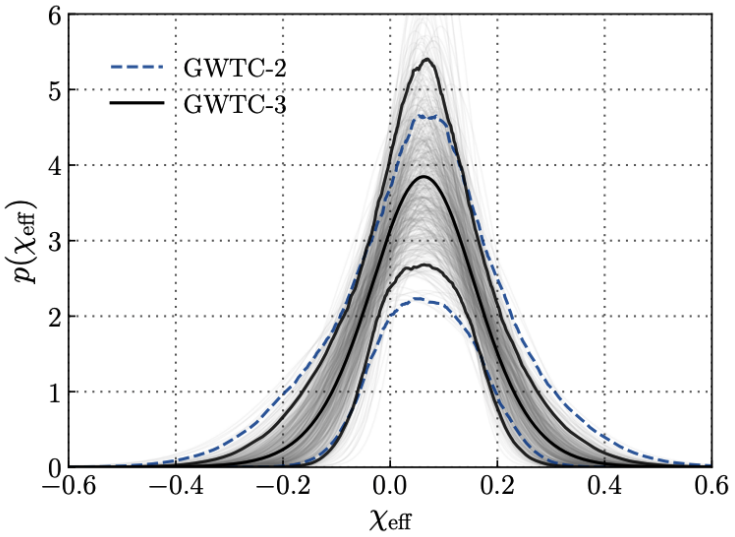

Figure 2.4: Distribution of effective spin parameter $\chi_{\rm eff}$ (see Eq. 2.12) of detections from the third and earlier LIGO-VIRGO-KAGRA observing runs, exhibiting a slight bias towards $\chi_{\rm eff} > 0$. Adapted from Abbott et al. (2023a)

such as GW190412 with $M_1 : M_2 = 3 : 1$ or the biggest outlier GW190814[4] with a mass ratio of roughly 9 : 1 (Abbott et al., 2020f).

The distribution of effective BH spins ($\chi_{\rm eff}$), shown in Figure 2.4, points to most merging systems having zero effective spin. In fact, Galaudage et al. (2021) estimate to 90% confidence that $69 - 90\%$ of observed systems have a negligible $\chi_{\rm eff}$. The left over percentage that have non negligible spins have a strong bias towards $\chi_{\rm eff} > 0$. The spin distribution may be coupled to the formation environment of the BH binary (see Sec. 2.6), so constraining the anticipated distribution from each merger channel is at present a very hot topic in the literature. As detailed later, this is a highly non trivial problem (Berti & Volonteri, 2008; Fragione & Kocsis, 2020; Tagawa et al., 2021b).

2.5.3 Eccentricity

Eccentricity arguably presents the best indicator for distinguishing formation channels, or at least between isolated stellar binary evolution and dynamical channels (i.e. BH scatterings in star clusters & AGN), see Sec 2.6. There is

[4]It is uncertain whether the smaller object is the smallest BH or the largest neutron star ever observed to date.

a large preference towards binaries with zero or near zero eccentricity (e.g. Romero-Shaw et al., 2019), with support for only four potentially eccentric binaries from -O3 having non-negligibly eccentric ($e > 0.1$) detections (e.g. Romero-Shaw et al., 2022), the strongest example being GW190521. Note that for the reasons detailed in Sec. 2.4, definitively determining binary eccentricities based on the GW signal morphology may not be possible due to the degeneracy with spin and the currently incomplete set of model waveforms for higher eccentricities. Until these waveforms are known, eccentricity in sources could be missed for highly eccentric sources.

2.5.4 Merger rates

From the results of all current observing runs from LIGO-VIRGO-KAGRA, the inferred merger rate spanning the entire mass distribution lies within $\sim 24.8 - 63.6\text{Gpc}^{-3}\text{yr}^{-1}$ (Abbott et al., 2023a). This figure assumes a constant merger rate with redshift, though there is strong evidence that the merger rate increases with redshift (e.g. Fishbach et al., 2018; Yang et al., 2020; Abbott et al., 2023a). When redshift is accounted for, the local ($z = 0.2$) rate is estimated to be $17-44\text{Gpc}^{-3}\text{yr}^{-1}$. The relative rate of binary mergers in certain mass bins can help constrain the contribution from each proposed merger mechanism, discussed in 2.6. In Abbott et al. (2023a), the merger rate density for binaries with primary mass M_1 in the ranges $[5\text{–}20]M_\odot$,$[20\text{–}50]M_\odot$ and $[50\text{–}100]M_\odot$ are 13-39, 2.5-6.3 and 0.1-0.4$\text{Gpc}^{-3}\text{yr}^{-1}$ respectively (Abbott et al., 2023a).

2.5.5 Sky localisation

Constraining the origin of GW sources on the sky is a difficult task. Before Virgo, localisation of GW sources using LIGO Livingston and LIGO Hanford could only generate a 90% confidence interval of at least a few hundred deg^2. Now with Virgo, the most accurately estimated positions lie within $\sim 20\text{deg}^2$ (e.g. Venumadhav et al., 2020). As a consequence, it has often not been possible to associate most GW events with a single host galaxy in the sky. Exceptions to this are the EM detection of the neutron star merger GW170817 (Smartt et al., 2017), discussed in 2.5.6 below, and the possible flare coincident with S190521g (Graham et al., 2020).

2.5.6 Electromagnetic signatures

Even prior to the first GW detections, electromagnetic observations have shed light on compact objects in binaries. Observations of X-ray binaries (Negueruela & Coe, 2002; Mori et al., 2021) and gamma ray bursts (Dubus et al., 2017) could help constrain the number of compact object binaries. An X-ray binary is a binary system comprised of one star and one compact object (either a white dwarf, neutron star or BH). The separation of the binary objects is small enough that the compact object accretes matter from the star. The gravitational potential energy of the matter accreted by the compact object is emitted as X-rays[5], giving the system its name. The systems serve as direct observational evidence for compact objects existing as binaries in our universe. From the abundance of observed X-ray binaries in tandem with stellar evolution theory, we can put constraints on the abundance of BH binaries formed from binary star systems (Grimm et al., 2003; Fabbiano, 2006; Belczynski & Ziolkowski, 2009; Saxena et al., 2021). These studies find a sloped density profile for X-ray sources in galaxies, with a density cusp within $\sim$ 1pc from the galactic centre, (Fabbiano, 2006; Hailey et al., 2018). Before the advent of GWs, this was the only mechanism to directly deduce the mass of stellar mass BHs (see Figure 2.2), with observed values ranging from $5 - 20\mathrm{M}_{\odot}$.

More recently, observations of *detached* binaries consisting of a non-accreting BH with a luminous stellar companion have been made (e.g. Thompson et al., 2019; Giesers et al., 2018; Liu et al., 2019; El-Badry et al., 2023), one of which appears to exist in the mass gap (e.g. Jayasinghe et al., 2021).

Another method of observing BHs is through microlensing. When a BH passes between a telescope and a luminous field star, the measured brightness of the star is increased. From the brightness-time curve, the mass of the transiting BH can be estimated. Detecting BHs using microlensing suffers from its rarity in tandem with a possible degeneracy between the BH mass and its relative velocity (Sahu et al., 2022).

As for electromagnetic counterparts to GW signals themselves, there have been a few coincident GW-photometric observations. Such observations rely on the presence of a neutron star. Smartt et al. (2017) report the observation of a blue kilonova within the localisation area and distance margin of NS-NS GW source

[5]This energy transfer is highly efficient, emitting ∼10-40% of the material's rest mass (Makishima et al., 2000).

GW170817, identified through strong and short X-ray emission, see (Margutti et al., 2017). The features of a blue kilonova event are a transient ultra-luminous burst of emission, including highly exotic line emission from r-process elements (radioactively driven emission from atomic masses 90-140, see Kasen et al. 2017). The power of the line emission follows a characteristic power law $P \propto t^{\beta_r}$ (Woosley et al., 1994). The r-process emission and its characteristic decay constant $\beta_r \sim 1.1 - 1.4$ provides the observational signatures of a NS-NS merger, driven by a combination of magnetically driven jets and hydrodynamical spiral outflows (e.g. Metzger & Berger, 2012; Metzger, 2019; Darbha et al., 2021). Based on the assumption that kilonovae occur at 1% of the supernovae rate (an upper bound), the probability of the EM detection being a coincidence was estimated at $\sim 10^{-5}$, making the detection highly confident. In theory, a similar emission signature exists for NS-BH mergers. For this to occur, the BH mass must be sufficiently small so that the NS can be disrupted *outside* the BH's event horizon, otherwise there is a direct collapse with no EM counterpart (Miller, 2005). GW evidence of NS-BH mergers include GW200105 (Abbott et al., 2021b) and GW200115 (Mandel & Smith, 2021), though there is so far little evidence for associated EM counterparts (Dichiara et al., 2021).

Because GWs travel at the speed of light, any time delay between GW emission and EM emission associated with the merging system allows us to observe the localisation volume of the GW signal in the hope of identifying a delayed EM event (Pankow et al., 2018). The delay can also be used in tandem with the distance to the source to constrain cosmological parameters, including the Hubble constant (Schutz, 1986; Baker et al., 2017) as well as the theory of gravity (Abbott et al., 2019c).

Recently, more efficient protocols have been made to enhance the chance of capturing more of these multi-messenger signals of merging compact objects (Chase et al., 2022; Bom et al., 2024).

2.6 Proposed BH merger mechanisms

There are several proposed astrophysical mechanisms that could allow stellar mass BHs to merge within a Hubble time. As suggested by the inefficiency of BHs to merge on their own above separations of 0.1au, most proposed mechanisms rely on external influences to draw the BHs close enough to one another in order to merge.

2.6.1 Isolated stellar binary evolution

The first natural avenue of inquiry is whether massive binary star systems (which make up a significant fraction of high mass stars, e.g. Lada, 2006; Raghavan et al., 2010) can evolve, die and leave two remnant BHs which can be brought to merger through interaction with the remaining gas. The attractive feature of this channel is the lack of a need to explain the initial formation of a BH binary. Instead, the question is whether both BHs are retained as a binary after their natal kick (e.g. Janka, 2013). During the core collapse of a star, asymmetric ejecta from the star during the supernova must coincide with asymmetric accretion onto the formed BH at its centre in order for linear momentum to be conserved, leading to a birth or 'natal' kick for the BH formed. The strength of a kick typically depends on the mass and metalicity of the star as well as the mass of the BH formed. Smaller BHs tend to receive larger kicks (to conserve momentum with the asymmetric mass ejecta) and BHs from lower metalicity stars tend to receive smaller kicks (e.g. Mapelli, 2020; Giacobbo & Mapelli, 2020). Evidence of natal compact object kicks in nature comes from observations of high velocity pulsars and newly formed BH-star binaries (Cordes et al., 1993; Gualandris et al., 2005; Chatterjee et al., 2005; Vigna-Gómez et al., 2024). For BH binaries created from a single stellar binary, this means both BHs must remain bound after receiving their kicks. Though, it has been suggested that local gas can help prevent the decoupling of a binary via dynamical friction, particularly for the formation of the second BH (e.g. Tagawa et al., 2018).

In this channel, there are many physical considerations that affect the internal evolution of the stars, their resulting BH masses/kicks and the orbital evolution of the stellar binary to BH-star binary to BH-BH binary. After life on the main sequence, a massive star can swell to several thousand solar radii, which for a binary can be close to or within an order of magnitude of the binary semi-major axis (typically 0.02–4000au, with a uniform distribution in log space according to Öpik's law, see Öpik 1924; Tokovinin 2000; Kobulnicky & Fryer 2007). This close separation leads to Roche lobe overflow and even the formation of a common envelope (e.g. Eggleton, 1983; Sana et al., 2012; Röpke & De Marco, 2023). Provided the first formed BH is not ejected by a natal kick, the BH-star binary experiences strong gas drag due to mass transfer from the star to the BH. This mechanism is expected to be particularly efficient if the BH evolves in the common envelope

of the star. If the second remnant BH remains bound, then the initial BH-BH binary semi-major axis can be much smaller, on the order of a few solar radii, and thus merge within a Hubble time.

Observationally, ignoring the twin peak structure, the merging mass distribution (Figure 2.3) is reminiscent of the stellar initial mass function (IMF), following a power law. Although, the merging distribution is more top heavy, with many more BHs above the threshold of $15M_{\odot}$ than predicted from isolated stellar evolution (Di Carlo et al., 2019; Mapelli, 2016, 2020). Note this depends strongly on the assumed metalicity (Belczynski et al., 2010a). Additionally, since there is a bias towards lower mass BHs being formed with higher spins (Bavera et al., 2020; Kumamoto et al., 2021; Arca Sedda et al., 2023), one should expect the mass and spin magnitudes to be correlated. Since orbital eccentricity of a BBH decays more quickly than its semi-major axis (e.g. Peters, 1964), combined with circularisation from gas/tides in the overflow/common envelop stage during the stellar binary evolution (Zahn, 1977, 2008), the GW waveforms produced from isolated binary mergers should reflect highly circular BH binaries. It is worth noting that these signatures are still subject to large unknowns, primarily in relation to the uncertainties regarding the common envelope/Roche overflow phase of the binary evolution (Dominik et al., 2012; Iorio et al., 2023).

2.6.2 BH scatterings in star clusters

Another possible merger mechanism involves BH interactions in dense star clusters (e.g. Mouri & Taniguchi, 2002; Miller & Hamilton, 2002; Portegies Zwart & McMillan, 2002; Portegies Zwart et al., 2004; Kocsis et al., 2006; Rodriguez et al., 2016; Liu & Lai, 2021; Di Carlo et al., 2020). The high density of stellar and compact objects in clusters leads to a short two-body relaxation timescale, of order $\sim$ 100Myr (Binney & Tremaine, 2008; Hamilton et al., 2018). Hence they are highly collisional systems. In this pathway, BHs formed from the end result of typical high mass stellar evolution can encounter one another within the highly populous nuclear and globular star clusters within galaxies. The main driver of the mergers is specifically the random scattering of BHs in a cluster rather than through interaction with another medium (i.e. gas), though young gas rich clusters may enhance the hardening of formed binaries (e.g. Rozner et al., 2022). These scattering scenarios include two-body BH

scatterings, three body scatterings (with another star or BH) that can leave behind a bound binary, binary-binary scatterings, as well as the formation of stellar binaries (Heggie, 1975; Heggie et al., 1996; Meylan & Heggie, 1997; Heggie & Hut, 2003; Pooley et al., 2003; Zevin et al., 2019a). Once a BH is formed, further encounters with other stars/BHs can either harden or soften the binary.

If one considers a BBH with some energy E_b, semi-major axis a and component masses M_1, M_2 encountering a third object of mass M_3, with the kinetic energy between the binary centre of mass (COM) and third object K_3, there are a range of possibilities:

- The original binary is preserved and the third object extracts orbital energy from the binary and the final kinetic energy between the binary and single object $K_{3,\mathrm{f}}$ is higher than prior to the interaction $K_{3,\mathrm{i}}$, i.e. $K_{3,\mathrm{f}} > K_{3,\mathrm{i}}$. Since energy must be conserved, $K_{3,\mathrm{i}} - E_{\mathrm{b,i}} = K_{3,\mathrm{f}} - E_{\mathrm{b,f}}$ and hence $E_{\mathrm{b,f}} - E_{\mathrm{b,i}} = K_{3,\mathrm{f}} - K_{3,\mathrm{i}}$. So if $K_{3,\mathrm{f}} > K_{3,\mathrm{i}}$, the binding energy of the binary increases and the semi major axis shrinks:

$$E_{\mathrm{b,f}} = -\frac{GM_1M_2}{2a_f} < -\frac{GM_1M_2}{2a_i} = E_{\mathrm{b,i}} \implies a_f < a_i \tag{2.13}$$

- The single object loses a portion of its energy K_3 and which is added to the energy of the binary E_b, i.e. In such cases the expression of Eq. (2.13) becomes inverted and E_b increases, softening the binary.

- Instead of reducing the binding energy of the existing binary, a third BH can exchange itself with one of the existing BHs, which is typical when the third object mass is the intermediate one (i.e. $M_2 < M_3 < M_1$) or the largest.

As this is a three body problem, the resulting outcome is extremely sensitive to the approach parameters of the single (velocity, impact parameter, inclination to binary) as well as binary parameters (relative orbital phase, semi-major axis, eccentricity). Often there will be multiple interactions with the single before one object is finally kicked out and all three scenarios above can play out intermittently for a single binary-single encounter. As a rough predictor for a binary's fate, one can assume that for a binary in a cluster with a mean velocity dispersion of σ and average mass $\langle m \rangle$, the binary will likely be ionised if $|E_b| > \langle m \rangle \sigma^2/2$ and

hardened when $|E_b| < \langle m \rangle \sigma^2/2$. Binaries meeting the former and latter conditions are labelled as *soft* and *hard* binaries, respectively.

This merger channel, unlike the isolated channel in Sec. 2.6.1, can more easily result in mergers where one or more of the BHs are in the mass gap. This is achieved through repeated mergers in the clusters (Mapelli, 2016; O'Leary et al., 2016; Rodriguez et al., 2019; Hong et al., 2020). However as the channel is purely collisional (i.e. little to no gas), the expected spin distribution of merging BHs is isotropic (assuming the cluster and scattering processes are also approximately isotropic). Therefore, the channel currently cannot explain the bias in $\chi_{\rm eff}$ towards positive values shown in Figure 2.4 (Gerosa et al., 2018; Callister et al., 2022). The eccentricity distribution of merging binaries, driven again by dynamical collisions, allows for far more eccentric mergers. For each scattering event, the eccentricity of the remaining binary is randomised according to the thermal eccentricity distribution $f(e) = 2e$, allowing for very eccentric binaries (Zevin et al., 2019b; Dall'Amico et al., 2024; Fabj & Samsing, 2024). With more GW detections, it will be possible to constrain the proportion of GW sources from this channel and the AGN channel compared to the isolated binary channel (Breivik et al., 2016).

2.6.3 Formation and merger of BH binaries in AGN discs

Recently, it has been suggested that the highly dense accretion discs around the SMBHs in AGN could host many BH-BH encounters and mergers (e.g. Tagawa et al., 2020a). Both theoretical arguments (Bahcall & Wolf, 1976, 1977; Miralda-Escudé & Gould, 2000) and observational evidence (e.g. Hailey et al. 2018) indicate that approximately 2×10^4 BHs reside within $\sim$ 1pc. Compared to the central low-mass stellar population, the distribution of these heavier objects in the centres of galaxies is expected to be less spherically symmetric and more disc-like due to a process known as vector resonant relaxation (Rauch & Tremaine, 1996; Szölgyén & Kocsis, 2018; Gruzinov et al., 2020; Magnan et al., 2022; Máthé et al., 2022). If a gas disc is present, gas dynamical friction (Ostriker, 1999) with the disc can reduce the inclination of the orbits crossing the disc (e.g. Bartos et al. 2017b; Panamarev et al. 2018) and thereby increase the chance of encounters. A flattened distribution is observed in the distribution of the X-ray BH binary population of the Milky Way (e.g. Mori et al. 2021) as well as in the high-mass stellar population close to its SMBH Sgr

A* (e.g. Bartko et al. 2009; Ali et al. 2020). A similarly disc-like population of the higher-mass objects is predicted by N-body simulations in rotating star clusters (e.g. Szölgyén et al. 2019, 2021). The compression of the BH distribution in the vertical axis is expected to increase the likelihood of close encounters and hence the chance for binary captures and mergers (e.g. Vergara et al., 2021). Additionally the deep gravitational potential of the SMBH can more easily retain BHs after post merger kicks, potentially leading to multiple generations of merging binaries (Tagawa et al., 2020a; Gerosa & Fishbach, 2021; Varma et al., 2022). All of these effects together lead to a favourable probability for BH-BH encounters in AGN discs.

There are three mechanisms that produce BH binaries in AGN: high mass stellar binary evolution, three body scatterings with at least two BHs and two body BH scatterings within the disc. The merger of pre-existing BH binaries was considered in Bartos et al. (2017b), where BH binaries in the cluster could embed themselves in the disc and then be driven to merge by dissipating energy via interaction with the surrounding gas (Kim & Kim, 2007; Kim et al., 2008; Haiman et al., 2009; O'Neill et al., 2024) within the lifetime of the AGN (Secunda et al., 2019, 2020; McKernan et al., 2020a; Ford & McKernan, 2022). Tagawa et al. (2020a) modelled pre-existing binaries and isolated BHs in AGN in a 1D semi-analytic N-body scheme. They identified that a large fraction of BHs could dissipate energy during a two body scattering event and become bound through gas drag during the encounter (which will be labelled 'gas-assisted' or 'gas-captured' binaries throughout this thesis). In fact, the population of initially isolated BHs was found to dominate the number of mergers in AGN, making up >85% of the merging BBHs. The overall rate density of mergers predicted by Tagawa et al. (2020a) ranged from $\sim 0.02 - 60\mathrm{Gpc}^{-3}\mathrm{yr}^{-1}$, covering the observed rate from GW instruments of $\sim 17 - 44\mathrm{Gpc}^{-3}\mathrm{yr}^{-1}$. Stemming from these optimistic rates and the apparent efficiency of gas-assisted binary mergers in AGN, there has since been an explosion in works to understand binary formation, evolution and mergers in AGN discs. Understanding this astrophysical problem has been the goal of my own work over the course of my doctoral studies and represents the primary subject of this thesis.

2.7 BH scatterings in AGN as a 3-body problem

The binary formation process itself is a complex phenomenon and has similarities to the problem of satellite capture in the Solar System, such as the capture of moons (e.g. Johnson & Lunine, 2005; Agnor & Hamilton, 2006; Nesvorný et al., 2007). If one considers a chance BH-BH encounter in an AGN *without* gas, then the high velocity dispersion of objects most often results in a single flyby, during which a sufficient amount of orbital energy has to be dissipated by GW emission for a capture (O'Leary et al., 2009). Alternatively, the two BHs can engage in a Jacobi capture interaction, during which they encounter each other multiple times within their mutual Hill sphere (Boekholt et al., 2023). This increases the probability of an eventual permanent capture if a dissipation mechanism is present, and thus the formation of a BBH. The resultant binary systems are highly eccentric, i.e. approximately super-thermal (i.e. steeper than $f(e) = 2e$, see Jeans 1919). Dynamical friction and accretion can potentially significantly increase the capture cross section and facilitate the subsequent binary hardening and mergers (Tagawa et al., 2018). However, the phase space related to gasless Jacobi captures is fractal (Boekholt et al., 2023; DeLaurentiis et al., 2022; Dodici & Tremaine, 2024), i.e. the outcome of an interaction depends sensitively on the initial impact parameter and speed of the encounter. The influence of the SMBH on the capture process may then be non-trivial even when including gas.

2.8 Hydrodynamics of the AGN channel

2.8.1 Isolated binary evolution

Numerous studies have looked at BBH formation and/or evolution in an AGN environment using semianalytic methods (e.g. Tagawa et al. 2020a; Gröbner et al. 2020; Secunda et al. 2019) for handling small-scale BH-gas interactions such as accretion, dynamical friction, capture and crucially the subsequent post-capture torques on the binary. The majority of these processes indicate that the presence of a dense gaseous medium can aid binary formation and merger by inducing a net negative torque on the system.

Recent high-resolution hydrodynamical simulations of isolated binary evolution, where there are only two objects at the centre of a circumbinary gas disk, rather than embedded in the local shear flow of a larger circum-SMBH disc, find that disk torques can be either negative (causing the binary to inspiral) or positive (causing outspiral). Several 2D studies of circular, equal-mass binaries embedded in relatively thick, locally isothermal disks with a fixed scale height to radius ratio $H/R = 0.1$ have, in particular, converged on positive torques (Tang et al., 2017; Muñoz et al., 2019; Moody et al., 2019; Tiede et al., 2020), which, in the case of Moody et al. (2019) was confirmed in a 3D simulation. Subsequent work has revealed that the disc torques become negative when the above assumptions are relaxed. Binary inspiral is found for cooler and thinner discs with $H/R \lesssim 0.1$ (Tiede et al., 2020; Heath & Nixon, 2020), with the precise critical H/R value dependent on viscosity (Dittmann & Ryan, 2022). Likewise, torques switch to a negative sign for eccentric binaries with $e \gtrsim 0.4$ (D'Orazio & Duffell, 2021). This may be the more typical case, since the disc tends to drive binaries to eccentricities above this value, unless they start very close to circular orbits (Zrake et al., 2021; D'Orazio & Duffell, 2021). Finally, unequal-mass binaries with $q \equiv M_2/M_1 \lesssim 0.05$ have also been found to inspiral (Duffell et al., 2020) (although these may be atypical for stellar mass BH mergers, see Tagawa et al. 2021d). In summary, it appears at least plausible for most binaries with a circumbinary gas disc to be driven towards merger. Caution must still be exercised as the above simulations remain idealised in several ways, and would, in any case, only apply for a stellar-mass binary deeply inside the Hill radius in our case.

There also remain some numerical issues, with some studies finding a sensitivity to sink prescriptions (Tang et al., 2017) and softening lengths (Li et al., 2021), although more recent work find torques to have converged with respect to the corresponding numerical choices, at least for circular binaries (Moody et al., 2019; Muñoz & Lithwick, 2020; Duffell et al., 2020; Westernacher-Schneider et al., 2022).

2.9 Embedded binary evolution

The first work considering disc embedded binaries (Baruteau et al., 2011) reported that gas dynamical friction hardens a pre-existing binary in a 2D gas disc, regardless

of whether it opens up a gap, where the binary is sufficiently massive to expel gas from its orbit around the SMBH faster than gas can refill it via viscosity driven diffusion (e.g. Goldreich & Tremaine, 1980). This result has been reaffirmed by Li et al. (2021) in the cases where the binary system orbit is retrograde with respect to its orbit around the disc/SMBH and is attributed to an increased velocity difference between the individual BHs in the binary and the local gas, leading to the destruction of positive torque sources near the BHs. Kaaz et al. (2021) consider a binary in a thick disc where the binary does not open a gap in the disc using 3D wind tunnel simulations and find binary hardening in all their models. At present, there is no clear consensus on how the differences in environment between isolated binaries, disc-embedded binaries Li et al. (2021, 2022c), and wind tunnel simulations (Li et al., 2022d; Li & Lai, 2022b, 2023; Kaaz et al., 2021) affect binary evolution.

While the problem of binary evolution is not yet settled, even less is known about the correlation between the rates of successful gas-assisted binary captures and the nature of the AGN host environment they take place in, which may vary considerably depending on the evolution of its host galaxy. An environmental dependence would therefore have implications for the rates of BH mergers in AGN over cosmic time, based on the redshift dependence of galaxy morphology, merger rates etc. that are tied to the number and evolution of AGN (e.g. Fanidakis et al., 2012; Conselice, 2014; Tagawa et al., 2020a).

A primary difficulty faced by hydrodynamic simulations of disc-embedded BBHs is achieving sufficient resolution to resolve the circumbinary "mini" discs (CMBDs) and the streamers between the individual components of the binary, whilst also modelling the larger global AGN gas disc or, more usually, annulus which the binary orbits within. This problem is commonly avoided by artificially increasing the BBH/SMBH mass ratio so the scale of the region of interest around the BBH increases relative to the disc, reducing the dynamical range to be covered. While this makes achieving an appropriate resolution around the binary less expensive, it describes a far more exotic scenario of two intermediate mass BHs (IMBHs) embedded in an AGN disc of a SMBH (e.g. Li et al. 2021), and it is unclear if these systems may be simply extrapolated to the case of stellar mass BBHs.

2.10 Binary formation via gas dissipation

Before the work of this thesis, literature on gas-assisted binary formation was scarce or employed only fully or semi-analytic methods (as first applied to interacting planetesimals in Goldreich et al., 2004). In Tagawa et al. (2020a), binary formation is considered successful when the timescale in which dynamical friction can dampen the relative velocity of the scattering objects is shorter than the crossing time of one object across the binary Hill sphere $r_{\rm H}$ of the two-BHs,

$$r_{\rm H} = R\left(\frac{M_{\rm bin}}{3M_\bullet}\right)^{1/3}. \tag{2.14}$$

Here, R is the radial position in the AGN disc, $M_{\rm bin}$ and $M_\bullet$ are the binary and SMBH masses respectively. Once the BHs exit this region, they are separated by the SMBH. However, the prescription of Tagawa et al. (2020a) assumes a constant density and unchanging uniform distribution of gas. Dynamical friction on a satellite in a uniform gaseous disc (Kim & Kim, 2007) has been shown to behave nearly identically to that in an infinite uniform medium (Ostriker, 1999) with the same limitations. Kim et al. (2008) analytically explored dynamical friction on two co-rotating perturbers in a uniform gaseous medium. They found dynamical friction still leads to inspiral though the dynamical friction force on each object is reduced due to the wake following the other. Similarly to the pre-existing binary simulations, this is only shown for circular, already bound binaries and ignores density gradients which can be expected to be large following the initial encounter, since the objects will have filled their Hill spheres with gas. Therefore the interaction between two satellites and the gas during their first encounter is largely unknown. Understanding this process and its efficiency is crucial for estimates of binary fractions and merger rates in AGN.

Figure 2.5 depicts a cartoon of the gas-driven binary formation process examined in this work. The left panel shows the large scale configuration of the system where two BH satellites moving initially on Keplerian orbits around the SMBH, embedded in the AGN disc, approach each other due to the difference in their angular velocities. The four panels on the right show a zoom-in on the BH satellites in different evolutionary stages in time, respectively, from left to right. Initially the BHs have distinct circum-single mini-discs (CSMDs) just prior to the encounter

(1st zoom-in panel). At the beginning of their encounter, these discs begin to be tidally stripped by one another (2nd panel) and there is also the opportunity for the discs to intersect which leads to strong accretion and gravitational drag forces on the BHs due to their interaction with the gas. This interaction is incredibly violent and leads to mass loss of gas from within the binary Hill sphere (3rd panel). It is this drag that decreases the energy and eccentricity of the BHs to the point that they can remain bound as a binary, as we will discuss in Chapter 4. The binary is further hardened by spiral gas outflows, originating from the CSMDs of the BHs that are continually being stripped of material. This is akin to the predictions of Kim et al. (2008). Once the binary is sufficiently hardened that their separation is much smaller than their mutual Hill sphere with respect to the SMBH, a CBMD forms around the binary (4th panel) and the binary transitions to the problem of a pre-existing disc embedded binary with a high eccentricity, where its evolution is predominantly governed by the CBMD.

A close analogy to this scenario is work on protostellar disc collisions. The SPH simulations of Watkins et al. (1998a) demonstrate successful formation of stellar binaries with coplanar protostellar discs, where the stars are initially energetically unbound. This is extended to non-coplanar configurations in their second paper (Watkins et al., 1998b) where they predict that for these systems 15% of disc-disc encounters lead to a protostellar binary. This is encouraging for AGN, however the velocity dispersion is far larger and encounters will be more energetic on average. Curiously, for star-disc encounters they find energy can be dissipated from *or* added to the stellar binary orbits (e.g. Boffin et al. 1998). More recently, at higher resolutions, Shen et al. (2010) corroborate (albeit as a rare case) that gas can aid stellar binary formation, though their paper primarily focuses on brown dwarf formation due to the disc-disc collision. Most recently, Muñoz et al. (2015) use the adaptive moving mesh grid code AREPO to investigate the binary evolution specifically following such encounters and its dependence on initial periapsis distance. They again verify that capture is possible and that this becomes more likely the closer the first periapsis pass is. With the exception of Muñoz et al. (2015), most other disc collision papers utilised SPH for their encounters, which is well suited given the strongly non-axisymmetric gas morphology compared to 2D grid based codes.

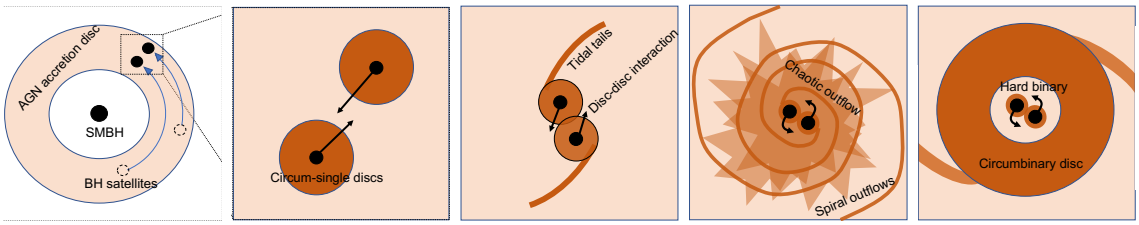

Figure 2.5: Cartoon of the gas-driven binary capture mechanism, where the darkness of the orange shading represents the density of the medium. From left to right, i) Zoom out of scenario showing the SMBH, AGN disc and BH satellites ii) Zoom in of BHs just prior to encounter with their circum-single mini-discs iii) beginning of encounter showing tidal disruption of BH discs and disc collision iv) gas outflows and density spirals generated by wakes behind BHs v) late evolution of now hardened binary with circum-binary mini-disc. Taken from Rowan et al. (2023).

2.11 AGN discs and accretion disc physics

In an accretion disc, gaseous material orbits a central body. In the context of this work, the central object will be either a BH or a SMBH. The vertical structure of the disc is solved by balancing the equation of hydrostatic equilibrium in the vertical $\hat{z}$ direction perpendicular to the disc, by approximating the vertical component of the gravity g_z from the disc as

$$\frac{1}{\rho}\frac{\mathrm{d}P}{\mathrm{d}z} = -g_z = -\frac{GM_\bullet}{R^2}\frac{z}{R} = -\Omega^2 z\,, \tag{2.15}$$

where ρ is the gas density, P is the pressure and $\Omega = \sqrt{GM_\bullet/R^3}$ is the Keplerian angular velocity. In the simplest case, where the disc can be assumed to be vertically isothermal at each radius in the disc, one uses the standard relation for the pressure in terms of the sound speed c_s, $P = \rho c_s^2$, in eq (2.15) to solve for the unperturbed vertical density structure of the disc in terms of the midplane density ρ_0

$$\rho(z) = \rho_0 e^{-\frac{z^2}{2H^2}}, \tag{2.16}$$

where $H = c_s/\Omega$ is the scale height of the disc that becomes larger for hotter discs.

The flow of material through a stable accretion disc is governed by viscous interactions in the gas from the velocity shear, $v_\phi \propto R^{-1/2}$. The four possible viscosity sources are i) magnetic field stresses, ii) turbulence, iii) molecular viscosity and iv) radiative viscosity. Molecular viscosity is negligible in the context of AGN discs as the typical gas densities and particle sizes are small (Lawrence, 2018). The

net effect of viscosity is to allow angular momentum to be transported from the inner portions of the disc to a smaller amount of material much further out in the disc. This drives a radial mass flow towards the central SMBH which then accretes at some fraction of the Eddington luminosity (Eddington, 1916), typically ranging from a few hundredths to approximately unity in AGN (Shen et al., 2011)

$$L_{\rm Edd} = \frac{4\pi G M_\bullet m_{\rm H} c}{\sigma_{\rm T}} = 3.2 \times 10^4 \left(\frac{M}{M_\odot}\right) L_\odot \,, \tag{2.17}$$

where $\sigma_{\rm T}$, $m_{\rm H}$, $L_\odot$ are the Thomson scattering cross section, mass of hydrogen and solar luminosity respectively. How the viscosity should be modelled is still currently an ongoing discussion, though analytic descriptions exist under certain assumptions. The most commonly adopted analytic solution for an AGN disc came from Shakura & Sunyaev (1973), known in the literature as α-discs. In the model, it is assumed that both thermally and magnetically induced, self-perpetuating turbulence, dominates the viscosity. The solution assumes the disc is very thin, (i.e. $H/R \sim 10^{-3}$) so that radiation transport vertically from the plane of the disc is highly efficient and thus radiative viscosity is minimal. The second assumption made is that the magnetic field energy density cannot exceed that of the thermal energy. In a turbulent medium, the viscosity $\nu \approx v_{\rm t} l_{\rm t}$ depends on the largest size of the turbulent cells $l_{\rm t}$ and their speed $v_{\rm t}$ (Abramowicz & Fragile, 2013). In the α-disc framework, the maximal turbulent cell size is taken to be the scale height H and their speed as the sound speed $c_{\rm s}$ as the disc is considered to be gas pressure dominated based on the two assumptions above. Thus in an α-disc, the viscosity is:

$$\nu_{SS} = \alpha c_{\rm s} H \,, \tag{2.18}$$

where α is a scaling parameter that so far is largely unknown, with predicted values ranging over orders of magnitude from $0.001 \lesssim \alpha \lesssim 0.4$, with an apparent disconnect between estimations from observational data and laboratory experiments (e.g. King et al., 2007), with the former predicting the higher estimates and vice versa.

The equations governing the disc structure are then derived from the equation of hydrostatic equilibrium and momentum conservation with α as the governing

free parameter. In the form derived in Goodman & Tan (2004), these are

$$T(R) = \left(\frac{3\kappa\mu m_{\rm H}}{64\pi^2\alpha\beta^{b-1}k_{\rm B}\sigma}\right)^{1/5} \dot{M_\bullet}^{2/5}\Omega^{3/5}\,, \tag{2.19}$$

$$\Sigma(R) = \frac{2^{6/5}}{9^{3/5}\pi^{3/5}}\left(\frac{\mu^4 m_{\rm H}^4\sigma}{k_{\rm B}^4}\right)^{1/5} (\alpha\beta^{b-1})^{-4/5}\kappa^{-1/5}\dot{M_\bullet}^{3/5}\Omega^{2/5}\,, \tag{2.20}$$

where $\dot{M}_\bullet$ is the SMBH accretion rate and Ω is the orbital frequency around the SMBH. The additional physical parameters are the opacity (κ), mean particle mass (μ), mass of hydrogen ($m_{\rm H}$), Boltzmann constant ($k_{\rm B}$) and Stefan-Boltzmann constant (σ). The β term represents the anticipated ratio of the gas pressure $P_{\rm gas}$ to the total pressure P (which includes the radiation pressure); $\beta \equiv P_{\rm gas}/P$. Throughout this work, it is assumed that we are in the gas-dominated regime where $\beta = 1$, see Sec. 4.4.

2.11.1 Features of the AGN merger channel

In the AGN scenario, the high density of the gas in an AGN disc is expected to harden the binary via gravitational or accretion processes. GW signals from AGN may be statistically identified using the angular power spectrum (e.g. Cusin et al., 2018; Gayathri et al., 2023), coincidence with electromagnetic surveys (Tagawa et al., 2023a; Rodríguez-Ramírez et al., 2023), cross-correlating the GW signal with AGN positions (e.g. Bartos et al., 2017a), or through the distribution of source parameters, i.e. mass distribution extending to high BH masses consistent with hierarchical mergers (Tagawa et al., 2021a,e). Further evidence includes: a large spin perpendicular to the binary orbital axis but the parallel spin component distributed around zero (e.g. Tagawa et al., 2020b, 2021a), and non-zero eccentricities at 10Hz (Tagawa et al., 2021c; Samsing et al., 2022). Individual 'smoking gun' identification may be possible with LIGO/VIRGO/KAGRA by identfying an astrophysical GW echo due to GW lensing by the host SMBH (e.g. Gondán & Kocsis, 2022), or by LISA measuring an acceleration of the centre of mass (e.g. Meiron et al., 2017; Inayoshi et al., 2021), or by electromagnetic observations of a coincident transient (e.g. Graham & Jung, 2017; Abbott et al., 2022a,b; Tagawa et al., 2023a,b,c).

3

Numerical Methods: PHANTOM

Contents

The range of physics as well as physical scales involved in the full system of a BH binary embedded in an AGN disc are immense. The extremely hierarchical nature of the 3-body system leads to a large disparity of timescales, length scales and mass scales associated with the inner binary (the orbit of the two stellar mass BHs around each other) and the outer binary (the orbit of the BBH around the SMBH), with the former being far smaller. Therefore, one must balance simulating a sufficient enough portion of the far larger AGN disc with the comparatively minuscule gas structures around the smaller BBH over a long enough timescale to monitor the binary's evolution. The largest hurdle to studies involving such varying scales is under-resolving strong and highly transient processes on small

scales which greatly affect the behaviour of the system, known as an 'inverse cascade' problem. In this work, this is the aforementioned gas dynamics close to the stellar mass BBH and the individual BHs themselves.

The smoothed particle hydrodynamics (SPH) code PHANTOM (Price et al., 2018) is a natural choice to simulate the system. Based on its far older parent sphNG (Benz, 1990), PHANTOM was designed from the ground up to simulate the complex hydrodynamics of accretion discs (primarily of protostellar discs). Its fixed particle mass setup provides a naturally adaptive resolution and its particle-like nature easily allows for the simulation of gas dynamics in 3D. For a review and detailed breakdown of the SPH approach to hydrodynamics, see Price (2012).

3.1 Nomenclature

From this point onwards in this work, *BH binary* or *BBH* or *inner binary* all refer to the stellar mass BH binary system in the AGN disc. References to the *outer binary* system, pertain to the binary system comprised of the SMBH and the inner binary COM. In the fluid equations to come, index i denotes the particle that is being evolved and j or k denotes the particle that particle i is interacting with.

3.2 Solving the hydrodynamical equations

3.2.1 The equations of motion

As the code evolves the motions and properties of particles, it solves the equations of hydrodynamics in Lagrangian form, where the SPH particles represent discrete portions of the fluid that is being simulated. The basic equation of motion and continuity equation which govern PHANTOM, in Lagrangian form are

$$\frac{\mathrm{d}\boldsymbol{r}}{\mathrm{d}t} = \boldsymbol{v} \tag{3.1}$$

$$\frac{\mathrm{d}\rho}{\mathrm{d}t} = -\rho(\nabla \cdot \boldsymbol{v}) \tag{3.2}$$

where $\boldsymbol{r}$, $\boldsymbol{v}$ and ρ is a particles position, velocity and density respectively. The full time derivative represents the material or Lagrangian derivative $\dfrac{\partial}{\partial t} + \boldsymbol{v} \cdot \nabla$ which can be rearranged to transform these expressions to the Eulerian frame.

In SPH, as the name suggests, the properties of each particle are 'smeared' across some spacial domain. Thus for a particle i in the simulation domain, its density is a weighted summation of the particles in the vicinity of r_i. The smearing of an SPH particle is governed by a weighing function W. The density of particle i, ρ_i, is given by

$$\rho_i = \sum_j m_{\mathrm{p},j} W(\|r_j - r_i\|, h_i), \tag{3.3}$$

where h_i is the characteristic smoothing length of the particle

$$h_i = 1.2(m_{\mathrm{p},i}/\rho_i)^{1/3}, \tag{3.4}$$

and $m_{\mathrm{p},j}$ is the jth particle's mass. PHANTOM uses a fixed mass scheme, i.e. $m_{\mathrm{p},i} = m_{\mathrm{p}}$ this implies the smoothing length and therefore resolution within a simulation scales with the density of the region. The softening kernel has the form

$$W(r,h) \equiv \frac{1}{\pi h^3} f(q), \tag{3.5}$$

where $q \equiv r/h$ is the dimensionless distance. The default form of smoothing kernel in PHANTOM is a cubic spline of the form.

$$f(x) = \begin{cases} 1 - \frac{3}{2}q^2 + \frac{3}{4}q^3 & 0 \le q < 1; \\ \frac{1}{4}(2-q)^3 & 1 \le q < 2; \\ 0 & q \ge 2, \end{cases} \tag{3.6}$$

For each timestep and for each particle, h_i is solved via Newton-Rhaphson iterations such that eqs. (3.3) and (3.4) are consistent, i.e.

$$\sum_{\mathrm{j}} \mathrm{m_p W}(\|\mathrm{r_j} - \mathrm{r_i}\|, \mathrm{h_i}) - \mathrm{m_p}(1.2/\mathrm{h_i})^3 = 0\,. \tag{3.7}$$

The particle properties are evolved according to the equations of compressible hydrodynamics, which in their full form concern evolving the momentum and internal energy u of the system as

$$\frac{\mathrm{d}\boldsymbol{v}}{\mathrm{d}t} = -\frac{\nabla P}{\rho} + \Pi_{\mathrm{shock}} + \boldsymbol{a}_{\mathrm{sink-gas}} + \boldsymbol{a}_{\mathrm{selfgrav}} \tag{3.8}$$

$$\frac{\mathrm{d}u}{\mathrm{d}t} = -\frac{P}{\rho}(\nabla \cdot \boldsymbol{v}) + \Lambda_{\mathrm{shock}} - \frac{\Lambda_{\mathrm{cool}}}{\rho} \tag{3.9}$$

where P is the pressure, $\boldsymbol{a}_{\mathrm{sink-gas}}$ is the acceleration from sink particles (see 3.4), $\boldsymbol{a}_{\mathrm{selfgrav}}$ is the acceleration from self gravity, Λ_{cool} is a cooling term, Π_{shock} and Λ_{shock}

are dissipative terms governing shock evolution. Due to the immense computational expense, it is assumed in this work that shocks will radiate their heat efficiently ($\Lambda_{\rm shock}$=0) with no cooling ($\Lambda_{\rm cool}=0$) or self gravity ($\boldsymbol{a}_{\rm selfgrav}$=0). It is also assumed that the temperature at each radial point in the AGN disc is fixed, thus the equation of state is simply:

$$P = c_{\rm s}^2 \rho \,. \tag{3.10}$$

3.2.2 Viscosity

Viscosity is included in PHANTOM via the shocking $\Pi_{\rm shock}$ term

$$\Pi_{{\rm shock},i} = -\sum_j m_{p,j} \left[\frac{q_{i,j}}{\rho_i^2 \Omega_i} \nabla_i W_{i,j}(h_i) + \frac{q_{i,j}}{\rho_j^2 \Omega_j} \nabla_i W_{i,j}(h_j) \right], \tag{3.11}$$

where $\Omega_i \equiv 1 - \frac{\partial h_i}{\partial \rho_i} \sum_j m_{p,j} \frac{\partial W_{ij}(h_j)}{\partial h_j}$ is related to the gradient of the smoothing length. The artificial viscosity terms q are given by

$$q_{i,j} = \begin{cases} -\frac{1}{2} \rho_i v_{{\rm sig},i} \boldsymbol{v}_{ij} \cdot \hat{\boldsymbol{r}}_{ij} & \text{if } \boldsymbol{v_{ij}} \cdot \hat{\boldsymbol{r}}_{ij} < 0, \\ 0 & \text{otherwise,} \end{cases} \tag{3.12}$$

where $\boldsymbol{v}_{ij} \equiv \boldsymbol{v}_i - \boldsymbol{v}_j$ is the relative velocity, $v_{\rm sig}$ is the maximal signal speed and $\hat{\boldsymbol{r}}_{ij} \equiv (\boldsymbol{r}_i - \boldsymbol{r}_j)/\|\boldsymbol{r}_i - \boldsymbol{r}_j\|$ is the unit position vector. Thus the q term is only non-zero for particles i and j when they are approaching each other.

For accretion discs, the q term for a particle i interacting with particle j can be modelled as

$$q_{i,j} = \begin{cases} -\frac{\rho_i h_i}{2\|\boldsymbol{r}_{ab}\|} (\alpha^{AV} c_{s,i} + \beta^{AV} \|\boldsymbol{v}_{ij} \cdot \hat{\boldsymbol{r}}_{ij}\|) \, \boldsymbol{v}_{ij} \cdot \hat{\boldsymbol{r}}_{ij} & \text{if } \boldsymbol{v}_{ij} \cdot \hat{\boldsymbol{r}}_{ij} < 0, \\ -\frac{\rho_i h_i}{2\|\boldsymbol{r}_{ab}\|} \alpha^{AV} c_{s,i} \, \boldsymbol{v}_{ij} \cdot \hat{\boldsymbol{r}}_{ij} & \text{otherwise.} \end{cases} \tag{3.13}$$

In order to implement the artificial α and β viscosities (α^{AV} & β^{AV} respectively) such that it mimics a disc viscosity, the following rules are set

1. $v_{\rm sig} \equiv c_s$.
2. α^{AV} is held constant such that $\alpha \approx \frac{\alpha^{AV}}{10} \frac{\langle h \rangle}{H}$, where $\langle h \rangle$ is the column averaged smoothing length of particles at some radius, see Price et al. (2018).
3. viscosity applies to both approaching and receding particles.
4. viscosity varies spatially from SPH particles by a factor h/r_{ab}.

The disc viscosity behaviour in PHANTOM has been tested via measuring the diffusion rate of the surface density against 1D codes (see Figure 4 in Lodato & Price 2010).

3.3 Modifying PHANTOM for AGN binaries

The application of PHANTOM to AGN discs, as opposed to proto-planetary discs is fairly trivial as the two systems have a similar geometry. The far higher temperature of the inner AGN disc ($T \gtrsim 4000$K) would annihilate any dust grains and allows us to neglect and switch off modules handling dust in PHANTOM. Since we are specifically concerned with the evolution of the inner binary rather than the outer binary system, the time sampling of important quantities relating to the BHs (position, velocities, mass etc) is substantially increased. Not doing so results in not being able to temporally resolve these properties on timescales less than the BBH orbit.

As a Shakura-Sunyaev alpha disc is assumed, the value of β^{AV} term in Eq. (3.13) is set to zero, giving a single expression for q:

$$q_{ij} = -\frac{\rho_i h_i}{2\|\boldsymbol{r}_{ab}\|}\alpha^{AV} c_{s,i}\, \boldsymbol{v}_{ij} \cdot \hat{\boldsymbol{r}}_{ij}\,. \tag{3.14}$$

To avoid wasting precious computing resources on areas of the disc which negligibly affects the binary evolution in the simulations, only the gas within a set radial annulus is actually simulated, see Sec. 4.4.

3.4 Sink particles

The BHs are represented in PHANTOM by sink particles, point-like particles which neither exert nor respond to pressure gradients from any surrounding gas. The sinks interact gravitationally with other sinks and the gas in addition to accreting gas and absorbing its momentum. Initially introduced to SPH to model star formation (Bate et al., 1995), sink particles are very well suited to mimicking the BHs in an AGN disc since they are effectively point masses.

3.4.1 Sink equations of motion

The general equation of motion for a sink in PHANTOM is given by the acceleration between sinks and sinks $\boldsymbol{a}_{\rm sink-sink}$ and between sinks and the gas $\boldsymbol{a}_{\rm sink-gas}$

$$\frac{{\rm d}\boldsymbol{v}_{\rm sink}}{{\rm d}t} = \boldsymbol{a}_{\rm sink-sink} + \boldsymbol{a}_{\rm sink-gas}\,. \tag{3.15}$$

By default and as used in this work, sink-sink interactions are unsoftened since we want to accurately model close periapsis passages. Therefore the sink-sink accelerations are calculated through direct N-body summation

$$\boldsymbol{a}_{{\rm sink-sink},i} = -\sum_{j,j\neq i} \frac{GM_j}{\|\boldsymbol{r}_i - \boldsymbol{r}_j\|^3}\boldsymbol{r}_{ij}\,, \tag{3.16}$$

where the above corresponds to the acceleration of a single sink particle i interacting with $N_{\rm sink}-1$ other sinks of mass M_j. The sink-gas acceleration is given by summing over $N_{\rm part}$ gas particles of mass $m_{\rm p}$

$$\boldsymbol{a}_{{\rm sink-gas},i} = -m_{\rm p}\sum_{k}^{N_{\rm part}} G\zeta(\|\boldsymbol{r}_{ik}\|, \epsilon_{{\rm sink-gas},ik})\hat{\boldsymbol{r}}_{ik}\,. \tag{3.17}$$

Here, ζ is the force softening kernel, centred on sink i (Price, 2007),

$$\zeta(x,\epsilon) = \begin{cases} \frac{C_{\rm norm}}{x^2}\int_0^x f(x')x'^2dx' & \boldsymbol{r}_{ik} < \epsilon, \\ \frac{1}{x^2} & \text{otherwise,} \end{cases} \tag{3.18}$$

where $f(x)$ is the smoothing kernel (Eq. 3.6), ϵ is the softening length and the constant $C_{\rm norm}$ is determined such that $\zeta(\epsilon,\epsilon) = 1/x^2$. For BHs embedded within the AGN disc, a fixed minimum softening boundary $r_{\rm soft}$ is enforced for specifically gas-sink interactions. Thus the value of $\epsilon_{\rm sink-gas}$ is the maximum of the softening of the sink or the softening length of the gas particle itself $\epsilon_{{\rm gas},k}$. In other words $\epsilon_{{\rm sink-gas},ik} \equiv \max(r_{{\rm soft},i}, \epsilon_{{\rm gas},ik})$. By default, the value of $\epsilon_{{\rm gas},ik}$ is set to the SPH smoothing length of the gas particle, i.e. $\epsilon_{{\rm gas},ik} = h_k$.

3.4.2 Accretion

Sink particles may accrete gas (SPH) particles throughout the simulations and gain mass. Upon entering the accretion radius $r_{\rm acc}$ of a sink, gas may be accreted if three conditions are met:

1. $|L_{\rm gas}| < |L_{\rm acc}|$ i.e. the specific angular momentum of the gas is lower than a circular orbit at a distance of $r_{\rm acc}$
2. the particle is gravitationally bound to the BH (i.e. their mutual energy is < 0.)
3. the particle is more gravitationally bound to that sink than any other

Once a particle meets these three criteria and is accreted onto the sink, the linear momentum, angular momentum and mass of the system must be preserved. Preserving the linear momentum is achieved by updating the sink mass, position, velocity, acceleration as

$$M_{i,\rm new} = M_i + m_{\rm p} \tag{3.19}$$

$$\boldsymbol{r}_{i,\rm new} = \frac{\boldsymbol{r}_i M_i + \boldsymbol{r}_k m_{\rm p}}{M_i + m_{\rm p}} \tag{3.20}$$

$$\boldsymbol{v}_{i,\rm new} = \frac{\boldsymbol{v}_i M_i + \boldsymbol{v}_k m_{\rm p}}{M_i + m_{\rm p}} \tag{3.21}$$

$$\boldsymbol{a}_{i,\rm new} = \frac{\boldsymbol{a}_i M_i + \boldsymbol{a}_k m_{\rm p}}{M_i + m_{\rm p}} \tag{3.22}$$

Here the new updated positions, velocities and accelerations (denoted by the "new" subscript) are the mass-weighed average of the quantities calculated for sink i and particle k during the *current* time step before accretion. The angular momentum is in effect lost from the global simulation since the angular momentum of the accreted particles is not necessarily zero when accreted onto the sink. PHANTOM stores an effective 'spin' parameter $\boldsymbol{S}_i$ for each sink which is used as a placeholder to check angular momentum errors as the simulation evolves

$$\boldsymbol{S}_i = \boldsymbol{S}_i + \frac{m_{\rm p} M_i}{M_i + m_{\rm p}} [(\boldsymbol{r}_k - \boldsymbol{r}_i) \times (\boldsymbol{v}_k - \boldsymbol{v}_i)] \tag{3.23}$$

Note that this spin and the accretion process is far removed from the actual spin evolution and accretion process onto a BH, which requires resolving down to distances orders of magnitude smaller than the accretion radius in simulations of binary evolution in the literature and Chapters 4 and 5.

4

Black hole mergers in AGN through gas, a proof of concept

This Chapter is adapted from my publication Rowan et al. (2023) of which I am first author, principle investigator and personally wrote. Published in Monthly Notices of the Royal Astronomical Society.

Contents

4.1 Introduction

Since the first detection of a BH-BH merger in 2015 (Abbott et al., 2016), there have been numerous additional observations of compact object mergers (e.g. Abbott et al. 2019b; Venumadhav et al. 2020; Abbott et al. 2020a,d,e). Of particular interest are merging BHs with masses in the "mass gap" (Abbott et al., 2020c) associated with the mass loss predicted by pair-instability supernovae in the later stages of high mass stars' evolution (see 2.5.1). Since BHs of this mass cannot originate as stellar remnants, the objects are either the result of prior mergers (Gerosa & Berti, 2019; Gerosa & Fishbach, 2021) or accreted additional mass (Safarzadeh et al., 2020). It is shown in Tagawa et al. (2020a) that BHs can both accrete mass and merge with others in AGN discs. In many cases the BHs were found to merge more than once, producing BHs in the anticipated mass gap or above the anticipated BH masses from stellar evolution. This result could explain the observed high mass merger of GW190521 (the combined mass coming in at $\sim 150 M_{\odot}$). Mergers in this channel can come from both pre-existing binaries (e.g. Antonini & Rasio, 2016; Bartos et al., 2017b; Ford & McKernan, 2022) or perhaps more commonly from binaries formed from BHs embedded in the AGN disc, as suggested by Tagawa et al. (2020a). If the latter is indeed more common, then the estimations of merger rates within AGN depend significantly on our understanding of how efficiently gas can aid binary formation.

In this Chapter, the efficiency and efficacy of BBH formation via gas dissipation during two body scatterings in an AGN disc is investigated. How the AGN disc

mass and the influence of the SMBH affect the encounter is also examined. A total of 15 three-dimensional simulations of the approach of two isolated BHs in an AGN disc are performed. This chapter is structured as follows: the computational method used to model this system is described in Sec. 4.3, followed by a description of the initial conditions in Sec. 4.4. Fiducial simulation results showing a successful gas-assisted binary formation event are presented in Sec. 4.5 and the sources of torques and energy dissipation are discussed. Sec. 4.6 presents the outcome of all other simulations, showing that gas-assisted captures may occur for a broad range of initial conditions for sufficiently high initial gas densities. A discussion of the findings and methods is given in Sec. 4.7, followed by a summary and the conclusions in Sec. 4.8.

4.2 Setting the scene

Smoothed particle hydrodynamic (SPH) simulations are performed of two stellar-mass BHs orbiting in an AGN disc, which undergo a mutual close encounter. The setup differs from previous hydrodynamic simulations of binaries in AGN, since the binary has not yet formed at the start of the simulation. This setup allows us to investigate the gas-assisted binary formation process which Tagawa et al. (2020a) predicted to be the formation pathway for >90% of binaries that merge in AGN.

4.3 Computational Methods

The accretion disc is modelled by 2.5×10^7 gas particles around a SMBH of mass $M_\bullet = 4 \times 10^6 \mathrm{M}_\odot$, representing an object in the more numerous population of low redshift AGN as predicted by the AGN mass function (e.g. Shankar et al. 2004; Greene & Ho 2007; Li et al. 2011). Radiative and magnetic effects, which for the AGN disc are more relevant closer to the SMBH than the orbital radius of interest (Jiang et al., 2019; Davis & Tchekhovskoy, 2020), are neglected. The SPH code PHANTOM (as outlined in Chapter 3) is used to solve the fluid equations. These particles are placed in a circular annulus around a SMBH between an inner radius $R_{\rm in}$ and outer radius $R_{\rm out}$ using a Monte Carlo scheme.

The orbiting stellar-mass BHs are represented by sink particles which may accrete mass, momentum and angular momentum from infalling gas particles. The

corresponding accretion radii $r_{\rm acc}$ of these sinks are defined as a fraction of the Hill radius $r_{\rm H}$ of the associated object, as in Eq. (2.14). This fraction is set to $r_{\rm acc} = 0.01 r_{\rm H}$. Particles entering the accretion radius are checked to see if they meet multiple criteria before being accreted. Upon entering the sink accretion radius, a gas particle is accreted unconditionally inside $0.8 r_{\rm acc}$. As a reminder, in the region $0.8 r_{\rm acc} < r < r_{\rm acc}$, accretion occurs if three conditions are met: i) its specific angular momentum is less than that of a circular Keplerian orbit at its current distance from the accreting BH, ii) it is energetically bound to the particular sink, iii) it is more bound to that sink than any others. Particles are softened near the sinks based on PHANTOM's cubic spline kernel softening with a characteristic softening length equal to the inner boundary of $0.8 r_{\rm acc}$. These are the default sink prescriptions in PHANTOM, which have been shown to reduce the pressure imbalance at the hard accretion boundary of $0.8 r_{\rm acc}$ (see Price et al. 2018).

4.4 Initial Conditions

4.4.1 AGN Disc

The AGN disc in which the satellite BHs are embedded is represented by an annulus of radius $R_{\rm mid} = 0.0075\,{\rm pc}$ and radial width of $\Delta R_{\rm disk} = 20 r_{\rm H}$. The width is set so that any gap opening in the annulus is correctly captured by the simulation. This allows density spirals in the disc from the BHs to dissipate sufficiently upon reaching its edges, whilst not wasting resources solving for gas motions inside or outside this annulus. All models use a purely Shakura-Sunyaev disc (Shakura & Sunyaev, 1973) with a constant alpha viscosity of $\alpha_{SS} = 0.1$. This disc viscosity is applied to both approaching and receding particles according to Eq. (3.14). In the simulations, viscous and shock heating is neglected. The adopted values of the model parameters are listed in Table 4.1. The surface density follows a power-law profile of the form

$$\Sigma(R) = \Sigma_0 \left(\frac{R}{R_{\rm in}} \right)^{-p}, \tag{4.1}$$

where R is the 2D radial distance from the SMBH in the plane of the disc, $R_{\rm in} = R_{\rm mid} - \frac{1}{2}\Delta R_{\rm disk}$ is the inner radius of the annulus, $p = 0.6$ is the power-law exponent

ΔR_i	$\Delta\phi$	$\frac{M_\bullet}{\mathrm{M}_\odot}$	$\frac{M_{\rm BH}}{\mathrm{M}_\odot}$	$\frac{M_{\rm d}}{10^{-3}M_\bullet}$	$\frac{R_{\rm mid}}{\rm mpc}$	$\frac{\Delta R_{\rm disc}}{r_{\rm H}}$	
2.5–3.5	25°	4×10^6	25	$\{0.32, 1.6, 8\}$	7.5	20	
f	q	$\frac{H}{R_{\rm in}}$	$\alpha_{\rm SS}$	$L_{\rm E}$	ϵ	ξ	$\hat{\kappa}$
0.6	0.45	0.005	0.1	0.1	0.1	0.6	1.0

Table 4.1: Fiducial model parameters. Here $(\Delta R_i, \Delta\phi)$ are the initial radial offset and orbital phase between the two stellar BHs in their initially Keplerian orbits around the SMBH, $r_{\rm H}$ is the Hill radius, $(M_\bullet, M_{\rm BH}, M_{\rm d})$ are respectively the SMBH mass, the individual stellar BH masses, and the total enclosed gaseous disk mass (Eq. 4.5), hence the gas mass per $r_{\rm H}$ radial width is $\frac{7}{5}(r_{\rm H}/R_{\rm mid})M_{\rm d} = 0.026M_{\rm d} = \{23, 110, 570\}\mathrm{M}_\odot$, $(R_{\rm mid}, \Delta R_{\rm disk})$ are the mean radius and the width of the simulated gaseous annulus, p and q set the radial dependence for the sound speed and surface density across the annulus (Eqs. 4.3–4.1), H is the scaleheight ($H = 0.4\,r_{\rm H}$) which also sets the pressure and temperature in the disk via Eq. (4.3), $L_{\rm E}$ is the Eddington ratio, ϵ is the radiative efficiency, ξ is the mean molecular mass, $\hat{\kappa}$ is the opacity relative to the electron scattering opacity ($0.4\,\mathrm{cm^2 g^{-1}}$).

and Σ_0 is the density at $R_{\rm in}$. The sound speed, $c_{\rm s}$, assumes a locally isothermal equation of state and is described in a similar form to the density:

$$c_{\rm s}(R) = c_{\rm s,in}\left(\frac{R}{R_{\rm in}}\right)^{-q}, \tag{4.2}$$

$$c_{\rm s,in} = \left(\frac{H}{R}\right)_{R_{\rm in}}\sqrt{\frac{GM_\bullet}{R_{\rm in}}}\,. \tag{4.3}$$

Here $q = 0.45$ is a power-law index, $H = c_{\rm s}/\Omega$ is the disc scale height, $M_\bullet$ is the SMBH mass and $c_{\rm s,in}$ is the sound speed at $R_{\rm in}$, defined in Eq. (4.3) to satisfy the target H/R at $R_{\rm in}$ and G is the gravitational constant. Consistent with a geometrically thin disc (e.g. Szuszkiewicz et al. 1996), the value of $(H/R)_{\rm in} = 0.005$ is used for all models. Under the assumption of local thermal equilibrium, the vertical density is given by the usual relation:

$$\rho(R, z) = \frac{\Sigma(R)}{\sqrt{2\pi}H}\exp\left(\frac{-z^2}{2H^2}\right). \tag{4.4}$$

In alignment with the steady Shakura-Sunyaev alpha disc prescription of Goodman & Tan (2004) the inner density Σ_0 may be deduced from the enclosed disc mass

$M_{\rm d,0}$, dependent on $M_\bullet$ and α_{SS}:

$$M_{\rm d,0}(<R) \approx 4.82\times10^5 \alpha_{SS}^{-\frac{4}{5}} \hat{\kappa}^{-\frac{1}{5}} \mu_{\rm mol}^{-\frac{4}{5}} \left(\frac{L_E}{\epsilon}\right)^{\frac{3}{5}} \left(\frac{M_\bullet}{10^8 {\rm M}_\odot}\right)^{\frac{11}{5}} \left(\frac{R}{1000 r_s}\right)^{\frac{7}{5}} {\rm M}_\odot, \quad (4.5)$$

where $r_s = 2GM_\bullet/c^2$ is the Schwarzschild radius of the SMBH. The zero subscript denotes this as the fiducial disc mass which will later be modified. This relation provides the disc mass enclosed within some radius R given four parameters: the disc luminosity relative to the Eddington limit L_E, the mean molecular mass $\mu_{\rm mol}$, opacity $\hat{\kappa}$ and radiative efficiency ϵ. The adopted values listed in Table 4.1 correspond to an optically thick, geometrically thin, radiatively efficient disc. From the enclosed mass, Σ_0 is calculated via normalisation of the density function in Eq. (4.4) between $R_{\rm in}$ and $R_{\rm out}$ such that

$$2\pi \int_{R_{\rm in}}^{R_{\rm out}} \Sigma(R) R dR = M_{\rm d,0}(R_{\rm out}) - M_{\rm d,0}(R_{\rm in})\,. \quad (4.6)$$

4.4.2 BH Satellites

Two equal-mass BHs with $m_1, m_2 = 25{\rm M}_\odot$ are inserted with circular Keplerian orbits with no velocity dispersion around the SMBH, accounting for the radially enclosed disc mass, assuming cylindrical symmetry, with zero inclination. To simulate a possible capture within the limit of the observed density cusp at ∼0.01pc, the BHs are initialised symmetrically about 0.0075pc at an azimuthal separation of 20 degrees with the outer object ahead of the inner along its orbit. The orbital period of the BHs around the SMBH is ∼ 30yr. The BHs are inserted without their own accretion discs, but prior to closing their angular separation they quickly accumulate significant disc mass until after about 10 years and the buildup becomes more gradual. In this way, their discs are formed entirely self-consistently within the simulation and do not rely on their own separate set of initial conditions. The satellite BHs are given a small sink accretion radius to minimise the chance the BHs cross each other's accretion radii where gas dissipation cannot take effect. The accretion radii for the BHs was set to $r_{\rm acc} = 0.01 r_{\rm H}$ to solve for the smallest practical accretion radius ensuring dynamical friction is incorporated directly and as accurately as possible from the local SPH particles.

4.4.3 Different Models

A total of 15 simulations are run, labelled $Cap_{X,Y}$. The effect of varying the initial disc mass is examined using three alternate enclosed disc masses denoted in the first subscript $X = 0.2, 1, 5$ corresponding to models with 1/5, 1 and 5 times the disc mass of the standard Shakura-Sunyaev disk ($M_{\rm d,0}$) according to Eq. (4.5) respectively. For each of these 3 cases, 5 models are run with different initial radial separations, ΔR_i. This allows us to observe any stochastic behaviour in encounters with the same AGN disc mass as well as sample slightly different approaches for the encounter. In units of the BHs' initial Hill radii these have separations 2.5, 2.75, 3, 3.25 and 3.5. These are similarly denoted in the second subscript as $Y = 2.5, ..., 3.5$. Therefore, the model with five times the expected disc mass and an initial radial separation of 3.5 $r_{\rm H}$ is labelled $Cap_{5,3.5}$. It may seem that the choice for the range of radial separations is large and that one should expect only weak encounters between the BHs. However, as shown in one of my collaborative papers that models this system in a pure N-body framework (Boekholt et al., 2023), as well as by others (e.g. Higuchi & Ida, 2016), gravitational focusing can still lead to close encounters well within the Hill sphere even where the initial radial separation is beyond this distance. Since gas is now included this range is increased further to allow for the fact the mass within the Hill radii of the objects will grow as they accrete mass and form CSMDs from the surrounding gas, which will lead to increased focusing in the lead up to the encounter. This was tested based on initial lower resolution test runs. All models with varying radial separations maintain 0.0075pc as the radial midpoint of the BHs as well as the annulus. As a visual example, Figure 4.1 shows the initial gas annulus, its surface density, as well as the positions of the BHs in the disc. All surface density plots in this thesis are rendered using SPLASH (see Price 2007). This figure corresponds to the first panel of the cartoon in Figure 2.5. I summarise all parameterised initial conditions in Table 4.1.

4.5 Results (Fiducial)

For clarity, let us begin the discussion considering only a single model due to the many components of these simulations and their analysis that must be defined. The

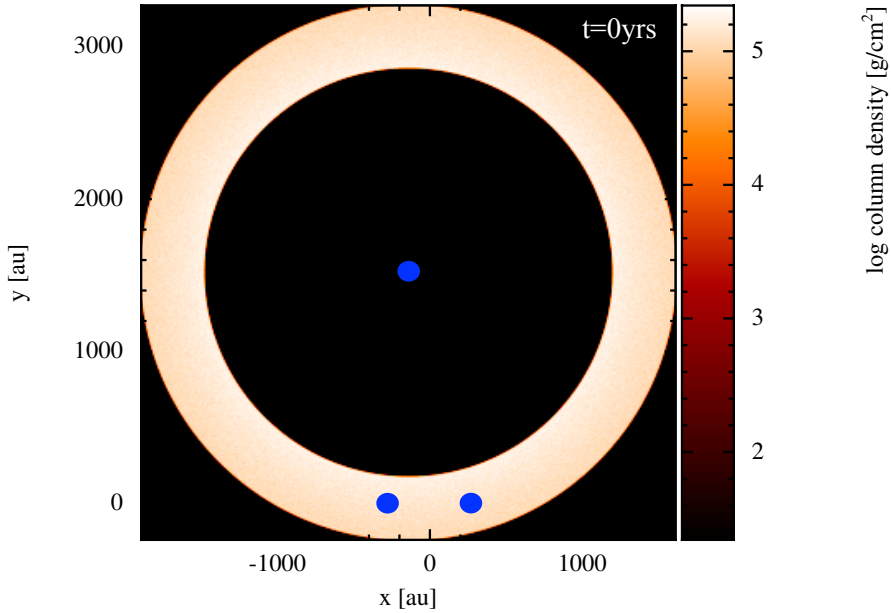

Figure 4.1: Initial gas surface density profile of $Cap_{5,3.5}$ with the SMBH and satellite BHs represented by the blue markers.

fiducial model is $Cap_{1,2.5}$ with initial radial separation $\Delta R_i = 2.5 r_{\rm H}$ and $M_{\rm d} = M_{\rm d,0}$, corresponding to a standard Shakura-Sunyaev accretion disc, see Sec. 4.4.3.

4.5.1 Capture Overview

Gas Morphology

Figure 4.2 shows the surface density of the fiducial simulation just prior to, during and long after the first encounter, in direct correspondence to the last 4 panels in the cartoon of Figure 2.5. This gives a visual example of the simulated formation of a binary via gas dissipation. In the first panel, gas is observed to accumulate around each BH and forms CSMDs (1st panel), reaching out to $\sim r_{\rm H}/2$. At the same time, the presence of the objects leads to an underdensity of about one order of magnitude compared to the AGN disc between them as the gas on initially approximately Keplerian orbits is deflected towards each BH, forming dense gas streams feeding their accretion minidiscs. This is well understood in literature surrounding planets in protostellar discs (e.g. Lubow et al. 1999, Ogilvie & Lubow 2002, Kley & Nelson 2012).

The self-consistently formed CSMDs in the simulations orbit prograde (anticlockwise) with respect to the SMBH disc. This results from local gas following horseshoe

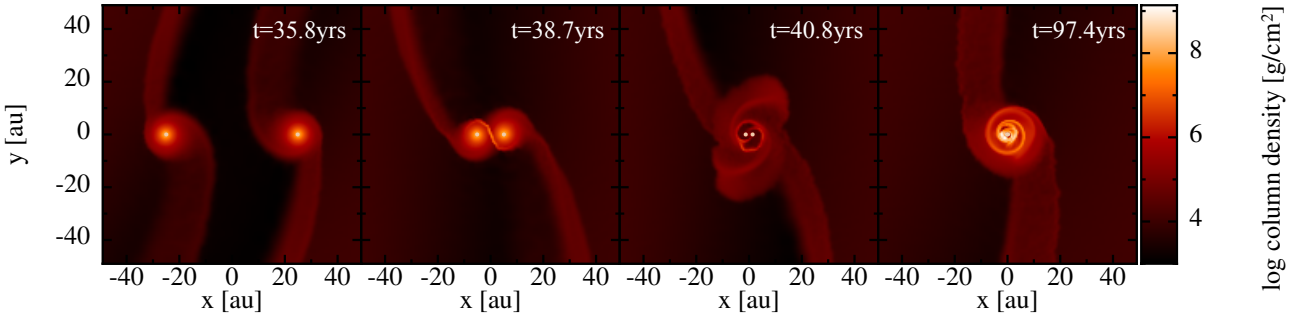

Figure 4.2: Time series of capture process for the fiducial model, snapshots taken at 35.81, 38.63, 40.79 and 97.33yr. The BHs are moving clockwise around the SMBH with the SMBH to the left. Each panel is orientated to the line connecting the two BHs. *From left to right:* i) the two BHs and their accretion discs shortly before encounter, ii) initial intersection of accretion discs leading to overdensity at the point of contact, iii) violent gas outflows and spiral structure as material is stripped from their circum-single discs, iv) final snapshot of simulation showing a well defined circumbinary disc around a well hardened binary.

streamlines around the BHs in its rotating frame around the SMBH, against the background flow of the AGN disc around the BH (see also Lubow et al., 1999). If the satellite BHs had some initial eccentricity, this could lead to retrograde CSMDs (see Li et al., 2022b), which warrants further study in this context. Distinguishing the sense of the disc rotation is important as it implies that when the BH accretion discs intersect, their flows meet head on rather than in parallel if their disc rotations were opposite. This is depicted in the second panel of the figure as the density increases by three orders of magnitude above the AGN disc at the point where the two discs intersect. This pileup is also observed in simulations of protostellar disc collisions, see for example Figure 2 in Shen et al. (2010).

Strong spiral gas outflows are generated during the close encounter (3rd panel) due to strong tidal stripping of the initially well defined circumsingle accretion discs of the BHs as they orbit the COM prograde with respect to the AGN disc. These outflows remove a portion of the mass initially retained in the individual Hill spheres of the BHs. Another portion is accreted onto the BHs. After a relatively short period of time (few tens of orbits of the newborn binary), the spiral structure dissipates and the binary is sufficiently hardened so that a circum-binary mini-disc (CBMD) may form around it (4th panel). At this point, the evolution of the binary is governed by more complex and secular interactions with the CBMD and inner

gas dynamics. This marks the transition from the novel initial conditions to the much more widely studied problem of a pre-existing binary satellite (see references in Section 2.9) that will be compared to in Section 4.7.1.

Binary Dynamics

Figure 4.3 shows the orbital elements of the simulated binary, including the eccentricity e, separation Δr and semi-major axis a, in addition to the total binary mass $M_{\rm bin}$ and specific two-body energy as a function of time. I express the quantities in the natural units of the binary where $r_{\rm H}$ is the initial satellite Hill radius and $\Omega_{\rm CM}$ is the orbital period of the COM of the binary about the SMBH. The eccentricity is calculated via

$$e = \sqrt{1 + \frac{2E_{\rm bin}L^2}{G^2 M_{\rm bin}^2 \mu^3}}\,, \tag{4.7}$$

where $M_{\rm bin} = m_1 + m_2$ is the binary mass, $\mu = m_1 m_2 / M_{\rm bin}$ the reduced mass, G is the gravitational constant and $L = \mu(\boldsymbol{r}_1 - \boldsymbol{r}_2) \times (\boldsymbol{v}_1 - \boldsymbol{v}_2)$ is the angular momentum with $\boldsymbol{v}_i$, $\boldsymbol{r}_i$ being the velocities and positions of the BH satellites $i = (1, 2)$. The two-body energy $E_{\rm bin}$ is calculated in the COM frame of the binary as

$$E_{\rm bin} = \frac{1}{2}\mu \|\boldsymbol{v}_1 - \boldsymbol{v}_2\|^2 - \frac{G M_{\rm bin}\mu}{\|\boldsymbol{r}_1 - \boldsymbol{r}_2\|}\,. \tag{4.8}$$

Initially the BHs do not form a bound system, as implied by $E_{\rm bin} > 0$, $e > 1$.

The binary forms at $t \sim 40\,{\rm yr}$, indicated by the sudden drop in separation and specific two-body energy. At this point the energy of the binary becomes negative and the separation begins to oscillate as the BHs orbit the binary COM, indicating the BHs are now energetically bound and the capture is successful. After this point the binary is hardened, visible in the decreasing semi-major axis and orbital energy. As indicated by the drop in orbital energy, the energy dissipation during the first encounter is highly efficient. This is necessary for capture to be successful. Since the encounter occurs in such a short time, the positive energy of the binary must be dissipated within the time the binaries are in each other's Hill spheres, otherwise they cannot remain bound. In practice, the energy must be reduced to well below zero to form a permanently bound binary and ensure that the central SMBH does not ionise the binary if it were loosely bound. Furthermore, the panel on $M_{\rm bin}$ in

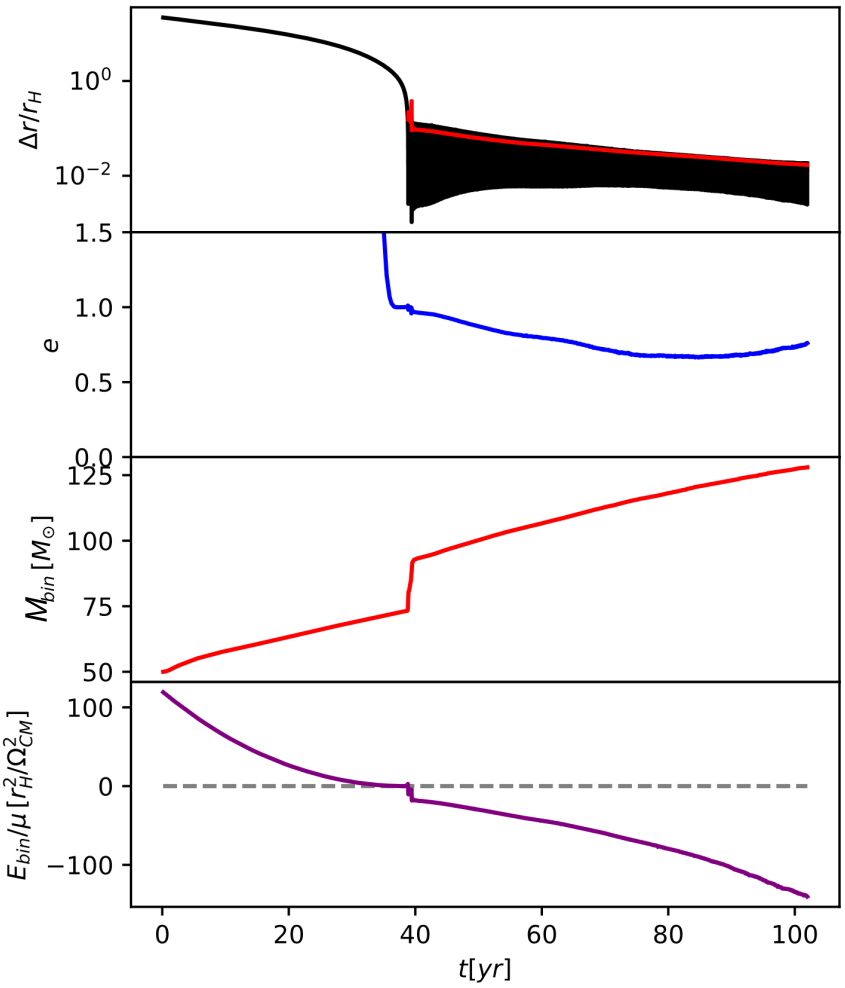

Figure 4.3: Binary orbital elements as a function of time. From top to bottom, panel (i) shows the separation as a fraction of the binary Hill sphere (black) with the semi major axis overlaid (red). (ii) The binary eccentricity showing the initial hyperbolic encounter with $e > 1$. (iii) The binary mass as a function of time, showing a rapid accretion period during the encounter. Finally, (iv) the energy per unit mass of the binary which crosses the axis.

Figure 4.3 shows that a significant amount of gas is also accreted during the chaotic outflows. This rate is considerably super-Eddington at $\simeq M_{\odot}$yr. Such significant accretion driven mass change effects can also enhance capture and stabilise satellite orbits (Heppenheimer & Porco, 1977) by increasing the contribution of the negative two-body potential term in the internal energy equation in Eq. (4.8) and the size of the Hill sphere of the satellites. Though super-Eddington accretion is permissible, the rate here is highly unstable and would be limited by radiative effects (Tagawa et al., 2022). However as we will see in Chapter 5, this overestimation does not change the overall results of the binary encounter or evolution.

The results agree well with analogous findings in the literature of proto-planetary disc collisions (e.g. Watkins et al., 1998a,b; Shen et al., 2010; Muñoz et al., 2015) and even show similar behaviour to the star-disc encounters of Boffin et al. (1998) provided the star actually crosses the accretion disc in their simulations like the BHs do in this case. In particular, the sudden drop in orbital energy over the first orbital period is consistent across the literature, provided there is intersection with the disc. Likewise, the sudden drop in eccentricity and semi major axis followed by a gradual decrease is also consistent with Muñoz et al. (2015), where the post-encounter orbital evolution is also considered. The origin for the later increase in eccentricity that occurs after roughly 80 years in the simulation (equivalent to ~ 1000 inner binary orbits) is unclear, however the range in the eccentricity is particularly interesting. Over the entire binary lifetime, the binary eccentricity does not decrease below 0.6, consistent with Muñoz et al. (2015). Provided AGN binary satellite models assume a gas-capture formation origin, as Tagawa et al. (2020a) predicts the majority will be, this draws the assumption in most pre-existing gas-embedded binary simulations that the binary should be initialised with minimal eccentricity into question.

4.5.2 Orbital energy dissipation at first encounter

To understand the change in orbital energy of the binary at capture, the various mechanisms which can alter its energy must be understood. There are three such mechanisms in the simulations, each defined in terms of energy per unit time removed/added to the binary:

1. **SMBH interaction**, $\varepsilon_{\rm SMBH}$ - energy per unit time exchanged by the binary system and the SMBH.

2. **Gas gravitational dissipation**, $\varepsilon_{\rm grav}$ - from the gravitational interaction with the surrounding gas.

3. **Accretion**, $\varepsilon_{\rm acc}$ - due to conservation of linear momentum of accreted gas particles onto the BHs.

These quantities represent the rate of work done on the binary, which are calculated per unit mass of the binary by taking the time derivative of Eq. (4.8):

$$\varepsilon = \frac{d}{dt}\left(\frac{E_{\rm bin}}{\mu}\right) = (\boldsymbol{v}_1 - \boldsymbol{v}_2)\cdot(\boldsymbol{a}_1 - \boldsymbol{a}_2) - \frac{G\dot{M}_{\rm bin}}{\|\boldsymbol{r}_1 - \boldsymbol{r}_2\|}. \tag{4.9}$$

Here the first term represents the work done by all external forces (i.e. excluding their mutual attraction) and momentum transfer which drive a relative acceleration $\boldsymbol{a}_1 - \boldsymbol{a}_2$ of the satellites ($\boldsymbol{v}_1$ and $\boldsymbol{v}_2$ is the relative velocity) and the second term is sourced by accretion, resulting from the increase in the second term in Eq (4.8). The SMBH contribution $\varepsilon_{\rm SMBH}$ is calculated from the force differential due to the gravitational interactions with the SMBH,

$$\varepsilon_{\rm SMBH} = (\boldsymbol{v}_1 - \boldsymbol{v}_2)\cdot(\boldsymbol{a}_{1,\rm SMBH} - \boldsymbol{a}_{2,\rm SMBH}) \tag{4.10}$$

where the acceleration of BH $i = (1, 2)$ due to the SMBH is

$$\boldsymbol{a}_{i,\rm SMBH} = GM_\bullet \frac{(\boldsymbol{r}_i - \boldsymbol{r}_\bullet)}{||\boldsymbol{r}_i - \boldsymbol{r}_\bullet||^3}\,. \tag{4.11}$$

Here $\boldsymbol{r}_\bullet$ is the SMBH position, which is generally very close to centre of mass of the simulation.

The gas gravitational dissipation term $\varepsilon_{\rm grav}$ is analogous to $\varepsilon_{\rm SMBH}$ by summing over the gravitational forces acting on the BHs from all $N_{\rm p}$ gas particles of mass $m_{\rm p}$,

$$\varepsilon_{\rm grav} = (\boldsymbol{v}_1 - \boldsymbol{v}_2)\cdot(\boldsymbol{a}_{1,\rm gas} - \boldsymbol{a}_{2,\rm gas}), \tag{4.12}$$

where the acceleration of BH $i = (1, 2)$ due to the gas is

$$\boldsymbol{a}_{i,\rm gas} = \sum_{p=1}^{N_p} Gm_p \frac{(\boldsymbol{r}_i - \boldsymbol{r}_p)}{||\boldsymbol{r}_i - \boldsymbol{r}_p||^3}\,. \tag{4.13}$$

The accretion term $\varepsilon_{\rm acc}$ represents the work done on the binary due to the change in the linear momentum of the BHs when they accrete gas particles. Upon accretion of a particle by a BH, the BH's position, velocity and acceleration are modified by a mass weighted average of all $N_{\rm acc}$ accreted particles during that timestep as

$$\Delta \boldsymbol{a}_i = \frac{M_i \boldsymbol{a}_i + m_{\rm p} \sum_j^{N_{\rm acc}} \boldsymbol{a}_{\rm p,j}}{M_i + N_{\rm acc} m_{\rm p}} - \boldsymbol{a}_i \,. \tag{4.14}$$

$$\Delta \boldsymbol{v}_i = \frac{M_i \boldsymbol{v}_i + m_{\rm p} \sum_j^{N_{\rm acc}} \boldsymbol{v}_{\rm p,j}}{M_i + N_{\rm acc} m_{\rm p}} - \boldsymbol{v}_i \,. \tag{4.15}$$

Here $\boldsymbol{a}_i$, $\boldsymbol{v}_i$ are the accelerations and velocities of the $i = (1, 2)$ satellite BHs prior to accretion during that timestep (since accretion is evaluated last), $\Delta \boldsymbol{a}_i$ is the contribution from the SPH particles to the ith BH's acceleration just prior to accretion and $\Delta \mathbf{v}_i$ is the change in its velocity due to the impulsive momentum transfer upon accretion. The $\boldsymbol{a}_{\rm p,j}$ and $\boldsymbol{v}_{\rm p,j}$ terms are the SPH particles' acceleration and velocity upon accretion. The change in velocity, whilst instantaneous, can be treated as an acceleration over the length of the timestep, Δt. Using Eqs. (4.14) and (4.15) dissipation due to accretion can be written as

$$\varepsilon_{\rm acc} \approx (\boldsymbol{v}_1 - \boldsymbol{v}_2) \cdot (\boldsymbol{a}_{1,\rm acc} - \boldsymbol{a}_{2,\rm acc}) - \frac{G \dot{M}_{\rm bin}}{\|\boldsymbol{r}_1 - \boldsymbol{r}_2\|}, \tag{4.16}$$

where

$$\boldsymbol{a}_{i,\rm acc} = \left(\Delta \mathbf{a}_i + \frac{\Delta \mathbf{v}_i}{\Delta t} \right), \tag{4.17}$$

assuming that the impulsive momentum transfer takes place at the end of the timestep. Note that this is a non exact value of $\varepsilon_{\rm acc}$ since the $\Delta \mathbf{v}/\Delta t$ term is an average over the timestep. This approximation is more accurate the higher the particle accretion rate. Unlike in grid codes where a smooth sink *rate* is used, SPH codes have the caveat that accretion relies on discrete particle accretion which can be highly volatile if the number of accreted particles per timestep is low.

Figure 4.4 shows the rate of work due to each component during the binary capture process, including their cumulative value over the domain of the plot. In the figure, dissipation due to the local gas gravity is initially positive, owing to strong density pileups at the inner edge of their circumsingle discs (ahead of the individual BHs) generated as the BHs accelerate through the local gas. After the first encounter, these inhomogeneities begin to orbit the BHs, leading to small oscillations in $\varepsilon_{\rm grav}$. Just prior to the first pericentre passage, which occurs at 38.8yr,

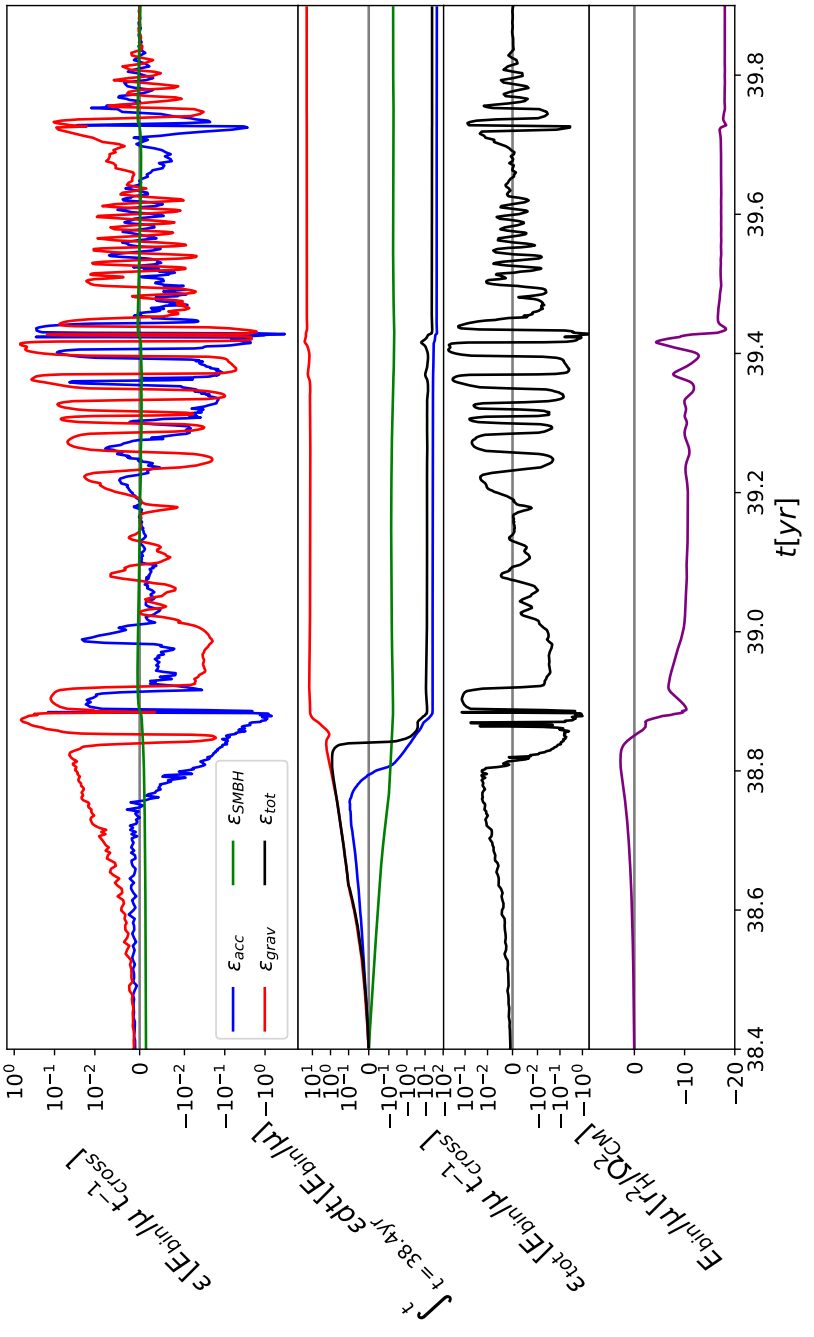

Figure 4.4: *1st row:* The contribution to the rate of binary orbital energy dissipation, in units of initial binary orbital energy upon entering the Hill sphere per crossing time, for each individual process: accretion ($\varepsilon_{\rm acc}$, Eq. 4.17), gas gravity ($\varepsilon_{\rm grav}$, Eq. 4.12), and SMBH tidal force ($\varepsilon_{\rm SMBH}$, Eq. 4.10).*2nd row:* The cumulative contribution of the work done by all three mechanisms including the cumulative total. *3rd row:* The sum of the three components shown in the top panel, $\epsilon_{\rm tot}$. *4th row:* The binding energy of the two BHs from eq (4.8). The sharp dip in $\epsilon_{\rm tot}$ during the close approach leads to a significant permanent decrease of the orbital energy.

strong accretion removes a significant portion of energy. This is the hallmark of the gas-capture process. The energy lost in this interaction allows for the energetic retention of the binary, as indicated in the bottom panel showing the total energy of the binary transitioning form positive to negative, dipping after each of the two first encounters. If the binary did not dissipate enough energy at the first encounter then its energy would remain positive and the two objects would remain on an unbound orbits in the two body regime. The force differential due to the SMBH is insignificant compared to forces due to accretion and gas gravity. From the cumulative work done, the gas is shown to actually do net positive work on the binary while accretion leads to negative work, overcoming the positive contribution from ε_{grav}.

The local gas gravity is shown to vary on scales shorter than the binary period. Figure 4.5 deconstructs the contributions to the rate of work done on the binary from the gas gravitational component ($\varepsilon_{\rm grav}$) as a function of position in 2D. To achieve this, gas particles are binned in a 200×200 grid in x-y and the sum in Eq. (4.13) is restricted accordingly. In each of these bins, the dissipation can be positive or negative depending on whether the gas is lagging behind or ahead of the path of the BHs respectively. The 2D dissipation maps are shown separately with respect to only one of the BHs or both BHs to illustrate the morphology of the work done on a single object and the binary system during the first encounter. Also shown is the cumulative radial energy dissipation constructed by radially binning the particles in $R = \sqrt{x^2 + y^2}$ from the centre of each BH. The cumulative dissipation as a function of R from the BHs is shown in Figure 4.5 (right panel) in units of the binary energy when the BHs enter each other's Hill sphere per the crossing time t_{cross} for the Hill sphere, taking crossing time to be r_H divided by the relative speed when entering the Hill sphere. The figure indicates a very strong energy transfer onto the binary from material very close to the BHs ($\sim 0.1a$), while energy is removed outside this very small distance. During this period there is a resolution of ∼100,000 SPH particles within r_H, with particle densities being highest in the CMSDs. Therefore variation emerging from small number statistics close to the sinks in the simulation is confidently ruled out. Outside of $3a$ there is no significant effect of the gas on the binary energy. The two other panels showing the 2D distribution show very dense gas buildups just ahead of the BHs and (less) dense trails following them. Though the size of the trails are larger than the density pileups, they are not able to

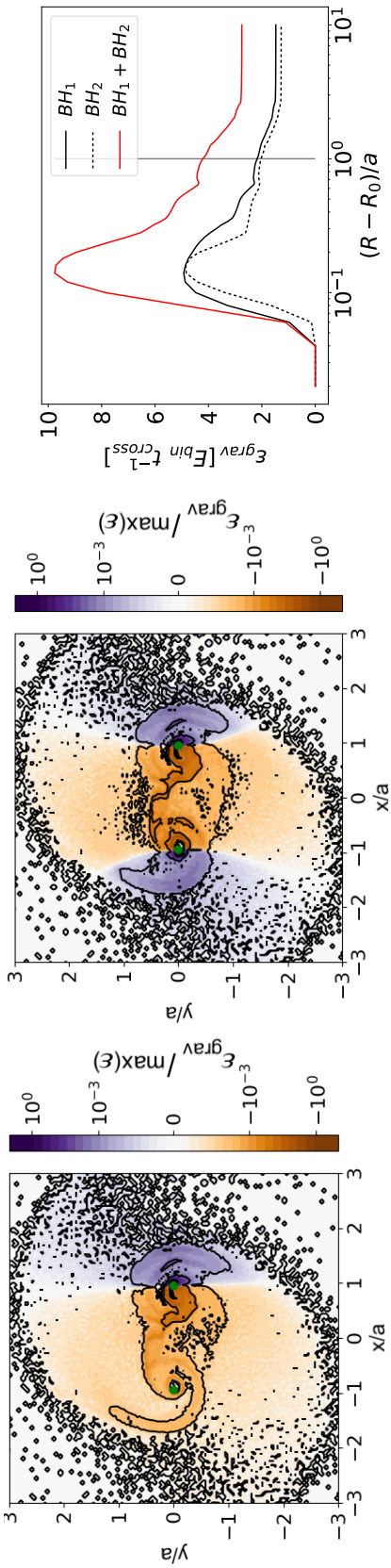

Figure 4.5: The rate of work done by the gas gravity, in units of the energy upon entering each other's Hill sphere per crossing time, on the binary ($\varepsilon_{\rm grav}$) at 39.01yr, shortly after the first close approach at 38.88yr. Left and middle panels show respectively the 2D maps of the gravitational work density by the gas on one binary component and the full binary at a representative timestep. The right panel shows the cumulative radial distribution of $\varepsilon_{\rm grav}$ on each BH, respectively as well as the total. BHs are represented by green dots at (-1,0) and (1,0).

overcome the acceleration on the BHs due to material ahead of their path, leading to a net gain in energy of the binary, as shown in the third panel. This picture reflects the findings and discussion of positive torque sources in the isolated binary simulations of Tiede et al. (2020) but with greater fluctuation.

Angular momentum transfer

The specific torques due to each of the three physical phenomena described earlier can be similarly labelled as $\tau_{\rm SMBH}$, $\tau_{\rm grav}$ and $\tau_{\rm acc}$. Their calculation is analogous to equations (4.10), (4.12), and (4.17) by crossing the relative accelerations with the relative positions

$$\tau_{\rm SMBH} = (\boldsymbol{r}_1 - \boldsymbol{r}_2) \times (\boldsymbol{a}_{1,\rm SMBH} - \boldsymbol{a}_{2,\rm SMBH})\,, \tag{4.18}$$

$$\tau_{\rm grav} = (\boldsymbol{r}_1 - \boldsymbol{r}_2) \times (\boldsymbol{a}_{1,\rm gas} - \boldsymbol{a}_{2,\rm gas}), \tag{4.19}$$

$$\tau_{\rm acc} \approx (\boldsymbol{r}_1 - \boldsymbol{r}_2) \times \left[\left(\Delta\boldsymbol{a}_1 + \frac{\Delta\boldsymbol{V}_1}{\Delta t}\right) - \left(\Delta\boldsymbol{a}_2 + \frac{\Delta\boldsymbol{V}_2}{\Delta t}\right)\right]. \tag{4.20}$$

Following the same procedure as in the previous section for the energy change, Figure 4.6 shows the instantaneous torque contribution of each component as a function of time. Initially, the gas gravitational torque ($\tau_{\rm grav}$) dominates the torque until the BHs cross each other's CSMDs at 38.8 yr and accretion ($\tau_{\rm acc}$) promptly dominates. Significant oscillations are seen in the gas gravitational torques acting on the binary, matching the periodicity of the energy dissipation rate in Figure 4.4. Following the first encounter, the net gas torque is dominated by the gravitational attraction of the gas in the immediate vicinity of the objects. On top of these oscillations, there is a net increase in angular momentum from accretion which helps circularise the binary. The eccentricity is then reduced during each encounter (see Figure 4.3). Figure 4.7 shows the 2D torque map at two different times within a single orbit (39.8 yrs and 39.01 yrs) to show the spatial source of the torques when their net value is positive and negative, along with the cumulative torque as a function of distance from the COM. The times of both snapshots are shown as vertical lines in Figure 4.6. In the left panel the net torque on the binary is initially consistently positive, before it begins to oscillate (as shown in Figure 4.8). The primary source of the positive contribution to the torque occurs at the separation of the BHs (dashed 1st line in the plot). This indicates that the main source

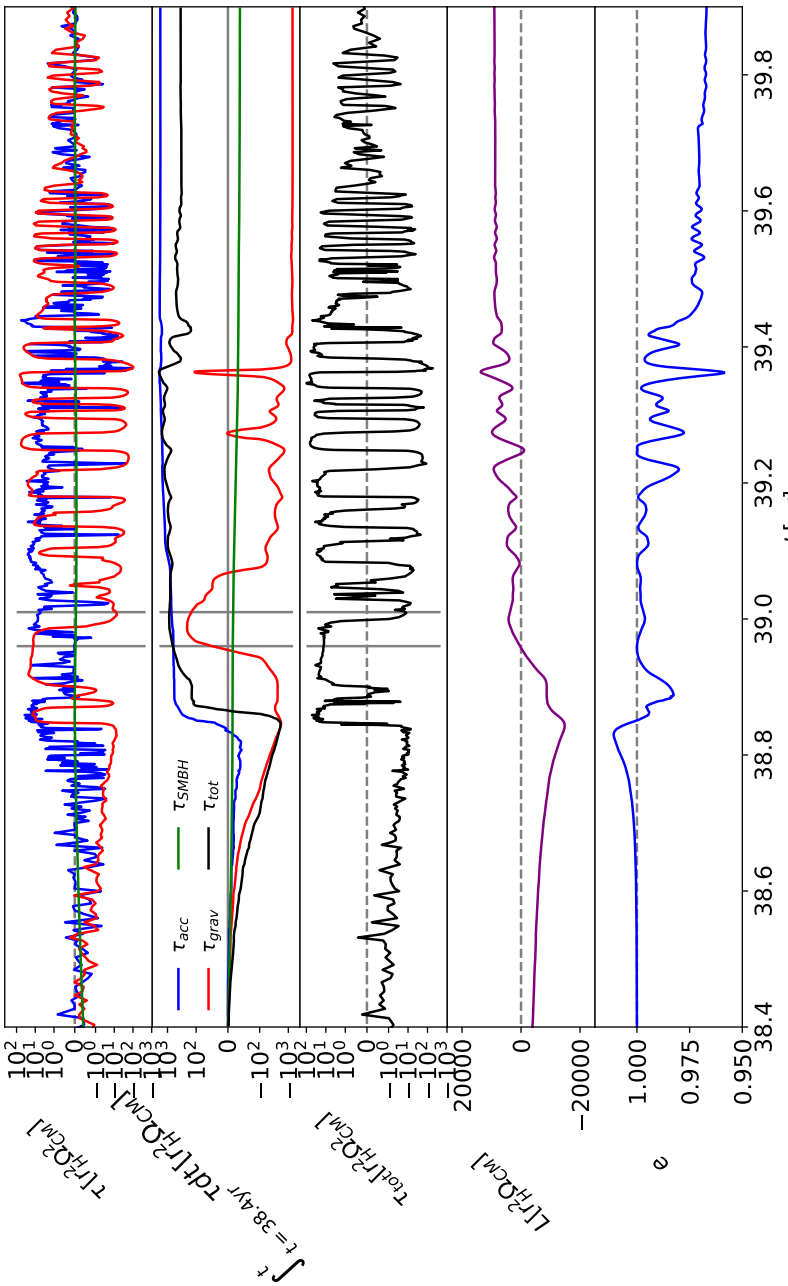

Figure 4.6: *1st row:* The contribution of different processes to the specific torque: accretion ($\tau_{\rm acc}$, Eq. (4.20)), gas gravity ($\tau_{\rm grav}$, Eq. (4.19)), and presence of SMBH ($\tau_{\rm SMBH}$, Eq. (4.18), practically negligible throughout). *2nd row:* Cumulative contribution of each torque mechanism over the figure's time domain showing accretion dominates and circularises the binary. *3rd row:* The net torque from the sum of the three components shown in the top. *4th row:* The orbital angular momentum of the BH binary around its center of mass, its component perpendicular to the gas disk. *5th row:* Binary eccentricity in the corotating frame (Eq. (4.7)). Though the torques are considerably stochastic, there is a systematic increase in angular momentum and a decrease in eccentricity. The vertical grey lines indicate the positions where 2D snapshots of the $\tau_{\rm grav}$ are taken in Figure 4.7.

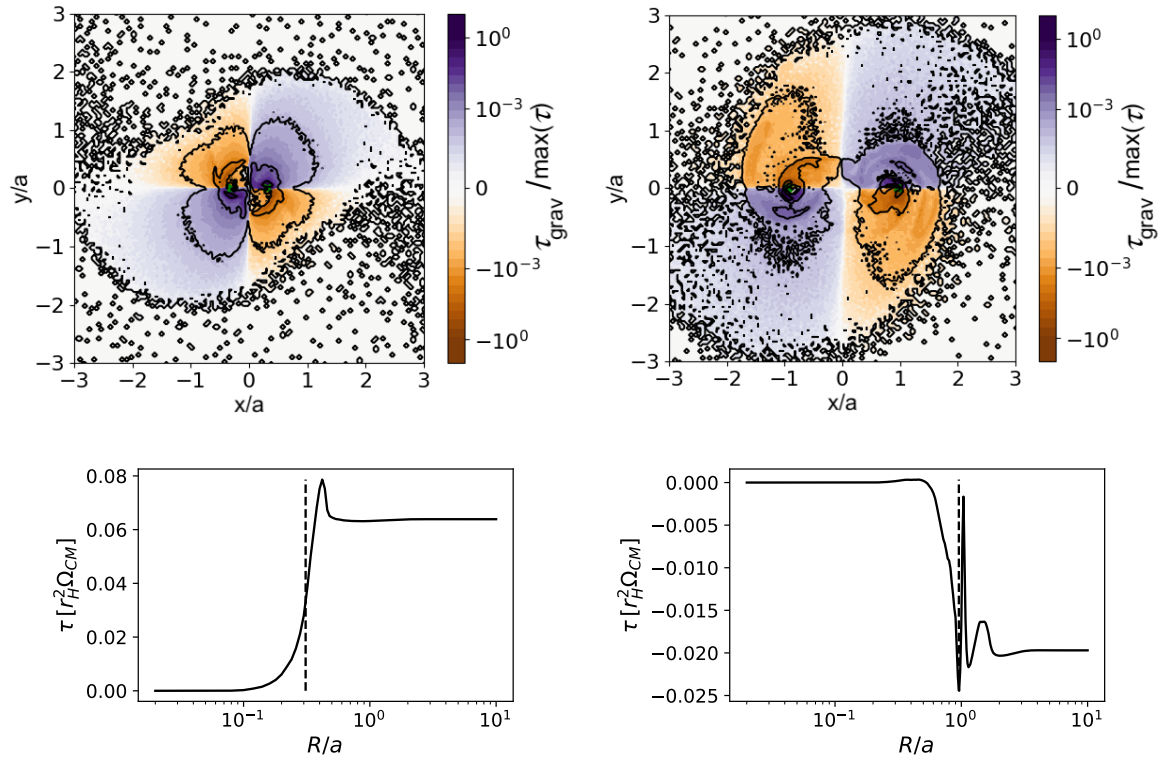

Figure 4.7: (Top row, left to right) Gravitational torque per unit area, normalised to the maximum value within the 200x200 grid shown at 39.8 and 39.01 yrs respectively. Black contours are used to outline equally dense regions of gas. In the second panel, trailing gas structure begins to form behind the binary which is orbiting counter-clockwise (prograde with AGN disc). (Bottom row, left to right) cumulative specific torque on binary as a function of distance from the COM at the same respective times as the above 2D plots. Vertical dashed lines show the position of binary BHs in the snapshot. These show that the strongest contributions to the gravitational torque come from gas very close to the individual BHs and can change sign within a single orbit as the nonaxisymmetric perturbations to the CSMDs orbit their BHs.

of torque arises from structure at the orbital radius of the binary. During this period, the aforementioned density pileups dominate the gravitational torques, shown in the top plot as the large purple wakes ahead of the BHs in the top left plot, outlined by the innermost black density contours. In the next 0.2 years the dense, truncated CSMDs are significantly perturbed by the owners' sibling BH and in the frame of each BH a large cylindrically non-axisymmetric lump of gas begins to orbit around each individual BH. At 39.01 yrs (right column of Figure 4.7) the cumulative torque is dominated by negative torques at similar distances to the BH as the positive torques in the left column. The 2D torque map at this

later time shows that the gas density close to the BH has larger and more extended contours in the negative torque (yellow) quadrants. It is this asymmetry close to the BH which orbits around the BHs and leads to strong oscillations in the gravitational torque until the second close encounter where the discs are nearly entirely disrupted due to the extreme depth of the periapsis.

The change in eccentrity during the encounter is consistent with findings for stellar accretion disc encounters (e.g. Muñoz et al. (2015) also finding an eccentricity decrease after each periapsis passage. Additionally, Bonetti et al. (2020) also find that for massive BBHs subject to dynamical friction with mass ratios larger than 10^{-3}, the eccentricity also decreases.

4.5.3 Binary evolution

In the previous section it was shown that the initial encounter(s) of the binary can reduce the two-body energy and eccentricity of the binary so it is energetically bound via interaction with the gas. Here, I discuss the subsequent secular evolution of the torques, dissipation mechanisms and resultant effect on the binary orbital elements.

Figure 4.8 shows the energy dissipation and torque from each physical mechanism as a function of time for the period following the capture, alongside the binary energy. The results show a continual removal of energy from the binary (predominantly due to accretion) until $\varepsilon_{\rm grav}$ drops below zero. The reason for the flipping in $\varepsilon_{\rm grav}$ as the binary hardens is unclear. Though, D'Orazio & Duffell (2021) find differing evolutions for isolated binaries in the domain of $e < 0.4$ and $e > 0.4$ that could have an analogue in this embedded binary scenario. Comparing the raw data to the running mean, which has a window of one year, their values differ on average by about an order of magnitude, indicating significant variability in the forces the binary experiences. The running mean indicates an approximately constant dissipation rate in the binary orbital energy as a function of time, corroborated by the binary energy vs. time panel which displays relatively low variability over the simulation runtime. As accretion is found to have a hardening effect on the binary, it suggests that its inclusion in works such as Li et al. (2021) that neglect accretion may yield different evolutions for their out-spiralling binaries.

Consider now the secular torques, shown in the right panel of Figure 4.8. For the fiducial case, the torques are dominated by the gas gravity as shown by the

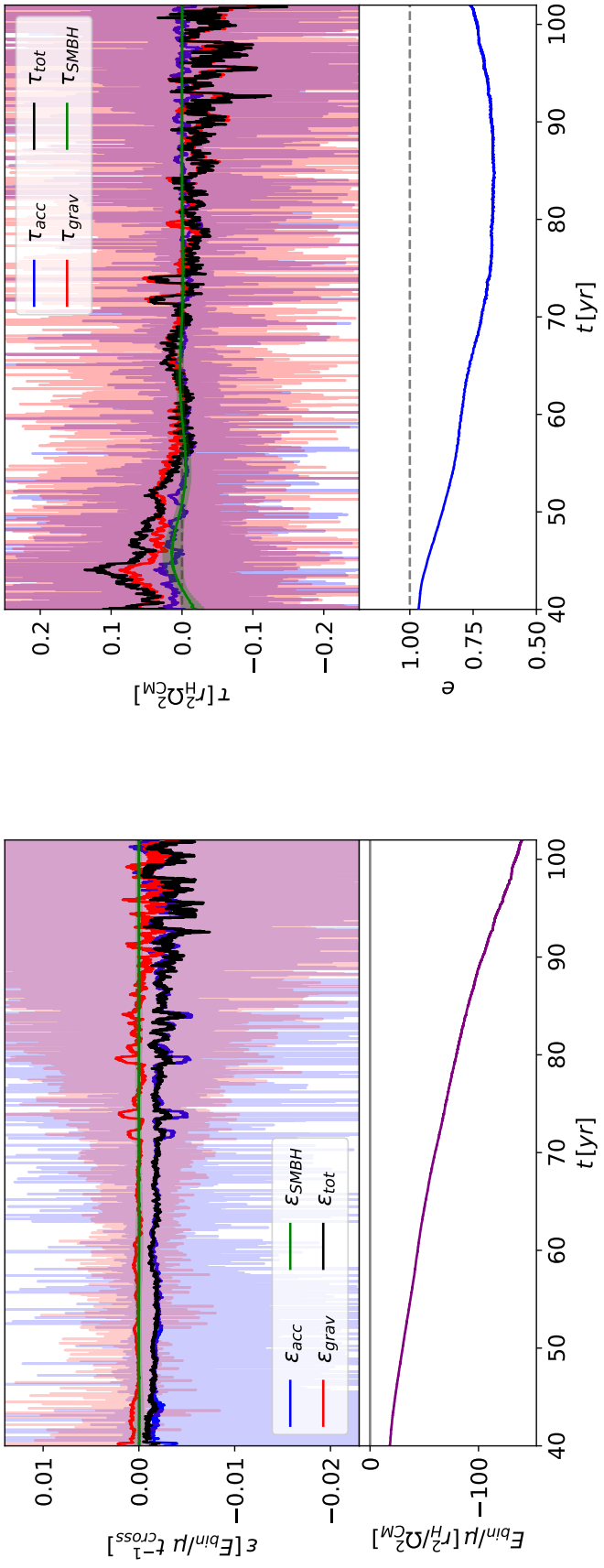

Figure 4.8: (Top panel) Torques as a function of time for each of the three mechanisms showing a net loss of angular momentum from the binary. Bold lines show the running mean compared to the raw data in the background (opaque lines). (Bottom Panel) Binary eccentricty as a function of time.

behaviour of $\tau_{\rm grav}$. Curiously, for the first half of the evolution, up to around 80 years, the net torque is initially positive and later switches to negative values. The result of this shift is an initially decreasing eccentricity before plateauing and then increasing gradually. Comparing this result to works looking at pre-existing gas-embedded binaries, this result disagrees with those the wind tunnel simulations of Li & Lai (2022a) where their initially eccentric binaries still experience damping, though their most eccentric binary ($e = 0.5$) is still less eccentric than the minimum achieved here. The torque reversal is also inconsistent with the findings of Dempsey et al. (2022) since here the torques are positive for $a/r_{\rm H} < 0.05$ and for $a/r_{\rm H} > 0.05$ they are negative, just the opposite as in Dempsey et al. (2022). However their study agrees on the separation where the torques reverse sign. In this work the torques reverse when the binary has semi-major axis $a/r_{\rm H} = 0.05$ which is reasonably close to the the turnover at $a/r_{\rm H} = 0.1$ in Dempsey et al. (2022). However, there are several important differences in these studies which could play a role in the binary evolution. Most notably, Dempsey et al. (2022) consider pre-existing low eccentricity binaries in a shearing box configuration with no viscosity implementation. With these differences they achieve higher resolution around their binaries than shown here in this paper, yet the comparison to the highly eccentric binaries in this study, which includes viscosity, is difficult.

As the binary is highly eccentric, the separation of the BHs varies drastically between $\Delta r = a(1 \pm e)$ where the gas density is highly nonlinear. Thus one might expect violent variations in the gaseous torques and the resulting evolution to be stochastic. To investigate the distribution, I calculate the average strength of each torque source in bins of orbital separation, shown in Figure 4.9. The torques vs binary separation are shown in units of the apoapsis so the bounds of the radial binning has a fixed range between zero and unity. In this representation one can observe how the strength of the torque varies with orbital separation by binning these quantities over many orbits. I average these torques over two periods, the first when $\tau_{\rm grav}$ is positive in Figure 4.8 (42-80yr) and when $\tau_{\rm grav}$ is negative (80+yr). As separation is directly coupled to the phase ϕ of the orbit via $\Delta r = a(1 + e)/(1 + e\cos(\phi))$, this is akin to probing the torque as a function of the binary orbital phase. It is reaffirmed from Figure 4.9 that the torques are dominated by $\tau_{\rm grav}$ at all times and that it is positive between 42-80yr and negative thereafter. The strength of the

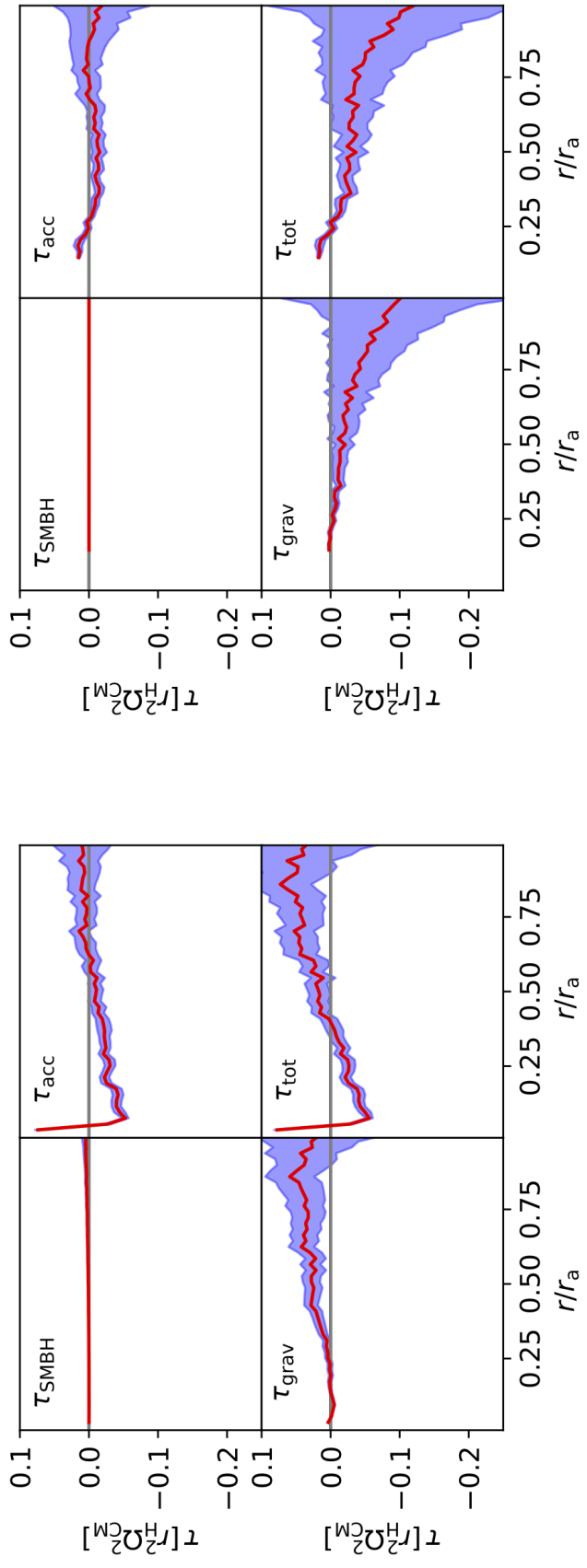

Figure 4.9: Torque as a function of binary separation due to the SMBH, accretion, gas gravity, as well as the total. Shaded blue regions show the $1-\sigma$ variance of the torques about the mean (red). Values at each radius, in units of the instantaneous orbital periapsis, are averaged over two time frames. On the left, the period of time where the torque is positive (42-80yrs) and on the right, when the torque is negative (80-end of simulation). Torque is dominated by gas gravity in both cases when the binary is near apoapsis where the gravitational torque skews positive at earlier times and switches to negative after 80 yrs.

gravitational torque is indeed dependent on radius, being maximal when the binary is at apoapsis and minimal at periapsis. The physical mechanism driving this is the interaction between the binary and the gas as the objects reach their maximum separation. At apoapsis, the objects approach higher density gas flows near the cavity wall and therefore perturb the cavity more strongly. In conjunction, the high eccentricity leads to a minimal velocity at apoapsis far less than the orbital motion of the gas disc, which is orbiting in the opposite direction to the binary. Hence the accreted material is accreted from behind (i.e. trailing the binary) and induces a positive torque on the binary when the momentum of the accreted gas is added to the binary via Equations 4.14 and 4.15. Gas that is perturbed by the BHs' close proximity to the cavity wall, that is not accreted, arcs in front of the BHs and also tugs them forward due to the mass of the gas, serving to add even more angular momentum to the system. Though the average total torque is negative at smaller at separations of $\Delta r/r_{\rm a} \leq 0.3$, the resulting angular momentum change is minimal as the binary spends only a small amount of time at close separation due to its high eccentricity. While the gravitational torque is positive for the first half of the evolution between 42-80yrs the sign flips for the second half and becomes negative when the binary is near apoapsis which is in agreement with Figure 4.8. In their paper, Zrake et al. (2021) find that their isolated eccentric binaries flip also torques, at a slightly lower eccentrity of $e \sim 0.45$ compared to $e \sim 0.6$ in this case.

4.5.4 Summary of Fiducial Model

To summarise, the fiducial model demonstrated that BHs can form a bound binary system following a dynamical encounter when the BHs are embedded in an accretion disc, even though their two-body energy when first crossing each other's Hill spheres is greater than zero and their eccentricity is greater than unity. For this model, this is primarily achieved through very strong accretion against the motion of the binary (Figure 4.8) where momentum conservation from head on accretion leads to a drag on the BHs and reduces their relative energy so they remain energetically bound. Strong oscillations in the gravitational torque and energy exchange between the gas and BHs following the first encounter arise from strong asymmetries in the CSMDs, which are destroyed through tidal forces by the deep second encounter. After their destruction, the torques become more stochastic and evolve the binary secularly.

This result challenges the assumption that dynamical friction will efficiently dissipate the two-body energy of the binary, as analytically proposed in Tagawa et al. (2020a), as moments of inverse dynamical friction occur when the BHs cross each other's CSMDs due to a pileup of gas in front of the BHs. Nonetheless, after the first crossing of the CSMDs and after a significant amount of gas is expelled, the gas gravity acts in tandem with accretion to dissipate the binary energy on the second encounter. I therefore conclude that whether dynamical friction helps or hinders binary formation in this channel depends *strongly* on the local gas morphology and rather than simply the uniform background (AGN disc) gas density and relative motion. Note that the significantly super-Eddington accretion during the encounter will likely invalidate the assumption of local isothermal equilibrium and negligible radiative effects. Although, including such effects is prohibitively expensive. I also note that enhanced circumsingle and circumbinary disc temperatures are shown to actually harden binaries more rapidly (i.e Li et al., 2022c). During the first encounter, gravitational drag from the local gas circularises the binary whilst simultaneously depositing energy into the binary. This energy increase is mitigated by accretion drag, which dominates the energy change of the binary and reduces the total orbital energy in the COM frame of the two BHs to below zero so that a bound binary is formed.

Following the encounter, a prograde binary is formed and all binary properties evolve on the timescale of hundreds of binary orbits. Orbital energy is then gradually removed through accretion and the gas gravity that further hardens the binary. Interaction from the gas continues to circularise the binary until reversing when the binary reaches an eccentricity of 0.65. The reason for this is unclear, though I identify that this torque (regardless of sign) is maximal when the binary is at its apoapsis due to its stronger interaction with the cavity wall as well as greater leverage on the binary.

4.6 Results (Parameter study)

In this section, all 15 of the models are considered, consisting of the 5 different initial radial separations between the two interacting BHs and 3 different AGN disc densities.

4.6.1 Capture

Snapshots from the 15 simulations are shown just prior to merger, at first encounter and at the termination of each simulation in Figures 4.10, 4.11 and 4.12 respectively. Figure 4.10 illustrates individual BH gas discs and their tidal streams in all the models. All BH satellite discs are prograde with the SMBH disc as expected. In the high disc mass cases, very large gas outflows are observed which remove a portion of mass on the same order of magnitude as the mass of the binary system itself, visible through the sharp drop of the enclosed gas mass as a function of time in Figure 4.13. In both the snapshots and Figure 4.13 it is clear that the mass loss scales with the gas density of the AGN disc, due to the larger amount of mass bound to the objects before capture with increasing $M_{\rm d}$. While not surprising, the trend has implications for the efficiency of the energy transfer from the two BHs to the surrounding gas.

The binary separation, Δr, eccentricity, e, and $\hat{z}$ component of the specific angular momentum, L_z/μ as a function of time are shown for all models in Figures 4.14, 4.15 and 4.16 respectively. Together they describe the orbital evolution of the binary. Of first note is the decoupling of $Cap_{1,2.75}$ and $Cap_{0.2,3}$ and three failed captures, $Cap_{1,3.5}$, $Cap_{0.2,3.25}$ and $Cap_{0.2,3.5}$. The failed captures are a consequence of their impact parameters at first encounter being comparable or larger than the binary Hill radius $r_{\rm H}$, so these represent weak encounters between the objects and are immediately perturbed by the SMBH. In the parameter space of ΔR_i and $M_{\rm d}$, represented by the grid itself, these three models populate the bottom right corner. In addition to accretion, the mass of gas within the Hill sphere of each BH for the $0.2M_{d,0}$, $1M_{d,0}$ and $5M_{d,0}$ models reflects the mass difference in the AGN disc, i.e. 0.2, 1 and 5 times as much mass. This leads to an increased gravitational attraction and focusing between BHs during their approach, where BHs in higher AGN disc masses can be deflected towards each other earlier along their Keplerian orbits. This, in tandem with the increased accretion, explains the reason all five $5M_{d,0}$ models lead to a capture.

BHs in models with higher ΔR_i and low $M_{\rm d}$ are far more likely to have a weak encounter as they do not accrete as much mass and therefore don't increase their Hill radius as much when they encounter each other. So the impact parameter in units of Hill radii is larger than in the $5M_{\rm d}$ models and hence more likely to be a

Figure 4.10: Surface density plots of all 15 models just prior to the first encounter of BH satellites. The arrangement follows increasing initial radial separation from left to right and decreasing AGN disc mass from top to bottom. Each model is labelled in the top left of its panel.

Figure 4.11: Surface density plots of all 15 models at apoapsis immediately following their first encounter, demonstrating significant mass ejection in the high disc mass cases (top row).

Figure 4.12: Surface density plots of all 15 models at their end point, i.e. the decoupling of the binary or upon termination of the simulation. The final results show a variety of systems, highly asymmetric flows in the top row, three smooth circumbinary discs, and three failed captures in the bottom right corner.

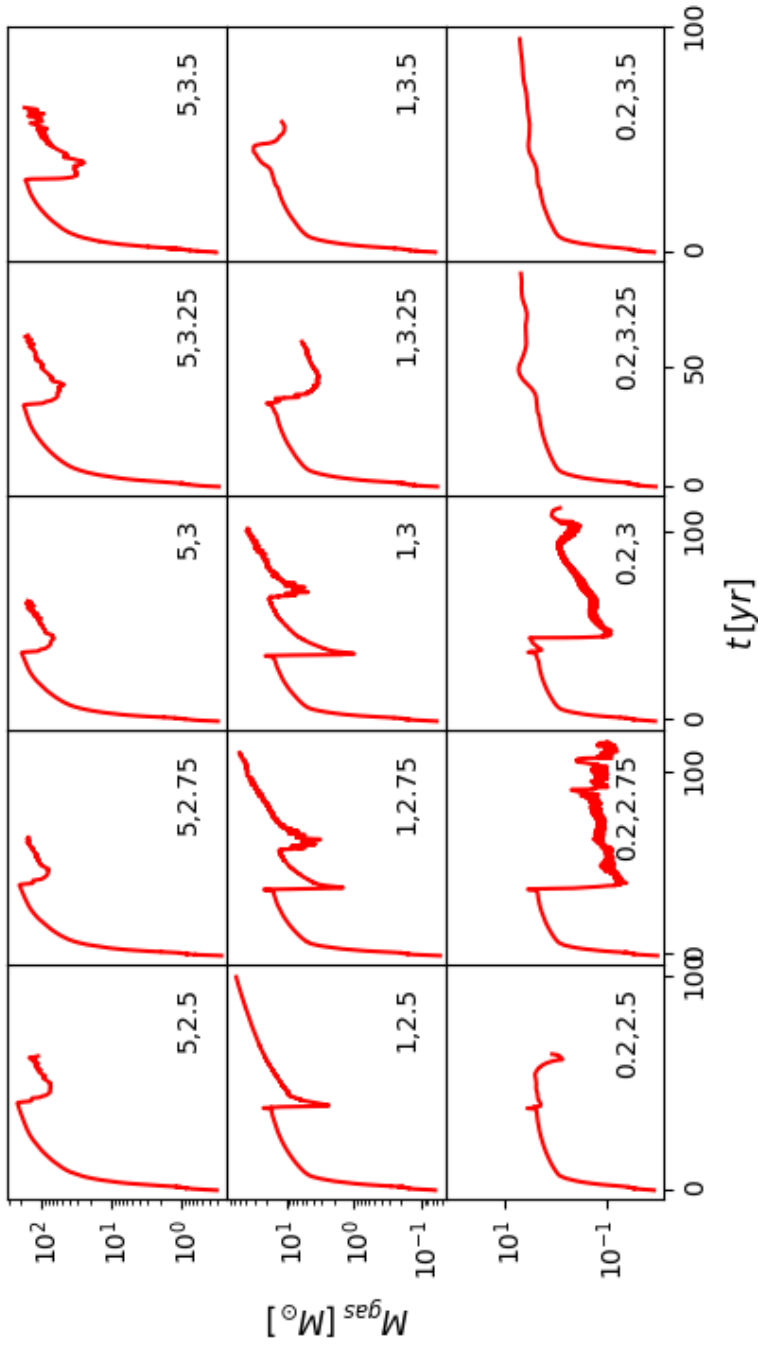

Figure 4.13: Enclosed gas mass around the binaries within the defined volume of Eq. (4.22) as a function of time for all 15 models. The initial spike in enclosed mass is due to the volume enclosing a greater extent of each BHs streamers as the volume evolves from approximately two spheres around each BH to a single volume of larger radius about their COM.

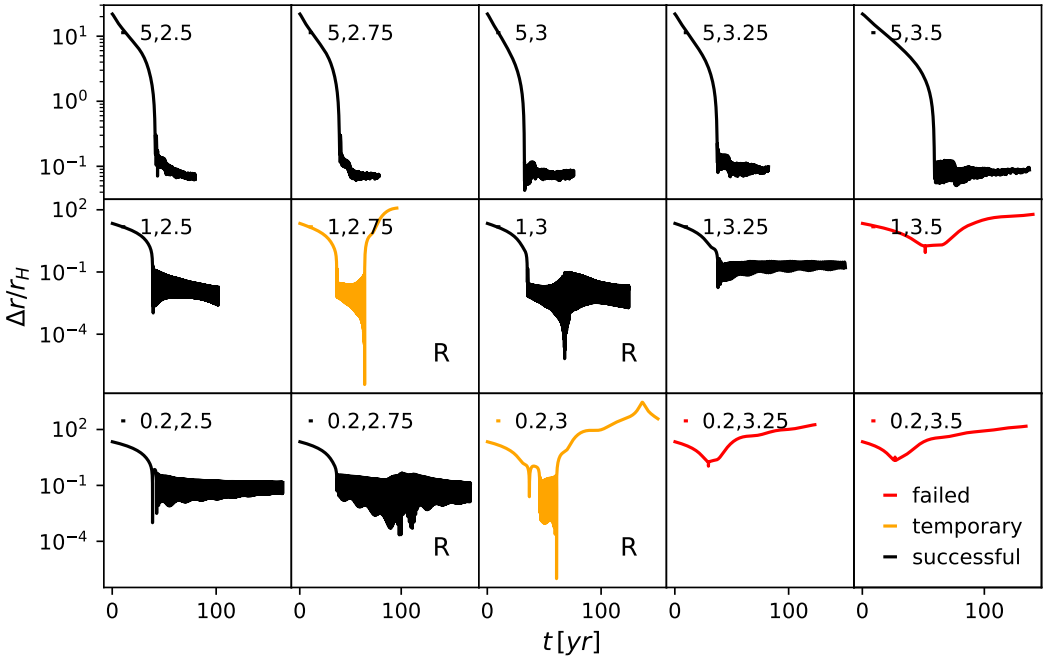

Figure 4.14: Binary separation in units of single-object Hill radius as a function of time. The panels correspond to the 15 models with varying disc mass (by row) and initial orbital separation (by column), represented by the two numbers in each panel). I label failed, temporary and successful captures in red, orange and black respectively. The R labels indicate which models are retrograde binaries.

weak encounter. Additionally, the reduced gas mass interacts less strongly with the binary, affecting its efficiency of energy removal. This explains the failed captures in the bottom right corner. From the three plots, the $5M_{\rm d}$ models (top row) have far more similar behaviour across the five simulations compared to the other two rows which have greatly different morphologies. This could suggest that higher AGN disc masses lead to more consistent subsequent evolution, though it is more likely that this is only due to all their periapses being so large. Recall that Muñoz et al. (2015) find the depth of the first encounter to be extremely important for the later evolution of the binary.

Looking at the eccentricities of Figure 4.15 there is a strong contrast between the eccentricity evolution of the $5M_{\rm d}$ models and the others. Firstly, all systems in this row have damped eccentricities, unlike the other two rows. This coincides with the fact that all binaries in the top row are *prograde* binaries (indicated by having

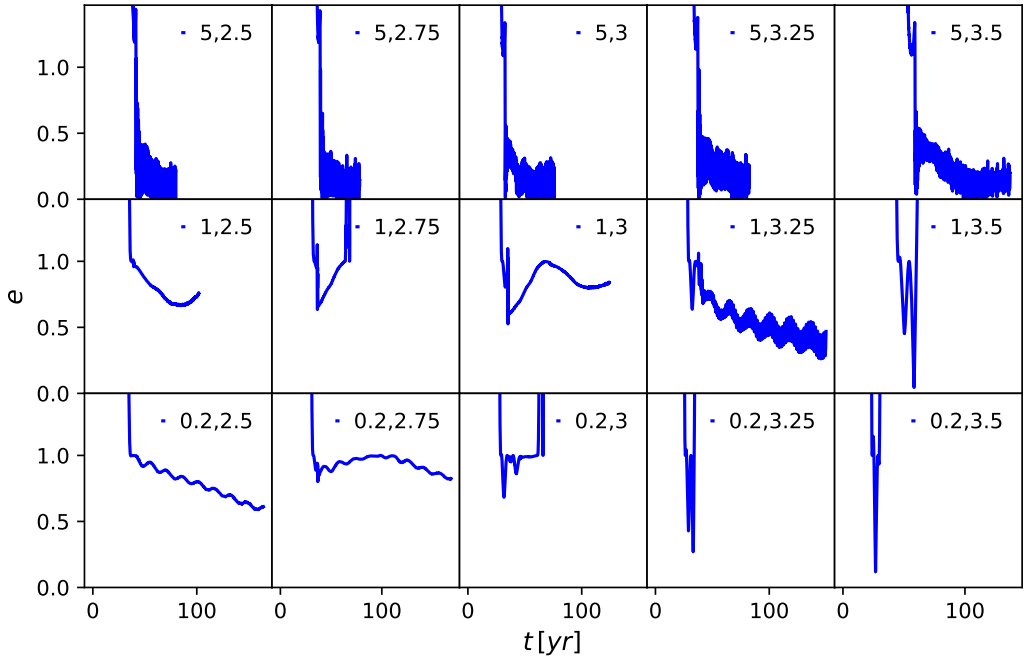

Figure 4.15: Binary eccentricity as a function of time for all 15 models.

positive angular momentum, see Figure 4.16) unlike the other two which have some retrograde binaries: $Cap_{1,2.75}$, $Cap_{1,3}$, $Cap_{0.2,2.5}$ and $Cap_{0.2,3}$. For all the captures, those in prograde orbits experience eccentricity damping while retrograde binaries are excited to higher eccentricities after an initial damping from the first encounter. This reiterates one of the major distinctions between the simulations here and those of pre-existing binaries in accretion discs, where binaries are not formed with low eccentricities, as assumed in pre-existing binary simulations. The $5M_{\rm d}$ models also have a larger variability in eccentricity over each orbit. This is attributed to the far more volatile and more dense flows around the binary perturbing the binary over the course of each orbit, especially considering their larger separations, since torque scales with separation. This is also observed later in $Cap_{1,3.25}$ as its separation approaches $0.5r_{\rm H}$. In all of the retrograde binaries, angular momentum is lost with time, leading to an increase in eccentricity. This continues until either decoupling ($Cap_{1,2.75}$, $Cap_{0.2,3}$) or the binary *flips* orbital direction and begins orbiting prograde ($Cap_{1,3}$, $Cap_{0.2,2.75}$). For the binaries that flip, the eccentricity behaviour transitions from increasing to decreasing at the same

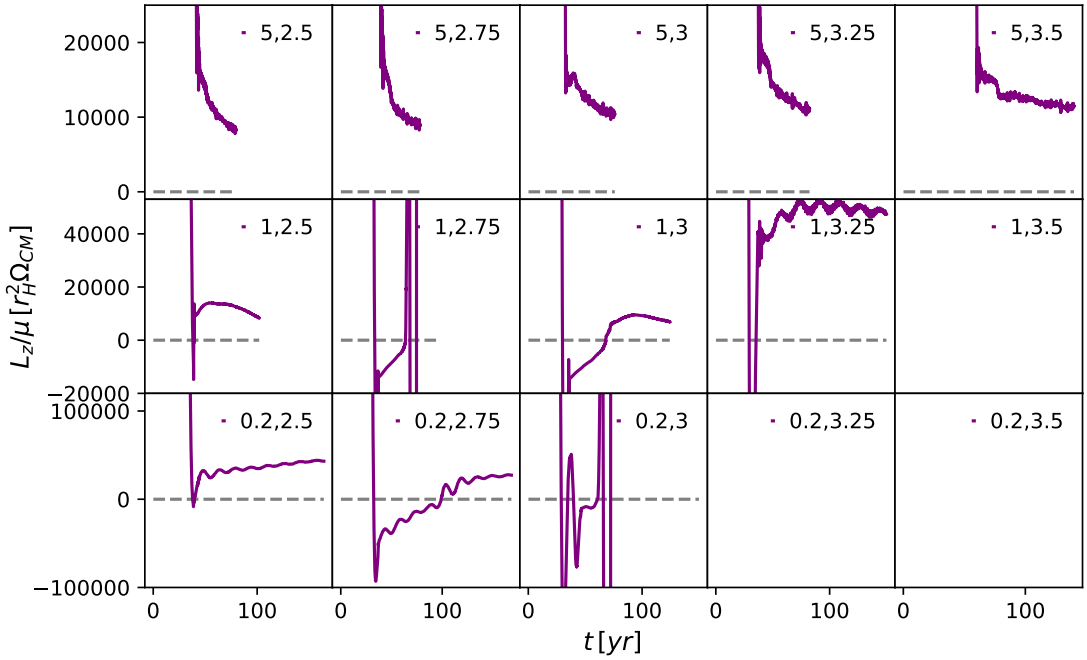

Figure 4.16: Binary z component of specific angular momentum, as a function of time for all 15 models. Here, positive and negative values of L_z correspond to prograde and retrograde orbits, respectively.

point the binary rotation flips, such that they then behave identically to the initially prograde binaries. Secular oscillations are also present in the eccentricity due to resonant behaviour with the SMBH. When the inner binary eccentricity vector (which points from apoapsis to periapsis) is parallel with the radial position vector to the SMBH, this coincides with the period of higher eccentricity due to increased tidal forces from the SMBH and lower eccentricity when perpendicular as the gas re-circularises the binary. The vectors align approximately twice per AGN orbit, leading to a beat period of two times the outer binary orbital period.

4.6.2 Summary of Models

To summarise the models, shown in tabular form in Table 4.17, there are 12 successful captures, two of which later decouple. For the remaining 10, the majority of the binaries are either inspiralling slowly or stalled, with the exception of $Cap_{1,3.25}$ and $Cap_{0.2,2.5}$ that appear to be outspiralling. Note that references to inspiralling or outspiralling are made in reference to the evolution of the binary separation Δr

Sim Label	$\frac{M_{\rm d}}{M_{\rm d,0}}$	$\frac{\Delta R}{r_{\rm H}}(t=0)$	capture	pro/retrograde	endpoint	endpoint (inc. GWs)	e evolution
$Cap_{5,2.5}$	5	2.5	yes	pro	inspiralling	unchanged	damped
$Cap_{5,2.75}$	5	2.75	yes	pro	inspiralling	unchanged	damped
$Cap_{5,3}$	5	3	yes	pro	stalled	unchanged	damped
$Cap_{5,3.25}$	5	3.25	yes	pro	stalled	unchanged	damped
$Cap_{5,3.5}$	5	3.5	yes	pro	stalled	unchanged	damped
$Cap_{1,2.5}$	1	2.5	yes	pro	inspiralling	unchanged	damped
$Cap_{1,2.75}$	1	2.75	yes	retro	decoupled	merger	excited
$Cap_{1,3}$	1	3	yes	retro→pro	inspiralling	merger	excited→damped
$Cap_{1,3.25}$	1	3.25	yes	pro	stalled	unchanged	damped
$Cap_{1,3.5}$	1	3.5	no	N/A	flyby	unchanged	N/A
$Cap_{0.2,2.5}$	0.2	2.5	yes	pro	stalled	unchanged	damped
$Cap_{0.2,2.75}$	0.2	2.75	yes	retro→pro	inspiralling	unchanged	excited→damped
$Cap_{0.2,3}$	0.2	3	yes	retro	decoupled	merger	excited
$Cap_{0.2,3.25}$	0.2	3.25	no	N/A	flyby	unchanged	N/A
$Cap_{0.2,3.5}$	0.2	3.5	no	N/A	flyby	unchanged	N/A

Figure 4.17: Summary of all models including initial conditions, capture success, rotation relative to SMBH, eccentricity behaviour and the end result of their evolution with and without including GW dissipation.

in units of $r_{\rm H}$, so while Δr could be increasing, $\Delta r/r_{\rm H}$ can still decrease. Such a case is still labelled an inspiral as although the physical separation may be increasing the binary is still hardening, as the Hill radius is increasing at a faster rate due to accretion. Simultaneously the Schwarzschild radii r_s and innermost stable orbits (what the BHs must cross in order to merge) of one or both the objects, which scales with M rather than $M^{1/3}$ for the Hill radius is therefore increasing at an even faster rate than the increase in Δr. So, in addition to hardening, the binary is also coming closer to merging. Defining the GW merger timescale as $t_{merger} \equiv a/(da/dt)$, for fixed a, this increases with M^3 (Hansen 1972). So non-negligible accretion can facilitate a merger despite even an increasing separation. The units of $\Delta r/r_{\rm H}$ are then more appropriate than $\Delta r/r_s$ as it is possible to have $\Delta r/r_s$ decreasing but $\Delta r/r_{\rm H}$ increasing for a binary with increasing $\Delta r/r_s$ if their derivatives have $\dot{r_s} > \dot{\Delta r} > \dot{r_{\rm H}}$. In such a case the binary may still decouple when the separation approaches the Hill radius even though the separation relative to the merger radius is decreasing. Therefore, I maintain $\Delta r/r_{\rm H}$ as the metric to label the binaries as inspiralling/outspiralling.

4.6.3 Gas dissipation of energy

It is demonstrated that captures are possible for all AGN disc masses and is more successful in the higher-mass cases for the same range in ΔR_i. This indicates that the local gas plays a direct role in aiding capture and preventing the objects decoupling via increasing eccentricity. As indicated by Figure 4.13 there is significant mass loss from the region at capture. In this section, the energy exchange is quantified directly by considering the gains and losses of the energy stored in the BH orbits and the surrounding gas.

First, a boundary must be defined from which to measure the inflow/outflow of gas and its energy relative to the COM of the binary. Due to the inherently chaotic nature of disc-disc collisions, care must be taken with the assumptions of symmetry and evolution of the region when defining a boundary. To account for both, the region considered is defined as an evolving volume defined where Eq. (4.21) is satisfied, where M_1, M_2 & $M_\bullet$ are the masses of the two stellar mass BHs and

SMBH, r_1, r_2 &$r_\bullet$ similarly are the positions and G is the gravitational constant:

$$\frac{Gm_\mathrm{p}M_1}{||\boldsymbol{r}-\boldsymbol{r}_1||^2}+\frac{Gm_\mathrm{p}M_2}{||\boldsymbol{r}-\boldsymbol{r}_2||^2}-\frac{Gm_\mathrm{p}M_\bullet}{||\boldsymbol{r}-\boldsymbol{r}_\bullet||^2}\geq 0. \tag{4.21}$$

In simple terms, the volume inside which a particle experiences a greater gravitational force, in magnitude, by the binary system than the SMBH. The alternative of summing the vector forces of the binaries prior to calculating its magnitude is avoided as this would lead to quantities of gas between the binary objects being excluded due to cancellation of the forces between the two objects. Given $M_\bullet \gg M_1, M_2$, this then reduces to

$$\frac{M_1}{||\boldsymbol{r}-\boldsymbol{r}_1||^2}+\frac{M_2}{||\boldsymbol{r}-\boldsymbol{r}_2||^2}-\frac{M_\bullet}{||\boldsymbol{r}||^2}\gtrsim 0. \tag{4.22}$$

With this description, the evolution of the system in time is accounted for, including its increasing size due to the increasing Hill radius of the binary due to accretion onto the BHs.

Using this boundary, particles are checked to see if they are part of the binary system at each timestep. In this region the kinetic energy of both the BHs and gas particles, K_BH and K_g respectively as well as the potential energy associated with the sinks U_{BH-BH} and the combined sink-gas component U_{BH-g} are calculated from a standard N-body summation in the centre-of-mass frame of the binary:

$$K_\mathrm{BH}=\frac{1}{2}(M_1V_1^2+M_2V_2^2), \tag{4.23}$$

$$K_g=m_\mathrm{p}\sum_{i=1}^{N_{enc}}\frac{V_{\mathrm{p},i}^2}{2}+\frac{3}{2\mu m_H}k_BT_i, \tag{4.24}$$

$$U_{BH-BH}=-\frac{GM_1M_2}{||\boldsymbol{r_1}-\boldsymbol{r}_2||}, \tag{4.25}$$

$$U_{BH-g}=-m_\mathrm{p}\sum_{i=1}^{N_{enc}}\frac{GM_1}{||\boldsymbol{r_i}-\boldsymbol{r}_1||}+\frac{GM_2}{||\boldsymbol{r_i}-\boldsymbol{r}_2||}\,. \tag{4.26}$$

In these expressions, V_1 and V_2 are the velocities of the two binary objects, V_p and r_p are velocity and position of a gas particle respectively and m_H is the mass of monatomic hydrogen. The summation in Eq. (4.26) is performed over all N_{enc} enclosed gas particles in the volume. The thermal contribution of a gas particle with temperature T_i is added to the kinetic energy using the usual ideal gas energy equation, where k_B is the Boltzmann constant. These values then construct the

total energy associated with the sinks, gas and entire system, labelled $E_{\rm BH-BH}$, $E_{\rm BH-g}$ and $E_{\rm tot}$ respectively. These are easily calculated in Eqs. (4.27-4.29):

$$E_{\rm BH-BH} = K_{\rm BH} + U_{\rm BH-BH}, \tag{4.27}$$

$$E_{\rm BH-g} = K_{\rm g} + U_{\rm BH-g}, \tag{4.28}$$

$$E_{\rm tot} = E_{\rm BH-BH} + E_{\rm BH-g}. \tag{4.29}$$

Since self-gravity is neglected, there is no potential term *between* gas particles in this calculation.

In Figure 4.18 each of these energies are shown as a function of time for each model. The efficiency of gas dissipation and accretion drag during the capture can be characterised by two factors. Firstly, the initial drop in total energy is observable as the initial sudden drop in $E_{\rm BH-BH}$ and $E_{\rm tot}$, followed by a more gradual exchange should the binary remain bound after the first encounter. For the $1M_{\rm d}$ and $0.2M_{\rm d}$ models that are successful, the first effect can be clearly seen as $E_{\rm BH-g}$ has a sudden increase while $E_{\rm BH-BH}$ shows a decrease of the same magnitude. Comparing the fiducial model ($Cap_{1,2.5}$) panel to the energy dissipation of the binary in Figure 4.8, the initial drop in $E_{\rm BH-gas}$ corresponds to the energy deposited back into the binary during the first encounter followed by the opposite during the second encounter where a large amount of energy is removed by the gas, represented by the jump up to nearly zero. This occurs due to strong gravitational drag when they pass deeply into each other's CSMDs for the second time, visible in Figure 4.19 as a jump in the total mass of the binary $M_{\rm bin}$. During this brief episode the accretion rate is significantly super-Eddington. Considering the magnitude of the energy change and mass accretion in such a short timescale, these instances can be treated more as soft collisions, as opposed to a dynamical exchange of energy.

After this episode, $E_{\rm BH-g}$ remains steady, near zero, while $E_{\rm BH-BH}$ continues to decrease. This demonstrates the second phase of a continuous transfer of positive energy from the binary objects to the gas or accretion (recall accretion is not energy conserving since the collision is inelastic with no emission of the lost kinetic energy). Despite re-accumulating in the binary region (See Figure 4.13) the gas retains a near constant, loose coupling to the binary while the binary binding energy continues to decrease. For the $5M_{\rm d}$ models, the local gas mass exceeds the BH masses and

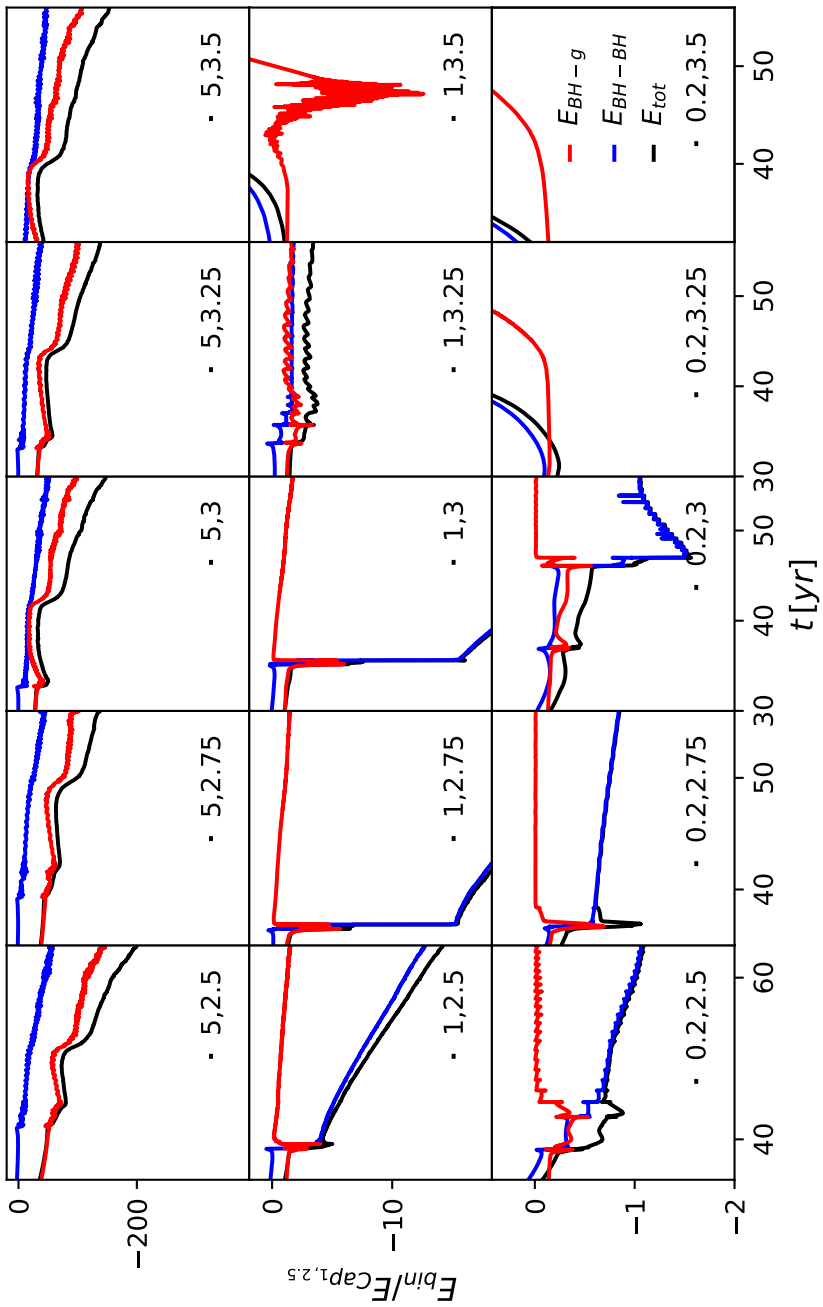

Figure 4.18: Two body energy of the BHs, $E_{\rm BH-BH}$ (blue) (eq 4.8), between BHs and gas, $E_{\rm BH-g}$ (red) (eq 4.28) and total energy $E_{\rm tot}$ (black) as a function of time, showing transfer of energy from sinks to gas and energy loss due to gas being expelled during capture for the $5M_{\rm d}$ cases. All energies are normalised to the initial two body energy at Hill the sphere crossing in the fiducial model $Cap_{1,2.5}$

.

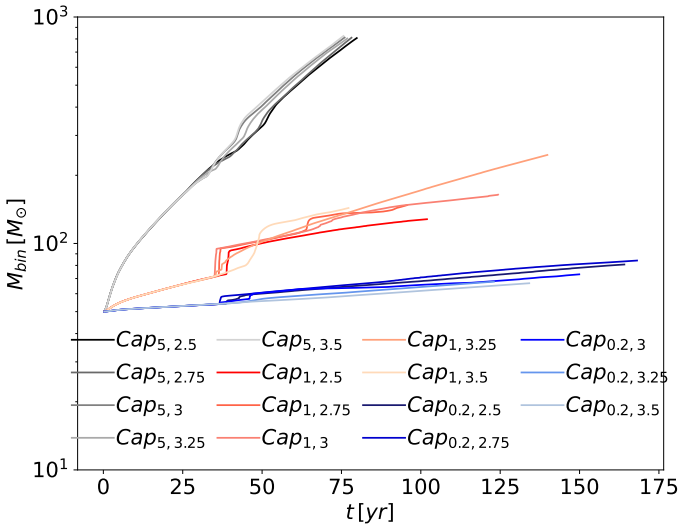

Figure 4.19: Total binary mass as a function of time for all 15 models, showing a large accretion of mass at the first encounter for models with $1M_{\rm d}$ and $0.2M_{\rm d}$.

is the larger contributor to the binding energy. In these cases the initial drop in $E_{\rm BH-BH}$ is still observable but $E_{\rm BH-g}$ remains the dominant contributor to $E_{\rm tot}$. In contrast to the lower disc mass cases, there is no discernible jump in binary mass at the first encounter. This can be explained by observing from Figure 4.14 that in all high-mass cases the first encounter is not as close and therefore they do not cross each other's CSMDs as deeply, if at all. As a result, the initial drop in $E_{\rm BH-BH}$ is far smaller. The retention of the discs leads to a more gradual stripping of the CSMDs via the trailing streams of gas, which then form spirals out from the edge of each BH's accretion disc opposite from the COM in a spiral manner as in the top panel of Figure 4.11. This spiralling continues in an ordered manner for a few tens of orbits, leading to a decrease in energy and M_{enc}. After this period the gas flows around the binary become more chaotic, marking the shift where $E_{\rm BH-g}$ begins to decrease alongside $E_{\rm BH-BH}$ and the re-accumulation of gas.

Going from the low to high $M_{\rm d}$ runs in Figure 4.18 (bottom to top row), paying attention to the vertical scale, the energy of the gas gained and the energy of the BHs lost appears to scale with the AGN disc mass. To visualise the scaling of the dissipation with disc mass, the rise in $E_{\rm BH-g}$ and loss in $E_{\rm BH-BH}$ over the encounter timescale are taken from Figure 4.18 and plotted for each value of $M_{\rm d}$. Here the encounter timescale is taken to be the time needed for the spiral structure

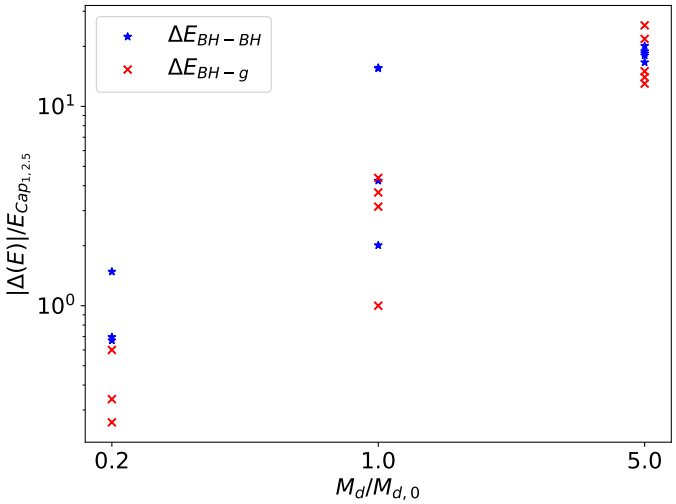

Figure 4.20: Loss in energy of BHs (blue) and gain in energy stored in the local gas (red), showing that for higher AGN disc masses, more binary energy is dissipated and transferred to the gas, a lot of which is then lost over time for the high-mass cases. All energies are normalised to the initial two body energy at Hill the sphere crossing in the fiducial model $Cap_{1,2.5}$.

to dissipate, specifically when the local gas environment settles and $E_{\rm BH-g}$ either begins to decrease again or remain at a steady level. In the $5M_{\rm d}$ cases, this requires a longer amount of time due to the development of the strong and prolonged spiral structure. The results are shown in Figure 4.20.

In the figure, it becomes clear that an increased AGN disc mass (resulting in higher ambient and BH disc gas density) is able to gain a larger amount of energy from the binary. Normalisation to the binary mass softens but does not remove the trend from $E_{\rm BH-BH}$. All $5M_{\rm d}$ models dissipate more $E_{\rm BH-BH}$ than the $M_{\rm d}/5$ cases. The two very high blue points in the middle column correspond to $Cap_{1,2.75}$ and $Cap_{1,3}$. This is a result of the aforementioned extreme accretion in the first periapsis of the capture. Given the discrepancy between the depth of the first encounters between these two and the rest of the captures, it may be that if their approach did not result in this very deep crossing of their discs, then this would result in less scatter in the dissipation across $M_{\rm d}$, but there is not enough data points to confirm this. The changes in $E_{\rm BH-BH}$ and $E_{\rm BH-g}$ are not one-to-one since gas is still flowing into the region and becoming bound from streams parallel to the binary motion around the SMBH. Therefore there is a tendency to have $\Delta E_{\rm BH-BH} > \Delta E_{\rm BH-g}$. As

a fraction of the energy in the system, this gap is far smaller for the $5M_{\rm d}$ and for one case the opposite is true. This is a result of the more significant mass loss in these models where gas particles that exit the volume defined in Eq. (4.22) cease to be counted in the summation of Eq. (4.26).

To further highlight the efficiency of the gas-capture, the effect of removing the gas just prior to the encounter is explored. From the four successful captures with the fiducial AGN disc mass, the instantaneous positions, velocities and masses are recorded at the moment the satellite BHs' Hill radii intersect. Using these as initial conditions, the models are repeated as purely 3-body problems. As another test, the instantaneous enclosed gas mass at the Hill sphere intersection is also recorded and added to the mass of the BHs in proportion to their individual masses. By doing this, 3-body encounter is more accurately modelled as the mass of the gas in the circum-single discs, which alters the approach, is incorporated into the BH masses. This scenario more accurately reflects the energy of the system to the gas case, but removes the ability for the objects to transfer this energy to a background medium via dynamical friction, or slow via direct accretion onto the BHs. The separations as a function of time for these two tests are shown in Figure 4.21. Looking at the results in the Figure, it is clear that removing the gas dissipation leads to qualitatively different results. In all cases, for both gasless tests, the two BHs have one close encounter before being disrupted as they go on to exit each other's Hill sphere. The closest approaches of the gasless cases are also less deep due to the absence of dynamical friction which helps remove orbital energy on the approach to the first encounter. These results show qualitatively that it is the gas which is responsible for retaining the two objects as a binary. More specifically, concerning the second gasless setup, I show that it is the mechanism where the binary objects do work on the gas that is crucial for this binary formation pathway, rather than simply having an increased amount of mass in the binary Hill sphere. Otherwise one would expect the 3-body re-runs where the enclosed mass is added to the binary in Figure 4.21 to more closely match the original model.

4.6.4 The Retrograde Case

To compare the difference between prograde and retrograde binaries, I discuss the outcome of $Cap_{1,2.75}$, which forms a retrograde binary. The formation of retrograde

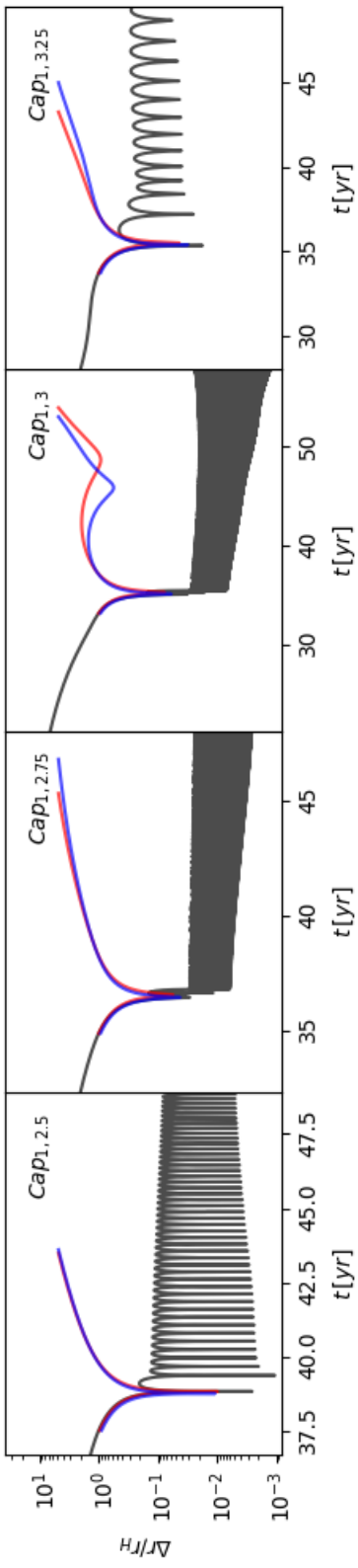

Figure 4.21: Separation as a function of time for the four successful captures from the fiducial AGN disc mass models (black) compared with captures with gas removed just prior to capture where the local gas mass is not added to the BHs (red) and when it is (blue). In both gasless scenarios the binary makes only one encounter and is immediately disrupted.

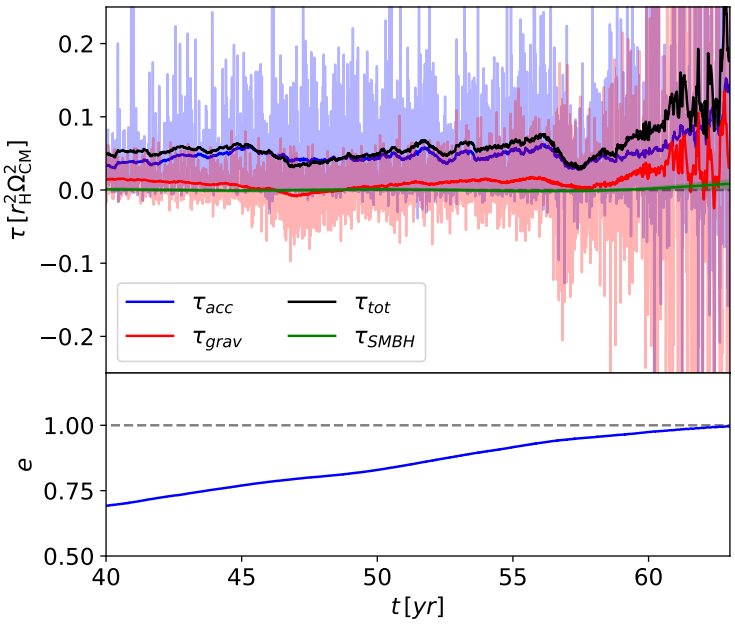

Figure 4.22: The specific torque components and net torque (top) and specific angular momentum (bottom) for the retrograde binary $Cap_{1,2.75}$ as a function of time for the time frame where binary separation is less than the binary Hill radius. The value of $\tau_{\rm SMBH}$ remains negligible until the separation approaches the Hill radius. The strongest source of torque in $Cap_{1,2.75}$ comes from the positive accretion torque, which drives the binary to inspiral.

binaries occurs when the inner object is not deflected around the outside of the outer object and encounters it from lower R. The form of these orbits are explored in great detail in Boekholt et al. (2023), see Figure 6 within. Other than the initial approach trajectory, the capture process for retrograde binaries shows no difference in behaviour to the prograde models, yet the following evolution differs significantly. Figure 4.22 shows the time evolution of the post capture torques, deconstructed into each component, $\tau_{\rm grav}, \tau_{\rm SMBH}, \tau_{\rm acc}$ and the net value, τ_{tot}. As the binary is rotating in retrograde (clockwise for the problem), positive torque increases the negative angular momentum of the binary towards zero, i.e. inducing inspiral. The dominant torque contribution comes from the accretion torque which drives a rapid inspiral of the binary. The nature of this inspiral can be described by the reduction of the angular momentum alongside an increasing eccentricity towards unity, until ultimately decoupling the binary as the apoapsis, $r_a = a(1+e)$, of the

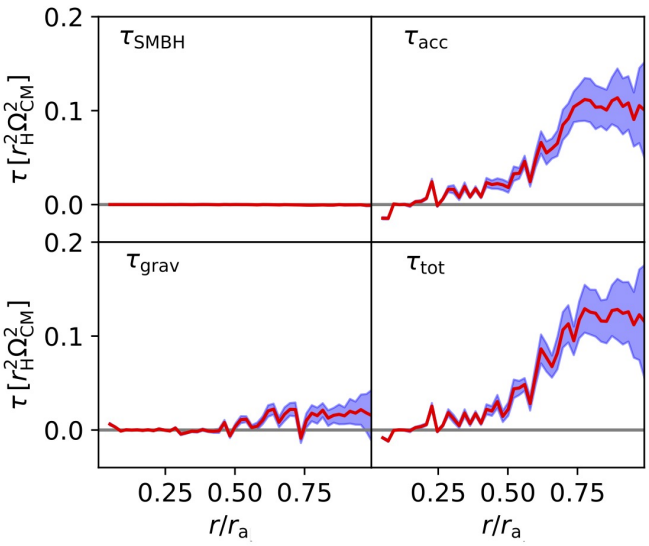

Figure 4.23: Radial dependence of torque sources for retrograde binary $Cap_{1,2.75}$. Accretion torque as binary interacts with cavity wall (top right panel) dominates the net torque on the binary. The shaded blue region represents the $1-\sigma$ variation the torques.

orbit exceeds the binary Hill radius where it is significantly perturbed by the SMBH and decouples. However, while the apoapsis increases, the periapsis, $r_{\rm p} = a(1-e)$, continues to decrease to significantly small values as $e \to 1$. Should this separation be small enough, orbital energy dissipation via GW waves can be significant enough to begin to circularise the orbit such that periapsis does not continue to increase, which would otherwise lead to the binary decoupling.

The average torque as a function of orbital separation for the retrograde binary generated over the period of time the binary is bound is shown in Figure 4.23. In all panels there is an increase in the spread of the torques in each bin of dr and with the exception of $\tau_{\rm acc}$ the spread is highly symmetric. This can be explained by the highly stochastic torques (see the raw torque values in Fig 4.22) being enhanced by the $(\boldsymbol{r}_1 - \boldsymbol{r}_2)$ terms in Equations 4.18, 4.19 and 4.20 when the binary is near apoapsis. The highly symmetric spread of the torques leads to the mean being far closer to zero than the overall spread, particularly for $\tau_{\rm grav}$. This indicates the binary experiences very strong but competing torque sources from the surrounding gas over its evolution. As pointed out, the accretion torque has a steep inclination from symmetric to positive torques when the binary separation is greater than $0.2r_{\rm a}$, implying a bias for the accretion of particles *against* the direction of the BH's

velocity vector. The physical mechanism driving this is the interaction between the binary and the gas as the objects reach their maximum separation. The process driving this bias is the same as described in section Sec. 4.5.3, where accretion and gas-gravitational drag due to the velocity difference of the eccentric binary and CBMD.

The torques shown here for a retrograde binary are an inversion of the prograde case, where accretion drag now dominates. The net torque also behaves inversely, acting in opposition of the orbital motion of the binary (since the retrograde binary orbits in the opposite direction to the CBMD). This corroborates the eccentricity excitation of the retrograde binaries in Figure 4.15. As the gas orbits in the opposite direction to the binary, accretion onto the front of the BHs decelerates the binary rotation, reducing the angular momentum. Similarly, unaccreted gas is perturbed behind the BHs as they approach the cavity wall, tugging them backwards. Why the gravitational drag dominates over accretion in the prograde binaries, in contrast with the retrograde ones, is unclear and requires further investigation. One possible interpretation can be made through analogy with the standard Ostriker prescription for dynamical friction. The force F_{DF} on an object due to dynamical friction (Ostriker, 1999)

$$F_{DF} = \frac{4\pi G^2 M_{\rm BH}^2 \rho_0}{v_{rel}^2} I(\mathcal{M}). \tag{4.30}$$

In this description the dynamical friction is directly proportional to the background density of the medium ρ_0 and inversely proportional to the square of v_{rel}, relative velocity of the perturber and the medium. The $I(\mathcal{M})$ term, is a function of the Mach number $\mathcal{M}$. The relative velocity is approximated as the difference between the apsidal velocity and the orbital velocity of gas at the cavity wall. For prograde binaries, this quantity will be less as the binary is orbiting in the same direction of the gas, so one would expect the dynamical friction due to gas curving round a perturber to be greater, as observed here.

4.6.5 Dependence on disc mass and initial separation

Now considering the other models, starting again with the torque evolution, the torque components over time are compared in Figure 4.24 for three different scenarios. These are i) a prograde binary of fiducial M_{disc}, ii) a retrograde binary of fiducial

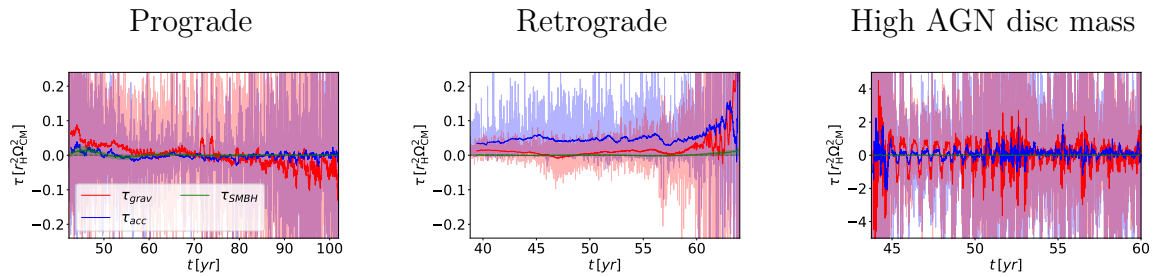

Figure 4.24: Torque as a function of time for the three physical sources, SMBH (green), gas gravity (red) and accretion (blue) shown for three models. These models (left to right) are a prograde binary with fiducial $M_{\rm d}$ ($Cap_{1,2.5}$), a retrograde binary with the same $M_{\rm d}$ ($Cap_{1,2.75}$) and a prograde binary from the high $M_{\rm d}$ simulations ($Cap_{5,2.5}$). The results are qualitatively the same for other models with the same disc mass and orbital rotations.

M_{disc} and iii) a prograde binary of the $5M_{disc}$ models. Moving on to the third panel of Figure 4.24, the high mass binaries show significant oscillation of the gas gravitational torques for the initial encounter, this continues until the strong gas spiral structure transitions into more chaotic behaviour. While the torques oscillate about zero during this period, the torque remains positive for longer at apoapsis and an order of magnitude stronger than the $1M_{\rm d}$ examples. This causes the very rapid damping in eccentricities of binaries in the high AGN disc mass simulations. The increase in strength is attributed directly to the higher local gas density, which enhances the gas dynamical friction acting on the binary. After the gas morphology becomes more chaotic the accretion and gravitational torques also become highly disordered and the binary eccentricities vary between $\sim 0-4$. Though the binary separation evolution varies considerably per model, the level of eccentricity damping/excitation scales consistently with $M_{\rm d}$ in all the models. The damping of e for prograde binaries and excitation of e in retrograde binaries is increasingly significant for higher $M_{\rm d}$. This is in line with the expected enhancement of $\tau_{\rm grav}$ due to increased densities, as expected from the Ostriker formula in Eq. (4.30), in conjunction with enhanced $\tau_{\rm acc}$ due to more linear momentum transfer through accreting in a denser medium.

4.6.6 Work done

Since the binary evolution problem begins with an initial highly eccentric (sometimes hyperbolic) encounter, the initial eccentricities are all very high (>0.5). Therefore the assumption for circular binaries that radial forces on the BHs with respect to the

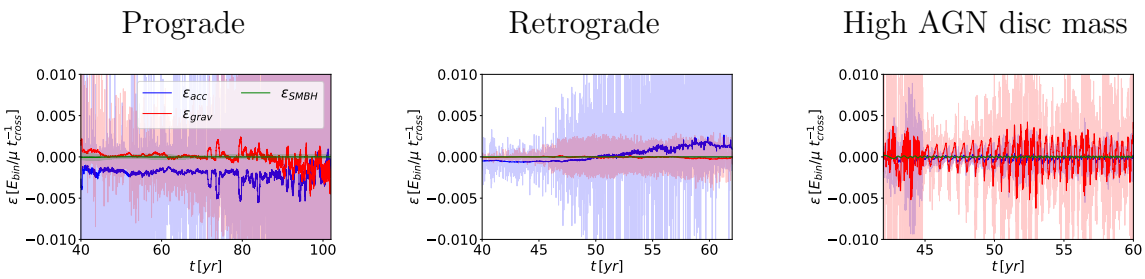

Figure 4.25: Orbital energy dissipation as a function of time shown for three models for the three physical sources, SMBH (green), gas gravity (red) and accretion (blue). These models (left to right) are a prograde binary with fiducial $M_{\rm d}$ ($Cap_{1,2.5}$), a retrograde binary with the same $M_{\rm d}$ ($Cap_{1,2.75}$) and a prograde binary from the high $M_{\rm d}$ simulations ($Cap_{5,2.5}$). The results are qualitatively the same for other models with the same disc mass and orbital rotations.

binary COM are negligible is invalid. The work done per unit mass per unit time is shown for three examples: prograde and retrograde models with equal $M_{\rm d}$ and for a high mass prograde case in Figure 4.25. For both prograde and retrograde binaries the net dissipation through gravitational interaction with the gas is minimal as $\varepsilon_{\rm grav}$ oscillates about zero. In a similar manner to the torques, the orbital energy evolves differently for prograde binaries depending on how close the first encounter is and whether a well defined CBMD can form. For the cases this is true, accretion drives a slow but steady reduction in the orbital energy of the binary (see left panel of Figure 4.25). For prograde binaries that do not, all contributions to ε oscillate about zero after the initial encounter before the orbital energy reaches a steady value and the binary stalls (see $Cap_{0.2,2.5}$ in Figure 4.14 as an example).

The high mass models (recall all of which are prograde) do not form defined CBMDs and similarly have variability in $\varepsilon_{\rm grav}$ and $\varepsilon_{\rm acc}$ about zero. The increased AGN disc mass leads to stronger, well defined oscillations in both $\varepsilon_{\rm grav}$ and $\varepsilon_{\rm acc}$ in resonance with the orbital period. The variation in the former is a result of the far more massive circumsingle discs of the BHs dominating the gravitational forces in Eq. (4.13). When the BHs are enroute to apoapsis, the force differential dotted with the relative velocity vector is strongly negative, zero at apoapsis, before flipping as the binary approaches periapsis. Retrograde binaries have an interesting feature where there is a period of time post capture, when the eccentricity is lower, when the components of ε are identical to the prograde case, until the eccentricity reaches

considerably high ranges of ~ 0.8 and above and $\varepsilon_{\rm acc}$ rapidly transitions from negative to strongly positive and the binary semi-major axis increases. The reason for this is unclear though likely related to behaviour changing at the cavity wall.

4.6.7 GW Dissipation

For merger, the periapsis must be smaller than the sum of the innermost stable circular orbits of the BHs. Assuming equal masses, the separation for direct merger is $r_{merge} = 12GM_{\rm BH}/c^2$. For the parameters this is an extremely small distance of $5 \times 10^{-6} r_{\rm H}$. However, in $Cap_{1,2.75}$ the final apoapsis of the binary prior to decoupling passes within this value, thus if one were to include GW dissipation then this system would undergo merger. One can also consider the increasing GW dissipation of orbital energy in the leadup to decoupling. The orbital energy lost via GWs at periapsis, in the high eccentricity limit, can be calculated using the expression in Peters (1964); Hansen (1972), see also Samsing et al. 2018:

$$\Delta E_{\rm GW} \approx \frac{85\pi}{12\sqrt{2}} \frac{G^{7/2}}{c^5} \frac{M_1^2 M_2^2 \sqrt{M_1 + M_2}}{r_{\rm p}^{7/2}}. \tag{4.31}$$

This quantity is expressed as a fraction of the orbital energy E_{BH-BH} that is dissipated during a pericentre passage, namely

$$\eta(r_{\rm p}) = \left| \frac{\Delta E_{\rm GW}(r_{\rm p})}{E_{\rm BH-BH}} \right|. \tag{4.32}$$

An η value of one or greater implies the binary would be able to dissipate equivalent to 100% of its current orbital energy in one periapsis pass and undergo a rapid merger. The value of η is shown as a step function evaluated at each periapsis pass along side the separation of the binaries for all 4 retrograde systems in Figure 4.26. No prograde binaries reach close enough separations to warrant this analysis at the time of termination for the simulations. In Figure 4.26 the merger of $Cap_{1,2.75}$ is confirmed, since η exceeds unity during the last orbit. Though the orbital energy of the binary is actually increasing at this point via the accretion driven radial forces described in the previous section, it is outrun by GW dissipation. Here it is assumed that including GW dissipation live in the simulations will not significantly decrease η at this point. If one considers the η values in the lead up to the final event, they are orders of magnitudes below unity, so this assumption is relatively

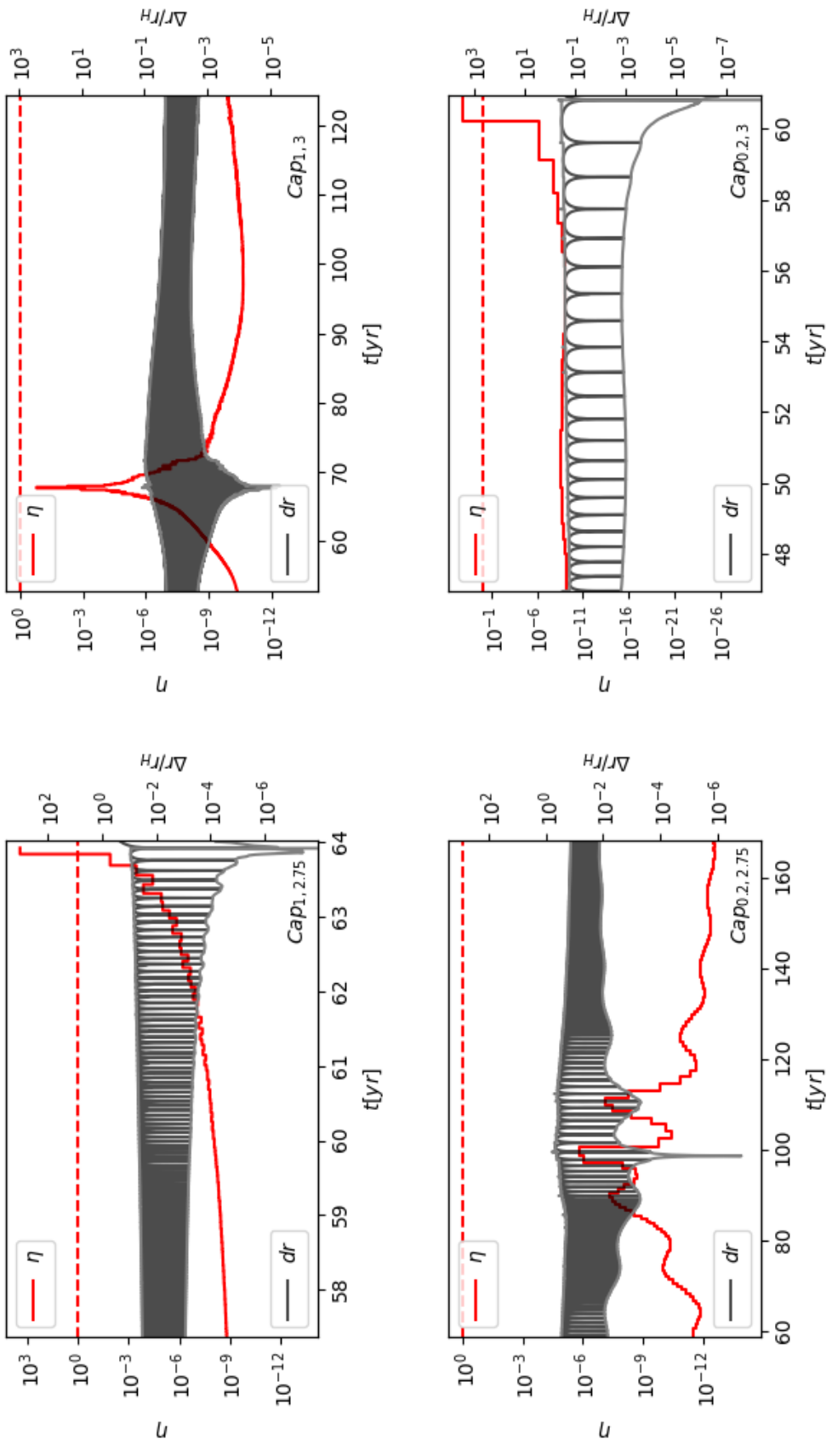

Figure 4.26: Orbital energy dissipation as a fraction of binary orbital energy per periapsis pass η (red) along side separation (black) for the four retrograde binaries. Grey lines represent the apoapsis and periapsis of the binary orbit calculated from the instantaneous orbital elements. The Binaries in models $Cap_{1,2.75}$ and $Cap_{0.2,3}$ undergo definite merger as η exceeds unity.

safe. The result also affirms the earlier short calculation of a direct merger as η exceeds one for the last periapsis pass (expectedly where $r_{\rm p}$ drops below 5×10^{-6}). $Cap_{0.2,3}$ can also be identified as a merger, while $Cap_{0.2,2.75}$ fails to merge before the binary flips to prograde and the eccentricity begins to be damped by accretion and dynamical friction. The fate of the final retrograde binary, $Cap_{0.2,3}$, remains ambiguous. At the closest approach during its evolution at around 70 years, it loses 30% of its orbital energy before becoming prograde. This is significant, though the critical question is whether this dissipation would lead to another significantly close encounter and finally merge the binary, or whether it will still flip to prograde and re-circularise. As GW effects are calculated in post, this remains unknown. Since the rate of eccentricity excitation in retrograde binaries speeds up when its value nears unity, they have a very small number of orbits where they have high enough eccentricity such that $r_{\rm p}$ is small enough for GW emission to be significant before the binary either decouples ($Cap_{1,2.75}$,$Cap_{0.2,3}$) or flips to prograde ($Cap_{1,3}$,$Cap_{0.2,2.75}$). Therefore the specific moment where the binaries make their closest approach in relation to the instantaneous orbital elements is *extremely* influential to whether merger takes place or not. For example, in the $Cap_{0.2,3}$ panel of Figure 4.26, the instantaneously calculated $r_{\rm p}$ passes within r_{merge} but the binary begins to re-circularise before the next periapsis passage and so GW dissipation reduces sharply due to its steep $1/r_{\rm p}^{3.5}$ dependence and the binary fails to merge.

4.7 Discussion

4.7.1 Comparison to similar studies

As this work was being finalised, three preprints looking into the specific problem of binary formation through gas drag in AGN discs appeared on the arXiv. Rozner et al. (2022) and DeLaurentiis et al. (2022) both simulate the orbits of two BHs interacting around a SMBH assuming a gas drag term in their orbital integrations given by the Ostriker prescription (Ostriker 1999), rather than performing hydrodynamical simulations. These studies adopt an undisturbed background gas, and therefore do not capture the gas dynamics during the close interaction of the binary components, as done here. They nevertheless both conclude that capture is possible and should be common, and provide insight into the role of dynamical friction in the capture

process. DeLaurentiis et al. (2022) perform an academic exercise in which the drag from dynamical friction is artificially switched off once the trajectories of the orbits (in the binary comoving frame) become significantly perturbed, i.e. once the binary strongly interacts. This is motivated by the fact that after this stage, the velocity of the objects relative to the gas becomes dominated by motion about the binary COM, and Ostriker's assumption of unaccelerated linear motion relative to the background medium manifestly breaks down. They find that energetically bound binaries are still able to form, typically with eccentric orbits that precess, but no longer shrink their semi-major axes beyond this point. Their estimates of the timescales required for capture in AGN via dynamical friction include the formation time of the binaries, albeit here accretion dominates the negative drag instead of gravitational drag. There is also excellent agreement with the predictions on the initial eccentricities typically being $\gtrsim 0.8$, as well as on the formation of both prograde and retrogade binaries. When dynamical friction is switched off after the first encounter, the binaries in DeLaurentiis et al. (2022) remain at these high eccentricities as there is no source of post-capture torque to further alter the eccentricity, as there is in the simulations here.

Rozner et al. (2022) take a similar approach to DeLaurentiis et al. (2022) and derive analytic functions for the energy dissipation during the a close fly-by between two compact objects. Their treatment looks at two-body encounters, which may be applicable more broadly, and do not include the tidal forces from massive third body (i.e. they solve the two-body problem with the gas drag force added in). They also find binary capture through dynamical friction when the relative velocity prior to the encounter is below a critical threshold. They allow the dynamical friction to affect the binary orbits beyond the first encounter which leads to continued efficient energy removal post capture, as well as rapid eccentricity damping (also found in the majority of cases examined by DeLaurentiis et al. 2022). In the hydro simulations here, the binaries shrink far more slowly (with respect to the outer binary orbital period) via a combination of gas gravity and accretion which is also highly stochastic and in some cases stall completely. The binaries here orbit roughly 100 times closer to the SMBH compared to their work, i.e. at ~ 0.01pc instead of $\sim$ 1pc, possibly affecting the results.

Most closely related to this study, Li et al. (2022a) explore the binary capture problem in AGN using 2D hydrodynamical simulations. They also find successful captures for binaries with mass ratios very similar to ours, formed via gravitational interaction with the gas alone with no accretion. Interestingly, they form predominantly retrograde binaries which harden on a similar time frame to the prograde binaries. The reason that they find far more retrograde binaries, unlike here (as well as the studies above), is unclear. One explanation could be because Li et al. (2022a) examine only a single impact parameter and instead vary the azimuthal separation. In addition, the eccentricity evolution of their retrograde binaries differs from the results shown here, where eccentricity is damped similarly to the prograde binaries and at a similar rate to the $M_d = M_{d,0}$ cases. A possible reason for the hardening and damped eccentricities could be the softening lengths around the sinks. Comparing the sink/softening scales with Li et al. (2022a), the sinks here have a softening/accretion radius of approximately one fifth the size, where smaller softening lengths have been shown to lead to larger torques originating from the regions very close to the BHs (Li et al. 2021, 2022c). During capture, the oscillatory gravitational work and torque at capture (Figures 4.4 & 4.6) generally do net positive work and torque on the binary initially and originates from the inner regions around the BHs in the simulations, which may not be simulated for higher softening lengths. This could suggest softening plays a strict role during capture as well as the subsequent evolution of the binary. Additionally, Li et al. (2022a) allow the BHs to build up their circumsingle discs prior to their first encounter for far longer than shown here, which could potentially change the strength and behaviour of gas gravitational drag at the encounter.

Due to the lengthy runtimes involved, repeated scattering events like in Li et al. (2022e) are not considered. The results of Li et al. (2022e) suggest a decoupled binary may interact again as the inner BH catches back up to the outer BH. This possibility, along with the fact that in reality there is a population of $\gtrsim 10,000$ BHs in the AGN disc, allows us to hypothesise that failed captures could be deflected into the trajectory of other orbiting BHs and lead to multiple opportunities for binary formation.

4.7.2 Caveats

Several assumptions were made in this study, which are to be relaxed in follow up studies:

- It was assumed gas heating/thermal shocks are minimal over the entire simulation domain. While this is a good assumption for the main body of the annulus, the high speed intersections of the accretion discs of the BHs will in practice lead to *significant* heating of their material due to their high density and relative velocity. The effect of this heating in such an encounter on the forces the binary experiences (dynamical friction etc) is unknown. Most likely, it will enhance the gas loss in the region due to the increased pressure associated with higher temperatures achieved in the local. This would be represented by an increase in the thermal term of term in Eq. (4.24).

- The simulations predict accretion rates orders of magnitude higher than the Eddington limit. This outcome also stems from the omission of feedback mechanisms (radiative and heating) in the simulations. Very recently, Tagawa et al. (2022) show that including these effects results in less rapid accretion during the encounter due to enhanced supportive pressure from radiative feedback from the inner CSMDs.

- Mostly for computational reasons, the self-gravity of the gas in the simulations was neglected. For the models where the binary mass remains larger than the total gas mass within their mutual Hill sphere, this assumption is reasonable. However, for the most massive disc model, we are in the opposite regime and one can expect that the gas dynamics during capture will differ and perhaps lead to easier binary capture if there is an additional binding term between gas particles that can prevent as much mass loss.

- The initial distribution of BHs being limited to circular orbits with zero velocity dispersion or inclination is a simplification of their true distribution. In reality the BH population of an AGN will have a range of eccentricities and inclinations. Encounters with variations of these parameters may alter the ease of the gas-capture process shown here due to varying relative velocities

upon intersecting each other's Hill sphere. As suggested by Li et al. (2022e), allowing for non zero inclination reduces the probability of close encounters.

4.8 Summary and Conclusions

In this work I performed 15 simulations of two isolated BHs encountering each other in an AGN disc. Of these 15, 12 successfully form binaries, 4 retrograde and 8 prograde. Two of the retrograde binaries go on to merge within the timescale of the models when GWs are considered. I summarise the key findings below:

- The gas dissipation binary formation channel is efficient enough to form binaries from BHs on hyperbolic orbits. The amount of energy dissipated and torques scale with the density of the local medium due to increased dynamical friction and accretion drag.

- The depth of the initial encounter greatly affects the nature of the energy transfer of the binary to the surrounding gas as well as the subsequent evolution. If the impact parameter is large, strong spiral outflows are generated due to the BHs tidally stripping each other's accretion discs. This carries away energy and angular momentum from the binary over a period of time until an equilibrium is reached. The spiral outflows are greatly enhanced for higher AGN disc masses and lead to rapid eccentricity damping of the binary. If the impact parameter is small, then the BHs can cross each other's discs, creating more violent and disordered outflows as well as inducing significant accretion drag on the BHs. The latter case results in a CBMD and faster hardening of the binary compared to the former, where the binary after formation, as a fraction of the Hill sphere, has a far larger semi-major axis, prohibiting the formation of a CBMD.

- All the binary objects initially encounter each other with eccentricities greater than unity. Immediately after the initial encounter, its value is still only just shy of this value, implying that initial conditions for binaries formed via this channel having $e \sim 0$ is very nonphysical. For the fiducial AGN disc mass/density e remains greater than 0.4 by the end of the runtime which corresponds to thousands of binary orbits for the tighter binaries. This would

suggest binaries formed in this pathway would more easily merge secularly via the newly proposed evection induced merger pathway in AGN (e.g. Muñoz et al. 2022, Gautham Bhaskar et al. 2022). However, for retrograde binaries, eccentricity increases due to the gas interactions on far shorter timescales and the binary undergoes a direct merger rather than through GWs over many orbits.

- Accretion is significantly super-Eddington during capture for the simulation parameters and this dominates the removal of orbital energy of the binary and its circularisation. Therefore I conclude that accretion should not be neglected in similar future studies.

- The torques of prograde binaries are governed by gravitational interaction with the local gas in the CBMD, while retrograde binaries are governed by the accretion. Both torque sources operate within the same order of magnitude and therefore I encourage future studies to include both effects.

- Strong bimodality in the binary evolution is identified between prograde and retrograde (with respect to the CBMD and AGN disc) binaries. Prograde binaries always exhibit eccentricity *damping* due to resonant gas gravitational and accretion torques in favour of the binary motion at apastron. Due to the inverted orbital angular momentum of the retrograde binaries, the resonant torques *excite* their eccentricities. This effect is stronger in both cases for higher AGN gas disc densities where torques from the gas and accretion are stronger and for higher e. For prograde binaries formed via close encounters, once the binaries are circularised to $e < 0.3$ the torques switch from net positive to net negative and begin to reduce the semi-major axis as opposed to affecting e. This is a result of the gravitational drag of quasi-stable streams of gas stretching from the BHs to the cavity being able to form at lower eccentricities.

- For two out of the four retrograde binaries, the increasing torques push apastron to the Hill radius of the binaries as $e \to 1$ and they decouple due to strong perturbations from the SMBH. In the other retrograde models it is demonstrated that the torques can flip the binary orientation from

retrograde to prograde as they are not perturbed significantly enough to decouple at the point of flipping. After this transition they then flip to the same aforementioned prograde damping of e.

- When GW dissipation at periastron is considered for highly eccentric retrograde binaries, the amount of energy dissipated in the last few orbits before decoupling/orbit flipping can exceed the binary orbital energy. This suggests that the two decoupled retrograde binaries actually undergo merger when GW effects are taken into account. The opportunity for the merger of retrograde falls in a very short window of time as its angular momentum tends to zero and eccentricity to unity. The sole determinant is whether there is a periapsis pass close enough to the moment these quantities reach these values, otherwise the binary can decouple or flip rotation and re-circularise and the pericentre becomes too shallow for GWs to drive inspiral.

Through this hydrodynamic approach the full chronology of a BBH merger in the AGN gas-capture channel was simulated under the above assumptions. The results show that gas aids the formation of binaries and can induce secular torques to harden and merge the binaries. This initial proof of concept study suggests that the AGN channel can potentially be highly efficient at forming and merging BBHs.

5

Gas Effects on Black Hole Satellite Scatterings

This Chapter is adapted from my publication Rowan et al. (2024) of which I am first author, principle investigator and personally wrote. Published in Monthly Notices of the Royal Astronomical Society.

Contents

5.1 Introduction

While the overall evolution of embedded binaries is still an ongoing problem, the formation of such binaries is an even less understood topic. As discussed in Sec. 2.6.3, the highly detailed 1D semi-analytical work by Tagawa et al. (2020a) suggests that of order $\sim 90\%$ of merging binaries in AGN discs will have formed within the lifetime of the AGN disc. These binary formations predominantly take place through what is known as a *gas-assisted* capture whereby upon the scattering of two BHs in the AGN disc, a complex interplay between the binary and the surrounding gas and their CSMDs leads to a net removal of the binaries' kinetic energy (e.g. Goldreich et al., 2002), such that they remain bound. This was investigated very recently in semi-analytical studies (e.g. DeLaurentiis et al., 2022; Rozner et al., 2022). These studies assumed orbital energy is dissipated by an Ostriker (1999) like dynamical friction prescription between the binary BHs and the local gas. The first full hydro simulations of this process, Rowan et al. (2023) (Chapter 4) and also Li et al. (2022a) corroborated the overall analytical and semi-analytical expectation that scattering encounters in gas may lead to binary formation, even when the initial orbital energy is positive upon first entering the binary Hill sphere, but the details may differ from those of previous semi-analytical models. In Chapter 4, that for this chapter will be referred to via its associated published paper (Rowan et al. (2023), hereafter Paper I), the subsequent evolution of the binaries was also directly simulated following their formation. Paper I also demonstrated that the evolution of the binary semi-major axis and eccentricity evolution depends on the AGN disc mass and their orbital configuration (i.e. prograde or retrograde). Inspiral was observed in some prograde cases and for retrograde binaries, eccentricities were excited to high enough values in short enough times for binary mergers to occur within timescales of only a few AGN orbits. Both Paper I and Li et al. (2022a) found in-spiralling binaries that form with very high initial eccentricities, possibly explaining the discrepancy with studies that used near circular initial binaries (e.g.

Baruteau et al., 2011; Kaaz et al., 2021; Li et al., 2022d,c). Li & Lai (2022a) further corroborated this with a positive correlation between eccentricity and inspiral rate.

Now that the viability of the gas assisted capture mechanism has been justified, the next natural question is to quantify the efficiency of this process based on pre-encounter parameters. In my collaborative study of gasless BH scatterings (Boekholt et al., 2023) there were three 'islands' in the parameter space of the impact parameter (i.e. initial radial separation relative to the central SMBH) p of BH encounters that lead to more than one encounter, i.e. "a Jacobi capture". The parameter space of the number of encounters (orbits) during the Jacobi capture and the impact parameter exhibits a fractal structure. Furthermore, the large statistics of the work allowed one to very finely sample the parameter space of the encounter to quantify the fraction of the parameter space p that lead to temporary binary formation. Here, I examine if these temporary binaries formed without gas in Boekholt et al. (2023) lead to permanent capture through gas hardening. I also study how gas affects the fractal structure of the parameter space of initial conditions that allow for successful binary capture. In Paper I and Li et al. (2022a), the gas capture process was validated using a full hydrodynamical approach for the first time. In Paper I the formation and long term evolution of each binary was modelled self consistently in one continuous simulation, so the starting conditions of the binaries were directly set by their formation and not based on any assumptions. The work demonstrated that both prograde and retrograde binaries may form in varying AGN gas densities and identified a bimodality in the eccentricity evolution where prograde binaries circularised over time and retrograde binaries became more eccentric.

In this Chapter, I explore the regions of phase space that permit the formation of a binary from two initially isolated BHs embedded in a gaseous accretion disc of a third massive body (SMBH) and the role of gas in shaping this space using a global 3D hydrodynamical simulation based on smoothed particle hydrodynamics (SPH). This work forms the second in my series of papers investigating each element of the gas-induced binary merger mechanism in AGN. The Chapter builds on Paper I by probing the binary capture process in far greater detail using a much finer sampling (114 simulations total) in impact parameter, providing great enough statistics to probe the stochasticity of the gas-assisted formation process and develop statistical correlations between pre-encounter parameters and important physical

processes during the encounter. Such correlations can then be used to generate a vastly improved analytic prescription for semi-analytic works that discuss binary formation in accretion discs like that of Tagawa et al. (2020a). I present this work alongside another collaborative paper, Whitehead et al. (2023a), that models the same scattering problem considered here but using a local shearing box approach and employing the grid code Athena++ instead of an SPH implementation. As discussed later in detail, the results of both papers are largely consistent with one another. Such similarities include the relationship between the initial approach trajectory of the BHs and the level of dissipation and the dependence on gas density. The numerical method and initial conditions are detailed in Sec. 5.2, and the results are presented in Sec. 5.3. I discuss the results in Sec. 5.4 and the caveats of the models in Sec. 5.5 before summarising and concluding in Sec. 5.6.

5.2 Computational Methods

5.2.1 Hydrodynamics

The simulations are largely the same as in Chapter 4. The setup considers a three-body system consisting of a central SMBH of mass $M_\bullet = 4 \times 10^6 \mathrm{M}_\odot$ and two stellar BHs with masses $M_{\rm BH} = M_1 = M_2 = 25\mathrm{M}_\odot$ embedded in a gas disc. The BHs are inserted symmetrically about a radial encounter distance from the SMBH, $R_{\rm mid} = 0.0075\,\mathrm{pc}$. The gas disc is resolved about the BHs as an annulus of radial width $\Delta R_{\rm disc} = 20 r_{\rm H}$ where $r_{\rm H} = R((M_1 + M_2)/(3M_\bullet))^{1/3}$ as before. Based on the annulus width this gives $R_{\rm in} = R_{\rm mid} - 10r_{\rm H}$ and $R_{\rm out} = R_{\rm mid} + 10r_{\rm H}$. An identical resolution of 25 million particles is used. Radiative and magnetic effects are again neglected. Such effects may be important for modelling the CSMDs of the satellite BHs but are often ignored due to their computational expense. The AGN disc is consistent with its implementation in the previous work in Paper I, where the surface density Σ is given by eqs. (4.1) & (4.6). The fiducial AGN disc mass $M_{\rm d,0}$ given by Eq. (4.5). The free parameters of Eq. (4.5) are again fixed at $\alpha_{\rm SS} = 0.1$, $l_E = 0.1$, $\mu_{\rm mol} = 0.6$, $\hat{\kappa}$=1.0 and $\epsilon = 0.1$. The sound speed $c_{\rm s}$ is given by eqs. (4.2) & (4.3) for a scale height to radius ratio of $H/\mathrm{R}_{\rm in} = 0.005$.

5.2.2 Initial Conditions

In a similar manner to the previous work of the gasless case in Boekholt et al. (2023) how binary formation varies with the encounter parameters is investigated. These parameters are: the radial impact parameter p, closest approach $r_{\rm min,1}$, relative two-body energy, and the AGN gas density. The simulation setup is as follows. Two BH satellites are initialised on circular orbits around the SMBH with varying initial radial separations which represents their impact parameter $p = \mathrm{R}_2 - \mathrm{R}_1$ where R_1 and R_2 are the respective radial positions of the inner and outer satellite in the SMBH disc (analogous to ΔR_i in Chapter 4). The impact parameter p is sampled using 39 evenly spaced points over the range $[1.75, 4.25]r_{\rm H}$. This is an $\sim 8\times$ increase in the number of simulations compared to Paper I which only considered 5 impact parameters per set of initial parameters. In the previous paper, this limitation prohibited any statistical analysis of the effect of varying impact parameters. Now, using far more models, it is possible to perform a more accurate parameter space study of binary formation across the aforementioned parameters. Past studies indicate binaries can dissipate their relative energy more efficiently in denser AGN discs (e.g. Li et al., 2022a; DeLaurentiis et al., 2022; Rowan et al., 2023). To also probe the effect of density, another simulation suite with a modified disc mass is also performed. This consists of an additional 45 simulations using an AGN disc with a mass of $3\mathrm{M}_{\rm d,0}$. Both suites are also compared to a gasless sample with the same initial conditions as reference (see Boekholt et al., 2023, for a detailed study of the gasless case). This gives the mass of gas contained within an annulus of width $r_{\rm H}$ of $0\mathrm{M}_\odot, 110\mathrm{M}_\odot$ and $330\mathrm{M}_\odot$ for the gasless, fiducial and $3\mathrm{M}_{\rm d,0}$ models respectively, highlighting the high amount of gas present in the simulations. Incorporating hydrodynamics adds several additional complexities that can affect the interpretation of the results compared with the gasless case. First, BHs form circum-single mini disks (CSMDs) before their encounter. The discs enhance the gravitational attraction between the satellite BHs since their masses can be approximately added to their host BH to leading (monopole) order in a multipole expansion. Additionally, the masses of the BHs can change via accretion in the lead up to the encounter which again can alter the amount each satellite perturbs the other prior to the encounter itself. To have a more similar set of BH and CSMD masses at their encounter, the initial azimuthal separation $\Delta\phi$ of each

p	$\Delta\phi$	$\frac{M_\bullet}{\mathrm{M}_\odot}$	$\frac{M_{\rm BH}}{\mathrm{M}_\odot}$	$\frac{M_{\rm d}}{10^{-3}M_\bullet}$	$\frac{R_{\rm mid}}{\rm mpc}$	$\frac{\Delta R_{\rm disk}}{r_{\rm H}}$	
1.75–4.25	14°–34°	4×10^6	25	$\{0, 1.6, 4.8\}$	7.5	20	
f	q	$\frac{H}{R_{\rm in}}$	$\alpha_{\rm SS}$	$L_{\rm E}$	ϵ	ξ	$\hat{\kappa}$
0.6	0.45	0.005	0.1	0.1	0.1	0.6	1.0

Table 5.1: Fiducial model parameters. Here $(p, \Delta\phi)$ are the initial radial offset and orbital phase between the two stellar BHs in their initially Keplerian orbits around the SMBH, $r_{\rm H}$ is the Hill radius, $(M_\bullet, M_{\rm BH}, M_{\rm d})$ are respectively the SMBH mass, the individual stellar BH masses, and the total enclosed gaseous disk mass (Eq. 4.5), hence the gas mass per $r_{\rm H}$ radial width is $\frac{7}{5}(r_{\rm H}/R_{\rm mid})M_{\rm d} = 0.026M_{\rm d} = \{0, 110, 330\}\mathrm{M}_\odot$, $(R_{\rm mid}, \Delta R_{\rm disk})$ are the midpoint radius and the width of the simulated gaseous annulus, q and f set the radial dependence for the sound speed and surface density across the annulus (Eqs. 4.3–4.1), H is the scaleheight ($H = 0.4\,r_{\rm H}$) which also sets the pressure and temperature in the disk via Eq. (4.3), $L_{\rm E}$ is the Eddington ratio, ϵ is the radiative efficiency, ξ is the mean molecular mass, $\hat{\kappa}$ is the opacity relative to the electron scattering opacity ($0.4\,\mathrm{cm^2 g^{-1}}$).

object is scaled depending on their impact parameter p such that their approach time is approximately the same. Specifically, $\Delta\phi$ is scaled so all simulations have the same approach time as that with $p = 2.5r_{\rm H}$ and $\Delta\phi = 20°$, i.e.

$$\Delta\phi(\mathrm{R}_1, \mathrm{R}_2) = \frac{\sqrt{\frac{M_\bullet}{\mathrm{R}_1}} - \sqrt{\frac{M_\bullet}{\mathrm{R}_2}}}{\sqrt{\frac{M_\bullet}{R_{\rm mid}-1.25r_{\rm H}}} - \sqrt{\frac{M_\bullet}{R_{\rm mid}+1.25r_{\rm H}}}} \times 20°\,. \tag{5.1}$$

This ensures that the amount of accretion and growth of the CSMDs is approximately equal for each simulation with different p. The simulation parameters and initial conditions are summarised in Table 5.1.

5.3 Results

In this section, I present and discuss the results of the simulation suites. Starting with an overview of the shape and size of the formation parameter space in Sec. 5.3.1, how the energy dissipation of the encounter is influenced by the closest approach is discussed in Sec. 5.3.2. The time dependence of each mechanism that can alter the orbital energy of the binary during the encounter is described in Sec.

5.3.3. Accretionless encounters are considered in Sec. 5.3.4 and the effects of an increased AGN disc density are presented in Sec. 5.3.5.

5.3.1 The capture cross section with gas driven dissipation

The periapsis distance of each first encounter is shown in Figure 5.1. These are compared directly to resimulated gasless encounters using the exact same initial conditions for the BHs. As the computational cost without gas is orders of magnitude lower, a much finer resolution of 16k (i.e. 2^{14}) models with impact parameters in the range $p = [1.5, 3.5]$ are used. It is immediately obvious that gas leads to a much larger window in impact parameters for encounters to penetrate less than a Hill radius. Moreover, there is only one wide valley of captures in the space of p, with the minimum separations varying gradually across p, unlike in the gasless case where there are two separated capture windows and sharp changes in the minimum separation for very particular initial conditions (as identified in Boekholt et al. 2023). Note that the deep troughs observed in the gasless case are possibly missed by the relatively coarse sampling in impact parameters for the simulations with gas. Additionally, gas leads to binary formation at far larger p than in the gasless simulations, i.e. at larger separation at the first closest approach, $r_{\rm min,1}$. To quantify directly the size of the parameter space in p where multiple encounters may happen, I define the initial one-dimensional capture *cross section* λ as the total "length" in the 1D parameter space of the impact parameter p that allows for at least *two* encounters within the binary Hill sphere. Even though many gasless encounters decouple after this point, I examine the criterion required for a binary to initially be bound, not whether the system is stable to the 3-body interaction with the SMBH in the long term. More generally, the cross section for encounters to have exactly n encounters within the Hill sphere is defined in Boekholt et al. (2023) as

$$\lambda\left(N_e = n\right) = \sum_i \Delta\lambda_i \delta_{n,N_{e,i}}, \tag{5.2}$$

where N_e is the number of encounters of a simulation, i represents the simulation number, δ is the Kronecker delta which vanishes unless simulations have n total encounters and $\Delta\lambda_i = \frac{1}{2}\left(p_{\rm i+1} - p_{\rm i}\right)$ is the length of the impact parameter interval between the discrete samples around the simulation i. Here we are interested in

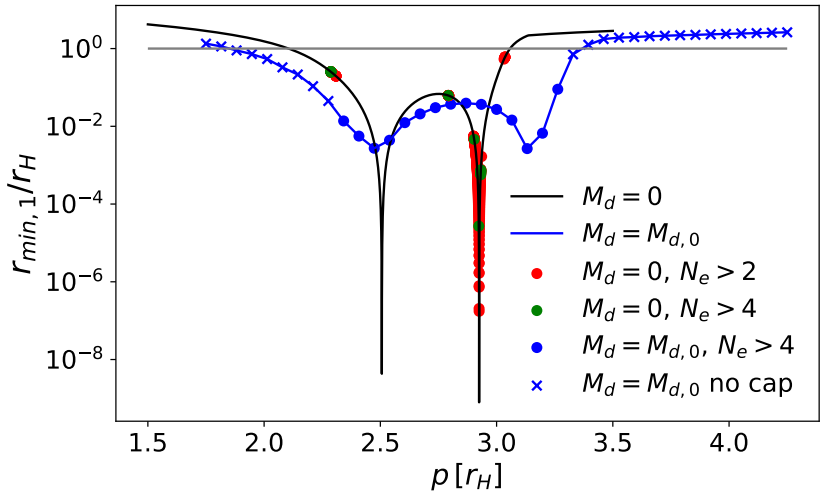

Figure 5.1: Minimum separation for the fiducial run (blue) compared to the gasless case (black) for the first approach as a function of the "impact parameter", i.e. the initial radial separation relative to the SMBH, denoted by p. The horizontal line indicates the Hill radius of one of the objects for comparison. The gas clearly broadens the range of impact parameters of close encounters. In the gasless $M_\mathrm{d} = 0$ simulation suite, binaries with a number of encounters of $N_e \geq 2$ and $N_e \geq 4$ are shown in red and blue respectively. For the the hydrodynamic simulation, all binaries with two encounters also performed four and remain bound.

the cross section for *all* models which have $N_e \geq 2$. So the Kronecker delta is replaced with an indicator function $I_A(x)$

$$I_A(x) = \begin{cases} 1 & \text{if } x \in A \\ 0 & \text{otherwise} \end{cases}, \tag{5.3}$$

that vanishes if case x is not part of set A. For the problem, this becomes

$$I_{[N_e \geq 2]}(N_{e,i}) = \begin{cases} 1 & \text{if } N_{e,i} \geq 2 \\ 0 & \text{otherwise} \end{cases}. \tag{5.4}$$

All together this gives explicitly the initial capture cross section λ

$$\lambda\,(N_e \geq 2) = \sum_i \Delta\lambda_i I_{[N_e \geq 2]}(N_{e,i}), \tag{5.5}$$

with an associated error $\delta\lambda$ of

$$\delta\lambda\,(N_e \geq 2) = \sqrt{\frac{1}{2}\sum_i \left(\Delta\lambda_i I_{[N_e \geq 2]}(N_{e,i})\right)^2}. \tag{5.6}$$

This calculation is performed on all 2^{14} gasless and all 39 of the fiducial gaseous simulations. This gives a cross section for two or more encounters of $\lambda(N_e \geq 2) = (0.0407 \pm 0.0011)\, r_{\rm H}$ for the gasless simulations and $0.98 \pm 0.13 r_{\rm H}$ when gas is included. The cross section for four encounters then drops to ($\lambda(N_e \geq 4) = (0.00219 \pm 0.00025)\, r_{\rm H}$ for the gasless case but remains identical for the simulations with gas. The drop in the gasless case follows as there is no dissipation mechanism to remove energy once the binary is formed other than through its interaction with the SMBH which is entirely chaotic, thus they all inevitably decouple after usually only a short number of orbits after being disrupted by the SMBH, see Boekholt et al. (2023) for details. The fact $\lambda(N_e \geq 2) = \lambda(N_e \geq 4)$ when gas is included indicates that gas can dissipate their orbital energy rapidly enough so that all binaries that undergo two encounters harden sufficiently to prevent their disruption from the SMBH. Furthermore, based on these values I conclude that for the initial conditions, there is a ~ 25 times larger cross section to have multiple orbits when gas is included based on $\lambda(N_e \geq 2)$ with and without gas. Indicating that form more easily (at least in a quasi-stable state) in the presence of gas. Whether these binaries are permanent is examined below. Directly comparing the $\lambda(N_e \geq 2)$ and $\lambda(N_e \geq 4)$ cross sections of the gasless simulations to those of Boekholt et al. (2023) ($\lambda(N_e \geq 2) = 0.12 r_{\rm H}$, $\lambda(N_e \geq 4) = 0.0051 r_{\rm H}$) the cross sections are slightly lower, while still within the same order of magnitude for both values. Though note that Boekholt et al. (2023) employed a far larger initial azimuthal separation, so the gravitational focusing will of course be different across those simulations compared to the simulations in this investigation. The slope of $d\log_{10}(\lambda)/dN_e$ was shown in Boekholt et al. (2023) to be constant at ~ 0.68. I calculate this slope to be ~ 0.64, in good agreement.

5.3.2 Dissipation as a function of minimum separation

Though the encounters lead to largely chaotic gas flows, I develop ready-to-use semi-analytical prescriptions based on the high-resolution simulations to improve the accuracy of purely semi-analytical studies such as by Tagawa et al. (2020a), DeLaurentiis et al. (2022) and Rozner et al. (2022). In this chapter, *first encounter* is explicitly defined as the period between the BHs entering within $2r_{\rm H}$ separation and either the first apoapsis or upon reaching $1r_{\rm H}$ separation after the first encounter where the choice of end point depends on whether the binary remains bound or not,

respectively. If the binary becomes bound (even if temporarily) then the *second encounter* is defined as the period between first apoapsis and second apoapsis or the time of exiting the Hill sphere, and so on for higher numbers of encounters. The two-body energy of the binary is given by

$$E_{\rm bin} = \frac{1}{2}\mu\|\boldsymbol{v}_1 - \boldsymbol{v}_2\|^2 - \frac{GM_{\rm bin}\mu}{\|\boldsymbol{r}_1 - \boldsymbol{r}_2\|}, \tag{5.7}$$

where $M_{\rm bin} = M_1 + M_2$ is the total mass of the binary, $\mu = M_1 M_2/M_{\rm bin}$ is the reduced mass, $\boldsymbol{r}_i$, $\boldsymbol{v}_i$ are the positions and velocities of satellite BH $i = (1, 2)$ and G is the gravitational constant.

Figure 5.2 shows $\Delta E_{\rm bin}$, the change of the binary energy during the first encounter as a function of closest approach in the fiducial simulation setup expressed in the natural units of $E_{{\rm H},c}$ defined as

$$E_{\rm H,c} = \frac{GM_{\rm bin}\mu}{2r_{\rm H}}\,, \tag{5.8}$$

i.e. the absolute value of the orbital energy of a binary with a semimajor axis equal to the Hill sphere of one of the BHs, where the sign of $\Delta E_{\rm bin}$ is denoted by different markers. Also plotted is a best-fit line for the analytic power-law profile as

$$\Delta E_{\rm bin} = -a\left(\frac{r_{\rm min,1}}{r_{\rm H}}\right)^b E_{\rm H,c}\,. \tag{5.9}$$

where $r_{\rm min,1}$ is the minimum separation of the first encounter, a and b are dimensionless fitting parameters. By construction, this expression gives the energy *loss* of the binary during the encounter. Figure 5.2 indicates an inverse power law relationship between the depth of the first encounter and the amount of energy dissipated, i.e. deeper encounters tend to dissipate more energy.[1] There is a large scatter where the energy dissipated in a small bin of closest separations can vary by up to two orders of magnitude for small $r_{\rm min,1}$. This scatter may be interpreted as an error in the predicted power-law exponent b as shown. For the initial conditions of this problem (see Sec. 5.2.2), the binary objects intersect each other's CSMDs at $\Delta r \sim 0.05 r_{\rm H}$[2]. Thus since the trend continues outside of this

[1]The existence of this dissipation-periapsis relation was hinted in Chapter 4, where dissipation was found to be more efficient when binaries directly intersect each other's CSMDs although not quantified until now.

[2]The size of the CSMDs is determined by the assumed equation of state, among other parameters (e.g AGN disc temperature, viscosity)

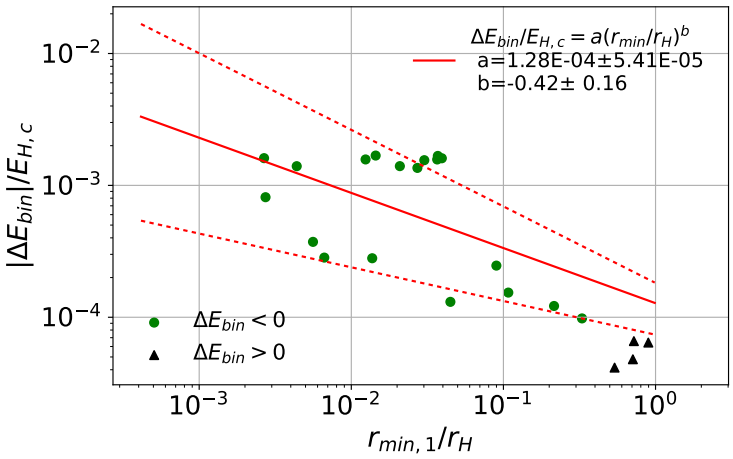

Figure 5.2: The change in the binary energy during the first encounter, $\Delta E_{\rm bin}$ normalised to $E_{\rm H,c}$, as a function of the first periapsis passage $r_{\rm min,1}$. The sign of $\Delta E_{\rm bin}$ is indicated by the symbol type: circular green points indicate where energy is removed from the binary while the black triangular points represent models where energy is *added*. Only binaries that pass within $r_{\rm H}$ are shown since all encounters outside the Hill sphere result only in flyby encounters. The red solid and dashed lines show respectively the best-fit power-law relation to the dotted data points and the 1σ errors on the slope.

range, the coupling between the dissipation and periapsis changes continuously with $\Delta r/r_{\rm H}$, rather than akin to a step function at the intersection of the BH CSMDs as previously thought in Paper I. There is no correlation for the second and later encounters (Figure 5.3), as the gas morphology which determines the amount of energy dissipation becomes chaotic. The first encounter is naturally the most important for discussing energy dissipation as if the binary energy is still too high after the first encounter then no further encounters are possible. This excludes the possibility of an entirely separate second encounter of the objects as they orbit round the AGN, which is discussed in Li et al. (2022d).

5.3.3 Physical dissipation sources

Measurement of dissipation rates

To uncover the physical origin of the results in Figure 5.2, the cumulative energy dissipation per unit mass during the encounter period for the three energy dissipation terms are calculated. These terms, as in Chapter 4 are:

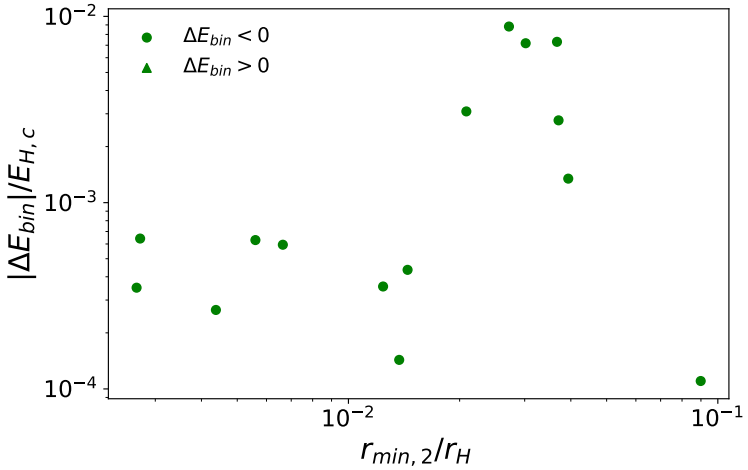

Figure 5.3: Similar to Figure 5.2 but showing the change in the binary energy during the second encounter, normalised to $E_{\rm H,c}$ as a function of the closest approach during the second encounter $r_{\rm min,2}$. Note that there are now naturally fewer data points as many models decouple after only their first encounter.

1. **SMBH interaction**, $\varepsilon_{\rm SMBH}$ - energy per unit time lost or gained by the binary system through shearing tidal forces induced by the SMBH (Eq. 4.10).

2. **Gas gravitational dissipation**, $\varepsilon_{\rm grav}$ - from the gravitational interaction with the surrounding gas (Eq. 4.12).

3. **Accretion**, $\varepsilon_{\rm acc}$ - due to conservation of mass and linear momentum of accreted gas particles onto the BHs (Eq. 4.16).

The total dissipation is then simply $\varepsilon = \varepsilon_{\rm SMBH} + \varepsilon_{\rm grav} + \varepsilon_{\rm acc}$.

If one integrates ε over some time window, this gives the cumulative or 'net total' energy exchange from the binary over the specified time window. Note that the integration matches the net change in the binary energy exactly as the dissipation sources are deconstructed and their instantaneous value recorded at *every* timestep in the simulation, so no inaccuracies arise due incomplete sampling of the timesteps.

Distinguishing orbit families

It is possible to differentiate between three different types of encounters by separating them into three families based on the form of their trajectories, determined by their impact parameters p, shown in Figure 5.4. In the frame of the inner BH, the first

family consists of encounters with low impact parameters where the approaching outer BH is perturbed to the left of the inner BH into a prograde orientation, i.e. orbiting in the same direction as around the SMBH. This family is referred to as *leftsided* encounters (LS for short)[3]. Encounters with intermediate impact parameters where the approaching outer BH initially passes on the inside (right) of the inner BH, dragging it into a retrograde orbit are labelled as *rightsided* (RS) encounters.[4] The third family takes an initially similar approach as the RS trajectories except they turn back on themselves and reverse to a prograde orbit, i.e. their trajectories are deflected by at least 180° in the final lead up to the encounter. These are labelled as *turnaround* (TA) encounters.

These three encounter types were also identified in Boekholt et al. (2023). However, since there was no dissipation mechanism in that study, the binaries were loosely bound with low angular momentum and could periodically switch encounter family. The complexity of the three-body problem and this ability to switch encounter families gave rise to a fractal structure in the number of encounters as a function of impact parameter. In Boekholt et al. (2023), three distinctly separated islands in p allow for temporary binary formation, which do not appear here. Instead, there is one formation window as a function of impact parameter. Although binaries may flip orientations afterwards, the first encounter trajectories of the binaries in Boekholt et al. (2023) obey the same three family classifications and rough position in the space of p. However the size of the successful capture region of each family is significantly smaller. More specifically, the *RS* encounters only result in binaries near the second trough at higher p in the curve of $r_{\mathrm{min},1}$ vs p, where encounters lead to binaries in the whole range between the two minima. Additionally the LS and TA encounters of the gasless study have their regions of possible temporary binary formation at higher $r_{\mathrm{min},1}$ and are much narrower in p. Hence, the inclusion of gas smooths out the troughs and blends the three possible windows for formation into one larger one. The three encounter families are separated by two direct collision trajectories at the two troughs in $r_{\mathrm{min},1}$ vs p. We can conclude that the complexity is removed as there is little to no changing of orbital families (and hence prograde/retrograde orientation) even after just two

[3]the satellites execute a left-handed turn with respect to their COM, $[(\boldsymbol{r}_{\mathrm{out}} - \boldsymbol{r}_{\mathrm{in}}) \times (\boldsymbol{v}_{\mathrm{out}} - \boldsymbol{v}_{\mathrm{in}})] \cdot [(\boldsymbol{r}_{\bullet} - \boldsymbol{r}_{\mathrm{in}}) \times (\boldsymbol{v}_{\bullet} - \boldsymbol{v}_{\mathrm{in}})] < 0$

[4]the satellites execute a right-handed turn in this case

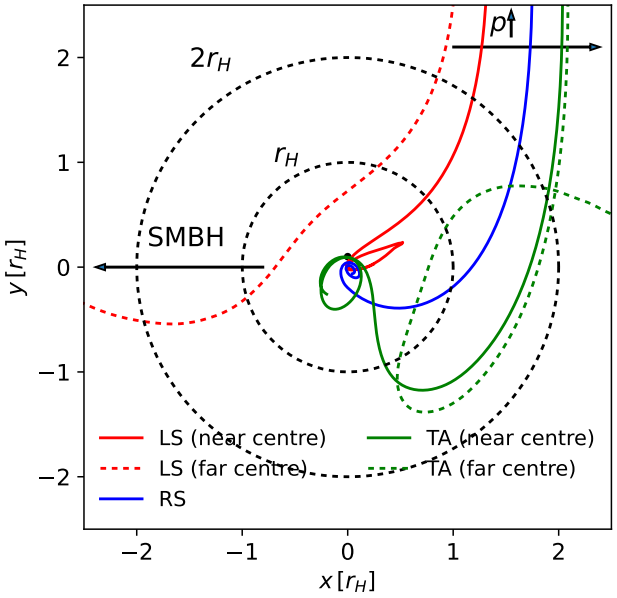

Figure 5.4: Classification of the trajectories of the first encounters between two sattelites moving on initially Keplerian circular orbits around a central SMBH. The trajectory of the outer satellite is shown in the frame of the inner satellite. A leftsided encounter is shown in red, rightsided in blue and turnaround in green. The dashed lines indicated the two failed encounters adjacent to each side of the capture window, to visualise how encounters far from the centre (far centre) of the capture window proceed. Their specific position on the impact parameter space is highlighted in Figure 5.5.

orbits as the gas is efficient at altering the energy and angular momentum of the binary to form a stable system, shown already in the previous paper Paper I.

Time evolution of the dissipation rates

Figure 5.5 shows the orbit families in the parameter space of p using the same colour code as in Figure 5.4 and compares their cumulative energy dissipation during the first encounter. As indicated by the top panel of Figure 5.5, the two large troughs in the encounter depth naturally mark the transition between each family and also between prograde and retrograde binary formation, where RS encounters are retrograde and LS and TA encounters are prograde. The first trough (on the left) locates the boundary in the space of p for LS and RS encounters and the second trough marks the boundary between RS and TA encounters. At these troughs is also where theoretically one can expect infinitely close encounters or direct *collisions* if

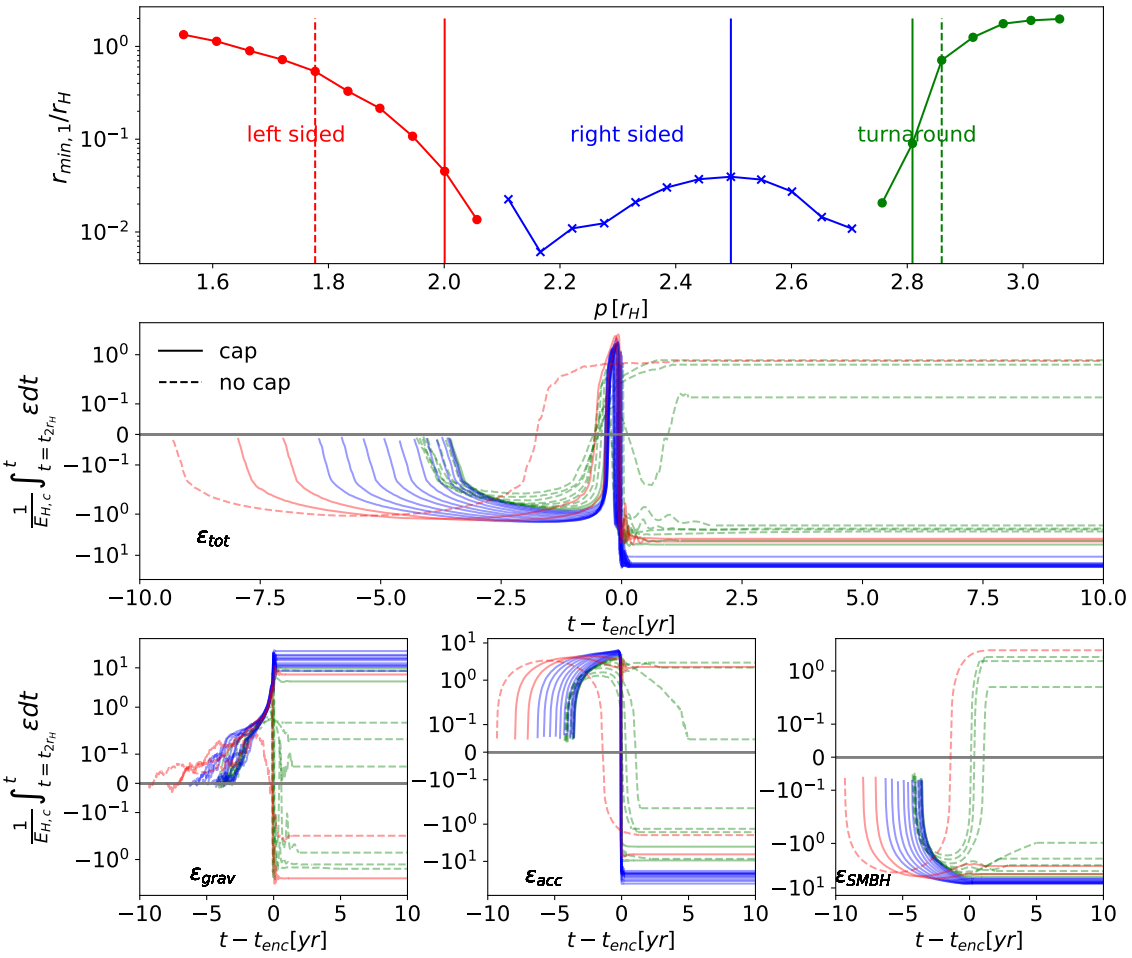

Figure 5.5: Cumulative energy change in all the binaries from the fiducial run during the first encounter from $2r_{\rm H}$ to apoapsis/exiting of Hill sphere. Results are colour-coded by encounter family; leftsided (red), rightsided (blue) and turnaround (green) encounters. The top panel re-illustrates which encounters belong to which family in the simulation suite. The dashed vertical lines indicate the two failed encounters adjacent to each side of the capture window and the bold lines highlight the three other selected models from each family used in Figure 5.4 using the same colour coding. The middle panel shows the total cumulative energy change for all fiducial models. The bottom row shows the cumulative energy transfer from the local gas gravity, accretion and SMBH respectively from left to right. The final cumulative value from the end point of the first encounter is artificially extended up to the ten year mark to more easily compare the net cumulative energy dissipation across models. Unsuccessful captures are denoted with dashed lines and successful captures with solid lines. From the colour-coded results, rightsided encounters lead to the most reliably efficient binary formation which is attributed to the encounter depth dependent dissipation of Figure 5.2. .

the impact parameters are fine tuned. Since there is a switch between prograde and retrograde orientations, there is naturally a possible set of orbits at minima of the troughs with zero angular momentum approach with an eccentricity of unity. These extremely close encounters are far better resolved in the gasless 3-body simulations. As shown in Boekholt et al. (2023) which considers the problem in a three-body framework, it is possible to fine tune the initial conditions to have arbitrary close encounters at these two impact parameters and at others for subsequent encounters provided numerical sampling is not a limitation.

The middle row of Figure 5.5 shows that the family of the encounter can be a good indicator of the type of energy exchange the binary will experience. RS encounters typically dissipate the most orbital energy when compared to leftsided and turnaround encounters. In all cases there is an initially positive contribution from accretion and gravitational torques as the BHs approach separations of $2r_{\rm H}$, as observed in Paper I, which is found to be a result of a gas pileup ahead of each BH on their approach. This is initially overpowered by the shearing force on the binary from the SMBH until the final year before the closest approach, where $\varepsilon_{\rm grav}$ dominates, driving the spike in $\varepsilon_{\rm tot}$ just prior to the first closest approach ($t - t_{\rm enc} = 0$) before $\varepsilon_{\rm acc}$ with some addition from $\varepsilon_{\rm SMBH}$ quickly overpower the gas gravitational forces, removing energy from the binary rapidly. Note that ultimately $\varepsilon_{\rm acc}$ and $\varepsilon_{\rm SMBH}$ have often the same order of magnitude, see further discussion in Sec. 5.3.4.

Deconstructing the dissipation contributions per orbital family, RS encounters typically dissipate the most energy and are most favourable for binary formation due to both strong accretion and the work done by the SMBH. Interestingly, the time-evolution of RS encounters are very consistent across all dissipation mechanisms, having net positive energy transfer from the gas to the satellites, an initially positive but rapidly negative contribution from accretion, and a negative contribution from the SMBH. Both LS and TA encounters have a range of contributions, both positive and negative, from each dissipation mechanism. Simulations with impact parameters close to the RS encounter window exhibit the same positive energy dissipation as the RS encounters. LS and TA encounters near the deep troughs in the top panel Figure 5.5 can therefore dissipate energy as efficiently as RS encounters, but only in this small region in the space of p. As they deviate to higher or lower impact parameters from the central RS encounter region, dissipation gradually becomes

less significant and flips when the impact parameter p is sufficiently high ($\gtrsim 2.8$) or low ($\lesssim 1.6$) for the parameters. This is explained by the coupling of $\Delta E_{\rm bin}$ with the close approach depth $r_{\rm min,1}$ and the behaviour of $r_{\rm min,1}$ with p. Where the binaries with the closest approaches, occurring in the RS encounter region, dissipate the most energy. Binaries outside the RS encounter regions have increasingly distant close approaches and so dissipate less energy.

In the wings of the encounter outside the RS region, gas gravity becomes more negative (removing energy from the binary) while dissipation from accretion becomes more positive due to less accretion during the closest approach and dissipation from the SMBH becomes positive. The reversal of the SMBH dissipation predominantly applies to the turnaround encounters as after they initially pass each other, SMBH shear flips from slowing down the binaries' approach, to accelerating them after the first periapsis passage. This is because the shear of the SMBH acts along the direction of the radial vector from the SMBH to the binary COM. As the binary approaches this shear acts against the binary motion, removing the relative kinetic energy of the binary. After a turnaround binary executes its first periapsis, the binary separation is increasing along this same vector, so the shear leads to an increase in their velocities and thus their relative energy, i.e. doing positive work.

Torques during the encounter

Similarly to the dissipation, the strength and sign of torques (eqs. 4.18, 4.19 and 4.20) induced on the binary depend on the impact parameter and family of the encounter. The cumulative torques over the first encounter (Figure 5.6) show that the net torque moves from positive to negative values as p increases. In terms of encounter families, LS encounters experience net positive torques, TA experience net negative torques and the net torque of RS encounters transitions smoothly from positive to negative. Due to the already highly eccentric nature of the binaries, I find torques highly insignificant for predicting the binary outcomes as the binary motion is almost entirely radial and so the torques $(\boldsymbol{r}_1 - \boldsymbol{r}_2) \times (\boldsymbol{v}_1 - \boldsymbol{v}_2)$ are minimal for the first encounter.

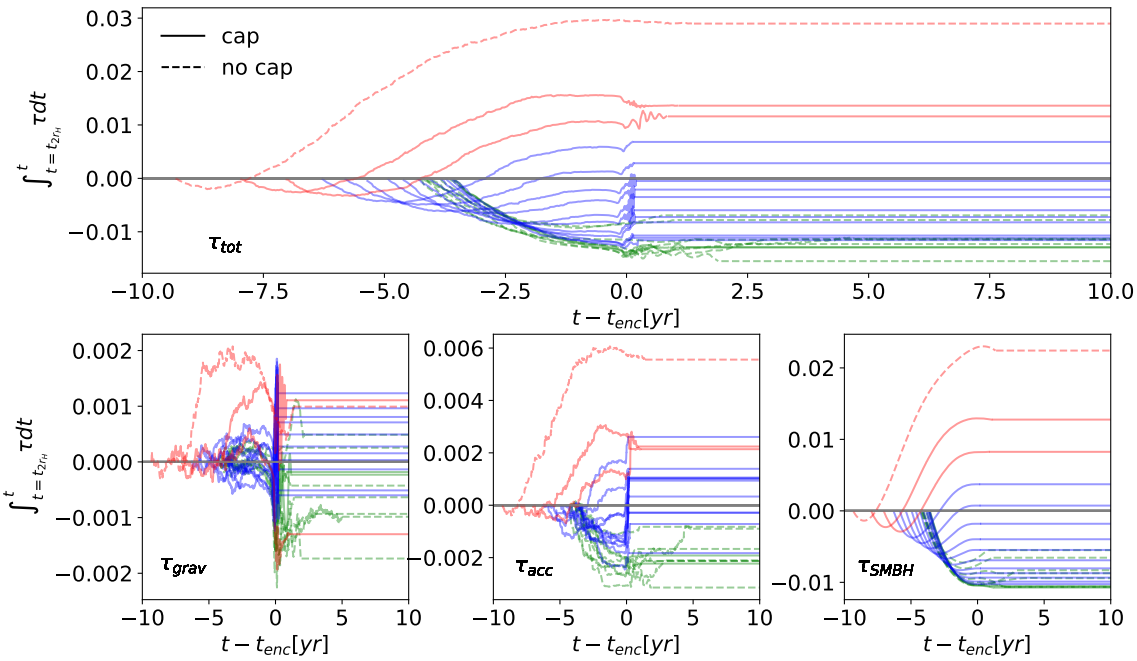

Figure 5.6: Cumulative torque/angular momentum change in all the binaries during the first encounter from $2r_{\rm H}$ to apoapsis/exiting of Hill sphere. Results are colour-coded by encounter family; leftsided (red), rightsided (blue) and turnaround (green) encounters. The top panel shows the total cumulative angular momentum change for all fiducial models. The bottom row shows the cumulative energy transfer from the local gas gravity, accretion and SMBH respectively from left to right. The final cumulative value from the end point of the first encounter is artificially extended up to the ten year mark to more easily compare the net cumulative torque across models. Additionally, unsuccessful captures are represented by dashed lines and successful captures with solid lines. From the colour-coded results, the torque switches sign smoothly when transitioning from leftsided to turnaround encounters. This results from the SMBH torque's dependence on the angle between the vectors from the SMBH and the binary COM and from one satellite to the other.

5.3.4 Accretionless encounters

In this work and in Paper I accretion appears to dissipate energy on the same order of magnitude as gravitational gas drag. Here, whether captures may still occur in the absence of accretion during the close encounter is tested. Figure 5.7 shows the separation vs time for the fiducial run along side 30 re-simulated runs of each simulation where accretion is switched off when the BHs have a separation less than $2r_{\rm H}$. The softening radius of $0.01r_{\rm H}$ is left unchanged. In switching off accretion at this point, the initial encounter trajectory and immediate pre-encounter mass

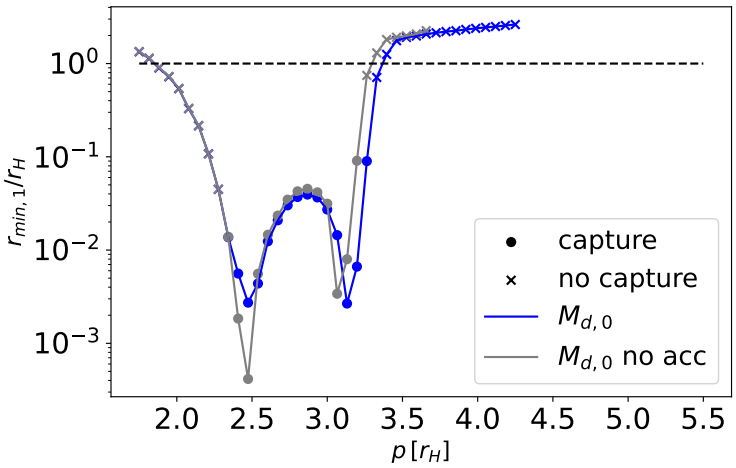

Figure 5.7: Minimum separation for the first approach for the fiducial run (blue) and the same run where accretion is turned off when the BH satellites get within 2 Hill radii of each other (grey) as a function of the initial radial separation p. Horizontal line indicates the Hill radius size of one of the objects. The outcome of all the simulations remains unchanged after switching off accretion.

of the fiducial models is preserved so they can be directly compared.

Figure 5.7 indicates that removing accretion leads to qualitatively identical outcomes with all successful binaries in the fiducial simulation suite also successfully forming in the accretionless suite and vice versa for unsuccessful captures. In addition to the scattering outcome, the depth of the initial encounter is largely unchanged, aside from the location of the two large troughs where accretionless encounters have deeper encounters for the assumed particular values of p. This is likely only coincident with the sensitivity of the depth with p at these two turnaround points between prograde and retrograde encounters, where it was shown in Boekholt et al. (2023) that fine tuning p can lead to extremely deep encounters for only small changes in p. Hence the small variations in the trajectory due to the exclusion of accretion can lead to very different depths at these two key points in the parameter space of p. The fact the encounter depths change minimally is unsurprising as although accretion is shown to dominate overall, this is only due to a sudden reversal at the first periapsis passage, $t - t_{\rm enc} \approx 0$. Thus the encounter trajectory is only perturbed by the SMBH and gas gravity prior to the close encounter, so the encounter depth remains largely unchanged. The capture

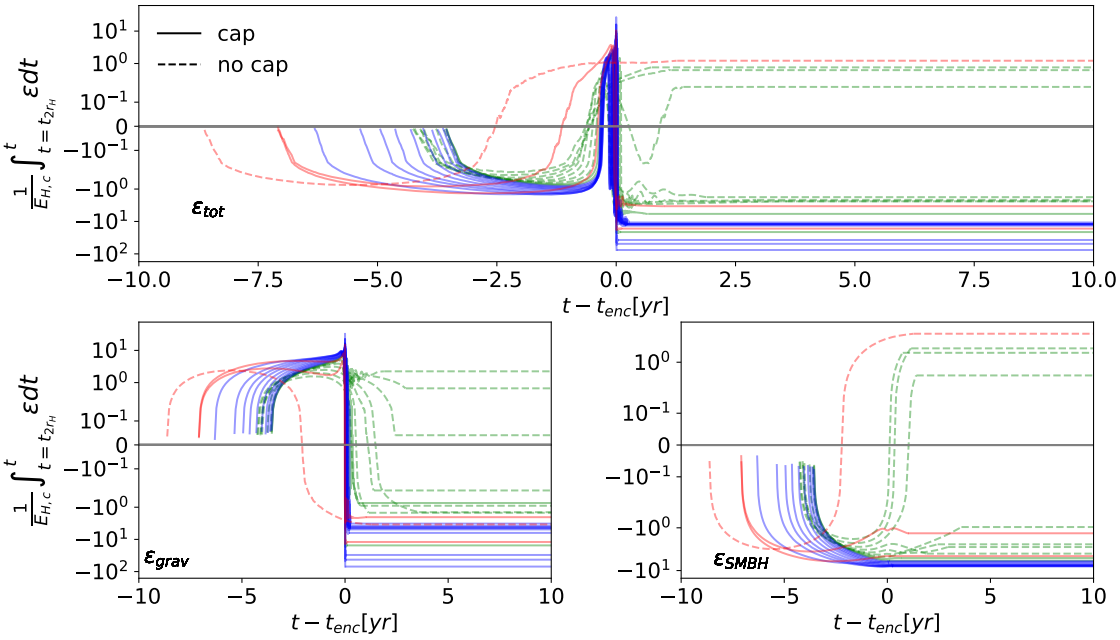

Figure 5.8: Cumulative energy change change in all the binaries from the no-accretion run during the first encounter from $2r_{\rm H}$ to apoapsis/exiting of Hill sphere. Results are colour-coded by encounter family; leftsided (red), rightsided (blue) and turnaround (green) encounters. The top panel shows the total cumulative energy change for all fiducial models. The cumulative energy transfer from the local gas gravity and SMBH are shown respectively on the left and right of the second row. The final cumulative value from the end point of the first encounter is artificially extended up to the ten year mark to more easily compare the net cumulative dissipation across models. Unsuccessful captures are shown in dashed lines and successful captures with solid lines. Turning off accretion leads to the replication of its effects in the dissipation from the local gas gravity.

cross section for accretionless encounters is then calculated to be $\lambda_{\rm noacc} = 0.92r_{\rm H}$ in the range $2.34r_{\rm H} < p < 3.26r_{\rm H}$, identical to the fiducial model.

The non-negligible effect of removing accretion is in the behaviour of $\varepsilon_{\rm grav}$ immediately after $t - t_{\rm enc} \approx 0$, shown in Figure 5.8. This occurs during the time frame we would expect the extremely negative energy dissipation from accretion at the first periapsis passage, $t - t_{\rm enc} \approx 0$. When accretion is removed, the time evolution of $\varepsilon_{\rm acc}$ in the fiducial simulations is reproduced in $\varepsilon_{\rm grav}$, demonstrating a highly efficient period of energy removal from the binary after $t - t_{\rm enc} \approx 0$, driving the cumulative dissipation to negative values. More formally, the time evolution of $\varepsilon_{\rm grav}$ without accretion mimics the rapid transition from positive to negative values observed in $\varepsilon_{\rm acc}$ in the accretion simulations. This is more akin to the

findings of Li et al. (2022a) where gravity acts to add energy prior to periapsis then reverses afterwards, resulting in a net energy removal. This is not present when accretion is enabled because accretion can alter the gas morphology close to the binary. When accretion is switched off, gas that would normally be accreted upon entering $r_{\rm acc}$ can instead pass around the BH. Alternatively, in the frame of the BH, the accretion headwind felt by the BH can now pass directly through the accretion boundary and accumulate behind the BH. To visualise this, we can calculate a surface density plot of the dissipation rate, averaged over the first encounter, from the local gas gravity $< d\varepsilon_{\rm grav}/dA >$ and show this alongside the radially integrated cumulative dissipation over the first encounter period in Figure 5.9 for an accretionless and accretion enabled simulation case. Figure 5.9 shows, as expected, that the morphologies are largely similar prior to the closest approach in the simulations with and without accretion. In the accretionless simulation there is a density buildup within the softening radius of the gas's gravitational effect on the satellites, $r_{\rm soft}$ though this is largely axisymmetric and does not strongly affect the binary trajectory at this moment. Just before and after the periapsis passage there are dense gas clumps behind each BH in the accretionless encounters where the gas has passed around the BH and accumulated behind them, similar to the wakes caused by dynamical friction.

Figure 5.10 shows a zoom-in on the cumulative work done by the gas gravity on the satellites in the simulations with and without gas accretion near the first periapsis passage. The dissipation from $\varepsilon_{\rm grav}$ oscillates violently over the close encounter period. This was first observed in Paper I and is a result of the formation of non-axisymetric, highly dense, inhomogeneities in the CSMDs from the BH tidal forces. As they orbit their respective BHs, the clumps tug on the BHs, resulting in a periodic oscillation in $\varepsilon_{\rm grav}$. The oscillations have an orbital frequency which is akin to a Keplerian orbit of $\sim 0.4 r_{\rm min,1}$. Though the strength of the oscillations in the binary energy warrants a discussion of the possibility they may have their own GW imprint on the encounter in a similar manner to other gas-induced GW signatures suggested in the literature (e.g. Kocsis et al., 2011a; Yunes et al., 2011; Hayasaki et al., 2013; Barausse et al., 2014, 2015; Cole et al., 2023; Nouri & Janiuk, 2023). However the characteristic frequency of the oscillations is typically of the order $\sim 10^{-7} - 10^{-6}$Hz which is unfortunately too low to be measured even with LISA.

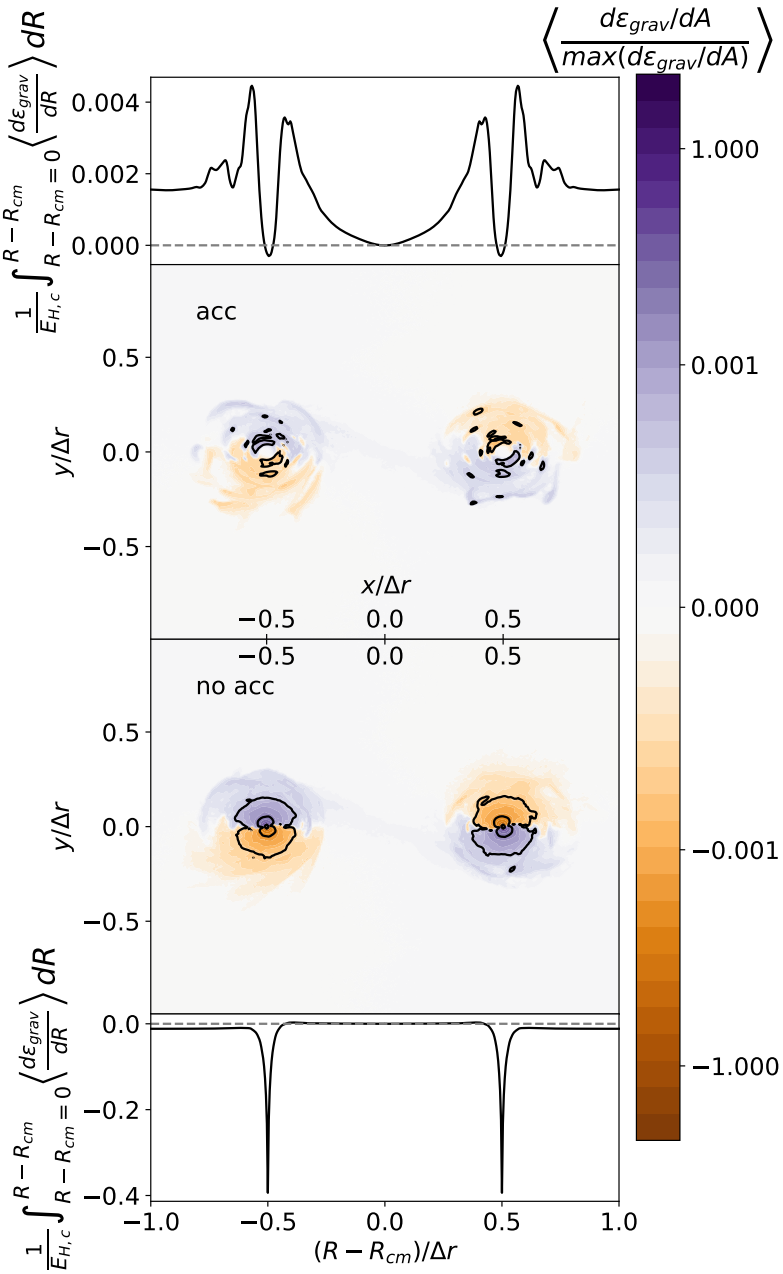

Figure 5.9: *Central two panels*: 2D average dissipation per area from gravitational interaction with the local gas (4.13) over the first encounter for a representative accretion-enabled (top) and accretionless (bottom) simulation with identical impact parameters. The map is centred on the COM $R_{\rm CM}$ of the binary and distances normalised to the current separation of the binary Δr. The dissipation is normalised to the max of both simulations to compare the relative strengths. The black lines show equal contours in each simulation, showing the enhanced dissipation close to the BHs in the accretionless case. *Top panel*: Average gravitational energy dissipation integrated from the $x-y$ COM radially outwards in the plane of the binary for the accretion-enabled case. *Bottom panel*: Same as the top panel but for the accretionless model. The radial and 2D maps are aligned so they can be directly compared along their axes. The binaries execute their orbit in a counter clockwise direction.

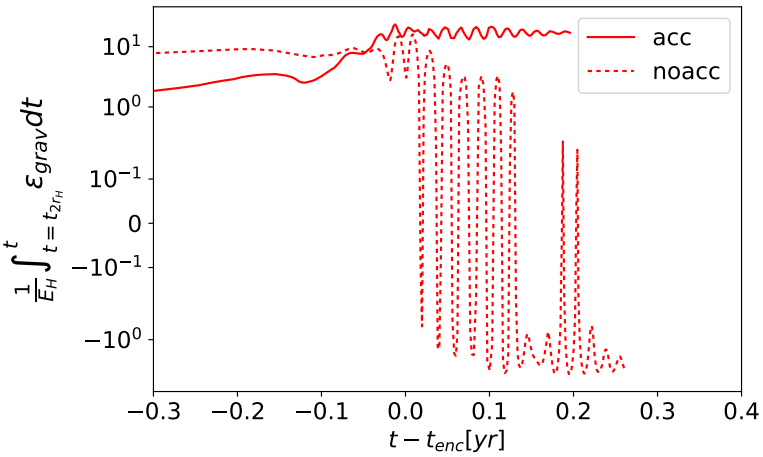

Figure 5.10: A zoom-in on the cumulative energy change of the simulations with gas accretion being enabled and turned off, respectively, in Figure 5.9 around the first periapsis passage. Artificially turning accretion off leads to far stronger oscillations in the work done on the binary, due to the stronger gravitational tug of the gas minidiscs.

The formation of these inhomogeneities is attributed to the tidal warping of the CSMDs being maximal at the periapsis of the encounter. This is further evidenced by the fact they form exactly during this part of the binary orbit (see Figure 5.10). The characteristic orbital radius of the inhomogeneities is therefore unsurprising as the BHs do not pass within $0.5r_{\min,1}$ of each other's CSMDs, so the gas in these regions is better retained around their original BH following periapsis. Thus gas can remain at high densities within distances smaller than the periapsis separation (i.e. $|R - R_1| < 0.5r_{\min,1}$ for the inner BH).

The oscillating dissipation phenomenon from the inner CSMDs is present in both simulations with and without accretion, where the oscillations are larger in the latter case. The cumulative effect of the rapidly varying $\varepsilon_{\rm grav}$, is a net dissipation in the binary energy by the time of the first apoapsis passage. In the simulations with accretion, this is net positive in most cases, i.e. the binary gains energy and becomes less bound, in agreement with the previous results in Paper I. In contrast, in the accretionless simulations, the net dissipation is significantly negative. This is the result of the allowed permeation of what would have been the accretion radius in the previous accretion enabled simulations by the gas. Gas that would normally accrete *against* the BHs motion (see Figure 5.5) and produce

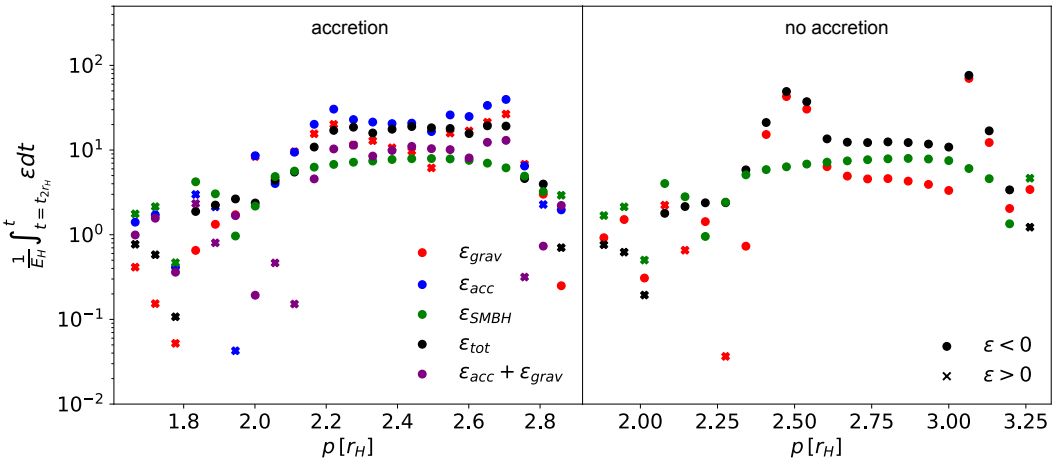

Figure 5.11: Net energy change of the binaries over their first encounters, comparing the fiducial simulations where gas accretion is possible (left) to the simulations where accretion is turned off (right). The net contributions from different physical processes are shown with different colours. In the accretion-enabled panel, also shown is the strength of $\varepsilon_{\rm grav} + \varepsilon_{\rm acc}$ to compare with $\varepsilon_{\rm grav}$ in the accretionless simulations. When accretion is turned off, the sign of the net gravitational dissipation switches from positive to negative. Though accretion is the most efficient remover of energy, its omission only changes the dissipation by roughly a factor two. This indicates that it fairly accurately models the net dissipation from $\varepsilon_{\rm acc}$ contributions near the accreting boundary. In otherwords one may neglect accretion and retain fairly similar results qualitatively.

the strong negative dissipation instead accumulates behind the BH. While the CSMDs perturbations are still present, this permeation leads to a net removal of binary energy via gravitational drag.

Figure 5.11 directly compares the net contribution of various physical processes to the binary energy dissipation during the first encounter. As shown, artificially removing the accretion leads to qualitatively similar behaviour, with the RS encounters dissipating the most energy, where now it is dominated by $\varepsilon_{\rm grav}$ and $\varepsilon_{\rm SMBH}$ instead of $\varepsilon_{\rm grav}$ and $\varepsilon_{\rm acc}$. While enabling accretion significantly alters the impact parameter dependence of the integrated $\varepsilon_{\rm grav}$,the relative strength of the gas effects is similar across the range of impact parameters when comparing $\varepsilon_{\rm acc} + \varepsilon_{\rm grav}$ to $\varepsilon_{\rm grav}$ in simulations with and without accretion. This suggests that although the dominant dissipation term shifts from gas gravity to accretion when accretion is enabled, it preserves the overall expected time-dependent variance and strength of the overall dissipation at least to within a factor of few.

5.3.5 Dependence on different accretion disc densities

Now consider BH scatterings in a 3 times higher density environment than in the fiducial model but otherwise identical initial conditions so that the disk mass is $M_{\rm d} = 3M_{\rm d,0}$. This includes the modelling of accretion as in the fiducial simulations. This suite is comprised of 45 simulations, 6 more than the fiducial run to span the larger space of impact parameters for hard encounters. Figure 5.12 compares the encounter depth vs impact parameters. The window of captures in p is greatly enhanced with additional gas. This matches the conclusion of DeLaurentiis et al. (2022), Li et al. (2022a) and the sibling paper; Whitehead et al. (2023a). The added gas also has the effect of shifting the 'valley' of the encounter depths to higher impact parameters. This explains the differences in encounter depths across the three AGN disc densities considered in Paper I for fixed impact parameter.

There are two effects causing this shift. First, the increased mass buildup in the CSMDs (which can effectively be added to the BH masses when they are sufficiently far away) means the BHs are perturbed earlier along their orbit. Secondly, accretion causes the Hill sphere of the objects to increase on their approach to each other. The accretion dependence of the window in the bottom panel is removed by normalising the cross sections to the Hill sphere of the BHs when they intersect twice each others Hill radii, $r_{\rm H_{2H}}$, instead of their initial Hill radii, $r_{\rm H_{t=0}}$. These re-normalised cross-sections are denoted with a tilde. The re-normalised cross section $\tilde{\lambda}$ is then

$$\tilde{\lambda}\left(N_e \geq 2\right) = \sum_i \frac{1}{2} \Delta\tilde{\lambda}_i I_{[N_e \geq 2]}(N_{e,i})\,, \tag{5.10}$$

where $\Delta\tilde{\lambda}$ is calculated as

$$\Delta\tilde{\lambda}_i = \frac{1}{2}\left(p_{\rm i+1}\frac{r_{\rm H_{t=0}}}{r_{\rm H_{2H}}} - p_{\rm i}\frac{r_{\rm H_{t=0}}}{r_{\rm H_{2H}}}\right)\,. \tag{5.11}$$

This centres the windows perfectly, showing that accretion is responsible for the shifting of the window. However, the overall window of the encounters is still larger, where the two troughs are further apart as well as the RS and turnaround encounter regions occur at lower and higher impact parameters, respectively. Additionally, captures successfully take place at shallower initial encounter depths, even when $r_{\rm min,1} > 0.1$ unlike in the fiducial model. This evidence points to encounters in AGN discs with higher densities being more favourable for binary formation; allowing

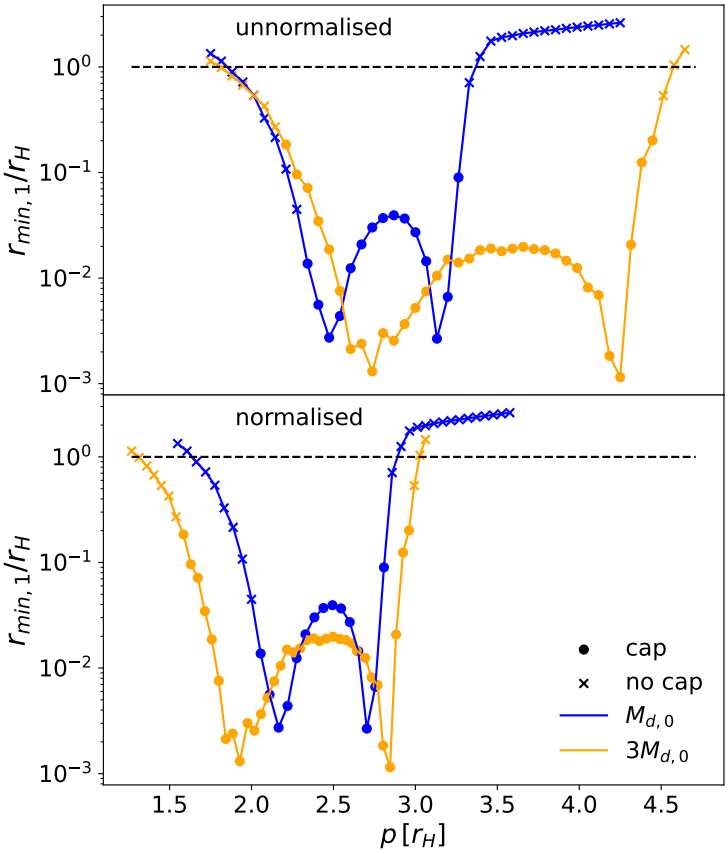

Figure 5.12: Minimum separation for the fiducial run (blue) compared to the $3M_{\mathrm{d},0}$ run (orange) for the first approach as a function of the initial radial separation p. On the top row is the unaltered initial form of the curve. On the bottom is the same two curves, where the minimum separations are now normalised to the size of the Hill sphere when the binaries reach $2r_{\mathrm{H}}$ in separation. The normalisation process is described by Eq. (5.10).

model	λ	$\tilde{\lambda}$	$\tilde{\lambda}/\tilde{\lambda}_{fid}$
fiducial	0.98 ± 0.13	0.86 ± 0.11	1
no gas	0.0407 ± 0.0011	0.0407 ± 0.0011	1.00 ± 0.13
$3\times$ gas density	2.30 ± 0.19	1.59 ± 0.13	1.81 ± 0.28
no-accretion	0.92 ± 0.19	0.80 ± 0.13	0.93 ± 0.25

Table 5.2: 1D cross sections λ in the space of the impact parameter p as calculated by Eq. (5.5) for successful binary formation. These values quantify formally the range in p that permits binary formation. Shown from left to right are the different simulation suites, the standard cross section λ, the accretion normalised cross sections $\tilde{\lambda}$ (see Eq. 5.10), and the ratio of the normalised cross sections to that of the fiducial simulation suite.

binaries more sparsely separated to have stronger encounters and affording binaries with weaker encounters a greater chance for formation.

Figure 5.13 shows the contributions of the different physical processes to the satellite energy dissipation and the torques over the first encounter and per source over time. Qualitatively, the overall trend is the same initially. Dissipation is initially negative due to the SMBH, before rapidly peaking positive just prior to encounter due to gas gravity followed by a sharp drop due to strong negative dissipation from accretion. The torque behaviour is also preserved from the fiducial model with the SMBH dominating the torque in the negative direction for nearly all models. The gas gravity and accretion induces negative torques in the TA encounters, gradually flipping to positive torque across the window of LS encounters ($p = 2r_{\rm H} - 2.8r_{\rm H}$) and inducing significantly positive torques for RS encounters. While the behaviour of the dissipation mechanisms is unchanged from the fiducial model, the strength of the dissipation and torques from both accretion and gas gravity are around a factor of $3\times$ larger (see Figure 5.14 for clarity). For the torques this is less impactful as the SMBH still dominates by a factor of a few. However, the increased dissipation indicates that more energy can be dissipated in higher gas density environments. Note that this is independent of any enhanced mass gain by the BHs as the energy unit normalisation $E_{\rm H,c}$ and its reduced mass μ dependence is calculated for each model. The capture cross section reflects this favourability, with a value of $\tilde{\lambda}_{3M_{\rm d}} = 1.591$. Table 5.2 summarises the normalised and unnormalised cross sections from each of the simulation suites. Recall from Figure 5.2 that the

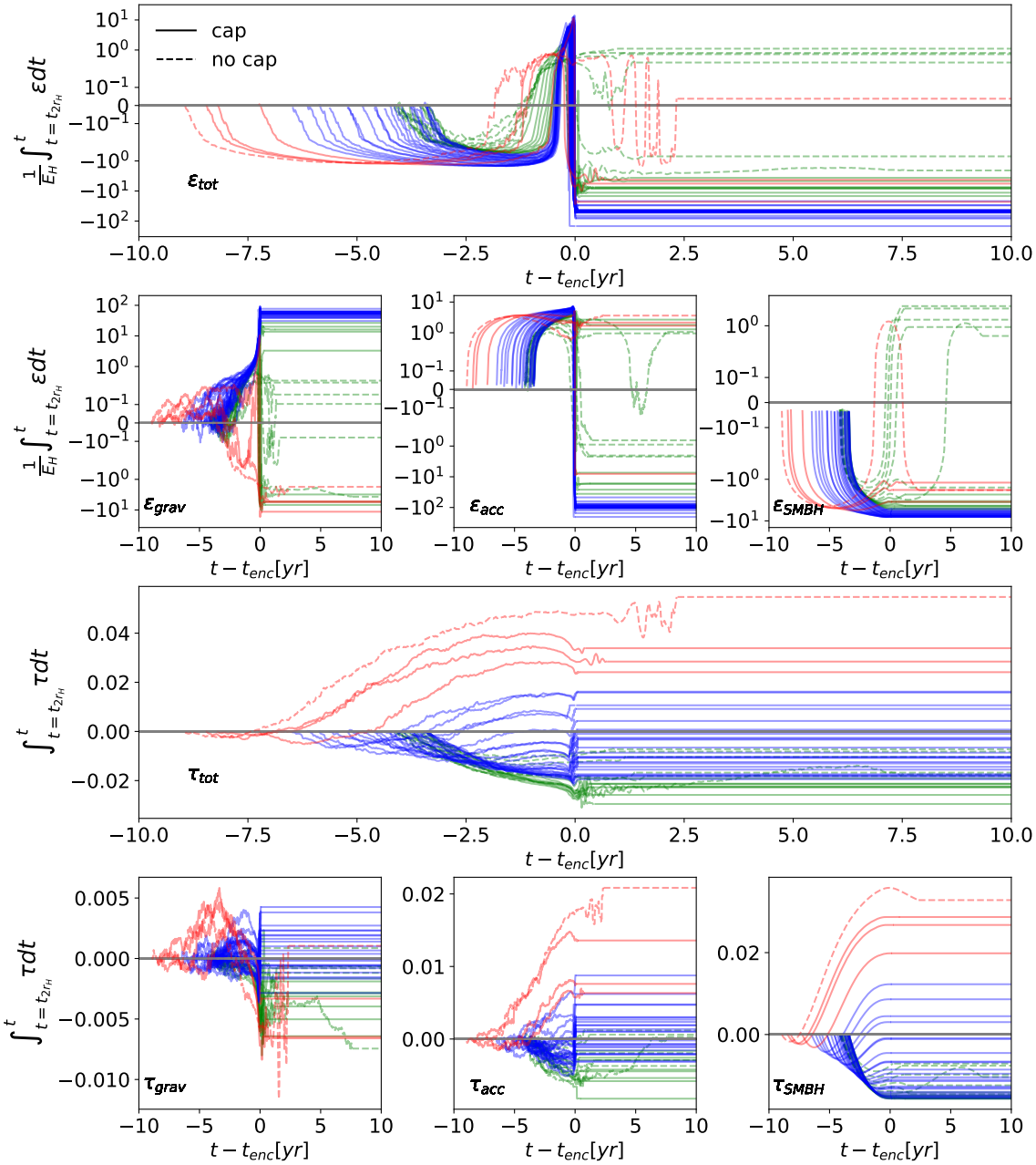

Figure 5.13: Cumulative energy and angular momentum change in all the binaries from the run with three times the AGN disc density ($3M_{\rm d,0}$) during the first encounter from $2r_{\rm H}$ to apoapsis/exiting of Hill sphere. Results are colour-coded by encounter family; rightsided (red), leftsided (blue) and turnaround (green) encounters. The top panel shows the total cumulative energy change for all fiducial models. The cumulative energy transfer from the local gas gravity, accretion and SMBH are shown respectively from left to right of the second row. The cumulative torque is shown on the 3rd row, with the breakdown from the three dissipation mechanisms similarly displayed in row 4. The final cumulative value from the end point of the first encounter is artificially extended up to the ten year mark to more easily compare the net cumulative torque across models. Unsuccessful captures are shown with dashed lines and successful captures with solid lines. The enhanced gas density does not change the form of the dissipation or torques but increases their strengths.

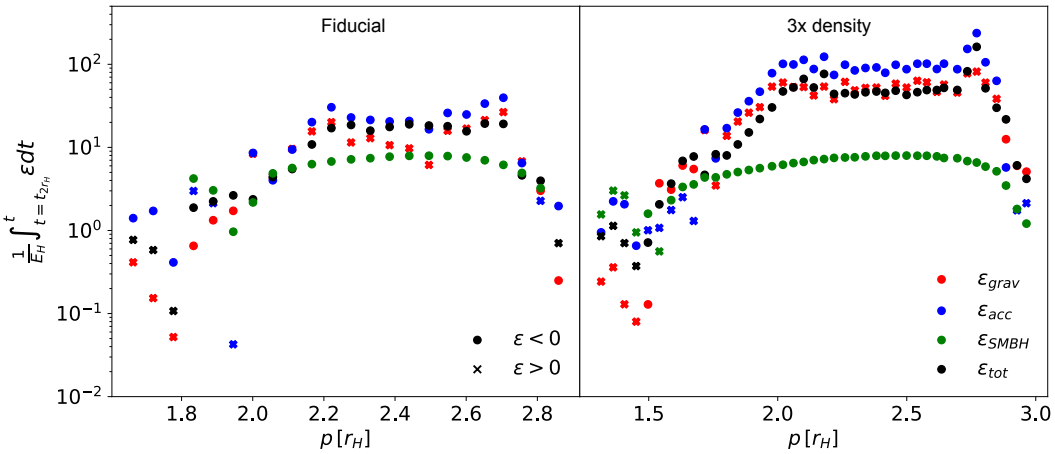

Figure 5.14: Net energy change of the satellites over their first encounters, comparing the fiducial simulations (left) to the $3M_{\mathrm{d},0}$ enhanced disc density simulations (right). Also shown are the net contributions from each dissipation mechanism. The enhancement of the dissipation from the increased ambient density is clear in the rightsided encounters (see Figure 5.5 for definition) in the central flat plateau of the encounter window, showing on average approximately three times greater energy dissipation.

depth of the first encounter greatly affects the orbital energy dissipation of the binary for simulations with fiducial disc model with different impact parameters. Figure 5.15 shows the energy dissipation vs closest approach for all the simulations, including those with an increased disk mass and those where accretion is turned off. Compared to the fiducial model, the density enhancement and removal of accretion leads to a steeper dependence of the energy dissipated with the periapsis distance $r_{min,1}$. Additionally, if we compare the coefficients, a, one can quantify the average energy dissipation increase with density. With a value of $3.48/1.28 = 2.69 \pm 1.33$ this corresponds to a scaling with the disc density Σ of $\Delta E_{\mathrm{bin}} \propto \Sigma^{0.9\pm0.44}$ close to the prediction from the other paper Whitehead et al. (2023a) that finds dissipation scales with density to the power of unity, albeit with a considerable error margin here.

5.3.6 Parameter space of captures

While analytic and semi analytic studies of BH binary population synthesis in AGN (e.g. Miralda-Escudé & Gould 2000; Freitag et al. 2006; Hopman & Alexander 2006; Bartos et al. 2017b; Rasskazov & Kocsis 2019; Secunda et al. 2019; Tagawa et al. 2020a; McKernan et al. 2020a) are well suited for simulating the large BH population in AGN, they currently utilise very simplistic assumptions for the

outcome of an encounter, oversimplifying the complex interactions with the gas. A revised, more physically motivated set of analytical tools for deducing the outcome of an encounter would provide far more realistic and reliable estimators for the binary formation rate which is essential for estimating the BH merger rate for GW astronomy. While an expression relating dissipation and encounter depth has been numerically derived, the encounter depth itself is affected non trivially by the gaseous effects. A more useful expression may be obtained if one ascertains a parameter space for captures using encounter parameters that are not largely affected by the complex gas morphology of the encounter itself. Two such parameter spaces are considered, starting with the the binary relative energy at the start of the encounter $E_{2\mathrm{H}}$ at $2r_{\mathrm{H}}$ and the impact parameter of the binary at the Hill radius $p_{1\mathrm{H}}$. These quantities are defined specifically in Eq. (5.12) and Eq. (5.13) respectively

$$E_{2\mathrm{H}} = \frac{1}{2}\mu\|\boldsymbol{v}_1 - \boldsymbol{v}_2\|^2 - \frac{GM_{\mathrm{bin}}\mu}{2r_{\mathrm{H}}}\,, \tag{5.12}$$

$$p_{1\mathrm{H}} = r_{\mathrm{H}}\sqrt{1 - \left(\frac{(\boldsymbol{v}_2 - \boldsymbol{v}_1)\cdot(\boldsymbol{r}_2 - \boldsymbol{r}_1)}{\|\boldsymbol{v}_2 - \boldsymbol{v}_1\|\,\|\boldsymbol{r}_2 - \boldsymbol{r}_1\|}\right)^2}\,, \tag{5.13}$$

where Eq. (5.12) is equation Eq. (5.7) evaluated when the binaries are at $2r_H$ separation. As before, $\boldsymbol{r}_i$ and $\boldsymbol{v}_i$ are the positions of the satellite BHs $i = (1, 2)$. $M_{\mathrm{bin}} = M_1 + M_2$ is the mass of the outer binary and $\mu = M_1M_2/M_{\mathrm{bin}}$ is its reduced mass. To reiterate, Eq. (5.12) is evaluated when the binary separation first reduces to $2r_{\mathrm{H}}$ and Eq. (5.13) is evaluated when the separation reaches r_{H}. One might consider using the energy at $2r_{\mathrm{H}}$ but the impact parameter at r_{H} an odd choice for the parameterisation. However, as shown in Figures 5.5, 5.8 and 5.13 the energy exchange of the binary becomes important at scales beyond the Hill radius. Although the dissipation from $2r_{\mathrm{H}}$ is important for determining the outcome, no binary formation occurs beyond $p_{1\mathrm{H}} \gtrsim 0.68r_{\mathrm{H}}$. Thus in semi-analytical studies, one needs only consider binaries entering a single Hill radius and have access to $E_{2\mathrm{H}}$ and $p_{1\mathrm{H}}$ to determine the scattering outcome.

Before constructing the analytic tool for predicting the energy dissipated, we first have to understand how much energy must be lost. Figure 5.16 shows the total energy of the binary after the first encounter, E_{f} (again defined at apoapsis or on return to a separation of r_{H}). In Figure 5.16, a very clear parameter space for successful binary formation emerges. At the bottom of the parameter space there is

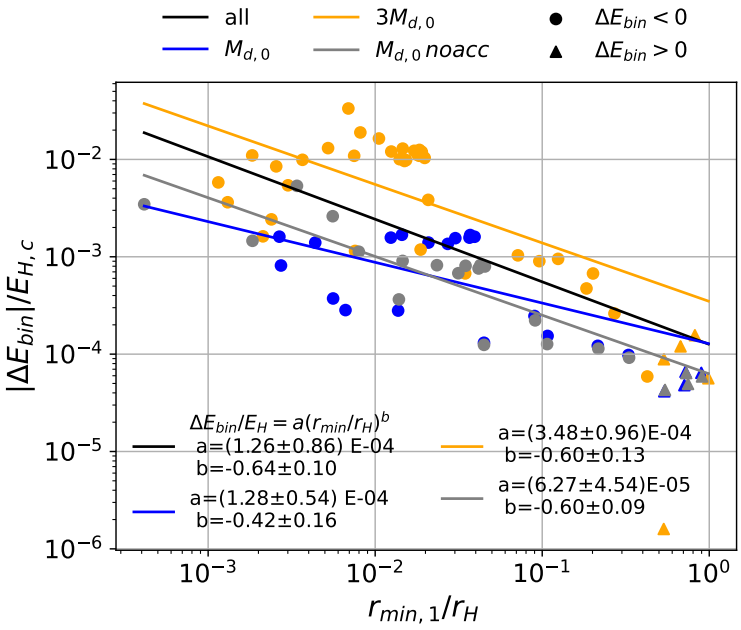

Figure 5.15: Energy change in the binaries, normalised to $E_{\rm H,c}$, during the first encounter as a function of the first periapsis $r_{\rm min,1}$ as in Figure 5.2 but for all simulations including those with an increased disk mass and those where accretion is turned off. Dotted points indicate where energy is removed to the binary while triangular points represent models where energy is *added*. Only binaries that pass within $r_{\rm H}$ are shown. Also shown in the same colour as the raw data are the power-law fits for the fiducial $M_{\rm d,0}$ (blue), $3M_{\rm d,0}$, accretionless $M_{\rm d,0}$ and whole sample (black).

an island of failed captures, where for $p_{\rm 1H}/r_{\rm H} \gtrsim 0.68$ energy is added to the binary. In the other failed capture region where $p_{\rm 1H}/r_{\rm H} \lesssim 0.68$, this means the binary did not dissipate enough energy to be sufficiently hard so as not to be decoupled by the SMBH. The slope in the boundary between each island implies that before first periapsis, a binary with identical initial energy must dissipate more to remain bound if its impact parameter is higher. This is no doubt due to correlation between $p_{\rm 1H}$ and the encounter depth $r_{\rm min,1}$, which is confirmed in Figure 5.17. The sloped boundary is defined as the function $E_{\rm f,crit}(p_{\rm 1H})$, shown below in Eq. (5.14).

$$\log_{10}(E_{\rm f,crit}/E_{\rm H,}c) = 1.31\frac{p_{\rm 1H}}{r_{\rm H}} - 4.34 \tag{5.14}$$

Next, scaling between $p_{\rm 1H}$ and $r_{\rm min,1}$ is determined, which is accurately informed by the full hydrodynamical approach and therefore includes the effects and stochasticity introduced by the gas. The function for $r_{\rm min,1}$ in terms of $p_{\rm 1H}$ (see Eq. 5.15) alongside the data in Figure 5.17.

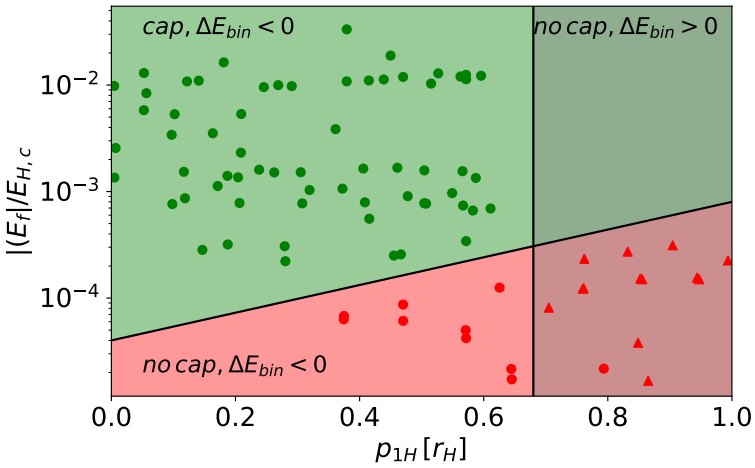

Figure 5.16: Orbital energy, in units of the energy of a circular orbit at the Hill sphere $E_{\mathrm{H,c}}$, of the binaries after the first encounter (either when executing first apoapsis or upon leaving the Hill sphere if unbound), E_{f} vs their impact parameter at one Hill radius $p_{1\mathrm{H}}$ as defined in (5.13). The results show three distinct regions of parameter space, 1) where binaries successfully form through sufficient energy dissipation, 2) where binaries dissipate energy but not sufficiently to remain bound and 3) where binaries decouple through energy gained during the encounter. The function of the positively sloped line separating the successful from unsuccessful formations is the critical final energy, $E_{\mathrm{f,crit}}$, needed to remain bound, represented by the log-linear function in Eq. (5.14).

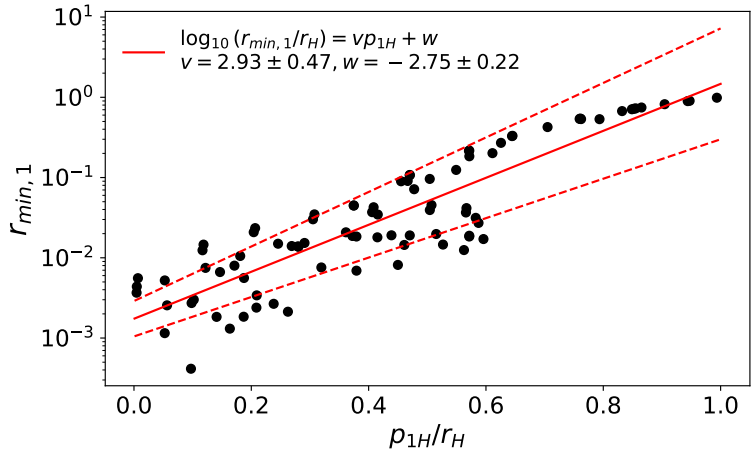

Figure 5.17: First encounter periapsis scattered against the impact parameter at one Hill radius $p_{1\mathrm{H}}$ (Eq. 5.13) for all simulations, showing that smaller impact parameters lead to closer encounters, with some scatter for lower values of $p_{1\mathrm{H}}$ where the very small periapses becomes increasingly sensitive to small changes in energy. Also shown is the log-linear line of best fit (solid red) and its error (dashed red) according to Eq. (5.15).

$$\log_{10}(r_{\mathrm{min},1}/r_{\mathrm{H}}) = v\frac{p_{1\mathrm{H}}}{r_{\mathrm{H}}} - w \tag{5.15}$$

with constants $v = 2.93 \pm 0.47$ and $w = -2.75 \pm 0.22$. This relation can then be inserted into (5.9) to obtain the function $\Delta E_{\mathrm{bin}}(p_{1\mathrm{H}})$.

Using the fits of the $\Delta E_{\mathrm{bin}}(r_{\mathrm{min},1})$ relation to each simulation suite, one constructs the parameter space of $p_{1\mathrm{H}} - E_{2\mathrm{H}}$ that allows for binary formation in Eq. (5.16)

$$\frac{E_{2\mathrm{H}}}{E_{\mathrm{H,c}}} < \left(\frac{E_{2\mathrm{H}}}{E_{\mathrm{H,c}}}\right)_{\mathrm{crit}} = E_{\mathrm{f,crit}}(p_{1\mathrm{H}}) - \Delta E_{\mathrm{bin}}(p_{1\mathrm{H}})\,. \tag{5.16}$$

In simple terms, this equation calculates the critical final energy required to remain bound based on the impact parameter $p_{1\mathrm{H}}$ and subtracts how much energy it was expected to dissipate based on the same impact parameter to calculate its expected energy at $2H$. Therefore, it calculates the expected energy at $E_{2\mathrm{H}}$ that would allow a binary to remain bound for its impact parameter $p_{1\mathrm{H}}$. In explicit form, both the first and second term take on power laws. When all constants combined and simplified this gives:

$$\frac{E_{2\mathrm{H}}}{E_{\mathrm{H,c}}} < \left(\frac{E_{2\mathrm{H}}}{E_{\mathrm{H,c}}}\right)_{\mathrm{crit}} = \overbrace{-10^{k_1\frac{p_{1\mathrm{H}}}{r_H}+c_1}}^{E_{\mathrm{f,crit}}(p_{1\mathrm{H}})} + \overbrace{10^{k_2\frac{p_{1\mathrm{H}}}{r_H}+c_2}}^{-E_{\mathrm{bin}}(p_{1\mathrm{H}})}\,. \tag{5.17}$$

The constants for this equation are determined for all of the simulations suites collectively and individually and display them in Table 5.3. According to the criterion, a BH-BH scattering will result in a successfully formed binary if the following is true

$$\left[\frac{E_{2\mathrm{H}}}{E_{\mathrm{H,c}}} < \left(\frac{E_{2\mathrm{H}}}{E_{\mathrm{H,c}}}\right)_{\mathrm{crit}}\right] \wedge \left[p_{1\mathrm{H}} < 0.68 r_{\mathrm{H}}\right]. \tag{5.18}$$

This new expression meets the aim of being independent of any variables that could be affected by the complex hydrodynamics of the encounter and since the energy is normalised to $E_{\mathrm{H,c}}$ it is also independent of the binary mass, thus is insensitive to any mass buildup due to accretion *before* the encounter. The construction the binary formation criterion is summarised in short steps below. Applying the criterion to the data (see Figure 5.18), the figure shows three distinct regions:

1. The already known region of zero binary formation at $p_{1\mathrm{H}} \gtrsim 0.68$.

2. The region of successful binary formation under the curve where the binary can remove enough energy to remain bound and unperturbed by the SMBH.

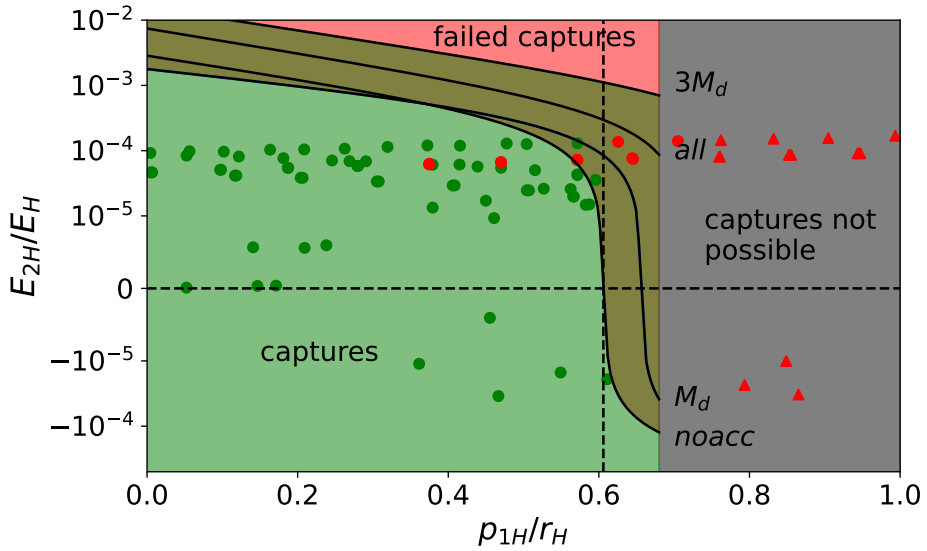

Figure 5.18: Encounter energy at two Hill radii, $E_{2\mathrm{H}}$, for all the models as a function of their impact parameter as measured at $p_{1\mathrm{H}}$ and the analytically derived parameter space for captures. The red area highlights where I expect failed captures due to a lack of sufficient energy removal. The green area is the parameter space where I expect successful captures. The grey area presents a firm barrier to capture as energy is added to the binaries in this region which don't pass deep into each other's Hill sphere. The overlapping red and green area is the area of the parameter space where the outcome depends on the simulation suite. The boundary of the successful formation region for each suite is traced by the black curves and labelled in the plot, calculated via Eq. (5.16).

3. The region above the curve where the binary was too energetic to dissipate enough energy to form a stable binary.

The vertical dashed line indicates the transition to where the binary must already have a negative two-body energy to remain bound for the fiducial model. The curves that separates the successful and unsuccessful captures are the criterion Eq. 5.17 calculated for each suite using the corresponding a and b values. The methodology of the capture criterion is summarised in the following numbered steps for a mock encounter between two BHs:

Summary of Binary Formation Criterion

Step I Verify that the two BHs had an encounter with a separation of less than their Hill radius (Eq. 2.14).

Step II Determine the BHs' two body energy at a separation of two Hill radii, $E_{\rm 2H}$, using Eq. (5.12).

Step III Determine the binary's impact parameter at separation of one Hill radii, $p_{\rm 1H}$, using Eq. (5.13).

Step IV Use the impact parameter $p_{\rm 1H}$ to determine the close approach distance $r_{\rm min,1}$ using Eq. (5.15).

Step V Determine the expected energy dissipation, $\Delta E_{\rm bin}$, with Eq. (5.9) using $r_{\rm min,1}$.

Step VI Calculate the minimum energy $E_{\rm f,crit}$ required to stay bound via Eq. (5.14) using $p_{\rm 1H}$.

Step VII Determine if the energy dissipation criteria, Eq. 5.17 is satisfied using $E_{\rm f,crit}$, $\Delta E_{\rm bin}$ and $E_{\rm 2H}$, using the constants for Eq. 5.17 provided in Table 5.3.

While this criterion is a significant improvement, it naturally still makes assumptions. These include its assumption of only 2D encounters and equal mass ratios for the two BHs. Further work is needed to determine generalisations for non-coplanar encounters misaligned with the AGN disc, and for asymmetric mass ratios. Additionally, the relationship may be depend on the mass of the BHs, since it is not yet verified that the mass of the minidiscs scales one to one with the BH mass. Given a large portion of the dissipation in rightsided encounters comes from colliding minidiscs, alternate ratios of minidisc to BH masses due to differing BH masses could affect the amount of energy dissipated in the same manner as changing the ratio via changing the AGN disc density.

The accuracy of the formation criterion is assessed in Figure 5.19 by breaking it down by suite and also showing the errors in the curves. Counting the false positives and false negatives in each suite it has predictive success rating of 94%, which for the errors in b and a of eq (5.9) is remarkable. While the criterion is dependent on the AGN disc density (based on the curves in Figures 5.18 & 5.19),

	k_1	c_1	k_2	c_2
$M_{\rm d,0}$	1.31	-4.34	-1.74	-2.52
$3M_{\rm d,0}$	1.31	-4.34	-2.48	-1.57
noacc	1.31	-4.34	-1.60	-2.65
all	1.31	-4.34	-2.21	-2.02

Table 5.3: Fit parameters for Eq. 5.17 for the $M_{\rm d} = M_{\rm d,0}$, $M_{\rm d} = 3M_{\rm d,0}$ and accretionless simulations, also shown is the average fit using all the simulations.

the relation only holds for the expected mean AGN density for the parameters and the inflated 3x density model. A more formal parameter sweep in the density would allow the relation to hold for arbitrary or at least a range of AGN densities, which is the subject of the sibling paper, Whitehead et al. (2023a).

5.4 Discussion

5.4.1 Implications for mergers

Given the high efficiency with which binaries form in the simulations and that most of them are retrograde, combined with the result from Paper I that retrograde binaries have a non-negligible merger rate, it would appear that overall the AGN channel is highly conducive to BBH mergers. In reality however, there is also non-zero radial and vertical velocity dispersion in the stellar mass BH population in AGN that is not incorporated in this work. The additional vertical component will naturally lead to interactions outside of the midplane where the gaseous background is less dense, leading to a lower probability of capture as indicated here, in Paper I and in Li et al. (2022a). Additionally, little is known of what gas morphology we should expect around satellites in an AGN disc with less idealistic configurations (i.e. co-planar and with circular orbits). One could expect encounters with BHs that have entered from outside or at the extremities of the AGN disc will involve less gas since they cannot replenish gas lost from their Hill sphere to the SMBH as quickly or at all prior to the encounter (Kratter et al., 2010; Kocsis et al., 2011a). Though this additional aspect to the problem will likely reduce the chance for binary formation and mergers, it is expected that the inclination of objects will decrease

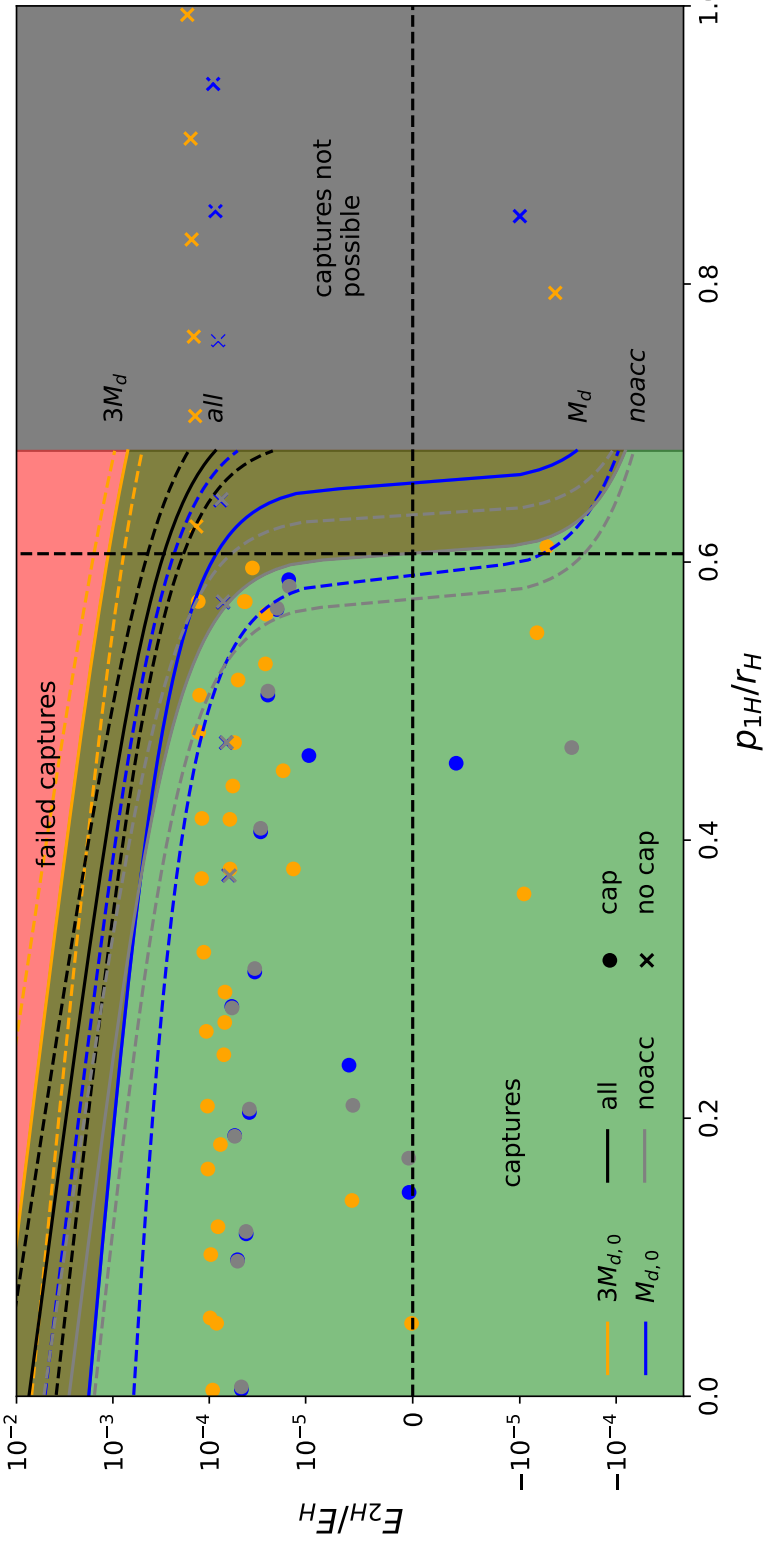

Figure 5.19: Encounter energy at two Hill radii, E_{2H}, as in Figure 5.18 but for all simulations including those with an increased disk mass and those where accretion is turned off as a function of their impact parameter as measured at p_{1H} overlaid on the analytically derived parameter space. The red area highlights where captures fail due to a lack of sufficient energy removal. The green area is the parameter space that leads to successful binary formation. The grey area presents a firm barrier to capture as energy is added to the binaries in this region which don't pass deep into each other's Hill sphere. The overlapping red and green area is the area of the parameter space where the outcome depends on the simulation suite. The boundary of the successful formation region for each suite is traced by the solid colour-coded curves according to the simulation suite. The dashed curves span the error range of the boundary region. Out of 115 simulations, there are only 5 outliers. The horizontal and vertical dashed lines highlight the point where accretionless encounters that already have a negative two body energy still need to dissipate energy further to remain bound.

significantly over the lifetime of the AGN due to dynamical friction (e.g. Tagawa et al., 2020a; Generozov & Perets, 2023) between the satellites and the SMBH disc.

Based on the density dependence of the capture criterion (Eq. 5.17) favouring higher densities this would suggest a bias towards the formation and merger of BH binaries closer to the SMBH according to Eq. (4.1). However there is the competing factor of the velocity shear of the satellites, which is more pronounced closer to the SMBH. An increased shear increases the value of $E_{\rm 2H}$ which is calculated via Eq. (5.7) by enhancing $v_{\rm rel}^2 = \|\boldsymbol{v}_1 - \boldsymbol{v}_2\|^2$. If we assume the radial density dependence $R^{-0.6}$ of Eq. (4.1) used here, and that $v_{\rm rel}^2 \propto R^{-1}$ then whether BH binaries are more likely to form closer or further from the SMBH depends on the steepness of the exponent of Eq. (5.17) with Σ (the surface gensity of the gas, Eq. (4.1)). For the binary formation probability to be independent of R then it would require the dissipation in the first encounter to scale as $\Delta E_{\rm bin}/E_{\rm H,c} \propto \Sigma^{1.6}$. Here the dependence is narrowed down to $\Sigma^{0.90\pm0.44}$. In conjunction, the wind tunnel simulations of Whitehead et al. (2023a) narrow this slope down to 1.01 ± 0.04. Thus one would expect the probability, $P(R)$, of a highly co-planar BH-BH strong encounter ($r_{\rm min,1} < r_{\rm H}$) forming a binary successfully to scale approximately $P(R) \propto R^{-0.6}$. Hence we would expect BH binaries to form more easily closer to the SMBH.

5.4.2 Comparison to similar studies

The work of this chapter is a natural extension of the pure 3-body results of Boekholt et al. (2023). In Boekholt et al. (2023), three-body scatterings of BHs orbiting a SMBH were performed using a purely N-body approach. In the absense of gas, the simulations showed the formation of temporary BH binaries, where binaries with more than 2 encounters are possible for a smaller range of impact parameters, though they are short lived. The range of impact parameters that lead to higher encounters numbers becomes exponentially smaller for each additional encounter. Whether they have a deep enough encounter for GWs to induce mergers is dependent on the chaotic evolution of the 3-body system, which can only rarely lead to these chance extremely close encounters. Aside from these extreme cases the lack of a dissipation mechanism leads to their eventual disruption by the SMBH, with probability of surviving multiple N encounters dropping off rapidly with N (e.g. Li et al., 2022d; Boekholt et al., 2023). As shown in this work, the inclusion of

gas leads to the formation of reliably hardened binaries in a single large window in impact parameter space, destroying the fractal structure observed in the paramater space of the impact parameter and number of encounters in Boekholt et al. (2023). This results from the inability of the binaries to switch orientations reliably after even one encounter due to the efficiency of the gas-induced energy dissipation enabling the binary to rapidly harden. DeLaurentiis et al. (2022) verify that at exceptionally low ambient gas densities, the fractal structure in the number of encounters vs impact parameter reappears in their 3-body scatterings that include semi-analytic dynamical friction. The recovery of the fractal structure at sufficiently low densities is also hinted in Whitehead et al. (2023a). Lower density encounters have a greater tendency to flip orientation, most commonly at the boundary between families. Although, the sampling is too course to make any reliable comment on the recovery of the fractal structure.

A closely related work to ours is the gas scattering experiments of Li et al. (2022a). In their 2D hydro study of embedded BH scatterings, which uses multiple density values, they show a roughly linearly increasing window in their impact window size as a function of initial ambient density. Instead of varying the radial separation they instead vary the initial azimuthal separation of their satellite BHs, which is possibly why they find nearly all binaries to be formed in a retrograde configuration. In this work, the azimuthal separation is scaled so the approach time for each simulation was identical. Using this alternate setup, both prograde and retrograde binaries form, with a larger cross section for retrograde encounters. Comparing the outcomes of the BH scatterings, there is good agreement in the dissipation mechanisms being positively correlated with the local gas density. There is also agreement that for lower AGN densities, the maximum allowed encounter energy is lower, as highlighted in the final figure of the paper, Figure 5.19.

Comparing to the recent semi-analytical studies, DeLaurentiis et al. (2022) consider three-body scatterings with an Ostriker dynamical friction prescription to account for gaseous effects. DeLaurentiis et al. (2022) find similar "island" regions of p to the purely gravitational study of Boekholt et al. (2023), where binaries may successfully form. With the inclusion of gas, only a single central valley of captures exists. Given they switch off their dynamical friction at the closest approach they neglect the subsequent dissipation between periapsis and their approach back

towards the Hill sphere, which can be significant, as shown in Figure 5.5 for example. This extra dissipation could harden the extremely low angular momentum encounters at the troughs that have the largest apoapses and naturally are more prone to being disrupted by the SMBH. Additionally they find increasing $M_{\rm d}$ leads to the formation window moving to lower p values which is the inverse of the findings here. Similarly to Li et al. (2022a), this discrepancy in the approach trajectories could be due to their azimuthal separation being far smaller than in this study.

In a sibling paper to this (Whitehead et al., 2023a), the same scenario posed in this paper is investigated using a shearing box model using the Eulerian grid code Athena++. The use of the new code allows us to compare the two different numerical approaches to the hydrodynamics and by using a shearing box, maintain a higher resolution inside the Hill sphere for less computational cost. Three is excellent agreement on several aspects of the BH-BH encounters. This includes the order of magnitude of dissipation expected for gas assisted encounters, which lies around $10-100$ times the energy of the binary upon reaching a separation of one Hill sphere. Also corroborated is the identification of the three encounter families that lie at low, moderate and high impact parameters, which have the orientations prograde, retrograde and prograde respectively (relative to the orbit about the AGN). The slope of $\Delta E/E_{\rm H,c}$ as a function of $r_{\rm min,1}/r_{\rm H}$ is also corroborated to within 10% percent of the values shown here. A larger sampling of $M_{\rm d}$ is performed in Whitehead et al. (2023a), which finds that at sufficiently low densities the single formation window splits down the centre into two separate islands of capture. Though the shape of the capture window in (Whitehead et al., 2023a) is identical to those here (i.e. a single window with three types of first encounter), the cross section and location of the window tends to be at lower values of p for the same AGN disc densities. However, comparing the size of the formation window of the global simulations here to the straight shearing box of (Whitehead et al., 2023a) directly is likely not reliable since the linear BH trajectories in the shearing box model will lead to different gravitational focusing during the initial approach.

5.5 Caveats

- In this chapter, only strictly co-planar encounters in the midplane of a 3D gaseous disk were considered, but in reality there is also a 3D distribution of BHs around AGN with some vertical velocity dispersion. Inclination has been shown by Li et al. (2022d) to reduce the likelihood of encounter, suggesting inclination in the initial BH orbits could alter the size of the capture windows shown here. As the study did not include gas, followup work is required to discern the inclination dependence more accurately.

- It is assumed the gas is sufficiently radiatively efficient that gas heating/thermal shocks do not significantly increase the gas temperature anywhere in the entire simulation domain. While this may be a good assumption for the main body of the annulus distant from the encounter, the high speed intersections of the accretion discs of the BHs will in practice lead to *significant* heating of their material due to their high density and relative velocity. Tagawa et al. (2022) show that even single BHs can provide a heating mechanism to the local gas through accretion driven jet outflows. Therefore I encourage future studies to include such effects if feasible.

- Despite the number of simulations shown here, we are still dealing with far fewer statistics than 3-body studies and recommend further simulations to further probe additional parameters that affect the dissipation processes.

- In addition to non inclined orbits, the BHs are initialised with only circular orbits around the SMBH. A more accurate nuclear BH population would include also include a radial velocity dispersion, i.e. orbits around the SMBH would have their own eccentricity as well, which would affect the energy of a binary going into an encounter.

- It has been shown gravitational dissipation and torques from the CSMDs during the encounter can be mimicked by the sinks' accretion, despite the accretion radius being far larger than its true value by many orders of magnitude. However there is still a factor of a few difference in the strength of these effects between some models. Additionally, as in Paper I, I find the accretion to be super-Eddington by several orders of magnitude. It is possible

that a more accurate handling of the accretion leads to results different to both the accretionless and accretion enabled results shown in this paper. However, accretion at such small scales necessitates extreme resolutions and the inclusion of radiative effects which becomes *extremely* computationally expensive.

5.6 Summary and Conclusions

Using a hydrodynamic numerical simulations, I performed a quantitative analysis of the binary formation process in AGN discs, with the aim of constraining the likelihood of binary formation depending on encounter parameters and providing the community with physically motivated analytical tools for predicting binary formation. A total of 114 hydrodynamic simulations were run, consisting of three suites: i) a fiducial suite with the expected AGN density for a thin Shakura-Sunyaev disc ii) a suite with ambient density three times higher and iii) a suite identical to the fiducial where accretion is turned off. Captures occur in each of the suites with varying success rates. The findings are summarised into key points below.

1. The addition of the gaseous AGN discs leads to captures from a wider range of radial impact parameters p in the disc and leads to consistently close ($\Delta r < 0.1 r_{\rm H}$) encounters within one large window, unlike the gasless case which has only two very narrow, separate regions. This results from increased gravitational focusing in the lead up to the encounter from the mass of the CSMDs and strong dissipation from gas effects in the immediate lead up to the first periapsis.

2. Binary scatterings in higher density environments form more easily in an even larger range of impact parameters. Additionally, they also allow the easier formation of binaries that have larger close separations, due to increased focusing from more massive CSMDs and stronger gaseous energy dissipation.

3. In the simulations with accretion, dissipation during the encounter is initially dominated by the SMBH whose shear removes energy from the binary. Once the binaries get closer ($\Delta r \lesssim 0.5 r_{\rm H}$) energy is then deposited into the binary from primarily the gas gravity and a little accretion as the CSMDs are

perturbed by the opposing BH. During the periapsis passage, when the CSMDs collide, accretion dissipation quickly switches sign and removes energy from the binary very efficiently, leaving it bound.

4. When accretion is switched off, gas can flow past the BHs during the close approach where they would normally be accreted, leading to a net accumulation of gas behind the BH and inducing a drag. When accretion is enabled, this drag is instead reflected in the accretion dissipation as a direct 'headwind' on the BHs. There is little change in the trajectory of the BHs when accretion is disabled and similar energy dissipation, indicating accretion mimics the gas drag well on the small scales around the BHs.

5. A detailed understanding of the chronology and characteristics of the encounter was developed. Three characteristic orbital trajectories, determined by their impact parameter p were identified (see Figure 5.4). Each trajectory type demonstrated specific behaviours in their dissipation processes. In the frame of the inner BH orbiting counterclockwise around the SMBH, the trajectory of the three families are as follows:

   (a) *Leftsided* encounters - encounters with low p that pass to the left of the inner BH which form prograde binaries.

   (b) *Rightsided* encounters - encounters with moderate p values that pass to the right of the inner BH and form retrograde binaries

   (c) *Turnaround* encounters - encounters with high p that pass initially to the right before looping back on themselves and going round the left of the inner BH, forming prograde binaries.

   Rightsided encounters are most favourable for successful binary formation as they are located in the centre of the space of p for successful binary formation. Leftsided and turnaround encounters with impact parameters that place them further from the rightsided region of p undergo encounters with increased minimum separations and are less likely to remain bound due to less energy dissipation from both accretion and local gas gravity.

6. Strong oscillations in the dissipation from gas gravity, first identified in Paper I, are again observed in all the simulations where the binaries have deeper encounters due to non-cynlindrically symmetric perturbations to the CSMDs arising from tides induced by the opposing binary BH. These perturbations dominate the gas dissipation during the close approach in both simulations with and without accretion, though the net dissipation is found to be positive in the former and negative in the latter case. The strength of the oscillations in the binary energy could leave a detectable GW signature, but the orbital frequency of these inhomogeneities is of the order $\sim 10^{-7} Hz$, putting them out of the low frequency sensitivity range of even LISA.

7. The dissipation during the first encounter in all simulation suites follows a power-law with the minimum separation. This slope is found to be steeper when the AGN disk density is increased.

8. I construct an analytic criterion for binary formation, Eq. (6.15). The relation is derived directly from the fully hydrodynamic simulations in this study yet only depends on pre-encounter properties. Thus, it is physically well informed but does not require the user to implement any such physics in order for it to operate, making it well suited to improving population studies such as (e.g. Tagawa et al., 2020a). Using the two-body energy at two Hill spheres separation and the impact parameter measured at one Hill sphere separation, the criterion can predict with a success rate >90% whether the binary will remain bound, for the AGN densities shown in the paper. The accuracy of the predictor is affirmed in Figure 5.19.

6

Constraining AGN merger rates from gas-assisted binaries

Contents

6.1 Introduction

Observing BHs in the universe is a difficult task due to their illusive nature. AGN provide a highly favourable environment for both BBH formation and mergers, due to the dense gaseous accretion disc orbiting the SMBH at their centre. Dynamical/accretion drag on objects crossing through the AGN disc can embed them within the geometrically thin disc for a high number density of BHs. These BHs can then encounter one another and form stable binaries by dissipating their relative two-body energy via a complex interaction with the surrounding gas. The efficiency of the gas-assisted binary formation mechanism has recently been validated from the hydrodynamical simulations of Chapters 4 and 5 as well as in Li et al. (2022a); Whitehead et al. (2023a). The very recent work of Dodici & Tremaine (2024) directly compares across previous numerical studies, finding good agreement for the island of parameter space in gas density and encounter impact parameter that leads to binary formation.

The evolution of a disc embedded binary is an ongoing problem. In Chapter 4, it was shown that binaries can inspiral on short timescales, orders of magnitude shorter than the typical lifetime of an AGN $t_{\rm AGN} = 10^7$yr. The merger can be especially rapid for retrograde binaries (retrograde with respect to the orbit around the SMBH), due to enhanced accretion and gravitational torques from the gas removing angular momentum. This picture is broadly consistent across other studies (e.g. Baruteau et al., 2011; Li et al., 2022d,a; Li & Lai, 2022b, 2023). For prograde binaries that are highly circular and at large separations, binaries have in some cases been found to out-spiral when an isothermal hydrodynamic treatment is used (e.g. Li et al., 2021; Dempsey et al., 2022; Rowan et al., 2023).

With the ever increasing amount of BBH merger detections from LIGO-VIRGO-KAGRA, the increasing amount of data further constrains the merger rates and the parameter distributions which can be used to test the possible astrophysical environment of the mergers. Population studies of semi-analytic works (e.g. Antonini & Rasio, 2016; Secunda et al., 2019, 2020; Tagawa et al., 2020a; McKernan et al., 2020b; Ford & McKernan, 2022; Vaccaro et al., 2024) that predict the rate of mergers in AGN tend to suffer from a simplified treatment of binary formation in gas, which naturally affects the anticipated rates. Arguably the most detailed of these studies

is the 1D N-body simulations of Tagawa et al. (2020a). The study accounts for a plethora of physical effects, including: radial migration, binary hardening and ionisation via binary-single interactions, capture into the AGN disc via dynamical friction, gas assisted binary formation (also through dynamical friction), merger kicks and repeated mergers, among many others. They found that gas-captured binaries make up the majority ($> 85\%$) of merging binaries in the AGN. If the gas-formation mechanism dominates BH mergers in AGN, as suggested by Tagawa et al. (2020a), it is vital that we accurately model the process. Tagawa et al. (2020a) assumed a binary was formed if the deceleration timescale from dynamical friction (e.g. Ostriker, 1999) was smaller than the binary Hill sphere crossing time. The validity of applying the Ostriker formula to this scenario is uncertain, as the formalism assumes a uniform density and motion of the gas, whereas the embedded BHs will have their own very dense and rotating circum-single discs. This uncertainty has been affirmed by detailed hydrodynamical studies (e.g. Li et al., 2022a; Rowan et al., 2023; Whitehead et al., 2023a; Rowan et al., 2024) that the drag on the BHs can be highly stochastic.

In this Chapter, I build off of Chapter 5, where a detailed binary capture criterion was derived from high resolution simulations of BH-BH scatterings. This physically motivated and numerically verified criterion is applied to a simple semi-analytic model of BHs in an AGN disc to determine the approximate merger rates in the AGN channel when a more accurate treatment of binary formation is applied. I discuss the semi-analytic model, its differences to that of Tagawa et al. (2020a) and the inclusion of the formation criterion in Sec. 6.2 and present the results in Sec. 6.3 before concluding in Sec. 6.4.

6.2 Methods

The core component of the AGN channel is the SMBH's accretion disc. This section outlines the properties of the disc, how the BHs become embedded into the disc, how gas can aid binary formation and finally how the binaries are driven to merge.

6.2.1 Disc setup

The disc equations for a geometrically thin, optically thick alpha disc (Shakura & Sunyaev, 1973) with the surface density Σ, scale height H, sound speed $c_{\rm s}$ and temperature T are adopted from Goodman & Tan (2004); Kocsis et al. (2011b). At a fiducial distance of $R_{\rm disc} = 10^{-2}$pc, in the region where gas pressure dominates, these are:

$$\Sigma \approx 2000 {\rm gcm}^{-2} (R/10^{-2}{\rm pc})^{-3/5} (M_\bullet/10^6 M_\odot)^{4/5} \,, \tag{6.1}$$

$$H \approx 10^{14} {\rm cm} (R/10^{-2}{\rm pc})^{21/20} (M_\bullet/10^6 M_\odot)^{-3/20} \,, \tag{6.2}$$

$$c_s \approx 2 {\rm kms}^{-1} (R/10^{-2}{\rm pc})^{-9/20} (M_\bullet/10^6 M_\odot)^{7/20} \,, \tag{6.3}$$

$$T \approx 800 {\rm K} (R/10^{-2}{\rm pc})^{-9/10} (M_\bullet/10^6 M_\odot)^{7/10} \,, \tag{6.4}$$

where R is the radial position in the disc, and $M_\bullet$ is the SMBH mass. This model assumes the following parameters:

- The SMBH accretion rate relative to the Eddington limit is $\dot{M}_\bullet/\dot{M}_{\bullet,{\rm Edd}} = 0.1$.
- The opacity is the electron scattering opacity.
- The alpha viscosity parameter is taken to be $\alpha = 0.3$ to maintain comparability to Bartos et al. (2017b).
- The radiative efficiency in terms of the Eddington luminosity has the value $\epsilon = L_{\bullet,{\rm Edd}}/(\dot{M}_{\bullet,{\rm Edd}} c^2) = 0.1$.

At the outer edge of the AGN disc the Toomre parameter must satisfy $Q \equiv c_{\rm s}\Omega/(\pi G\Sigma) > 1$, which occurs at $R \sim 10^{-2}$pc and is insensitive to $M_\bullet$. Beyond this point, the disc can fragment under its own self gravity. In this region the disc equations are not valid, so 10^{-2}pc is taken as the upper radial limit. Similar to Tagawa et al. (2020a), a lower radial limit of $R = 10^{-4}$pc is adopted. At lower radial distances, we are within the domain where the AGN disc is governed by radiation pressure, so the disc equations and binary capture criterion of Chapter 5 are no longer valid (e.g. Shakura & Sunyaev, 1973; Sirko & Goodman, 2003). As discussed in Sec. 6.3, merger rates within the small radial domain $R < 10^{-4}$pc should not contribute significantly to the prediction of the merger rates.

6.2.2 Objects crossing the disc

It is assumed that gas-assisted BBH formation and mergers can only occur within the disc, therefore it is necessary to know how many BHs are on orbits that cross the disc. Here, the number of objects that cross the disc within the region of validity ($10^{-4}\text{pc} \leq a \leq 10^{-2}\text{pc}$) is estimated. The number density of stars n_*, and by extension their remnant BHs, in terms of the orbital semi-major axis a is taken to be a mass segregated function consistent with the central O-star distribution Bartko et al. (2009) of our galaxy

$$n_*(a) \propto a^{-2.5}\,. \tag{6.5}$$

The distribution is assumed to be spherical with orbital inclinations i sampled uniformly in $\cos i$. The eccentricity of the orbits is taken from the thermal distribution $f(e) = 2e$. The maximal distance from the SMBH where the local dynamics are dominated by its presence is $R_{\rm inf} = GM_\bullet/\sigma_\bullet^2$, where $\sigma_\bullet$ is the velocity dispersion of objects in the central nuclear region. Using the $M - \sigma$ relation $M_\bullet = M_0(\sigma_\bullet/\sigma_0)^k$ (Ferrarese & Merritt, 2000; Gebhardt et al., 2000; Gültekin et al., 2009), adopting $k = 4.384$, $M_0 = 3.097 \times 10^8$ and $\sigma_0 = 200\text{km s}^{-1}$ from Kormendy & Ho (2013), this gives

$$R_{\rm inf} = \frac{GM_0}{\sigma_0}\left(\frac{M_\bullet}{M_0}\right)^{0.544} \tag{6.6}$$

The fraction of BHs crossing the disc is then given by

$$f_{\rm cross} = \frac{1}{N_{\rm BH}} \iint\limits_{\substack{a(1-e)<R_{\rm disc} \\ a<R_{\rm inf}}} n(a) f(e) 4\pi a^2 da\, de \tag{6.7}$$

where we integrate over the number of BHs $N_{\rm BH}$ within $R_{\rm inf}$ that have a periapsis within the outer radial limit of the disc $R_{\rm disc}$. The number of BHs sampled in our Monte-Carlo scheme to come in sec 6.2.6 is then $f_{\rm cross}N_{\rm BH}$.

6.2.3 Population sample

Based on the stellar initial mass function (IMF), various models for the BH initial mass function (BIMF) are used in the Monte-Carlo simulations of Sec. 6.2.6. Three

BH initial mass functions are considered, labelled according to their source. The stellar population is represented by the stellar mass function

$$\frac{dN_*}{dm_*} \propto m_*^{-\gamma}\,. \tag{6.8}$$

Here, m_* is the zero age main sequence mass of stars with an assumed stellar mass range of $0.1\mathrm{M}_\odot \leq m_* \leq 140\mathrm{M}_\odot$ and N_* is their abundance. The exponent γ has a range of $1.7 \leq \gamma \leq 2.35$, with the fiducial value taken to be $\gamma = 2.35$, consistent with Salpeter (1955). The stellar masses are sampled such that the total stellar mass within $R_{\rm inf}$ is $2M_\bullet$, in line with Binney & Tremaine (2008); Kocsis & Levin (2012); Bartos et al. (2017b).

BIMF 1

To make an accurate comparison to a highly relevant work to this one, the BIMF of Tagawa et al. (2020a), corresponding to a solar metallicity (see Belczynski et al., 2010b), is implemented as the fiducial model of this work. Its form takes

$$\frac{m_{\rm BH}(m_*/\mathrm{M}_\odot)}{\mathrm{M}_\odot} = \begin{cases} \text{no BH} & m_* < 20\mathrm{M}_\odot \\ m_*/4 & 20\mathrm{M}_\odot \leq m_* < 40\mathrm{M}_\odot \\ 10 & 40\mathrm{M}_\odot \leq m_* < 55\mathrm{M}_\odot \\ m_*/13 + 5.77 & 55\mathrm{M}_\odot \leq m_* < 120\mathrm{M}_\odot \\ 15 & 120\mathrm{M}_\odot \leq m_* \leq 140\mathrm{M}_\odot \end{cases}. \tag{6.9}$$

By sampling the stellar masses from Eq. (6.8) and applying Eq. (6.9), the initial BH mass distribution is obtained. Unlike in Tagawa et al. (2020a) the BH mass function is not evolved here, i.e. only 1st generation mergers are considered.

BIMF 2

To also compare with the pre-existing binary rates of Bartos et al. (2017b), their simplified power law distribution is adopted as the second BIMF,

$$\frac{dN_{\rm BH}}{dM_{\rm BH}} \propto M_{\rm BH}^{-\beta} \tag{6.10}$$

with the equivalent mass range of $5\mathrm{M}_\odot \leq M_{\rm bin} \leq 50\mathrm{M}_\odot$ and exponent $2.0 \leq \beta \leq 2.5$. The slope of mass distribution reflects the upper bound identified by in (Abbott et al., 2019d), which is more consistent with X-ray binary observations (e.g. Özel et al., 2010; Kochanek, 2015), which have even steeper dependence. The simplicity

of the function allows us to observe how the initial BH mass function compares to the merging mass function, discussed in Sec. 6.3.3. The same number of BHs as derived from the BIMF of Tagawa et al. (2020a) is maintained to compare directly the merger rate dependence on the mass distribution of BHs.

BIMF 3

Our only current inference of the BIMF from observations is from X-ray binaries and GW observations. As a third BIMF, the BH mass distribution of Baxter et al. (2021) is implemented. The function was derived by constraining the mass gap from the BH mass distribution from GW events (see Abbott et al., 2021a) in tandem with stellar evolution theory, incorporating the predicted mass gap from the GW mass distribution. The function is given by

$$\frac{dN_{\rm BH}}{dM_{\rm BH}} \propto M_{\rm BH}^{b}\left[1+\frac{2a^2 M_{\rm BH}^{1/2}(M_{\rm BHMG}-M_{\rm BH})^{a-1}}{M_{\rm BHMG}^{a-\frac{1}{2}}}\right], \tag{6.11}$$

where the $M_{\rm BHGP}$ is the low mass edge of the mass gap. The value of $M_{\rm BHGP}$ is set to $47.7{\rm M}_\odot$ and the dimensionless constants are taken to be $a = 0.39$ and $b = -2.2$, as suggested in Baxter et al. (2021). The same minimum BH mass of $5{\rm M}_\odot$ is maintained for consistency as well as using the same number of BHs as the other BIMFs.

The normalised distributions of all IMFs, which are hereafter referred to as $\rm BIMF_{Tagawa}$, $\rm BIMF_{Bartos}$ and $\rm BIMF_{Baxter}$ are shown in Figure 6.1. Qualitatively, $\rm BIMF_{Baxter}$ and $\rm BIMF_{Baxter}$ allow for larger BH masses up to $\sim 50{\rm M}_\odot$, whereas $\rm BIMF_{Tagawa}$ produces more BHs in the range of $10-12{\rm M}_\odot$ ($10-15{\rm M}_\odot$) for $\gamma = 2.35$ (1.7). For $\gamma = 1.7$, the overall number of BHs also increases by a factor of ~ 5 as there are more high mass stars, owed to the flatter stellar IMF. The spike at $M_{\rm BH} = 10{\rm M}_\odot$ comes from the $40-55{\rm M}_\odot$ condition of Eq. (6.9). As very few stars are formed with masses $120-140{\rm M}_\odot$, the anticipated spike at $M_{\rm BH} = 15{\rm M}_\odot$ is far less significant.

6.2.4 Gas dissipation during the encounter

The semi-analytic prescriptions derived in Chapter 5 is used to model the energy dissipation of a BH-BH encounter. As a brief reminder, the orbital energy dissipation $\Delta E_{\rm bin}$ follows a power law with the depth of the first periapsis passage $r_{\rm per}$

$$\Delta E_{\rm bin}(r_{\rm per}) = -a\left(\frac{r_{\rm per,1}}{r_{\rm H}}\right)^{b}|E_{\rm H,c}|\,, \tag{6.12}$$

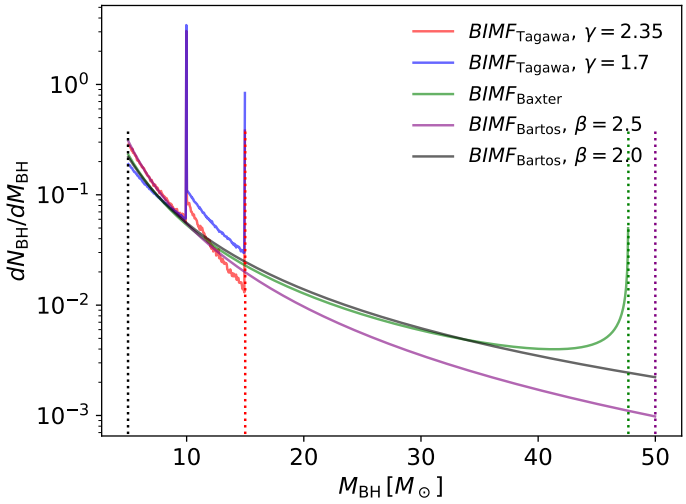

Figure 6.1: Normalised BH initial mass functions BIMF$_{\rm Tagawa}$, BIMF$_{\rm Bartos}$ and BIMF$_{\rm Baxter}$ (eqs. 6.9, 6.10 and 6.11 respectively). BIMF$_{\rm Tagawa}$ is shown for $\gamma = \{2.35, 1.7\}$ and BIMF$_{\rm Bartos}$ for $\beta = [2, 2.5]$. The vertical lines of BIMF$_{\rm Tagawa}$ are a result of the $40{\rm M}_\odot \leq m_* < 55{\rm M}_\odot$ and $120{\rm M}_\odot \leq m_* \leq 140{\rm M}_\odot$ conditions of Eq. (6.9). The vertical cutoff of BIMF$_{\rm Baxter}$, represents the lower boundary of the BH mass gap.

where $|E_{\rm H,c}| = \frac{GM_{\rm bin}\mu}{2r_{\rm H}}$ is the orbital energy of the binary at a separation of $r_{\rm H}$ in the co-rotating frame. The relation is extended to arbitrary densities based on the finding of my co-authored paper Whitehead et al. (2023a) that dissipation scales linearly with the gas density in the Hill sphere ρ_H. For the parameterisation of the AGN disc in Sec. 6.2.1, Eq. (6.12) is modified to account for the changing density in the Hill sphere at different points in the AGN disc assuming the radial profiles of eqs. (6.1)-(6.4).

The two effects that change ρ_H are the local sound speed and surface density as $\rho = \Sigma/(2H) = \Sigma\Omega/c_{\rm s}$, where $\Omega = \sqrt{GM/R^3}$ is the Keplerian angular frequency. It is assumed ρ_H scales with the ambient density ρ according to the findings of Whitehead et al. (2023a). The density then scales with radius as $\rho_H \propto \Sigma/(2H) \propto R^{-3/5}/R^{21/20} \propto R^{-33/20}$ and $M_\bullet$ as $\rho_H \propto M_\bullet^{19/20}$. Using the fiducial radius and SMBH mass of Rowan et al. (2024), Eq. (6.12) becomes

$$\frac{\Delta E_{\rm bin}(R, r_{\rm per})}{|E_{\rm H,c}|} = -a\left(\frac{r_{\rm per,1}}{r_{\rm H}}\right)^b \mathcal{C}(R, M_\bullet) \tag{6.13}$$

where

$$\mathcal{C}(R, M_\bullet) = \left(\frac{M_\bullet}{4\times10^6{\rm M}_\odot}\right)^{19/20}\left(\frac{R}{0.0075pc}\right)^{-33/20}. \tag{6.14}$$

The same methodology is applied from Sec. 5.3.6 to reconstruct Eq. (5.17) using Eq. (6.14). Using the fiducial values $a = 1.3 \times 10^{-4}$, $b = -0.4$, the full capture criterion is then

$$\left[\frac{E_{\rm 2H}}{|E_{\rm H,c}|} < \left(\frac{E_{\rm 2H}}{|E_{\rm H,c}|}\right)_{\rm crit}\right] \wedge \left[p_{\rm 1H} < 0.68 r_{\rm H}\right], \tag{6.15}$$

$$\left(\frac{E_{\rm 2H}}{|E_{\rm H,c}|}\right)_{\rm crit} = \underbrace{\mathcal{C}(R, M_\bullet) 10^{-1.74\frac{p_{\rm 1H}}{r_{\rm H}} - 1.57}}_{|\Delta E_{\rm bin}| \text{ for encounter}} - \underbrace{10^{1.31\frac{p_{\rm 1H}}{r_{\rm H}} - 4.34}}_{\text{max stable } E_{\rm bin} \text{ at } r_{\rm ap}} \quad . \tag{6.16}$$

The primary determinant for binary capture is then whether the energy condition of Eq. 6.15 is satisfied. At a distance of $2r_{\rm H}$, the relative velocity of the BHS, $v_{\rm rel}$, is taken to be the combined magnitude of the ambient velocity dispersion in the disc, $\sigma_{\rm disp}$ and the Keplerian shear over the radial separation of the BHs ΔR, i.e. $\sigma_{\rm Kep} = |R\,\Delta R\, d\Omega/dR| = \frac{3}{2}\Omega\Delta R$. The energy $E_{\rm 2H}$ is then

$$E_{\rm 2H} = \frac{1}{2}\mu v_{\rm rel}^2 - \frac{G M_{\rm bin}\mu}{2 r_{\rm H}}\,. \tag{6.17}$$

Using $v_{\rm rel}^2 = \sigma_{\rm kep}^2 + \sigma_{\rm disp}^2$, the average encounter energy is

$$E_{\rm 2H} = \frac{1}{2}\mu(\sigma_{\rm Kep}^2 + \sigma_{\rm disp}^2) - \frac{G M_{\rm bin}\mu}{2 r_{\rm H}}\,. \tag{6.18}$$

Expressing Eq. (6.18) in units of $E_{\rm H,c}$ (as required by Rq. 6.15), this gives

$$\frac{E_{\rm 2H}}{|E_{\rm H,c}|} = \frac{r_{\rm H}(\sigma_{\rm Kep}^2 + \sigma_{\rm disp}^2)}{G M_{\rm bin}} - 1\,. \tag{6.19}$$

The ambient velocity dispersion of objects in the disc $\sigma_{\rm disc}$ is assumed to be equal to the local sound speed so their mean vertical motion is of order H. This is a conservative assumption as it assumes BHs that have not yet aligned have zero chance of forming binaries via gas assisted captures and binaries in the disc do not further settle to the midplane. For the assumed parameters, $\sigma_{\rm disp}$ ranges from one to two orders of magnitude below $\sigma_{\rm Kep}$.

This formalism does not account for any eccentricity in the BH orbits around the SMBH due to gas effects when embedded objects open up a gap (Sari & Goldreich, 2004). Using equations 32 and 33 of Pan & Yang (2021) (see also Kocsis et al. 2011b), the criteria for a $10M_{\rm BH}$ to open a gap are only marginally satisfied for $M_\bullet \lesssim 10^5 {\rm M}_\odot$ for $\alpha = 0.3$. Therefore excluding this effect likely does not affect the predictions of the simulations. Embedded BHs may also have modified eccentricities

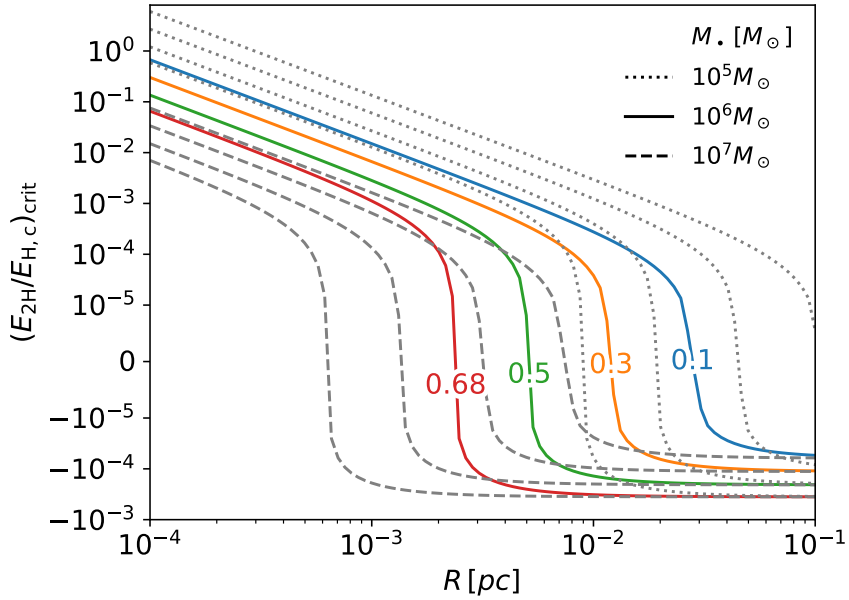

Figure 6.2: Maximum initial encounter energy $E_{2\mathrm{H}}$ of a binary that leads to a successfully formed binary for different impact parameters $p_{1\mathrm{H}}$, as labelled on curves, as a function of radial distance in the AGN disc R. Results shown for fiducial parameters $M_{\rm bin} = 20\mathrm{M}_\odot$ and $M_\bullet = [10^5, 10^6, 10^7]\mathrm{M}_\odot$. At lower R, the lower velocity dispersion and higher gas density allows BHs with larger initial encounter energies to dissipate enough energy to stay bound. Closer encounters at low impact parameters can extend binary formation to larger R.

and or encounter energies from two-body scatterings prior to the encounter. The two body relaxation timescale (calculated according to Tremaine et al., 2002; Naoz et al., 2022) of the system is $\{0.05, 1.5, 50\}$Myr for $M_\bullet = \{10^5, 10^7, 10^9\}\mathrm{M}_\odot$. This calculation assumes the size of the system is 0.01pc, the average BH mass is $10\mathrm{M}_\odot$ and the confinement of objects to the disc introduces a factor $\sim (H/0.01\mathrm{pc})^2$. Taking the lifetime of the AGN to be $t_{\rm AGN}$ ~10Myr, scattering could be important in the low $M_\bullet$ regime, however note this is an underestimate as it assumes all objects in the system have been embedded in the disc. The resulting additional velocity dispersion from two-body scatterings could potentially reduce the merger rate via an increase in the value of σ_{disp} in Eq. (6.19).

Figure 6.2 depicts the maximum allowable encounter energies $E_{\rm crit}$ that lead to successful binary formation for different values of $p_{1\mathrm{H}}$, assuming three values of $M_\bullet$. The contours of $E_{\rm crit}$ with $p_{1\mathrm{H}}$ at low R form a steep power law where initially

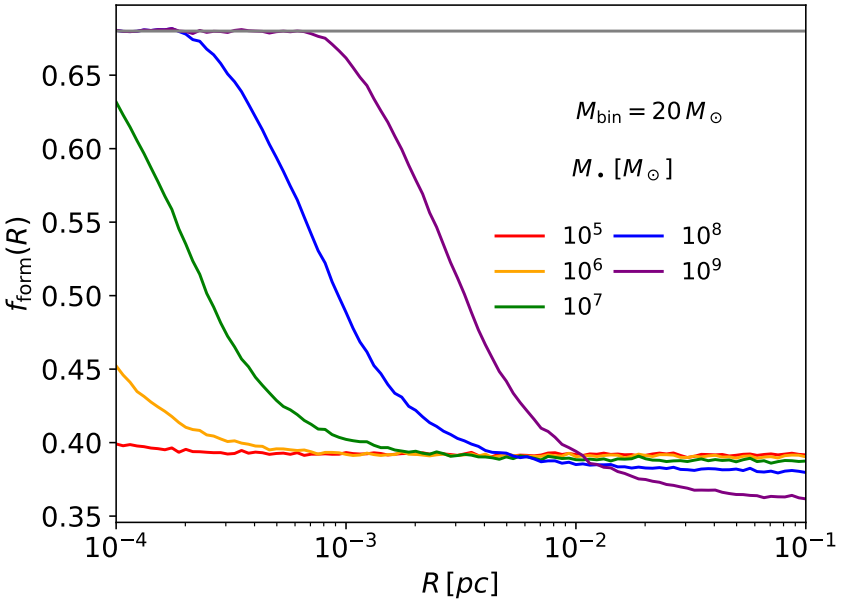

Figure 6.3: Fraction of encounters with impact parameters $p_{1H} < r_H$ that lead to successfully formed binaries as a function of radial distance in the SMBH disc for different $M_\bullet$. The function is shown for m and a uniform distribution of p_{1H} and ΔR is assumed. Results show AGN with higher $M_\bullet$ have an enhanced formation probability for low R. The form of the curves are highly insensitive to $M_{\rm bin}$.

unbound BHs can still be captured into binaries. Then, as $\mathcal{C} \propto R^{-\frac{33}{20}}$, the second term in Eq. (6.16) dominates at higher R and only increasingly negative energies will form stable binaries before plateauing at a value dependent on p_{1H}. Decreasing p_{1H} values lead to higher dissipation values and allows binaries to be more easily formed at higher energies further out in the AGN disc. The transition point from the power law to the plateau occurs at lower R for smaller $M_\bullet$.

6.2.5 The binary formation function

To determine the rate of BH mergers, it is necessary to define the statistical fraction of BH encounters that will lead to binary formation $f_{\rm form}(R, M_{\rm bin}, M_{\rm SMBH})$ and the dependence on its three parameters. Here, encounters are defined as events where the separation of two BHs is less than the binary Hill radius. In Figure 6.3, $f_{\rm form}$ is shown as a function of R for a range of $M_\bullet$, sampling the initial mass distribution from $\rm BIMF_{Tagawa}$. The ambient velocity dispersion term $\sigma_{\rm disp}$ is sampled from a

random Gaussian distribution with standard deviation $\sigma \equiv c_{\rm s}$ centred on zero. The upper bound of ΔR in accordance with Eq. (5.12) is taken to be $2r_{\rm H}$. Note that this is also a conservative assumption as Chapters 4 and 5 both indicated BHs can be focused into minimum encounter separations smaller than $r_{\rm H}$ for $\Delta R > 2r_{\rm H}$ depending on the disc density. The values of ΔR and $p_{\rm 1H}$ are sampled uniformly[1] between $0.01r_{\rm H} - 2r_{\rm H}$ and $0 - r_{\rm H}$ respectively for approaching BHs, where the lower ΔR value is given a non-zero value to avoid divergence in the calculation of the time between encounters later in Sec. 6.2.6.

From Figure 6.3, there is the maximal probability of $f_{\rm form} = 0.68$ from Eq. (6.15). Making use of the fact $c_s \ll \sigma_{\rm Kep}$ for the majority of encounters, Eq. (6.19) is independent of R, $M_{\rm bin}$ and $M_\bullet$

$$\frac{E_{\rm 2H}}{|E_{\rm H,c}|} \propto \frac{r_{\rm H}\sigma_{\rm Kep}^2}{M_{\rm bin}} \propto \frac{r_{\rm H}\Omega^2\Delta R^2}{M_{\rm bin}} \propto \frac{RM_{\rm bin}^{1/3}M_\bullet^{-1/3}R^{-3}M_\bullet R^2 M_{\rm bin}^{2/3}M_\bullet^{-2/3}}{M_{\rm bin}} = K \quad (6.20)$$

where the constant K depends on f_Δ in $\Delta R = f_\Delta r_{\rm H}$ where $0.01 < f_\Delta < 2$. Hence, whether the capture criterion (Eq. 6.16) is satisfied primarily depends on the value of ΔR for a particular encounter and is highly insensitive[2] to $M_{\rm bin}$. In the low R limit, the first term in Eq. (6.16) dominates and the BHs can dissipate energy efficiently during the encounter. For high $M_\bullet$, $f_{\rm form}$ takes its maximal value at low R. As R increases, an increasing fraction of encounters have encounter energies ($E_{\rm 2H}$) below $E_{\rm crit}$ and $f_{\rm form}$ decreases. In the high R limit, the critical energy required for the encounter to form a binary is less than zero and tends towards a fixed value depending on $M_\bullet$. Since the spread in encounter energies is also independent of R (Eq. 6.20) the value of $f_{\rm form}$ becomes fixed in the high R regime. The overall range in $f_{\rm form}$ is small with a maximal increase of only $\sim 50\%$ going from the outer to inner edge of the AGN disc for the range in $M_\bullet$ considered. Altogether, this result implies a favourable formation likelihood across both R and $M_\bullet$.

[1]In practice there is a correlation between $p_{\rm 1H}$ and ΔR, however as it is unclear how this should be affected by the ambient velocity dispersion $\sigma_{\rm disp}$, they are sampled randomly.

[2]The dependence on $M_{\rm bin}$ scales with the relative value of $\sigma_{\rm disp}$ to $\sigma_{\rm Kep}$, where the latter is typically always larger for most $\Delta R = [0.01, 20]$.

6.2.6 BH binary merger rates using a Monte Carlo approach

In order for an isolated BH to merge, it must satisfy four conditions *i*) the BHs must align with the disc, *ii*) encounter another BH, *iii*) successfully form a binary and *iv*) successfully merge, all within $t_{\rm AGN}$.

The timescales of the system

The alignment timescale is derived according to Bartos et al. (2017b). Given some initial vertical velocity v_z at the point of disc crossing and a typical velocity reduction Δv_z upon crossing the disc from accretion drag[3], the general expression for the characteristic timescale of disc alignment is

$$t_{\rm align} \simeq \frac{t_{\rm orb}}{2}\frac{v_z}{\Delta v_z}\,. \tag{6.21}$$

The remaining $t_{\rm orb} = 2\pi R^{3/2}(GM)^{-1/2}$ term is the orbital period, and the factor 2 accounts for two crossing per $t_{\rm orb}$. The fractional change in velocity of an object is equated to the ratio of the mass accreted during its crossing of the disc and its own mass such that $\Delta v_z/v_z = \Delta M_{\rm cross}/M_{\rm BH}$. The accreted mass is assumed to be that within its Bondi-Hoyle-Lyttleton radius $r_{\rm BHL} = 2GM_{\rm BH}/(\Delta v^2 + c_s^2)$, where $\Delta v = \sqrt{(1-\cos(i))^2 + \sin^2(i)} = 2v_{\rm orb}\sin(\frac{i}{2})$ is the relative velocity of the binary to the gas, which orbits the SMBH with velocity $v_{\rm orb} = \sqrt{GM_\bullet/R}$. The crossing mass is then $\Delta M_{\rm cross} = \Delta v t_{\rm cross} r_{\rm BHL}^2 \pi\Sigma/(2H)$ with crossing time $t_{\rm cross} \approx 2H/(v_{\rm orb}\sin i)$. Putting all this together, gives an alignment time of

$$t_{\rm align} = \frac{t_{\rm orb}}{2}\frac{\cos(i/2)(\Delta v^2 + c_s^2)^2}{4G^2 M_{\rm BH}\pi\Sigma}\,, \tag{6.22}$$

where the identity $\sin(i)/\sin(i/2) = 2\cos(i/2)$ has been applied. Note the strong dependence on the velocity term $(\Delta v^2 + c_s^2)^2$ to the fourth power, which makes it increasingly difficult to embed objects for larger SMBH masses for a fixed R.

The encounter timescale $t_{\rm enc}$ is given by:

$$t_{\rm enc} = \frac{1}{2n_{\rm BH}\langle r_{\rm H} z_{\rm H}\langle v_{\rm rel}\rangle_{\Delta \rm R}\rangle_{M_{\rm bin}}}\,, \tag{6.23}$$

where $n_{\rm BH}$ is the volume number density of BHs (see Sec 6.2.7), $z_{\rm H} = \min(H, r_{\rm H})$ is the vertical cross section for the encounter in the case $r_{\rm H} < H$ and $\langle v_{\rm rel}\rangle_{\Delta \rm R}$ is

[3]Since the velocity of inclined objects is hypersonic, dynamical gas drag is assumed to be inefficient.

the relative velocity averaged uniformly over ΔR. The quantity $\langle r_{\rm H} z_{\rm H} \langle v_{\rm rel} \rangle_{\Delta \rm R} \rangle$ is averaged over $M_{\rm bin}$ to give the typical encounter time for a BH in the disc. For a given BH, the second mass is randomly sampled from the distribution of $M_{\rm BH}$ at the current R, discussed in Sec. 6.2.7. The factor two arises from the radial cross section of $2r_{\rm H}$ in R. Once a BH encounters another in the disc, the formation likelihood is given by $f_{\rm form}$. This then modifies $t_{\rm enc}$ to give the effective formation timescale

$$t_{\rm form} = \frac{t_{\rm enc}}{f_{\rm form}} \,. \tag{6.24}$$

Perhaps the most uncertain timescale is the merger timescale. It has been shown that while retrograde binaries can reliably merge (e.g. Li et al., 2022d; Li & Lai, 2022b; Rowan et al., 2023; Li & Lai, 2023), prograde binaries can in some cases outspiral (e.g. Li et al., 2021; Dempsey et al., 2022). These binaries are typically given zero initial eccentricity, though it has been shown that eccentricity persists long after the initial formation. Additionally it has been shown that hotter, more realistic, circum-binary discs lead to reliable inspiral (e.g. Baruteau et al., 2011; Li et al., 2022c). In this work, like most other population studies (e.g. Tagawa et al., 2020a; Mapelli et al., 2021; Ford & McKernan, 2022), it is assumed a formed binary is reliably hardened by the gas. The merger timescale itself is significantly smaller than the AGN lifetime (e.g. Haehnelt & Rees, 1993; Cavaliere & Padovani, 1989). Nevertheless, given the uncertainty of the inspiral rate still present in the literature, the maximal merger timescale in Bartos et al. (2017b) of $t_{\rm merge} \sim 10^5$yr is used corresponding to $M_\bullet = 10^6 {\rm M}_\odot$ at 0.01pc. At higher $M_\bullet$ or lower R, the inspiral rate is shorter, but the value is maintained for all binaries as pessimistic assumption. Even at this upper bound, the merger timescale is still two orders of magnitude shorter than the AGN lifetime, leaving $t_{\rm align}$ and $t_{\rm enc}$ as the more impactful timescales for calculating merger rates.

Thus, the full timescale of a BH to merge, including the dependencies is

$$t_{\rm tot} = t_{\rm align}(R, M_{\rm BH}) + t_{\rm form}(R, M_{\rm BH}, n_{\rm BH}) + t_{\rm merge} \,. \tag{6.25}$$

The merger rate is then the number of BHs which satisfy $t_{\rm tot} < t_{\rm AGN}$ divided by $2t_{\rm AGN}$, where the factor 2 accounts for double counting.

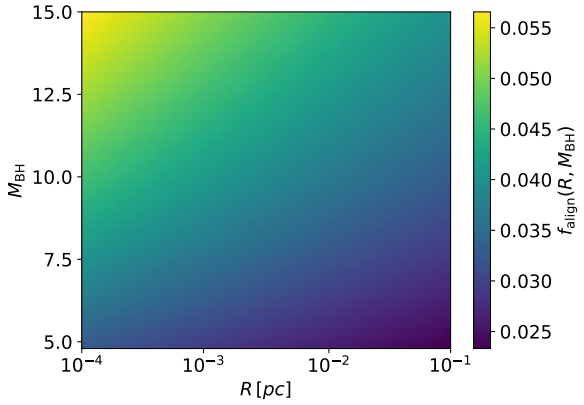

Figure 6.4: Fraction $f_{\rm align}$ of a BH with mass $M_{\rm BH}$ at radius R aligning with the AGN disc for fiducial parameters $M_\bullet = 4 \times 10^6 {\rm M}_\odot$ and $t_{\rm AGN} = 10^7 {\rm yr}$. Generated by evaluating equation Eq. (6.22) over uniform $\cos i$. Figure shows higher mass BHs can align quicker and the alignment timescale is also shorter at low R in the disc, where Σ is higher.

6.2.7 Resolving dependencies

BH number density

The complexities of the calculation lie within the dependencies of $n_{\rm BH}$ and $f_{\rm form}$. Starting with the former, the number density of BHs in the disc $n_{\rm BH}$ is determined from the initial sample of $\{M_{{\rm BH},i}\}$ and $\{R_i\}$ (see Sec. 6.2.3) that satisfy $t_{\rm align} < t_{\rm AGN}$. To smooth out the stochasticity in the sampling from the calculation of $n_{\rm BH}$, a probability grid in bins of $M_{\rm BH}$ and R, $f_{\rm align}(R, M_{\rm bin})$, is constructed by sampling over the full range of $M_{\rm BH}$ and R_i and calculating their alignment time using Eq. (6.22). For each point in $M_{\rm BH}$ and R, the alignment timescale is sampled over the full range of $\cos i$ and the probability of that BH to align is the number of instances where the alignment time condition is met as a fraction of the number of inclination samples. The grid is constructed in 100 bins of R and 50 bins in $M_{\rm BH}$. For a fiducial setup of $M_\bullet = 4 \times 10^6$, the probability of alignment across $M_{\rm BH}$ and R is shown in Figure 6.4. As predicted by Eq. (6.22), the figure indicates BHs of higher mass and smaller R embed themselves more easily in the AGN disc. The disc embedded number density is similarly calculated as a grid in $M_{\rm BH}$ and R by sampling over the full initial distributions of $\{M_{{\rm BH},i}\}$ and $\{R_i\}$, binning them into the same bins for $f_{\rm align}$ and then adding the probability for that BH to align with the disc. The number density is also represented as a grid in $M_{\rm BH}$

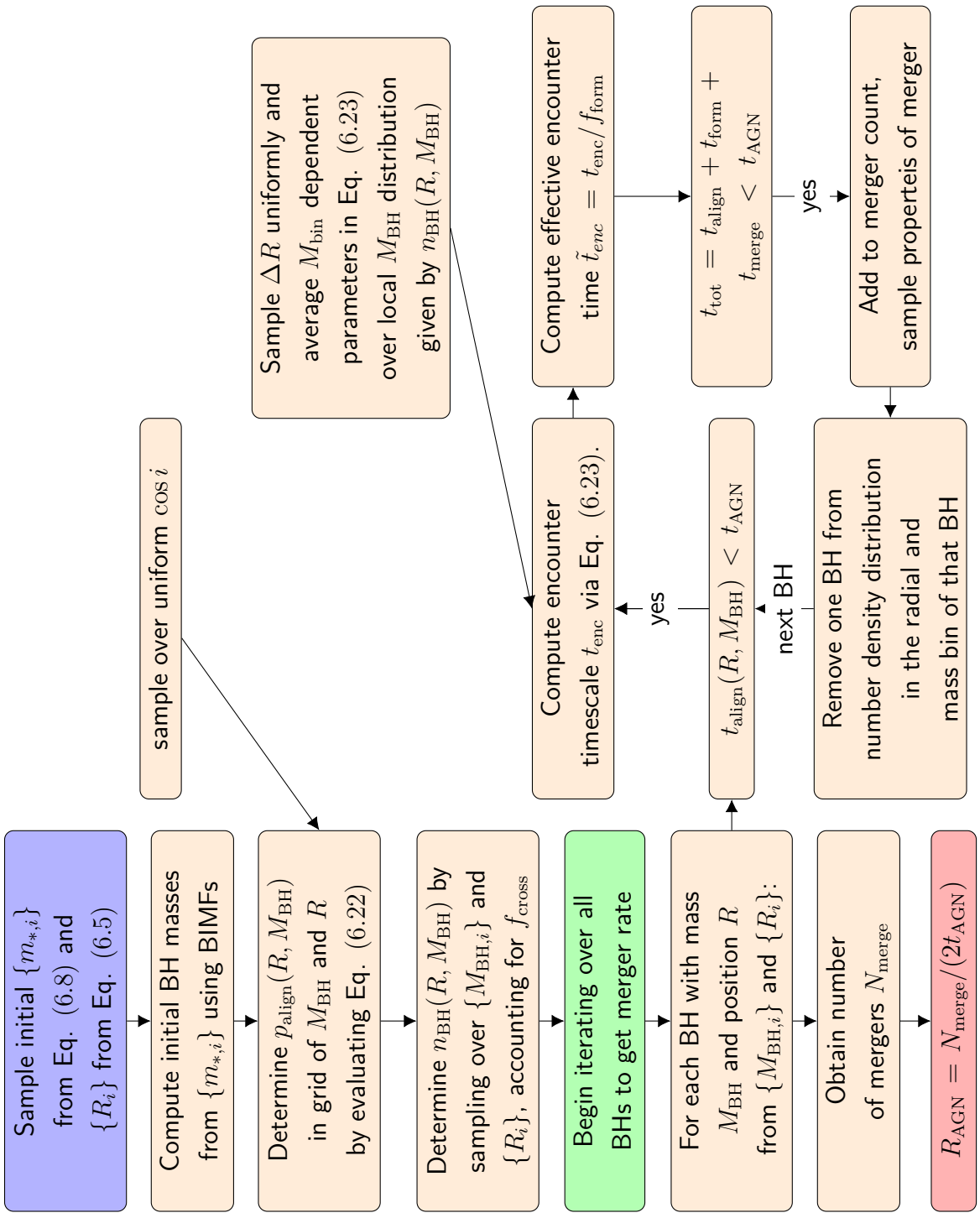

Figure 6.5: Summary of the fiducial semi-analytic procedure to determine BBH merger rates, from an initial sample of stars in the central stellar cluster.

and R to keep track of the mass distribution at each radius as this is required to determine t_{enc}. When evaluating $t_{\rm enc}$ in Eq. (6.23), the number density is the sum of the number densities across the mass bins.

6.2.8 Knock on effects

Extending the single BH calculation to a sample across the entire BH population requires accounting for knock on effects from the outcome of each calculation, i.e. was there a merger. To account for the finite number of BHs and the time dependence of $n_{\rm BH}$ the contribution of one BH is removed from the number density for each merger. Specifically, if a BH satisfies the time constraints of Eq. (6.25), a random BH merging partner is sampled from the current distribution of masses predicted by $n_{\rm BH}$ and its contribution to the number density is removed. The masses and position in the disc is recorded for all mergers, which is required to compute the anticipated merger rate from GW detectors. Though this is not a formal implementation of the time dependence of $n_{\rm BH}$ and one cannot comment on the change in merger rate over the AGN lifetime, it accounts for the overall reduction in the number of mergers within $t_{\rm AGN}$. Additionally, neglecting this effect would lead to over-counting higher mass binary encounters/mergers, since higher mass BHs have shorter encounter timescales. From Eq. (6.23) there is an overall $M_{\rm bin}$ dependence of $\sim M_{\rm bin}^{-1}$ (assuming $z_{\rm H} = r_{\rm H}$, which is true for the vast majority of $R, M_{\rm bin}$ and $M_\bullet$). However, the merger rate dependence on this assumption is small, as discussed in Sec. 6.3.2. For clarity, a detailed flow chart to summarise the overall Monte-Carlo Scheme is shown in Figure 6.5.

6.3 Results

6.3.1 $M_\bullet$ dependence

The merger rate *per* AGN per year Γ and observable merger rate distribution over $M_\bullet$ is shown in Figure 6.6. The merger rate distribution assumes the AGN number density in the Universe follows the function given by Greene & Ho (2007, 2009)

$$\frac{dn_{\rm AGN}}{dM_\bullet} = \frac{34000\ {\rm Gpc}^{-3}}{M_\bullet} 10^{-(\log_{10}(M_\bullet/M_\odot)-0.67)^2/1.22}\,. \tag{6.26}$$

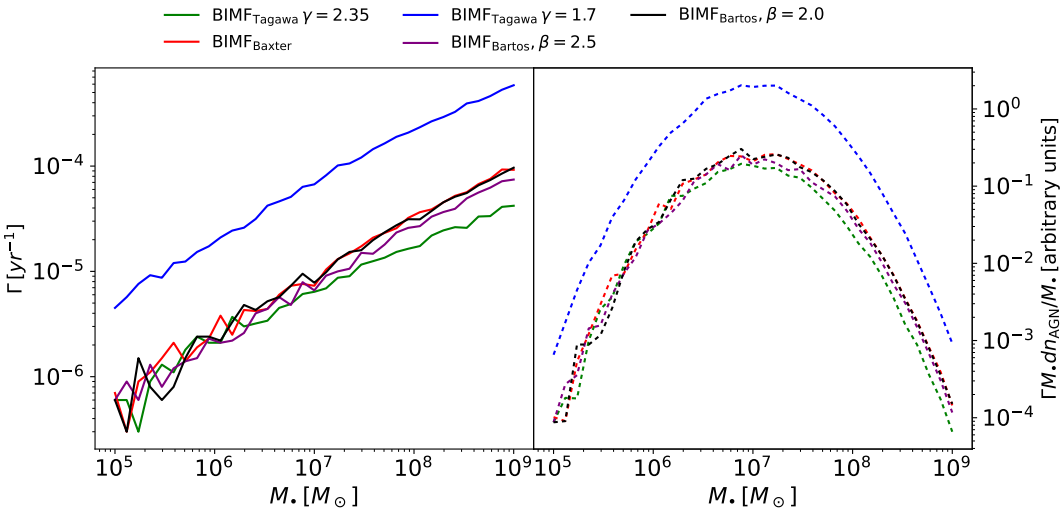

Figure 6.6: *Left:* The BH merger rate Γ per year per AGN with mass $M_\bullet$. *Right:* The merger rate across $M_\bullet$ weighted by the mass distribution of AGN (Eq. (6.29)). The different colours represent the assumed BH initial mass function (see 6.2.3). The graph indicates the observable rates should be dominated by AGN with $M_\bullet \sim 10^7 \mathrm{M}_\odot$.

The rate of BH mergers is highly dependent on SMBH mass. Considering only $\mathrm{BIMF}^{\gamma=2.35}_{\rm Tagawa}$ for now, the merger rates range from order $\sim 10^{-7}\mathrm{yr}^{-1}$ at $M_\bullet = 10^5\mathrm{M}_\odot$ to $\sim 10^{-5}\mathrm{yr}^{-1}$ at $M_\bullet = 10^9\mathrm{M}_\odot$ for a single AGN. These results are in good agreement with Tagawa et al. (2020a) and the low $M_\bullet$ results of Bartos et al. (2017b). At higher SMBH masses ($\sim 10^7\mathrm{M}_\odot$), the rate is around 50 times larger than the results of Bartos et al. (2017b). As Bartos et al. (2017b) considers only pre-existing binary mergers (i.e., the binaries did not form inside the AGN disc) , the steeper dependence on $M_\bullet$ here is a result of the binary formation function and encounter timescale, which have additional $M_\bullet$ dependence. Given the flatness of $f_{\rm form}$, the scaling primarily comes from $t_{\rm enc}$. At low masses, merger rates are restricted by the number of BHs in the system, the lowest number being ~ 500 BHs for $M_\bullet = 10^5\mathrm{M}_\odot$. As $M_\bullet$ increases, the number of available BHs within $R_{\rm inf}$ increases, at a faster rate than $f_{\rm cross}$ can limit the embedded number of BHs. The increased BH population results in a peak in the merger rate at $M_\bullet \sim 10^7\mathrm{M}_\odot$. Beyond this, the scarcity of AGN with $M_\bullet > 10^7\mathrm{M}_\odot$ limits the contribution to the merger rate despite $\Gamma(M_\bullet)$ being larger for these more massive AGN.

To investigate the main bottleneck of the merger process, we can consider the fraction of BHs that have $t_{\rm align} < t_{\rm AGN}$ (F1), then the fraction of those which

$M_\bullet$ [$M_\odot$]	F1(%)	F2(%)	F3(%)
10^5	4.5	43	> 99
10^7	1.4	65	> 99
10^9	0.21	80	> 99

Table 6.1: The fraction of BHs in the Monte Carlo simulations which satisfy $t_{\rm align} < t_{\rm AGN}$ (F1) and of those $t_{\rm align} + t_{\rm form} < t_{\rm AGN}$ (F2) and of those the fraction with $t_{\rm align} + t_{\rm enc} + t_{\rm form} < t_{\rm AGN}$ (F3). Indicating that the majority of BHs do not merge due to the aligment time.

have $t_{\rm align} + t_{\rm form} < t_{\rm AGN}$ (F2) and the fraction of those with $t_{\rm align} + t_{\rm form} + t_{\rm merge} < t_{\rm AGN}$ (F3). Assuming $\mathrm{BIMF}^{\gamma=2.35}_{\rm Tagawa}$, these values are shown in Table 6.1 for $M_\bullet/\mathrm{M}_\odot = 10^5, 10^7, 10^9$. The relative fractions imply that per BH, the primary bottleneck is the alignment time (F1) by approximately an order of magnitude, therefore constraining the inclination and radial distribution of BHs in the initial distribution is also crucial. Though F1 is the primary bottleneck, the formation timescale (unlike the merger timescale) is not negligibly small as a notable fraction of embedded BHs fail to form a binary within $t_{\rm AGN}$.

There is no significant (order of magnitude) difference in the overall merger rates from our fiducial model with $\mathrm{BIMF}_{\rm Baxter}$ and $\mathrm{BIMF}_{\rm Bartos}$. However we find a strong dependence on γ for $\mathrm{BIMF}_{\rm Tagawa}$, with the lower value of $\gamma = 1.7$ leading to a rate increase of about an order of magnitude. This stems from having many BHs from the more top heavy stellar mass distribution ($\sim$5 times more BHs) and the resulting top heavy BIMF compared with $\mathrm{BIMF}^{\Gamma=2.35}_{\rm Tagawa}$. The increase in merger rate is then driven by a higher embedded BH density $n_{\rm BH}$ since higher mass BHs more easily embed themselves within $t_{\rm AGN}$ and have shorter encounter timescales $t_{\rm enc} \propto n_{\rm BH}^{-1} M_{\rm bin}^{-1}$. As the range in $M_{\rm BH}$ ($M_{\rm bin}$) for $\mathrm{BIMF}_{\rm Tagawa}$ is only $5\mathrm{M}_\odot - 15\mathrm{M}_\odot$ ($10\mathrm{M}_\odot - 30\mathrm{M}_\odot$), this suggests the increase in overall BH number is the dominant factor in its increased rates for $\gamma = 1.7$.

6.3.2 Observable rates

Using the merger rates determined for each mass $M_\bullet$, the expected observational rate of mergers is calculated as follows. The rate density $\mathcal{R}_\rho$ in $\mathrm{Gpc}^{-3}\mathrm{yr}^{-1}$ is given by

$$\mathcal{R}_\rho = \int \Gamma(M_\bullet) \frac{dn_{\rm AGN}}{dM_\bullet} dM_\bullet \,. \tag{6.27}$$

BIMF	$\mathcal{R}_\rho$	$\mathcal{R}_\rho$[5-20]	$\mathcal{R}_\rho$[20-50]	$\mathcal{R}_\rho$[50-100]	$\mathcal{R}_\rho$[20-50]/[5-20]	$\Gamma_{\rm LIGO}$
$\mathrm{BIMF}^{\gamma=2.35}_{\rm Tagawa}$(f)	0.51	0.37	0.14	-	0.38	1.88
$\mathrm{BIMF}^{\gamma=1.7}_{\rm Tagawa}$	5.91	3.33	2.58	-	0.77	26.7
$\mathrm{BIMF}_{\rm Baxter}$	0.78	0.17	0.42	0.19	2.47	22.8
$\mathrm{BIMF}^{\beta=2.5}_{\rm Bartos}$	0.65	0.24	0.34	0.06	1.40	11.2
$\mathrm{BIMF}^{\beta=2.0}_{\rm Bartos}$	0.79	0.18	0.46	0.15	2.56	19.5
$R_{\rm disc} = 10^{-1}$pc	0.55	0.41	0.14	-	0.34	2.07
$n_{\rm BH} = \mathrm{const}$	0.53	0.39	0.14	-	0.36	1.90
Range	0.51-5.91	0.17-3.33	0.14-2.58	0.06-0.15	0.34-2.56	1.88-26.7
Range [w.o $\mathrm{BIMF}^{\gamma=1.7}_{\rm Tagawa}$]	0.51-0.79	0.17-0.41	0.14-0.42	0.06-0.15	0.34-2.56	1.88-22.8
Observed	17.9-44	13.3-39	2.5-6.8	0.1-0.4	0.09-0.29	

Figure 6.7: Table of results from different Monte Carlo runs with different BIMFs and variations of initial conditions. *From left to right:* The assume BIMF function and modifications to the model, the merger rate density $\mathcal{R}_\rho$ in $\mathrm{Gpc^3 yr^{-1}}$, the density rate in the binary mass range $5\mathrm{M}_\odot \leq M_{\rm bin} \leq 20\mathrm{M}_\odot$, density rate for $20\mathrm{M}_\odot < M_{\rm bin} \leq 50\mathrm{M}_\odot$, density rate for $50\mathrm{M}_\odot < M_{\rm bin} \leq 100\mathrm{M}_\odot$, ratio of density rates in second to first mass range, predicted detection rate of events for advanced LIGO, $\Gamma_{\rm LIGO}$. The f denotes the fiducial model which is used to test the merger rate change when the simulation outer bound is extended to 10^{-1}pc (6th row) and when the BH density is assumed to be constant (7th row). The ranges of merger rates is shown in row 8/9 when $\mathrm{BIMF}^{\gamma=1.7}_{\rm Tagawa}$ is/isn't included and compared to the currently available observed range from LIGO-VIRGO-KAGRA (Abbott et al., 2023a) in row 9.

To calculate the rate of BH mergers per year from Earth, the horizon distance $D_{\rm h}$ for Advanced LIGO is assumed, a binary with mass $M_{\rm bin}$ is detectable at a signal to noise ratio of 8 (see Dominik et al., 2015) according to

$$D_{\rm h}(M_{\rm bin}) = 0.45\left(\frac{M_{\rm bin}}{2.8{\rm M}_{\odot}}\right)^{5/6}{\rm Gpc}\,. \tag{6.28}$$

The comoving volume $V_{\rm c}$ in which we can detect a merger with binary mass $M_{\rm bin}$ is given by

$$V_{\rm c}(M_{\rm bin}) = \frac{4}{3}\pi\left(\frac{D_{\rm h}(M_{\rm bin})}{2.26}\right)^{3}(1+z)^{-3}\,, \tag{6.29}$$

where the redshift z is neglected for the purpose of this study (i.e. z=0). The observed rate $\Gamma_{\rm LIGO}$ per year is then, using the same method as Bartos et al. (2017b):

$$\Gamma_{\rm LIGO} = \iint V_{\rm c}(M_{\rm bin})\frac{d\Gamma(M_{\rm bin}, M_{\bullet})}{dM_{\rm bin}}\frac{dn_{\rm AGN}}{dM_{\bullet}}dM_{\rm bin}\,dM_{\bullet}\,. \tag{6.30}$$

The merger rate per binary mass term, $dR_{\rm AGN}/dM_{\rm bin}$ is evaluated using the merging binary mass distribution from each $M_{\bullet}$ value put through the Monte-Carlo model. For lower $M_{\bullet}$ masses that have a low merger number, the analysis is repeated until there is a merger sample of at least 500 BHs so that the merger rate for each value of $M_{\bullet}$ is converged and there is a sufficiently large population of mergers to analyse their parameter distributions. The merger rate densities and LIGO merger rate for all three BIMFs and for varying initial conditions are displayed in Table 6.7. Also shown are the merger rates for binary masses in the ranges $5{\rm M}_{\odot} \leq M_{\rm bin} \leq 20{\rm M}_{\odot}$, $20{\rm M}_{\odot} < M_{\rm bin} \leq 50{\rm M}_{\odot}$ and $50{\rm M}_{\odot} < M_{\rm bin} \leq 100{\rm M}_{\odot}$.

The merger rate from the 5 BIMFs ranges from $0.51 - 5.91{\rm Gpc}^{-3}{\rm yr}^{-1}$, compared to the rate of 17.9–$44{\rm Gpc}^{-3}{\rm yr}^{-1}$ from LIGO-VIRGO-KAGRA (Abbott et al., 2023a), When considerably large initial BH masses are permitted in the initial distribution, as in ${\rm BIMF}_{\rm Baxter}$, the rates become dominated by larger binary masses ($M_{\rm bin} > 20$), despite BHs of masses $> 10{\rm M}_{\odot}$ despite being fewer in number. This hardening of the merging mass function in AGN was found in Yang et al. (2019), in the context of pre-existing binary mergers, driven by migration traps and mass biased alignment time. Here, we again have the biased alignment time ($t_{\rm align} \sim M_{\rm BH}^{-1}$, Eq. 6.22). In addition to this, larger BHs have a shorter formation timescale as $t_{\rm enc} \propto M_{\rm bin}^{-1}$. Hence the assumed BIMF affects the anticipated rates in the AGN channel. This is more clear when comparing the increase in the rate from ${\rm BIMF}^{\beta=2.5}_{\rm Bartos}$ ($0.65{\rm Gpc}^{-3}{\rm yr}^{-1}$) to ${\rm BIMF}^{\beta=2.5}_{\rm Bartos}$($0.79{\rm Gpc}^{-3}{\rm yr}^{-1}$), that differ only in the slope of the BIMF β.

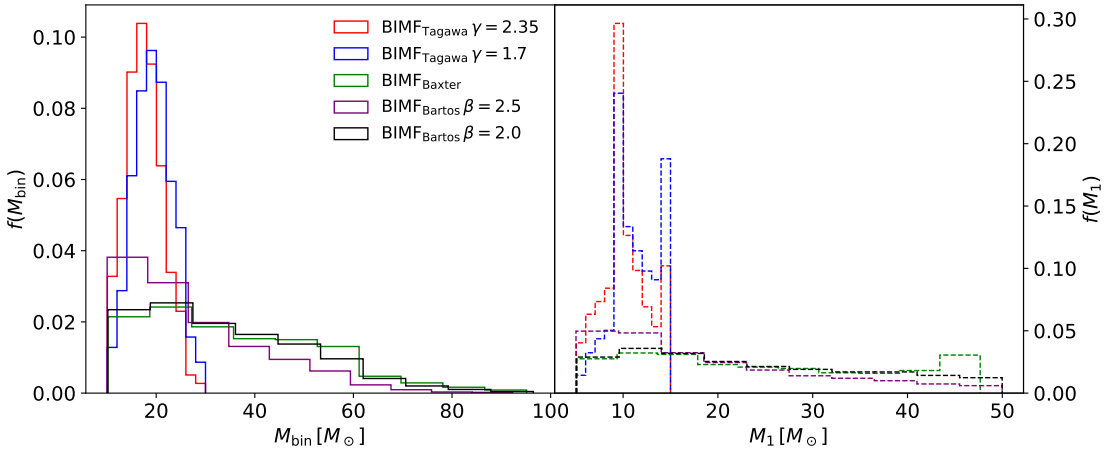

Figure 6.8: *Left:* Mass distribution of the merging binary mass $M_{\rm bin}$ for each BIMF outlined in sec 6.2.3, represented by different colours. *right:* Mass distribution of the primary BH mass M_1 of mergers. The results show a significant hardening of the merging BH mass function compared to the BIMF, indicating larger BHs have a much greater chance to form binaries and merge.

6.3.3 Merger properties

The distributions of mass, mass ratio and radial position of merging binaries generated by the simulations, weighted by the AGN mass function, are shown in Figures 6.8, 6.9 and 6.10 respectively. The mass distribution reaffirms the aforementioned mass hardening effect of the AGN channel. For example, consider BIMF$_{\rm Baxter}$, which demonstrates a near linear profile in $M_{\rm bin}$ compared to the original profile $\sim M_{\rm BH}^{-2.2}$. This is also reflected in the q distribution. For flatter BIMFs with higher limits on $M_{\rm BH}$ (i.e. BIMF$_{\rm Baxter}$ and BIMF$_{\rm Bartos}$), the q distribution becomes less steep and can even flip to favour more unequal mass ratio mergers. Qualitatively, this means less numerous high mass BHs can very easily encounter and merge with abundant low mass BHs. This has prospects for second (or higher) generation mergers as the merged BH can more easily repeat the formation and merger process thanks to its larger mass, potentially further hardening the merging mass distribution (Fishbach et al., 2017; Tagawa et al., 2020a). Such a scenario could easily explain massive and or unequal mass ratio binaries such as GW190814 and GW190521 (Abbott et al., 2020b,f). Comparing the rates in the three mass bins of Table 6.7, the possible fraction of observed mergers originating from the AGN channel in the bins $5 \leq M_{\rm bin} \leq 10$, $20 < M_{\rm bin} \leq 50$ and $50 < M_{\rm bin} \leq 100$

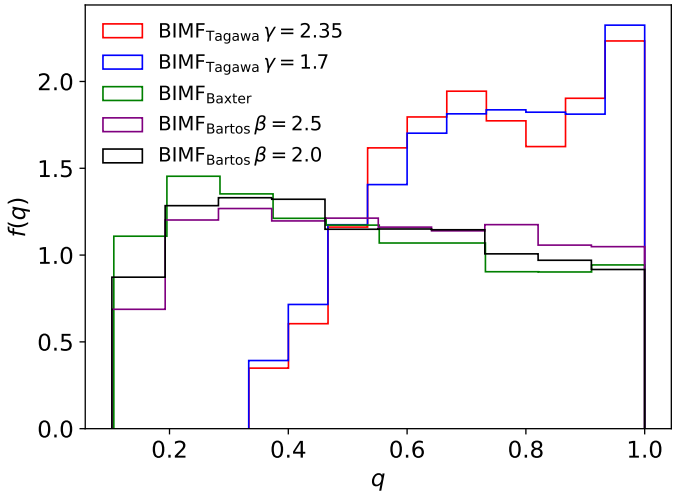

Figure 6.9: Mass ratio distribution $q = M_2/M_1$ for our merging binaries for each BIMF (colour coded). Demonstrating the AGN channel can potentially produce many unequal mass ratio mergers.

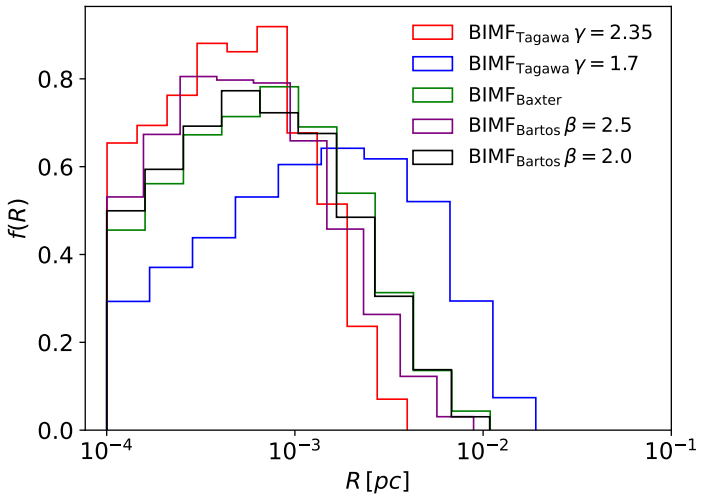

Figure 6.10: Distribution of radial positions in the disc R for our merging binaries for each BIMF (colour coded). Merger rate peaks within the limits of our simulation bounds, with more top heavy BIMFs peaking at higher R.

is $0.4\% - 25$, $2\% - 100\%$ and $\sim 15\% - 100\%$ respectively. Therefore, AGN may not be the primary source of observed low mass BH mergers, but account for a large fraction of high mass mergers. Hence, the relative contribution of the AGN channel could potentially be constrained using the ratio of merger rates in different mass bins (Yang et al., 2019). These results also suggest a large contribution to the rates from other channels for low mass mergers ($M_{\rm bin} < 20{\rm M}_{\odot}$). As more GW detections are made and the BIMF in AGN better constrained, it could then be possible to constrain more rigorously the relative contribution from the AGN channel from the merging mass distribution. In addition, more detailed modelling of the channel is needed to constrain the sensitive parameters of the merger rates, e.g. the stellar IMF, BH radial number density and BIMF.

The radial distribution of mergers peak within the radial bounds of the simulation. At lower radii, mergers are limited by a low number of BHs in such a small volume and increased Keplerian shear $\sigma_{\rm kep}$. At higher radii, the alignment time and low density Σ limit $n_{\rm BH}$ and $f_{\rm form}$ respectively (recall Figure 6.2). When the outer radial limit is extended[4] to 10^{-1}pc, the rates are largely unchanged, consistent with Tagawa et al. (2020a), who find >90% of gas-driven mergers occur in $R < 10^{-2}$pc.

6.4 Summary and Conclusions

In this chapter, a prediction was made for the merger rate of BBHs in AGN formed via BH-BH scatterings in an AGN disc using the physically motivated formation prescription of Rowan et al. (2024) and findings of Whitehead et al. (2023a). The primary goal was to test whether implementing the prescription, derived from high resolution fully hydrodynamical simulations, alters the rates significantly compared to simplified dynamical friction models. Using a range of initial BH mass functions, the merger rate density is constrained to $0.51 - 5.91{\rm Gpc}^{-3}{\rm yr}^{-1}$. These rates corroborate those from many analytical studies (e.g. Bartos et al., 2017b; Yang et al., 2019; Tagawa et al., 2020a; McKernan et al., 2020b). Given that the formation or merger timescale is not the main bottleneck of the rates, it is unsurprising that these rates agree well with Bartos et al. (2017b); Yang et al. (2019), who perform

[4]Note that the disc equations in Sec. 6.2.1 are now being applied outside their region of validity where disc fragmentation can take place.

similar analysis for pre-existing binaries, where these additional timescales do not need to be accounted for. Nearly all mergers are found to take place within 10^{-2}pc where the cutoff is due to long alignment timescales with the disc.

The mass distribution (in both the binary and primary mass) of merging BHs is significantly more top heavy than the BIMF, due to a favourability for high mass BHs to align with the disc and form binaries via gas-dissipation. Therefore the merger rates and masses are sensitive to the assumed BIMF, where more top heavy BIMFs lead to significant increases in the rates. This bias also leads to a merging mass ratio distribution. Thus, the AGN channel can easily explain the high mass and unequal mass ratio detections from GW observatories. The rates are also sensitive to the number of initial BHs, where the range in the assumed stellar IMF exponent produces a range of an order of magnitude in the BH merger rate.

The overall merger rate lies within $1\% - 33\%$ that of LIGO-VIRGO-KAGRA suggesting a smaller but not insignificant contribution from the AGN channel. However, due to the top heavy merging mass function, the AGN channel can potentially explain $2\% - 100\%$ mergers in the range $20\mathrm{M}_{\odot} < M_{\rm bin} \leq 50\mathrm{M}_{\odot}$ and $\sim 15\% - 100\%$ of mergers in $50\mathrm{M}_{\odot} < M_{\rm bin} \leq 100\mathrm{M}_{\odot}$. Due to the mass bias of the gas-assisted binary formation mechanism, I encourage future studies to account for repeated mergers using the physically motivated formation function, which may further increase the merger rate as indicated in Tagawa et al. (2020a). Reductions in the observational merger rate uncertainty and better constraints of the BIMF in AGN could allow us to constrain the relative contribution from AGN using the relative merger rates from low and high mass binaries.

Though a well motivated formation criterion has been utilised for the formation of binaries, the model is still subject to several important simplifying assumptions. The formation function was constructed from the simulations of Chapter 5, which assumed the hydrodynamics of the BH-BH encounters were isothermal. Recent collaborative work (Whitehead et al., 2023b) has showed that this is an oversimplification, where gas heating can be significant during the encounter. Here it is pessimistically assumed all BHs are formed in the stellar cluster and must align with the disc. In reality the parent stars could align first (and faster) before the BH is born. There is no account for migration in the disc, which could alter the BH encounter timescale. Additionally, binary-single scatterings with BHs or

stars that could potentially ionise or harden the BBH are ignored, along side BBH formations from three-body scatterings.

From this work, I conclude that BHs merging in AGN could be a non-negligible contributor to the observed BBH merger rates and a potentially dominant channel for high mass and unequal mass ratio mergers.

7

Summary and Conclusions

Gravitational waves, first predicted by Albert Einstein in early 20^{th} century, have now been observed within the last decade, with many more anticipated in the near future. Following this discovery, explaining the astrophysical origin of these signals has become one of the most pertinent problems in astrophysics. Our current GW detectors are sensitive to the mergers of stellar mass BHs $\sim$ 5–150$M_{\odot}$, yet the main mechanism(s) allowing such massive objects to be close enough to merge within a Hubble time are still subject to large unknowns. Within the last few years, the number of observations have allowed us to constrain statistically the properties of the GW signal: the spins, eccentricities, BH masses, mass ratios and overall merger rate. To explain these quantities, we first must understand the mechanism/environment in which these BHs are merging. This thesis explored one possible environment; the merger of BHs through BH-BH scatterings in the dense gas discs around the SMBHs in AGN using high resolution hydrodynamical and Monte-Carlo simulations.

Simulating the system of an AGN disc and two BHs with hydrodynamics presents a challenging computational task, stemming from the vast time and length scales between the disc and the orbit of two BHs residing within it. The AGN channel presents a unique system as the density of the disc can facilitate the formation of BBHs from only 2-body encounters through the BHs' interaction with the gas during the encounter. This scenario, as well as the binary evolution, was simulated

self consistently for the first time using a fully hydrodynamical treatment in Chapter 4. The gas-assisted binary formation process was then investigated in greater detail in utilising a much larger simulation suite in Chapter 5. The understanding gained from the previous two chapters was then used to predict the merger rate of BHs form this process and the distribution of GW signal masses and mass ratios in Chapter 6 utilising Monte-Carlo simulations and semi-analytic methods.

7.1 Thesis Summary

The overall timeline of the merger process in the AGN channel, starting from an isolated BH born in the central stellar cluster goes as follows. A BH will gradually become embedded within the AGN disc via gaseous drag each time it passes through the disc. It can then encounter another embedded BH and dissipate the relative energy of the BHs via a complex interaction with the gas, such that it remains bound. The binary then forms a circumbinary disc of its own that drives the binary to smaller separations via torques from the gas. Once the separation becomes small enough, the inspiral becomes dominated by GWs and the binary rapidly merges.

Hydrodynamically simulating the encounter of two BHs in the AGN disc for the first time in chapter 4, using 15 simulations, demonstrated highly complex gas morphology. By the end of the encounter, the BH-BH system can transfer a significant net amount of its two-body energy to the surrounding gas. This interaction generates chaotic outflows following close encounters and more spiral like outflows for wider encounters. The process is efficient enough to stabilise even hyperbolic encounters into gravitationally bound binaries. The dissipation is driven by a combination of drag from accretion and gas gravity, with the amount of energy dissipated scaling with the local gas density.

The long term evolution of the binaries was also simulated in Chapter 4, directly following their formation. The eccentricity of BBHs in the AGN channel were found to all be high ($e > 0.9$) immediately after formation. The following e evolution depends on the orientation of the binary orbit with respect to the orbit around the SMBH. In a prograde configuration, e is damped over time for prograde binaries, though all retain an eccentricity of $e \gtrsim 0.2$ at the end of the runtime (a few thousand inner binary orbits). Retrograde binaries have their eccentricities

excited by accretion and gas gravitational drags against the binary motion at apoapsis. This drives the eccentricity towards unity, where depending on the orbital elements during the last passage, the binary can undergo an extremely close periapsis passage, where GW dissipation would be highly efficient in merging the binary on timescales shorter than an orbit around the AGN. Alternatively, the eccentricity excitation can decouple the binary if its apoapsis is comparable to the Hill radius. The evolution of prograde binaries is varied, with some inspiralling, some stalling and some outspiralling. The rate of change of the orbital elements (a and e) also scales with the density.

The gas-assisted binary formation process was investigated more thoroughly with 114 simulations in Chapter 5, sampling finely over the initial radial impact parameter and assuming two different AGN disc densities. In the space of first periapsis distance $r_{\rm min,1}$ and radial impact parameter p, there is a singular large window that allows for binary formation. The curve of $r_{\rm min,1}$– p takes the form of a "W" (Figure 5.2) where the two troughs mark the transition point from binaries formed with retrograde configurations in the central region, to prograde binaries in the low and high impact parameter regimes. The results showed that there is a marginal preference for retrograde configurations. The size of the formation window (range in p that lead to formations) increases with the ambient gas density and is approximately linear, reaffirming Chapter 4's result that formation is more efficient in higher gas densities. Furthermore, a scaling relation is found between the dissipation and periapsis depth of the form $\Delta E \sim -a r_{\rm min,1}^{-b}$ (Eq 5.9), where $b \sim 0.4$ with a coefficient a that scales positively with the disc density. Hence, closer encounters in higher AGN densities are most preferential for binary formation.

Stable binaries are formed in a well defined region of the parameter space of the impact parameter at a Hill radius separation ($p_{\rm 1H}$) and their orbital energy at first apoapsis (Figure 5.16). Based on the minimum stable final energy and the expected dissipation for $p_{\rm 1H}$, a formation criterion (Eq. 5.17) was derived to evaluate whether a binary will form successfully via the gas capture process. The relation depends only on the *pre*-encounter variables $p_{\rm 1H}$ and the binary two-body energy at two Hill radii in separation, so one does not need to simulate the hydrodynamics of the encounter itself. Qualitatively, the relation describes how encounters with higher relative energies and higher $p_{\rm 1H}$ will be less likely to form binaries.

The expected merger rate and merger properties of the AGN channel is explored in Chapter 6 through Monte-Carlo simulations and the understanding gained from Chapters 4 & 5. Utilising the binary formation criterion of Chapter 5, Monte-Carlo simulations were performed, simulating a population of BHs embedding themselves in the disc, encountering one another, forming binaries and merging. These simulations covered the SMBH masses in the range $10^5 M_\odot \leq M_\bullet \leq 10^8 M_\odot$ and assumed a variety of BH initial mass functions (BIMFs). The overall binary merger rates lie approximately an order of magnitude below the observed rates. However the mass distribution of merging binaries skews reliably to a top heavy distribution and can possibly explain $\sim 15 - 100\%$ of observed mergers with binary masses $M_{\rm bin} > 50 M_\odot$ and up to $\sim 25\%$ of those with $20 M_\odot < M_{\rm bin} \leq 50 M_\odot$. Additionally the mass ratio distribution is flatter than the observed profile. Based on these results, it could then be possible to constrain the contribution from the AGN channel based on the slope of the mass and mass ratio distribution as more observations are made in the future. The results of Chapter 6 are subject to large theoretical and observational uncertainties such as the BH initial mass function, number of BHs in AGN and the AGN disc properties. Therefore, constraining these is also vital for making predictions about the AGN channel.

7.2 Towards the Future

Gravitational wave astronomy is still a rapidly growing area of astrophysics. Since the first GW detection in 2015, the sensitivity of current detectors are always being improved (Cooper et al., 2023; Goodwin-Jones et al., 2024; Koley et al., 2024). Additionally, several third generation ground based GW detector projects are now on the horizon with the Einstein telescope (Hild et al., 2008), Cosmic Explorer (Reitze et al., 2019), Voyager (Adhikari et al., 2020) as well as the space based instrument LISA (Amaro-Seoane et al., 2017). As more powerful detectors become available, we will be able to expand the detection volume and increase the detection rate. The Einstein telescope for example, if design sensitivity is achieved, will be able to detect sources up to redshifts of $z \lesssim 100$ for massive BBHs (Gair et al., 2011; Chamberlain & Yunes, 2017). With the anticipated increase in detection rates with these new or upgraded instruments, our understanding of the observed signals

will depend on the quality of our models for their origin. This thesis explored in detail the possibility of BBH formation and mergers in the gas discs of AGN, demonstrating its feasibility as a mechanism for BH mergers.

Chapters 4–6 all present exciting opportunities for future work. In Chapters 4 & 5, several physical parameters related to the AGN disc and embedded binary remained fixed, including: the radial distance of the encounter from the SMBH, the mass ratio of the BHs and only co-planar configurations for the BH-BH encounters. More work is necessary to understand how these additional parameters could affect the formation mechanism, particularly for unequal mass ratios anticipated for the AGN channel (Chapter 6). I am already investigating non co-planar encounters as part of an exciting new project. Preliminary results indicating binaries can still form efficiently with mean vertical motions equivalent to the disc scale height, suggesting (at least qualitatively) that the dissipation is still highly efficient for vertical velocity dispersions on par with the sound speed. Similarly, all of the work of within this thesis ignores interactions between embedded BBHs and other objects in the disc or the background spherical population. While three-body and even four-body encounters have been examined in an N-body framework, how the addition of gas could affect such encounters is still unknown. I am already in the early stages of simulating such systems, which will be my next major research goal. A final consideration is the back reaction from the thermal output of rapidly accreting embedded BHs as well as the contributions from stars on the AGN disc itself. Given the results from Chapter 5 for thicker discs, constraining the increase in the scale height from the heating of these objects is necessary since thicker discs will increase the effective formation timescale of BBHs. This increase could potentially alter the rates of Chapter 6. Based on the results of this thesis, I hope to begin relaxing the aformentioned simplifications and assumptions of BH-BH scatterings and population studies continue to reduce the uncertainty our models for BH mergers in AGN.

In conclusion, the AGN channel presents a promising source of BBH mergers. More detailed future simulations and analysis will provide further valuable understanding and constraints on this source of gravitational waves.

Bibliography

Abbott B. P., et al., 2016, Phys. Rev. Lett., 116, 061102

Abbott B. P., et al., 2017a, Phys. Rev. Lett., 119, 161101

Abbott B. P., et al., 2017b, ApJ, 848, L12

Abbott B. P., et al., 2017c, ApJ, 848, L13

Abbott B. P., et al., 2019a, Physical Review X, 9, 011001

Abbott B. P., et al., 2019b, Physical Review X, 9, 031040

Abbott B. P., et al., 2019c, Phys. Rev. Lett., 123, 011102

Abbott B. P., et al., 2019d, ApJ, 882, L24

Abbott R., et al., 2020a, Phys. Rev. D, 102, 043015

Abbott R., et al., 2020b, Phys. Rev. Lett., 125, 101102

Abbott R., et al., 2020c, Phys. Rev. Lett., 125, 101102

Abbott B. P., et al., 2020d, ApJ, 892, L3

Abbott R., et al., 2020e, ApJ, 896, L44

Abbott R., et al., 2020f, ApJ, 896, L44

Abbott R., et al., 2021a, SoftwareX, 13, 100658

Abbott R., et al., 2021b, ApJ, 915, L5

Abbott R., et al., 2022a, arXiv e-prints, p. arXiv:2203.12038

Abbott R., et al., 2022b, ApJ, 928, 186

Abbott R., et al., 2023a, Physical Review X, 13, 011048

Abbott R., et al., 2023b, Physical Review X, 13, 041039

Abramowicz M. A., Fragile P. C., 2013, Living Reviews in Relativity, 16, 1

Adhikari R. X., et al., 2020, Classical and Quantum Gravity, 37, 165003

Agnor C. B., Hamilton D. P., 2006, Nature, 441, 192

Alcubierre M., Brügmann B., 2001, Phys. Rev. D, 63, 104006

Ali B., et al., 2020, ApJ, 896, 100

Amaro-Seoane P., et al., 2017, arXiv e-prints, p. arXiv:1702.00786

Anninos P., Massó J., Seidel E., Suen W.-M., Towns J., 1995, Phys. Rev. D, 52, 2059

Antoniadis J., et al., 2013, Science, 340, 448

Antonini F., Rasio F. A., 2016, ApJ, 831, 187

Antonini F., Murray N., Mikkola S., 2014, ApJ, 781, 45

Apostolatos T. A., Cutler C., Sussman G. J., Thorne K. S., 1994, Phys. Rev. D, 49, 6274

Arca Sedda M., Mapelli M., Benacquista M., Spera M., 2023, MNRAS, 520, 5259

Askar A., Davies M. B., Church R. P., 2021, MNRAS, 502, 2682

Bahcall J. N., Wolf R. A., 1976, ApJ, 209, 214

Bahcall J. N., Wolf R. A., 1977, ApJ, 216, 883

Baker J. G., Centrella J., Choi D.-I., Koppitz M., van Meter J., 2006, Phys. Rev. Lett., 96, 111102

Baker T., Bellini E., Ferreira P. G., Lagos M., Noller J., Sawicki I., 2017, Phys. Rev. Lett., 119, 251301

Barausse E., Cardoso V., Pani P., 2014, Phys. Rev. D, 89, 104059

Barausse E., Cardoso V., Pani P., 2015, in Journal of Physics Conference Series. p. 012044 (`arXiv:1404.7140`), doi:10.1088/1742-6596/610/1/012044

Bartko H., et al., 2009, ApJ, 697, 1741

Bartos I., Haiman Z., Marka Z., Metzger B. D., Stone N. C., Marka S., 2017a, Nature Communications, 8, 831

Bartos I., Kocsis B., Haiman Z., Márka S., 2017b, ApJ, 835, 165

Baruteau C., Cuadra J., Lin D. N. C., 2011, ApJ, 726, 28

Bate M. R., Bonnell I. A., Price N. M., 1995, MNRAS, 277, 362

Bate M. R., Bonnell I. A., Bromm V., 2002, MNRAS, 336, 705

Bavera S. S., et al., 2020, A&A, 635, A97

Baxter E. J., Croon D., McDermott S. D., Sakstein J., 2021, ApJ, 916, L16

Belczynski K., Ziolkowski J., 2009, ApJ, 707, 870

Belczynski K., Bulik T., Fryer C. L., Ruiter A., Valsecchi F., Vink J. S., Hurley J. R., 2010a, ApJ, 714, 1217

Belczynski K., Dominik M., Bulik T., O'Shaughnessy R., Fryer C., Holz D. E., 2010b, ApJ, 715, L138

Belczynski K., et al., 2016, A&A, 594, A97

Bentz M. C., et al., 2013, ApJ, 767, 149

Benz W., 1990, in Buchler J. R., ed., Numerical Modelling of Nonlinear Stellar Pulsations Problems and Prospects. p. 269

Berti E., Volonteri M., 2008, ApJ, 684, 822

Bertone G., et al., 2020, SciPost Physics Core, 3, 007

Bildsten L., 1998, ApJ, 501, L89

Binney J., Tremaine S., 2008, Galactic Dynamics: Second Edition

Blanchet L., 2014, Living Reviews in Relativity, 17, 2

Boekholt T. C. N., Rowan C., Kocsis B., 2023, MNRAS, 518, 5653

Boffin H. M. J., Watkins S. J., Bhattal A. S., Francis N., Whitworth A. P., 1998, MNRAS, 300, 1189

Bom C. R., et al., 2024, ApJ, 960, 122

Bonetti M., et al., 2020, MNRAS, 493, L114

Boroson T. A., Green R. F., 1992, ApJS, 80, 109

Breivik K., Rodriguez C. L., Larson S. L., Kalogera V., Rasio F. A., 2016, ApJ, 830, L18

Buikema A., et al., 2020, Phys. Rev. D, 102, 062003

Burns E., 2020, Living Reviews in Relativity, 23, 4

Callister T. A., Miller S. J., Chatziioannou K., Farr W. M., 2022, ApJ, 937, L13

Campanelli M., Lousto C. O., Marronetti P., Zlochower Y., 2006, Phys. Rev. Lett., 96, 111101

Canuto C., Hussaini M. Y., Quarteroni A., Zang T. A., 2006, Spectral Methods, doi:10.1007/978-3-540-30726-6.

Caprini C., Figueroa D. G., 2018, Classical and Quantum Gravity, 35, 163001

Cavaliere A., Padovani P., 1989, ApJ, 340, L5

Chamberlain K., Yunes N., 2017, Phys. Rev. D, 96, 084039

Chandrasekhar S., 1931, ApJ, 74, 81

Chang C.-F., Cui Y., 2022, Journal of High Energy Physics, 2022, 114

Chase E. A., et al., 2022, ApJ, 927, 163

Chassande-Mottin E., Leyde K., Mastrogiovanni S., Steer D. A., 2019, Phys. Rev. D, 100, 083514

Chatterjee S., et al., 2005, ApJ, 630, L61

Chung S. M., et al., 2014, ApJ, 790, 54

Clesse S., García-Bellido J., 2017, Physics of the Dark Universe, 15, 142

Cole P. S., Bertone G., Coogan A., Gaggero D., Karydas T., Kavanagh B. J., Spieksma T. F. M., Tomaselli G. M., 2023, Nature Astronomy, 7, 943

Connelley M. S., Reipurth B., Tokunaga A. T., 2008, AJ, 135, 2526

Conselice C. J., 2014, ARA&A, 52, 291

Cooper S. J., et al., 2023, Review of Scientific Instruments, 94, 014502

Cordes J. M., Romani R. W., Lundgren S. C., 1993, Nature, 362, 133

Croton D. J., et al., 2006, MNRAS, 365, 11

Cusin G., Dvorkin I., Pitrou C., Uzan J.-P., 2018, Phys. Rev. Lett., 120, 231101

Cutler C., Flanagan É. E., 1994, Phys. Rev. D, 49, 2658

D'Orazio D. J., Duffell P. C., 2021, ApJ, 914, L21

D'Orazio D. J., Loeb A., 2020, Phys. Rev. D, 101, 083031

Dall'Amico M., Mapelli M., Torniamenti S., Arca Sedda M., 2024, A&A, 683, A186

Darbha S., Kasen D., Foucart F., Price D. J., 2021, ApJ, 915, 69

Davis S. W., Tchekhovskoy A., 2020, ARA&A, 58, 407

DeLaurentiis S., Epstein-Martin M., Haiman Z., 2022, arXiv e-prints, p. arXiv:2212.02650

Demorest P. B., Pennucci T., Ransom S. M., Roberts M. S. E., Hessels J. W. T., 2010, Nature, 467, 1081

Dempsey A. M., Li H., Mishra B., Li S., 2022, arXiv e-prints, p. arXiv:2203.06534

Di Carlo U. N., Giacobbo N., Mapelli M., Pasquato M., Spera M., Wang L., Haardt F., 2019, MNRAS, 487, 2947

Di Carlo U. N., et al., 2020, MNRAS, 498, 495

Dichiara S., et al., 2021, ApJ, 923, L32

Dimmelmeier H., Ott C. D., Marek A., Janka H. T., 2008, Phys. Rev. D, 78, 064056

Dittmann A. J., Ryan G., 2022, MNRAS, 513, 6158

Dodici M., Tremaine S., 2024, arXiv e-prints, p. arXiv:2404.08138

Doeleman S. S., et al., 2012, Science, 338, 355

Dominik M., Belczynski K., Fryer C., Holz D. E., Berti E., Bulik T., Mandel I., O'Shaughnessy R., 2012, ApJ, 759, 52

Dominik M., et al., 2015, ApJ, 806, 263

Dubus G., Guillard N., Petrucci P.-O., Martin P., 2017, A&A, 608, A59

Duffell P. C., D'Orazio D., Derdzinski A., Haiman Z., MacFadyen A., Rosen A. L., Zrake J., 2020, ApJ, 901, 25

Duquennoy A., Mayor M., 1991, A&A, 248, 485

Eddington A. S., 1916, MNRAS, 77, 16

Eggleton P. P., 1983, ApJ, 268, 368

Einstein A., 1918, Sitzungsberichte der Königlich Preussischen Akademie der Wissenschaften, pp 154–167

El-Badry K., et al., 2023, MNRAS, 518, 1057

Event Horizon Telescope Collaboration et al., 2019, ApJ, 875, L1

Event Horizon Telescope Collaboration et al., 2022, ApJ, 930, L12

Fabbiano G., 2006, ARA&A, 44, 323

Fabian A. C., 2012, ARA&A, 50, 455

Fabj G., Samsing J., 2024, arXiv e-prints, p. arXiv:2402.16948

Fanaroff B. L., Riley J. M., 1974, MNRAS, 167, 31P

Fanidakis N., et al., 2012, MNRAS, 419, 2797

Ferrarese L., Merritt D., 2000, ApJ, 539, L9

Fishbach M., Holz D. E., Farr B., 2017, ApJ, 840, L24

Fishbach M., Holz D. E., Farr W. M., 2018, ApJ, 863, L41

Fishbach M., et al., 2021, ApJ, 912, 98

Ford K. E. S., McKernan B., 2022, MNRAS, 517, 5827

Fragione G., Kocsis B., 2020, MNRAS, 493, 3920

Freitag M., Amaro-Seoane P., Kalogera V., 2006, ApJ, 649, 91

Fryer C. L., Woosley S. E., Heger A., 2001, ApJ, 550, 372

Fryer C. L., Belczynski K., Wiktorowicz G., Dominik M., Kalogera V., Holz D. E., 2012, ApJ, 749, 91

Gair J. R., Mandel I., Miller M. C., Volonteri M., 2011, General Relativity and Gravitation, 43, 485

Galaudage S., Talbot C., Nagar T., Jain D., Thrane E., Mandel I., 2021, ApJ, 921, L15

Gautham Bhaskar H., Li G., Lin D. N. C., 2022, arXiv e-prints, p. arXiv:2204.07282

Gayathri V., Wysocki D., Yang Y., Delfavero V., O'Shaughnessy R., Haiman Z., Tagawa H., Bartos I., 2023, ApJ, 945, L29

Gebhardt K., et al., 2000, ApJ, 539, L13

Generozov A., Perets H. B., 2023, MNRAS, 522, 1763

Gerosa D., Berti E., 2019, Phys. Rev. D, 100, 041301

Gerosa D., Fishbach M., 2021, Nature Astronomy, 5, 749

Gerosa D., Berti E., O'Shaughnessy R., Belczynski K., Kesden M., Wysocki D., Gladysz W., 2018, Phys. Rev. D, 98, 084036

Ghez A. M., et al., 2008, ApJ, 689, 1044

Giacobbo N., Mapelli M., 2020, ApJ, 891, 141

Giesers B., et al., 2018, MNRAS, 475, L15

Gillessen S., Eisenhauer F., Trippe S., Alexander T., Genzel R., Martins F., Ott T., 2009, ApJ, 692, 1075

Ginat Y. B., Reischke R., Rapoport I., Desjacques V., 2024, Phys. Rev. D, 109, 083526

Goldreich P., Tremaine S., 1980, ApJ, 241, 425

Goldreich P., Lithwick Y., Sari R., 2002, Nature, 420, 643

Goldreich P., Lithwick Y., Sari R., 2004, ARA&A, 42, 549

Gondán L., Kocsis B., 2022, MNRAS, 515, 3299

Goodman J., Tan J. C., 2004, ApJ, 608, 108

Goodwin-Jones A. W., et al., 2024, Optica, 11, 273

Graham P. W., Jung S., 2017, arXiv e-prints, p. arXiv:1710.03269

Graham M. J., et al., 2020, Phys. Rev. Lett., 124, 251102

Greene J. E., Ho L. C., 2007, ApJ, 667, 131

Greene J. E., Ho L. C., 2009, ApJ, 704, 1743

Grimm H. J., Gilfanov M., Sunyaev R., 2003, MNRAS, 339, 793

Gröbner M., Ishibashi W., Tiwari S., Haney M., Jetzer P., 2020, A&A, 638, A119

Gruzinov A., Levin Y., Zhu J., 2020, ApJ, 905, 11

Gualandris A., Colpi M., Portegies Zwart S., Possenti A., 2005, ApJ, 618, 845

Gültekin K., et al., 2009, ApJ, 698, 198

Haehnelt M. G., Rees M. J., 1993, MNRAS, 263, 168

Hailey C. J., Mori K., Bauer F. E., Berkowitz M. E., Hong J., Hord B. J., 2018, Nature, 556, 70

Haiman Z., 2013, in Wiklind T., Mobasher B., Bromm V., eds, Astrophysics and Space Science Library Vol. 396, The First Galaxies. p. 293 (arXiv:1203.6075), doi:10.1007/978-3-642-32362-1_6

Haiman Z., Kocsis B., Menou K., 2009, ApJ, 700, 1952

Hamilton C., Fouvry J.-B., Binney J., Pichon C., 2018, MNRAS, 481, 2041

Hansen R. O., 1972, Phys. Rev. D, 5, 1021

Hayasaki K., Yagi K., Tanaka T., Mineshige S., 2013, Phys. Rev. D, 87, 044051

Heath R. M., Nixon C. J., 2020, A&A, 641, A64

Heggie D. C., 1975, MNRAS, 173, 729

Heggie D., Hut P., 2003, The Gravitational Million-Body Problem: A Multidisciplinary Approach to Star Cluster Dynamics

Heggie D. C., Hut P., McMillan S. L. W., 1996, ApJ, 467, 359

Heppenheimer T. A., Porco C., 1977, Icarus, 30, 385

Higuchi A., Ida S., 2016, AJ, 151, 16

Hild S., Chelkowski S., Freise A., 2008, arXiv e-prints, p. arXiv:0810.0604

Hinderer T., Babak S., 2017, Phys. Rev. D, 96, 104048

Hindmarsh M. B., Kibble T. W. B., 1995, Reports on Progress in Physics, 58, 477

Hong J., Askar A., Giersz M., Hypki A., Yoon S.-J., 2020, MNRAS, 498, 4287

Hopman C., Alexander T., 2006, ApJ, 645, 1152

Huerta E. A., et al., 2018, Phys. Rev. D, 97, 024031

Inayoshi K., Kashiyama K., Visbal E., Haiman Z., 2021, ApJ, 919, 41

Iorio G., et al., 2023, MNRAS, 524, 426

Janka H.-T., 2013, MNRAS, 434, 1355

Jayasinghe T., et al., 2021, MNRAS, 504, 2577

Jeans J. H., 1919, MNRAS, 79, 408

Jiang Y.-F., Blaes O., Stone J. M., Davis S. W., 2019, ApJ, 885, 144

Johnson T. V., Lunine J. I., 2005, Nature, 435, 69

Kaaz N., Schrøder S. L., Andrews J. J., Antoni A., Ramirez-Ruiz E., 2021, arXiv e-prints, p. arXiv:2103.12088

Kasen D., Metzger B., Barnes J., Quataert E., Ramirez-Ruiz E., 2017, Nature, 551, 80

Kavanagh B. J., Gaggero D., Bertone G., 2018, Phys. Rev. D, 98, 023536

Khan S., Husa S., Hannam M., Ohme F., Pürrer M., Forteza X. J., Bohé A., 2016, Phys. Rev. D, 93, 044007

Kim H., Kim W.-T., 2007, ApJ, 665, 432

Kim H., Kim W.-T., Sánchez-Salcedo F. J., 2008, ApJ, 679, L33

King A. R., Pringle J. E., Livio M., 2007, MNRAS, 376, 1740

Kley W., Nelson R. P., 2012, ARA&A, 50, 211

Kobulnicky H. A., Fryer C. L., 2007, ApJ, 670, 747

Kochanek C. S., 2015, MNRAS, 446, 1213

Kocsis B., Levin J., 2012, Phys. Rev. D, 85, 123005

Kocsis B., Gáspár M. E., Márka S., 2006, ApJ, 648, 411

Kocsis B., Yunes N., Loeb A., 2011a, Phys. Rev. D, 84, 024032

Kocsis B., Yunes N., Loeb A., 2011b, Phys. Rev. D, 84, 024032

Koley S., et al., 2024, European Physical Journal Plus, 139, 48

Kormendy J., Ho L. C., 2013, ARA&A, 51, 511

Kratter K. M., Murray-Clay R. A., Youdin A. N., 2010, ApJ, 710, 1375

Kumamoto J., Fujii M. S., Trani A. A., Tanikawa A., 2021, arXiv e-prints, p. arXiv:2102.09323

Lada C. J., 2006, ApJ, 640, L63

Lawrence A., 2018, Nature Astronomy, 2, 102

Lehner L., 2001, Classical and Quantum Gravity, 18, R25

Li R., Lai D., 2022a, arXiv e-prints, p. arXiv:2202.07633

Li R., Lai D., 2022b, arXiv e-prints, p. arXiv:2207.01125

Li R., Lai D., 2023, arXiv e-prints, p. arXiv:2303.12207

Li Y.-R., Ho L. C., Wang J.-M., 2011, ApJ, 742, 33

Li Y.-P., Dempsey A. M., Li S., Li H., Li J., 2021, ApJ, 911, 124

Li J., Dempsey A. M., Li H., Lai D., Li S., 2022a, arXiv e-prints, p. arXiv:2211.10357

Li Y.-P., Chen Y.-X., Lin D. N. C., Wang Z., 2022b, ApJ, 928, L1

Li Y.-P., Dempsey A. M., Li H., Li S., Li J., 2022c, ApJ, 928, L19

Li J., Lai D., Rodet L., 2022d, ApJ, 934, 154

Li J., Lai D., Rodet L., 2022e, ApJ, 934, 154

Liu B., Lai D., 2021, MNRAS, 502, 2049

Liu J., et al., 2019, Nature, 575, 618

Lodato G., Price D. J., 2010, MNRAS, 405, 1212

Loutrel N., Yunes N., 2017, Classical and Quantum Gravity, 34, 135011

Lower M. E., Thrane E., Lasky P. D., Smith R., 2018, Phys. Rev. D, 98, 083028

Lubow S. H., Seibert M., Artymowicz P., 1999, ApJ, 526, 1001

Ma S., et al., 2022, Phys. Rev. D, 106, 084036

Magnan N., Fouvry J.-B., Pichon C., Chavanis P.-H., 2022, MNRAS, 514, 3452

Makishima K., et al., 2000, ApJ, 535, 632

Mandel I., Farmer A., 2022, Phys. Rep., 955, 1

Mandel I., Smith R. J. E., 2021, ApJ, 922, L14

Mapelli M., 2016, MNRAS, 459, 3432

Mapelli M., 2020, Frontiers in Astronomy and Space Sciences, 7, 38

Mapelli M., et al., 2021, MNRAS, 505, 339

Margutti R., et al., 2017, ApJ, 848, L20

Máthé G., Szölgyén Á., Kocsis B., 2022, arXiv e-prints, p. arXiv:2202.07665

McKernan B., Ford K. E. S., O'Shaughnessy R., 2020a, MNRAS, 498, 4088

McKernan B., Ford K. E. S., O'Shaughnessy R., 2020b, MNRAS, 498, 4088

Meiron Y., Kocsis B., Loeb A., 2017, ApJ, 834, 200

Metzger B. D., 2019, Living Reviews in Relativity, 23, 1

Metzger B. D., Berger E., 2012, ApJ, 746, 48

Meylan G., Heggie D. C., 1997, A&A Rev., 8, 1

Miller M. C., 2005, ApJ, 626, L41

Miller M. C., Hamilton D. P., 2002, MNRAS, 330, 232

Miralda-Escudé J., Gould A., 2000, ApJ, 545, 847

Misner C. W., Thorne K. S., Wheeler J. A., Kaiser D. I., 2018, Gravitation

Moody M. S. L., Shi J.-M., Stone J. M., 2019, ApJ, 875, 66

Mori K., et al., 2021, ApJ, 921, 148

Mouri H., Taniguchi Y., 2002, ApJ, 566, L17

Muñoz D. J., Lithwick Y., 2020, ApJ, 905, 106

Muñoz D. J., Kratter K., Vogelsberger M., Hernquist L., Springel V., 2015, MNRAS, 446, 2010

Muñoz D. J., Miranda R., Lai D., 2019, ApJ, 871, 84

Muñoz D. J., Stone N. C., Petrovich C., Rasio F. A., 2022, arXiv e-prints, p. arXiv:2204.06002

Naoz S., Rose S. C., Michaely E., Melchor D., Ramirez-Ruiz E., Mockler B., Schnittman J. D., 2022, ApJ, 927, L18

Negueruela I., Coe M. J., 2002, A&A, 385, 517

Nesvorný D., Vokrouhlický D., Morbidelli A., 2007, AJ, 133, 1962

Nouri F. H., Janiuk A., 2023, arXiv e-prints, p. arXiv:2309.06028

O'Leary R. M., Kocsis B., Loeb A., 2009, MNRAS, 395, 2127

O'Leary R. M., Meiron Y., Kocsis B., 2016, ApJ, 824, L12

O'Neill D., D'Orazio D. J., Samsing J., Pessah M. E., 2024, arXiv e-prints, p. arXiv:2401.16166

O'Shaughnessy R., Kalogera V., Belczynski K., 2010, ApJ, 716, 615

Ogilvie G. I., Lubow S. H., 2002, MNRAS, 330, 950

Öpik E., 1924, Publications of the Tartu Astrofizica Observatory, 25, 1

Oppenheimer J. R., Volkoff G. M., 1939, Physical Review, 55, 374

Ostriker E. C., 1999, ApJ, 513, 252

Ott C. D., 2009, Classical and Quantum Gravity, 26, 063001

Özel F., Psaltis D., Narayan R., McClintock J. E., 2010, ApJ, 725, 1918

Pan Z., Yang H., 2021, Phys. Rev. D, 103, 103018

Panamarev T., Shukirgaliyev B., Meiron Y., Berczik P., Just A., Spurzem R., Omarov C., Vilkoviskij E., 2018, MNRAS, 476, 4224

Pankow C., Chase E. A., Coughlin S., Zevin M., Kalogera V., 2018, ApJ, 854, L25

Peters P. C., 1964, Physical Review, 136, 1224

Peters P. C., Mathews J., 1963, Physical Review, 131, 435

Poisson E., Will C. M., 1995, Phys. Rev. D, 52, 848

Pooley D., et al., 2003, ApJ, 591, L131

Portegies Zwart S. F., McMillan S. L. W., 2002, ApJ, 576, 899

Portegies Zwart S. F., Baumgardt H., Hut P., Makino J., McMillan S. L. W., 2004, Nature, 428, 724

Pretorius F., 2005, Phys. Rev. Lett., 95, 121101

Price D. J., 2007, PASA, 24, 159

Price D. J., 2012, Journal of Computational Physics, 231, 759

Price D. J., et al., 2018, PASA, 35, e031

Pürrer M., 2014, Classical and Quantum Gravity, 31, 195010

Pürrer M., Hannam M., Ohme F., 2016, Phys. Rev. D, 93, 084042

Raghavan D., et al., 2010, ApJS, 190, 1

Rakavy G., Shaviv G., 1967, ApJ, 148, 803

Ramos-Buades A., Buonanno A., Khalil M., Ossokine S., 2022, Phys. Rev. D, 105, 044035

Rasskazov A., Kocsis B., 2019, ApJ, 881, 20

Rauch K. P., Tremaine S., 1996, New A, 1, 149

Reitze D., et al., 2019, in Bulletin of the American Astronomical Society. p. 35 (arXiv:1907.04833), doi:10.48550/arXiv.1907.04833

Remillard R. A., McClintock J. E., 2006, ARA&A, 44, 49

Reynolds C. S., Young A. J., Begelman M. C., Fabian A. C., 1999, ApJ, 514, 164

Rodríguez-Ramírez J. C., Bom C. R., Fraga B., Nemmen R., 2023, arXiv e-prints, p. arXiv:2304.10567

Rodriguez C. L., Chatterjee S., Rasio F. A., 2016, Phys. Rev. D, 93, 084029

Rodriguez C. L., Zevin M., Amaro-Seoane P., Chatterjee S., Kremer K., Rasio F. A., Ye C. S., 2019, Phys. Rev. D, 100, 043027

Romero-Shaw I. M., Lasky P. D., Thrane E., 2019, MNRAS, 490, 5210

Romero-Shaw I., Lasky P. D., Thrane E., 2022, ApJ, 940, 171

Romero-Shaw I. M., Gerosa D., Loutrel N., 2023, MNRAS, 519, 5352

Röpke F. K., De Marco O., 2023, Living Reviews in Computational Astrophysics, 9, 2

Rowan C., Boekholt T., Kocsis B., Haiman Z., 2023, MNRAS, 524, 2770

Rowan C., Whitehead H., Boekholt T., Kocsis B., Haiman Z., 2024, MNRAS, 527, 10448

Rozner M., Generozov A., Perets H. B., 2022, arXiv e-prints, p. arXiv:2212.00807

Safarzadeh M., Hamers A. S., Loeb A., Berger E., 2020, ApJ, 888, L3

Sahu K. C., et al., 2022, ApJ, 933, 83

Salpeter E. E., 1955, ApJ, 121, 161

Samsing J., MacLeod M., Ramirez-Ruiz E., 2018, ApJ, 853, 140

Samsing J., et al., 2022, Nature, 603, 237

Sana H., et al., 2012, Science, 337, 444

Sari R., Goldreich P., 2004, ApJ, 606, L77

Sasaki M., Suyama T., Tanaka T., Yokoyama S., 2016, Phys. Rev. Lett., 117, 061101

Saxena A., et al., 2021, MNRAS, 505, 4798

Schnetter E., Hawley S. H., Hawke I., 2004, Classical and Quantum Gravity, 21, 1465

Schutz B. F., 1986, Nature, 323, 310

Schwarzschild K., 1916, Abh. Konigl. Preuss. Akad. Wissenschaften Jahre 1906,92, Berlin,1907, 1916, 189

Schwarzschild K., 1999, arXiv e-prints, p. physics/9905030

Secunda A., Bellovary J., Mac Low M.-M., Ford K. E. S., McKernan B., Leigh N. W. C., Lyra W., Sándor Z., 2019, ApJ, 878, 85

Secunda A., et al., 2020, ApJ, 903, 133

Sesana A., Vecchio A., Colacino C. N., 2008, MNRAS, 390, 192

Shakura N. I., Sunyaev R. A., 1973, A&A, 500, 33

Shankar F., Salucci P., Granato G. L., De Zotti G., Danese L., 2004, MNRAS, 354, 1020

Shappee B. J., et al., 2014, ApJ, 788, 48

Shen S., Wadsley J., Hayfield T., Ellens N., 2010, MNRAS, 401, 727

Shen Y., et al., 2011, ApJS, 194, 45

Sirko E., Goodman J., 2003, MNRAS, 341, 501

Smartt S. J., et al., 2017, Nature, 551, 75

Szölgyén Á., Kocsis B., 2018, Phys. Rev. Lett., 121, 101101

Szölgyén Á., Meiron Y., Kocsis B., 2019, ApJ, 887, 123

Szölgyén Á., Máthé G., Kocsis B., 2021, ApJ, 919, 140

Szuszkiewicz E., Malkan M. A., Abramowicz M. A., 1996, ApJ, 458, 474

Tagawa H., Saitoh T. R., Kocsis B., 2018, Phys. Rev. Lett., 120, 261101

Tagawa H., Haiman Z., Kocsis B., 2020a, ApJ, 898, 25

Tagawa H., Haiman Z., Bartos I., Kocsis B., 2020b, ApJ, 899, 26

Tagawa H., Haiman Z., Bartos I., Kocsis B., Omukai K., 2021a, MNRAS, 507, 3362

Tagawa H., Kocsis B., Haiman Z., Bartos I., Omukai K., Samsing J., 2021b, ApJ, 907, L20

Tagawa H., Kocsis B., Haiman Z., Bartos I., Omukai K., Samsing J., 2021c, ApJ, 907, L20

Tagawa H., Kocsis B., Haiman Z., Bartos I., Omukai K., Samsing J., 2021d, ApJ, 908, 194

Tagawa H., Kocsis B., Haiman Z., Bartos I., Omukai K., Samsing J., 2021e, ApJ, 908, 194

Tagawa H., Kimura S. S., Haiman Z., Perna R., Tanaka H., Bartos I., 2022, ApJ, 927, 41

Tagawa H., Kimura S. S., Haiman Z., Perna R., Bartos I., 2023a, ApJ, 946, L3

Tagawa H., Kimura S. S., Haiman Z., Perna R., Bartos I., 2023b, ApJ, 950, 13

Tagawa H., Kimura S. S., Haiman Z., 2023c, ApJ, 955, 23

Tagoshi H., Sasaki M., 1994, Progress of Theoretical Physics, 92, 745

Tanay S., Klein A., Berti E., Nishizawa A., 2019, Phys. Rev. D, 100, 064006

Tang Y., MacFadyen A., Haiman Z., 2017, MNRAS, 469, 4258

Thompson T. A., et al., 2019, Science, 366, 637

Tiede C., Zrake J., MacFadyen A., Haiman Z., 2020, ApJ, 900, 43

Tokovinin A. A., 2000, A&A, 360, 997

Tremaine S., et al., 2002, ApJ, 574, 740

Trippe S., et al., 2008, A&A, 492, 419

Turner M., 1977, ApJ, 216, 610

Ushomirsky G., Cutler C., Bildsten L., 2000, MNRAS, 319, 902

Vaccaro M. P., Mapelli M., Périgois C., Barone D., Artale M. C., Dall'Amico M., Iorio G., Torniamenti S., 2024, A&A, 685, A51

Varma V., et al., 2022, Phys. Rev. Lett., 128, 191102

Vecchio A., 2004, Phys. Rev. D, 70, 042001

Venumadhav T., Zackay B., Roulet J., Dai L., Zaldarriaga M., 2020, Phys. Rev. D, 101, 083030

Vergara M. Z. C., Schleicher D. R. G., Boekholt T. C. N., Reinoso B., Fellhauer M., Klessen R. S., Leigh N. W. C., 2021, A&A, 649, A160

Vigna-Gómez A., et al., 2024, Phys. Rev. Lett., 132, 191403

Vitale S., Evans M., 2017, Phys. Rev. D, 95, 064052

Vitale S., Lynch R., Veitch J., Raymond V., Sturani R., 2014, Phys. Rev. Lett., 112, 251101

Wagoner R. V., Will C. M., 1976, ApJ, 210, 764

Walsh D., Carswell R. F., Weymann R. J., 1979, Nature, 279, 381

Watkins S. J., Bhattal A. S., Boffin H. M. J., Francis N., Whitworth A. P., 1998a, MNRAS, 300, 1205

Watkins S. J., Bhattal A. S., Boffin H. M. J., Francis N., Whitworth A. P., 1998b, MNRAS, 300, 1214

Westernacher-Schneider J. R., Zrake J., MacFadyen A., Haiman Z., 2022, Phys. Rev. D, 106, 103010

Whitehead H., Rowan C., Boekholt T., Kocsis B., 2023a, arXiv e-prints, p. arXiv:2309.11561

Whitehead H., Rowan C., Boekholt T., Kocsis B., 2023b, arXiv e-prints, p. arXiv:2312.14431

Woosley S. E., Wilson J. R., Mathews G. J., Hoffman R. D., Meyer B. S., 1994, ApJ, 433, 229

Yang Y., Bartos I., Haiman Z., Kocsis B., Márka Z., Stone N. C., Márka S., 2019, ApJ, 876, 122

Yang Y., Bartos I., Haiman Z., Kocsis B., Márka S., Tagawa H., 2020, ApJ, 896, 138

Yunes N., Kocsis B., Loeb A., Haiman Z., 2011, Phys. Rev. Lett., 107, 171103

Zahn J. P., 1977, A&A, 57, 383

Zahn J. P., 2008, in Goupil M. J., Zahn J. P., eds, EAS Publications Series Vol. 29, EAS Publications Series. pp 67–90 (`arXiv:0807.4870`), doi:10.1051/eas:0829002

Zevin M., Samsing J., Rodriguez C., Haster C.-J., Ramirez-Ruiz E., 2019a, ApJ, 871, 91

Zevin M., Samsing J., Rodriguez C., Haster C.-J., Ramirez-Ruiz E., 2019b, ApJ, 871, 91

Zrake J., Tiede C., MacFadyen A., Haiman Z., 2021, ApJ, 909, L13